National Library of Canada
Bibliothèque nationale du Canada

Acquisitions and Bibliographic Services Branch
Direction des acquisitions et des services bibliographiques

395 Wellington Street
Ottawa, Ontario
K1A 0N4

395, rue Wellington
Ottawa (Ontario)
K1A 0N4

Your file Votre référence

Our file Notre référence

NOTICE

The quality of this microform is heavily dependent upon the quality of the original thesis submitted for microfilming. Every effort has been made to ensure the highest quality of reproduction possible.

If pages are missing, contact the university which granted the degree.

Some pages may have indistinct print especially if the original pages were typed with a poor typewriter ribbon or if the university sent us an inferior photocopy.

Reproduction in full or in part of this microform is governed by the Canadian Copyright Act, R.S.C. 1970, c. C-30, and subsequent amendments.

AVIS

La qualité de cette microforme dépend grandement de la qualité de la thèse soumise au microfilmage. Nous avons tout fait pour assurer une qualité supérieure de reproduction.

S'il manque des pages, veuillez communiquer avec l'université qui a conféré le grade.

La qualité d'impression de certaines pages peut laisser à désirer, surtout si les pages originales ont été dactylographiées à l'aide d'un ruban usé ou si l'université nous a fait parvenir une photocopie de qualité inférieure.

La reproduction, même partielle, de cette microforme est soumise à la Loi canadienne sur le droit d'auteur, SRC 1970, c. C-30, et ses amendements subséquents.

Canada

THE UNIVERSITY OF ALBERTA

CLASSICAL AND QUANTUM VIBRATION IN A NONSEPARABLE, NONHARMONIC SYSTEM

by

KAREN MARIE McDONALD

©

A THESIS SUBMITTED

TO THE FACULTY OF GRADUATE STUDIES AND RESEARCH

IN PARTIAL FULFILMENT OF THE REQUIREMENTS

FOR THE DEGREE OF DOCTOR OF PHILOSOPHY

in

CHEMISTRY

DEPARTMENT OF CHEMISTRY

EDMONTON, ALBERTA

FALL, 1992

National Library of Canada
Acquisitions and Bibliographic Services Branch
395 Wellington Street
Ottawa, Ontario
K1A 0N4

Bibliothèque nationale du Canada
Direction des acquisitions et des services bibliographiques
395, rue Wellington
Ottawa (Ontario)
K1A 0N4

Your file Votre référence

Our file Notre référence

The author has granted an irrevocable non-exclusive licence allowing the National Library of Canada to reproduce, loan, distribute or sell copies of his/her thesis by any means and in any form or format, making this thesis available to interested persons.

L'auteur a accordé une licence irrévocable et non exclusive permettant à la Bibliothèque nationale du Canada de reproduire, prêter, distribuer ou vendre des copies de sa thèse de quelque manière et sous quelque forme que ce soit pour mettre des exemplaires de cette thèse à la disposition des personnes intéressées.

The author retains ownership of the copyright in his/her thesis. Neither the thesis nor substantial extracts from it may be printed or otherwise reproduced without his/her permission.

L'auteur conserve la propriété du droit d'auteur qui protège sa thèse. Ni la thèse ni des extraits substantiels de celle-ci ne doivent être imprimés ou autrement reproduits sans son autorisation.

ISBN 0-315-77326-X

Canada

THE UNIVERSITY OF ALBERTA

RELEASE FORM

NAME OF AUTHOR Karen Marie McDonald

TITLE OF THESIS Classical and Quantum Vibration in a Nonseparable, Nonharmonic System

DEGREE FOR WHICH THESIS WAS PRESENTED Ph. D.

YEAR THIS DEGREE GRANTED 1992

Permission is hereby granted to the UNIVERSITY OF ALBERTA LIBRARY to reproduce single copies of this thesis and to lend or sell such copies for private, scholarly or scientific research purposes only.

The author reserves other publication rights, and neither the thesis nor extensive extracts from it may be printed or otherwise reproduced without the author's written permission.

Karen McDonald

(Signed)

Permanent Address:
10959 34A Avenue
Edmonton, Alberta
CANADA T6J 2T9

Date 18 August 92

THE UNIVERSITY OF ALBERTA

FACULTY OF GRADUATE STUDIES AND RESEARCH

The undersigned certify that they have read, and recommended to the Faculty of Graduate Studies and Research for acceptance, a thesis entitled

CLASSICAL AND QUANTUM VIBRATION IN A
NONSEPARABLE, NONHARMONIC SYSTEM

submitted by Karen Marie McDonald in partial fulfilment of the requirements for the degree of Doctor of Philosophy.

Supervisor Dr. W. R. Thorson

Dr. J. E. Bertie

Dr. M. Klobukowski

Dr. J. Takats

Dr. J. A. Tuszynski

External Examiner Dr. J. B. Delos

Date 14 August 1992

For Eve

ABSTRACT

Studies of vibrational dynamics have been performed on a two-dimensional model potential surface $V(x, z; R)$, adapted from the *ab initio* surface previously used in this laboratory to analyze dynamics of the bifluoride ion $[\mathrm{FHF}]^-$. The model potential has C_{2v} symmetry, but is strongly anharmonic and nonseparable in the dynamical variables (x, z); its character changes as the parameter R is varied. Quantum and classical descriptions of vibrational states in this system are compared with corresponding *Self-Consistent Field* (SCF) approximations. Insights provided by each approach are assessed.

Systematic *Fermi resonances* appear in the quantum mechanical states (at energies up to approximately 10,000 cm^{-1}) arising from crossings of quantum SCF levels with two quanta of vibration exchanged between x and z modes. The lowest quantum states of each symmetry are well described by the SCF approximation except near such crossings. Calculations using Configuration Interaction were done to obtain accurate eigenstates and examine correlations in the quantum mechanics.

The *Classical* Self-Consistent Field (CSCF) method provides a description of the mechanics similar to that given by its quantum counterpart. Classical bound state methods based on semiclassical quantization of quasiperiodic trajectories are unable to give a corresponding description. At energies as low as the quantum ground state, the true classical dynamics is strongly disturbed by resonant interactions. At higher energies the number and strength of these disruptions is so great that the motion is largely irregular. The most prominent effect is a 1:1 frequency resonance associated with strong reorganization of the classical motion along pronounced valleys of the potential surface lying at ±26° to the x-axis. This phenomenon has been studied by analysis of the true dynamics and by application of classical canonical perturbation theory to the zero-order CSCF description. It is found that the latter gives a very accurate account of the true dynamics except when a reorganization occurs, and that it is able to signal the onset of strong disruptions. The disruption associated with 1:1 frequency resonance is the direct classical analogue of the Fermi resonance effects in the quantum mechanics of the system and relevant comparisons between the two descriptions have been made.

ACKNOWLEDGEMENTS

I would like to thank Professor Walter R. Thorson for kindly taking on the task of supervising a very dejected graduate student. His guidance enabled me to learn, to grow and finally to complete my degree with the confidence necessary for my future work. In addition, I would like to thank him for taking time for teaching and discussion of the philosophy of science; it has given me an appreciation of the challenge that awaits science in the future.

There are several individuals within the Department of Chemistry who deserve my thanks. Dr. Ted McClung has generously provided me with education on the TeX word processor and the use of his Laserjet printer; the production of this document would have been much more difficult without his help. I have been exposed to new ideas and cultures by Dr. Al Kalantar through our conversations which have explored almost every topic. I have been fortunate enough to have had three friends as role models of women in science. Dr. Anna Jordan's realistic and no-nonsense approach to balancing work and home has been an inspiration to me and the understanding that I have also to take time and energy to care for myself has been provided by Dr. Lois Brown. Lastly, Dr. Margaret Sisley's sense of independence has rounded out the valuable lessons I've received from these three women.

I must make a special acknowledgement of Dr. Fraser W. Birss who passed away while I was a graduate student of his. He taught me that it is possible to be a scientist and a gentleman. By example, he showed me methods of approaching problems in topics of both science and humanity. He is greatly missed.

My family has been a source of encouragement. In particular, my mother has always inspired me with her strength and pressed upon me the notion that I am a capable person even when I didn't believe it. My stepfather Ray has been nothing but kind and his presence in my life has had more of an effect than I think anyone else realizes. I would like to acknowledge the birth of my nephew Robert in May of 1991; I thank Chris for bringing this new life into our family at this time. I would also like to thank my father for being so proud of me even though I didn't choose a "profession".

There are many people who have become very important to me during my time in graduate school. I wish to acknowledge Dan Raymond who helped with my adjustment to life in Edmonton and so much more. Laurie and Deb Danielson have been friends through the thick and thin of it all. Lauren Warrack, my shopping buddy, has been a supportive companion (and thanks to Bill for putting up with us). Allan and Jean Warrack have shown me great hospitality at those times when I needed to feel part of a family. Helen Ross has provided me with personal confidence that could be gained in no other way. From my longest friend, Tene Barber, to my newest friend, Loni Shilliday, all of these people have given me their support when times seemed the hardest.

The financial support of the University of Alberta, Department of Chemistry is acknowledged. This support has been greatly appreciated given that I required somewhat more time than usual because of circumstance.

Finally, I would like to thank my husband, Bob McDonald, for giving me support and love. These past few years have been very trying for us as we both finished our degrees and obtained jobs in the city of Edmonton. I pray that our new home will be a comforting haven for many years.

Contents

1 Introduction **1**
- 1.1 Classical Vibrational Dynamics 1
- 1.2 The Vibrational Potential Surface 7
- 1.3 Outline of the Thesis 18

2 Quantum Mechanical Calculations **20**
- 2.1 Introduction 20
- 2.2 SCF Approximation in Vibrational Dynamics 22
- 2.3 Rapid Numerical Solution of SCF Equations 27
- 2.4 Analysis of Quantum SCF Results 31
- 2.5 Configuration Interaction 40
- 2.6 Analysis of CI Results 43

3 Semiclassical SCF Theory **81**
- 3.1 Introduction 81
- 3.2 Classical SCF Equations 84
- 3.3 Comparison of SCF Theories 91

4 Classical Vibrational Dynamics **101**
- 4.1 Introduction 101
- 4.2 Classical Theory 104
- 4.3 Technical Methods 116
- 4.4 Trajectory Analysis 122

5 Canonical Perturbation Theory **157**
- 5.1 Introduction 157
- 5.2 Perturbation Calculations 160
- 5.3 Classical Perturbation Results 169

6 Conclusions **196**

List of Figures

1.1 The [FHF]$^-$ System and its normal modes: 8
1.2 Potential Surfaces in the quarter plane for $3.80 \leq R \leq 4.80$ a.u. . . 14

2.1 Quantum SCF energies *vs.* n_x, n_z at $R = 4.30$ a.u. 32
2.2 Quantum SCF energies *vs.* n_x, n_z at $R = 4.70$ a.u. 33
2.3 Quantum SCF energy level diagram in A_1 symmetry 36
2.4 Quantum SCF energy level diagram in A_2 symmetry 37
2.5 Quantum SCF energy level diagram in B_1 symmetry 38
2.6 Quantum SCF energy level diagram in B_2 symmetry 39
2.7 Quantum CI energy level diagram in the A_1 symmetry: 44
2.8 Quantum CI energy level diagram in the A_2 symmetry: 45
2.9 Quantum CI energy level diagram in the B_1 symmetry: 46
2.10 Quantum CI energy level diagram in the B_2 symmetry: 47
2.11 Quantum CI wave functions for $R = 4.30$ a.u. states 52
2.12 Quantum CI wave functions near (2,0)x(0,2) 71
2.13 Quantum CI wave functions near (4,0)x(2,2) 74
2.14 Quantum CI wave functions near (6,0)x(4,2)x(0,4) 77

3.1 Double well diagram 87
3.2 Expectation values near a barrier top 89
3.3 Semiclassical SCF Energy Surface 95
3.4 A_1 semiclassical SCF energy levels 96
3.5 A_2 semiclassical SCF energy levels 97
3.6 B_1 semiclassical SCF energy levels 98
3.7 B_2 semiclassical SCF energy levels 99

4.1 Invariant torus for regular motion 107
4.2 Typical Boxlike Family Trajectory 112
4.3 Typical 1:1 Resonant Family Trajectory 113
4.4 Types of P.S.S. Integrated 119
4.5 Classical Trajectories at $E = 24.0$ c.e.u. & $R = 4.30$ a.u. 126
4.6 Composite P.S.S. at $E = 24.0$ c.e.u. & $R = 4.30$ a.u. 132
4.7 Poincaré surfaces-of-section in a rotated coordinate frame 141
4.8 Action variations with f_x 144

4.9 Frequency variations with f_x 145
4.10 Nonorthogonal average tracks at $E = 24.0$ c.e.u. 148
4.11 Classical Trajectories in a Bifurcation Region 150
4.12 Depiction of Global Behaviour 155

5.1 Boxlike Perturbation trajectories and P.S.S. 170
5.2 Classical and Perturbation Trajectories near a 3:5 Resonance 179
5.3 Composite Poincaré surfaces-of section by a 3:5 Resonance 180
5.4 Classical actions J_z versus J_x. 182
5.5 Perturbation and Classical Trajectories across a Bifurcation 185
5.6 Poincaré Surfaces-of-Section across a Bifurcation 191

List of Tables

1.1 Model Potential Parameters 12

2.1 Quantum CI and SCF State Energies at $R = 4.30$a.u. 48

4.1 X-Fourier Series at $E = 24.0$ c.e.u. and $f_x = 0.3$ 135
4.2 Z-Fourier Series at $E = 24.0$ c.e.u. and $f_x = 0.3$ 136
4.3 X-Fourier Series at $E = 24.0$ c.e.u. and $f_x = 0.55$ 137
4.4 Z-Fourier Series at $E = 24.0$ c.e.u. and $f_x = 0.55$ 138
4.5 Comparison of Action Calculations in boxlike trajectories 139
4.6 Actions and freqencies for the resonant family 142
4.7 X-Fourier Series at $E = 24.0$ c.e.u. and $f_x = 0.6$ 146
4.8 Z-Fourier Series at $E = 24.0$ c.e.u. and $f_x = 0.3$ 147
4.9 FFT Freqencies near the Bifurcation 154

5.1 Classical SCF-PT energies and frequencies at $E_{CT} = 24.0$ 175
5.2 CSCF-PTN Fourier series at $f_x = 0.30$ 176
5.3 CSCF-PTN Fourier series at $f_x = 0.55$ 177
5.4 Classical SCF Perturbation results across the gap region 184

Chapter 1

Introduction

1.1 Classical Vibrational Dynamics

This work is a comparative study of the classical self-consistent field approximation with exact classical dynamics and corresponding quantum mechanical descriptions of vibrational motion in a strongly nonharmonic and nonseparable model system. The model potential is a simplified two-dimensional analogue to a realistic extended potential surface based on *ab initio* calculations for the strongly hydrogen-bonded bifluoride ion, $[FHF]^-$. The latter was developed by Epa and Thorson [1,2,3] for an analysis of vibrational spectra in bifluoride systems. They showed that an accurate quantum mechanical description of vibrational energy levels of $[FHF]^-$ (up to about 10,000 cm^{-1} above the ground level) can be based on an adiabatic separation of proton motions (ν_2, ν_3) from the F–F stretch motion (ν_1) followed by an approximate separation of the proton bending and stretching modes via the self-consistent field (SCF) method. In particular, the overall success of the SCF description was striking given the complexity of the potential surface.

In the past 10–15 years, there has been considerable interest in classical mechanics as a means of understanding molecular vibrational levels. The motivation for the current investigations arose in an attempt to form similar comparisons for a system with marked anharmonic and nonseparable character. Except for work concerned specifically with irregular or *chaotic* motion in very highly excited systems, most applications of classical dynamics to molecular vibrations have tended to concentrate on nearly harmonic systems. Moreover, while the classical self-consistent field approximation has been used by Gerber and Ratner [16] to compute semiclassical energy levels for some systems, the general connections between the classical self-consistent field representation and the corresponding exact classical dynamics do not appear to have been explored. In view of the effectiveness of SCF theory as a quantum mechanical description for the bifluoride ion, the $[FHF]^-$ model offered a good opportunity for such exploration.

Some initial computations were carried out using the $[FHF]^-$ potential itself. Only proton dynamics were treated; the F–F separation coordinate, R(F–F), was regarded simply as a parameter affecting the bend-stretch potential surface for proton motion. Even so, the $[FHF]^-$ model system has certain complicating features which are not essential to the goals of this study. In particular, the angular momentum associated with the ν_2 bending mode and the use of prolate spheroidal coordinates for the proton both complicate the kinetic energy expression. To avoid unnecessary difficulties, the complete $[FHF]^-$ surface was adapted to a two-dimensional model employing Cartesian coordinates; R remains as a variable parameter which alters the surface as it does in $[FHF]^-$. The analogue problem preserves essential characteristics of the bifluoride ion potential surface, but is conceptually and computationally much simpler. Results presented in this thesis were obtained using this simpler model.

Particular interest in the comparison with quantum results arises from the fact that systematic crossings of quantum SCF levels occur at certain R separations; these become *avoided* crossings of the exact levels due to strong coupling between the

SCF states. Relations to corresponding phenomena in the classical description, such as frequency resonances and associated transitions between qualitatively different types of regular motions, have formed the general theme of this work.

This work does not directly address the typical concerns of nonlinear dynamics, such as the onset of irregular or chaotic motion. However, some understanding of the subject and its nomenclature is relevant, especially as it bears on Hamiltonian dynamics. We shall see that an interesting aspect of the self-consistent field theory is its tendency to suppress or ignore couplings which produce chaotic behaviour in the true classical dynamics.

Interest in nonlinear dynamical systems and their characteristic behaviour is extremely widespread since such behaviour pervades both the natural world and nearly all scientific models describing it. Literature on the subject ranges from highly technical and theoretical work [4,5] to accounts in popular science magazines [6]. The field is essentially a modern development, emerging only with the advent of high-speed digital computers. Most achievements of physical theory until about 1960 employed classic methods based on solving linear equations or approximations to nonlinear equations which render the systems linear under constraining conditions. Such methods were the only effective ones given the difficulty inherent in processing a large number of calculations by hand or with the limited computational tools available. With more powerful computers it became possible to model natural phenomena more realistically. Aided by improved computer graphics, information is visualized and patterns identified that would otherwise be lost if left merely as numerical output. The subject of nonlinear dynamics has developed out of the recognition that wide classes of problems present certain basic similarities in behaviour.

Nonlinear dynamics proper may be said to have begun in 1963 with Edward Lorenz [7] who was using the new computing tools to explore models of meterological systems with few parameters. In spite of the fact that the equations of motion for such models were entirely deterministic, he found that the predicted behaviour depended in a hypersensitive way on the initial conditions. This surprising result implied that, no matter how extensive or precise the computing or how accurate the input measurements for initial conditions might be, the weather could never be predicted beyond a limited time range. Lorenz's work pioneered the study of an essential feature of nonlinear dynamics, *deterministic chaos*. Even though completely deterministic in an analytical sense, behaviour in a dynamical system with nonlinear equations of motion cannot be predicted reliably because, in certain cases, the states of two identical systems with initial conditions arbitrarily close together will eventually diverge exponentially from one another. In other domains, depending on the nature of the nonlinear system, regularly predictable phenomena such as periodic or multiply periodic motion may be stabilized.

Since the original studies of Lorenz, a wide range of natural phenomena has been shown to exhibit nonlinear dynamical behaviour. Turbulent flow, the mixing of fluids, the interaction of biological populations, and feedback control in electrical circuits including the heart and brain are only a representative sample of problems currently being investigated. Chemical applications have included the treatment of oscillatory reactions, surface reactions and electrochemistry, as well as problems in molecular vibrational dynamics: the topic studied here.

In classical Hamiltonian mechanics for a conservative system, possible solutions to the nonlinear differential equations of motion include *periodic* and *quasiperiodic* solutions for *regular* motion and *chaotic* solutions for *irregular* motion. In both cases of regular motion, the system is characterized by the existence of constants of the motion for each degree of freedom called *action variables* and coordinates called *angle variables* that are canonically conjugate to them. The angles increase linearly with time and their time derivatives are the *frequencies* of the motion. Under these conditions, the coordinates and momenta describing the motion of the system in phase space may all be expanded as multiple Fourier series based on the fundamental frequencies. The distinction between periodic and quasiperiodic motion depends on whether the frequencies associated with different angle variables are, or are not, rationally commensurate. If the ratios of all frequencies are expressible as ratios of integers, then the orbit of the system closes upon itself in a finite time and the motion is periodic. Otherwise, the motion is quasiperiodic and the orbit will never exactly close upon itself. The trajectory over time covers a restricted region in phase space associated with a surface called the *invariant torus* for the motion. The case of irregular or chaotic motion occurs when action-angle variables do not exist and the motion cannot therefore be characterized by Fourier expansions involving a finite number of frequencies. This use of the term *chaos* should be distinguished carefully from the loose vernacular usage associated with concepts of randomness or noise. In natural systems, chaos is a mechanism for generating necessary variability in a somewhat *controlled* manner. In nonlinear dynamics, a general definition of chaos is any irregular behaviour which is deterministic but extremely sensitive to initial conditions [8]. Chaotic motion appears in transitional regions separating regular regimes associated closely with particular periodic trajectories as their paradigms; perhaps it may be viewed as the result of competition between alternative qualitatively distinct motions. Since periodic orbits are associated with rational frequency ratios, as the total energy of a dynamical system increases, the occurrence of chaotic motion is increasingly finely interspersed between shrinking domains of regularity. It is a widely held view that classical chaos appears to have little direct bearing on order/disorder in quantum systems, and even the *existence* of "quantum chaos" is controversial.

This work has no direct interest in chaotic behaviour itself but in the relations between regular motion and the corresponding quantum mechanical description of the same system. We have carried out an extensive calculation of the quantum states for proton motion in this model system and will briefly discuss the results. The Classical Self-Consistent Field (CSCF) method has been applied with semiclassical quantization conditions to obtain the analogous semiclassical SCF description of the quantum states for comparison with the quantum SCF description. As noted above, for low-lying states of the system, the quantum SCF approximation gives a remarkably good description. Concentrating on the range of energies for which this is the case, we have carried out extensive comparisons of the exact classical dynamics and the CSCF approximation. As classical states may have any set of action values, it is not necessary to impose semiclassical quantum conditions, so that a continuous map of the classical phase space can be generated. Canonical perturbation theory has been applied with the CSCF approximation as the zero-order description and the resulting motion is compared in detail with the true dynamics where the latter is regular. The general conclusions drawn from such comparisons are summarized in this thesis.

1.2 The Vibrational Potential Surface

The model potential employed in these studies is for a particle moving in two dimensions with Cartesian coordinates, (x, z). The potential $V(x, z; R)$ has C_{2v} symmetry with mirror planes in the Cartesian axes. It also depends parametrically on a third coordinate R, which is not treated dynamically, but affects the general shape of the surface. It is an adaptation from a realistic model surface for the bifluoride ion, $[\mathrm{FHF}]^-$, based on extended *ab initio* quantum chemical calculations for the ground electronic state of this species performed at the SCF-CID level (Self-Consistent Field and Configuration Interaction with Double replacement). These calculations and the construction of the $[\mathrm{FHF}]^-$ surface are described fully by Epa, Thorson and Klobukowski [1] and are briefly summarized here.

Starting from a $D_{\infty h}$ symmetry for F–H–F, let R be the F–F separation, z the stretching displacement of the proton from the geometric centre along the F–F axis, and (ρ, ϕ) the bending displacement and its azimuthal angle in cylindrical coordinates as displayed in Figure 1.1. *Ab initio* quantum chemical calculations were performed for the ion at more than 700 geometries covering a range of R-values $3.60 \leq R \leq 7.20$ a.u. and all (ρ, z) values with energies less than 30,000 cm^{-1} above the potential minimum of the resulting surface. The equilibrium $D_{\infty h}$ configuration occurs at $R^0_{eq} = 4.290513$ a.u. and the computed hydrogen bond dissociation energy (into H–F and F^-) is $\Delta E^e_{hy} = 48.13$ kcal/mol $= 0.076694$ a.u.

The surface model fitted to this data is based on a skeleton given by a sum of Morse potentials (one for each F–H interaction),

$$V_{Morse} = V_{HF}(r_1) + V_{HF}(r_2) - D_e, \qquad [1.1]$$

$$V_{HF}(r_i) = D_e\left[1 - e^{-a(r_i - r_{eq})}\right]^2, \qquad [1.2]$$

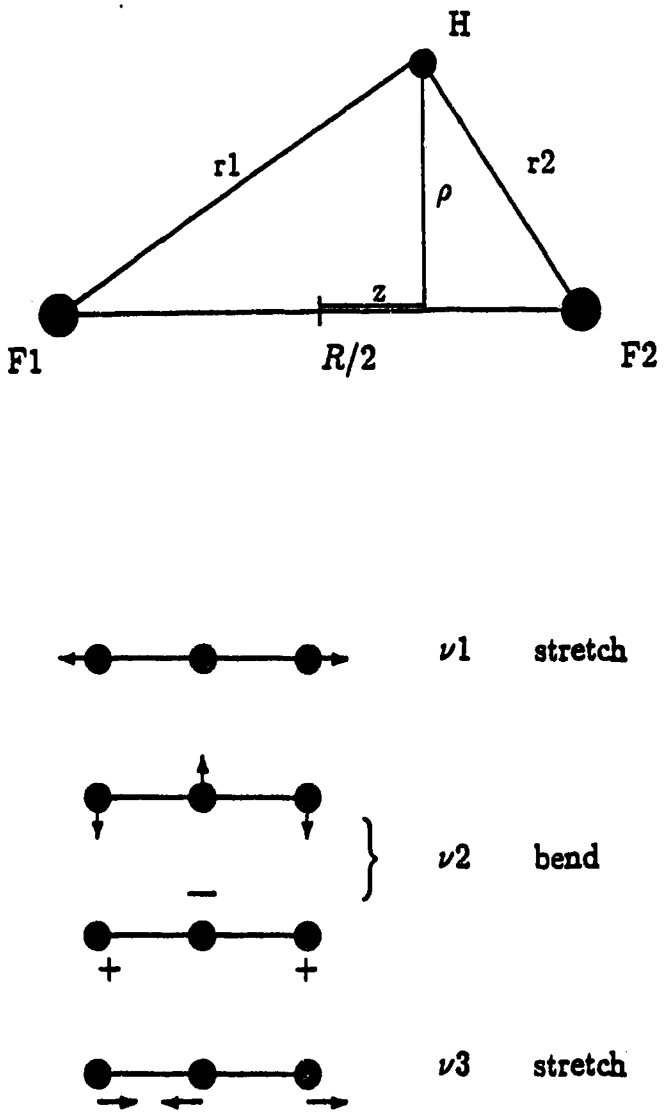
H
r1
r2
ρ
z
F1
R/2
F2
ν1
stretch
−
+
+
ν2
bend
ν3
stretch

Figure 1.1: The $[FHF]^-$ System and its normal modes:

where r_i is the distance from the proton to the ith fluorine atom. The equilibrium F–H separation $r_{eq} = 1.756088$ a.u. and the dissociation energy $D_e = 0.246429$ a.u. = 54083 cm^{-1} were determined by fitting a Morse potential to *ab initio* SCF-CID data for the HF molecule.

This skeleton describes the strongest variations on the surface. The correction needed to fit the *ab initio* SCF-CID data points for $[\mathrm{FHF}]^-$ is relatively smooth and slowly varying. Prolate spheroidal coordinates (ξ, η, ϕ) for the proton are well suited to describe the skeleton since

$$\xi = \frac{(r_1 + r_2)}{R}, \qquad \eta = \frac{(r_1 - r_2)}{R}, \tag{1.3}$$

and the correction potential V_{corr} was fitted by a 36-term polynomial of the form

$$V_{corr} = e^{-\beta(R-R_{eq})} \sum_{i=0}^{2} \sum_{j=0}^{2} \sum_{k=0}^{3} A_{ijk} (\xi - 1)^i \eta^{2j} (R - R_{eq})^k \tag{1.4}$$

with an r.m.s. deviation of 65.6 cm^{-1} for all 710 *ab initio* data points and 26.5 cm^{-1} for the 484 points less than 15,000 cm^{-1} above the minimum. The potential minimum for the model surface occurs at $R_{eq} = 4.2875112$ a.u. and lies 63.6 cm^{-1} above the correct *ab initio* hydrogen bond energy.

The resulting model surface is depicted graphically in Paper I [1] of the series on $[\mathrm{FHF}]^-$. At R-values less than about 4.5 a.u., it possesses a single potential minimum at the $D_{\infty h}$ configuration, but as R increases a double well potential with minima at $\rho = 0, z = \pm z_0$ and a barrier at (0,0) forms as the system begins to dissociate into HF + F^-. At still larger R values, a pronounced potential valley appears in each well for bending motion associated with libration of a dipolar H–F molecule about its equilibrium orientation toward the opposite F^- ion.

This surface was used by Epa and Thorson [2] to do a complete analysis of vibrational dynamics in the bifluoride system and apply it to the experimental IR and Raman spectra of both the free ion and its crystalline salts (KHF_2

and $NaHF_2$). The F–F (ν_1) symmetrical stretch associated with coordinate R is approximately separable from the proton motions by the adiabatic approximation which requires that the proton dynamics be solved at each R-value. This is analogous to the Born-Oppenheimer approximation for a diatomic molecule, wherein the electronic Schrödinger equation must be solved for each internuclear separation to produce electronic state potential curves and wave functions which depend parametrically upon the separation. To treat the proton vibrational dynamics, Epa and Thorson used the Self-Consistent Field (SCF) approximation to separate the proton asymmetrical stretching motion (ν_3) (prolate spheroidal coordinate η) from the bending/librational motion (ν_2) (prolate spheroidal coordinate ξ); of course, the angular momentum associated with the azimuth ϕ is exactly separable. Numerically accurate protonic eigenstates were then constructed as linear combinations of exact numerical SCF solutions in a large basis set following the method of Configuration Interaction (CI). For the first 3–5 states of each symmetry type, it was found that the SCF approximation yields a good description of individual proton eigenstates except near isolated *curve crossings* where strong mixing of two or more SCF states occurs. Avoided crossings of the true adiabatic proton eigenstates occur at these points. The portion of the IR spectrum accessible in experimental bifluoride systems lies entirely in this low-lying energy region. Higher levels of the system are increasingly complex and the SCF approximation is much less adequate as a zero-order description.

As stated earlier, some initial studies on the classical description of protonic states and dynamics in the $[FHF]^-$ model system itself were performed. However, it became evident that the features of the problem of greatest interest for this study are complicated unnecessarily by the angular momentum associated with the bending mode and the use of prolate spheroidal coordinates. Therefore, the model surface was adapted to a two-dimensional analogue which retains the features of interest. The analogue surface $V(x, z; R)$ is constructed by substituting the prolate spheroidal coordinates by their approximations near the origin. This warp mapping to Cartesian coordinates (x, z) is accomplished by

$$\sqrt{2(\xi - 1)} \rightarrow \bar{x} = \frac{2}{R}x; \qquad \eta \rightarrow \bar{z} = \frac{2}{R}z. \tag{1.5}$$

With these modifications, the potential has the form

$$V(x, z; R) = V_{Morse}(x, z; R) + V_{corr}(x, z; R), \tag{1.6}$$

where

$$\begin{aligned} V_{Morse} &= D_e \Big[1 - 4e^{a(r_e - R/2)} e^{\frac{-ax^2}{R}} \cosh(az) \\ &+ 2\,e^{2a(r_e - R/2)} e^{\frac{-2ax^2}{R}} \cosh(2az) \Big], \qquad [1.7] \\ V_{corr} &= \sum_{i=0}^{2} \sum_{j=0}^{2} A_{ij}(R)\, x^{2i}\, z^{2j}. \qquad [1.8] \end{aligned}$$

The coefficients $A_{ij}(R)$ at each R-value are given in terms of the 36-parameter set of fitted coefficients $\{A_{ijk}\}$ from equation [1.4] by

$$A_{ij}(R) = e^{-\beta(R - R_e)} \sum_{k=0}^{3} A_{ijk}\,(R - R_e)^k \left[\frac{2}{R}\right]^{2i+2j} \frac{1}{2^i}, \tag{1.9}$$

A list of potential parameters appearing in equations [1.8] and [1.9] is given in Table 1.1.

Conversion parameters :	1 a.u.	=	$2.194746354 \times 10^5\,\mathrm{cm}^{-1}$
	1 c.e.u.	=	2.795276×10^{-4} a.u.
	1 c.e.u.	=	$61.34922\,\mathrm{cm}^{-1}$
Physical parameters :	R_{eq}	=	4.28751115 a.u.
	r_{eq}	=	1.756088 a.u.
	D_e	=	0.246419 a.u.
Fitted parameters :	a	=	1.197991
	β	=	1.10

i	j	k	a_{ijk}	i	j	k	a_{ijk}
0	0	0	0.1045114	0	0	2	−0.03985370
1	0	0	−0.2581777	1	0	2	0.06045994
2	0	0	0.2543577	2	0	2	0.05203691
0	1	0	−0.3403733	0	1	2	0.3316855
1	1	0	2.303700	1	1	2	−1.310734
2	1	0	−3.766092	2	1	2	2.041520
0	2	0	0.2114033	0	2	2	−0.4505100
1	2	0	−3.899906	1	2	2	2.345956
2	2	0	9.768322	2	2	2	−3.914078
0	0	1	−0.02289255	0	0	3	−0.01992940
1	0	1	−0.2065459	1	0	3	0.08256237
2	0	1	0.4687226	2	0	3	−0.1395932
0	1	1	0.1962620	0	1	3	0.04622900
1	1	1	1.034715	1	1	3	−0.01855407
2	1	1	−3.262457	2	1	3	−0.9046483
0	2	1	−1.185633	0	2	3	0.01413139
1	2	1	5.651424	1	2	3	−0.05822805
2	2	1	−9.507244	2	2	3	1.616017

Table 1.1: Model Potential Parameters

A sequence of potential contour maps for the surface is shown for the quarter plane ($x, z \geq 0$) in Figure 1.2 for R-values from 3.8 to 4.8 a.u. at intervals of 0.1 a.u.The contours have a spacing of 25 c.e.u. ("convenient energy units"). The c.e.u., used widely throughout this work, was originally defined for the $[\mathrm{FHF}]^-$ system. It is equal to $\hbar^2/2ma_0^2$, where a_0 is one atomic distance unit (0.5286 Å) and $m = 2M_H M_F/(M_H + 2M_F)$ is the reduced mass for proton vibrational motion in $[\mathrm{FHF}]^-$; 1.000 c.e.u. = 61.34922 cm^{-1} = 2.79527610^{-4} Hartrees. The zero-point energy of the ground vibrational state is 25–30 c.e.u. depending upon R.

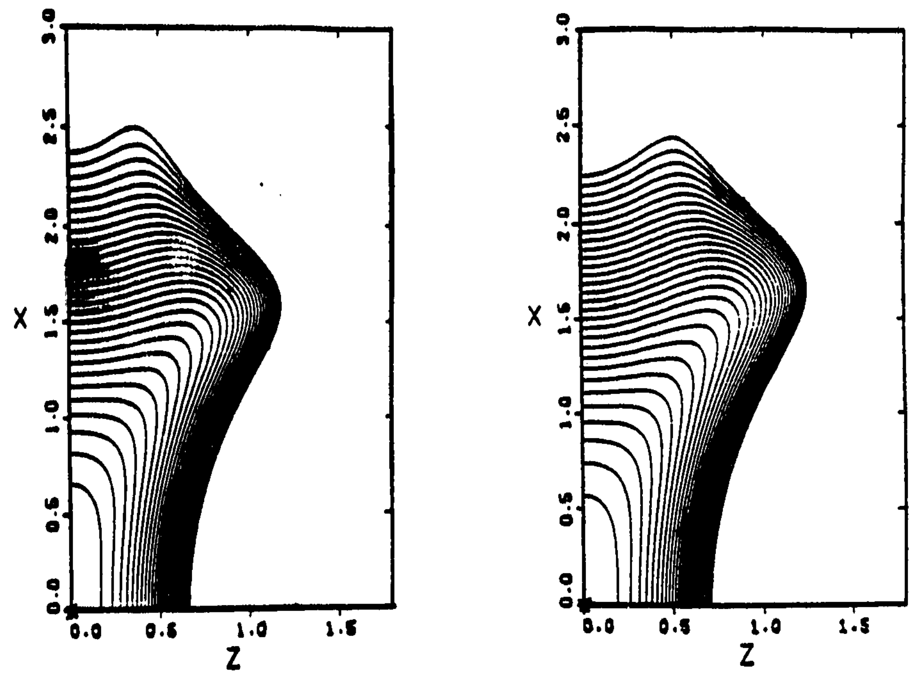

Equipotential contours for R = 3.80 Equipotential contours for R = 3.90

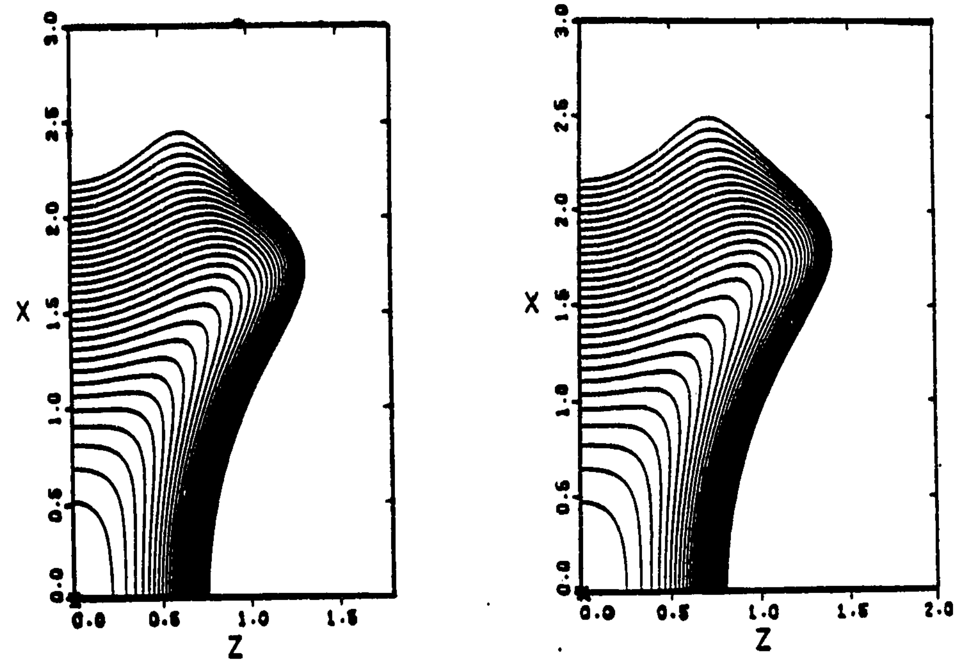

Equipotential contours for R = 4.00 Equipotential contours for R = 4.10

Figure 1.2: Potential Surfaces plotted in the quarter plane for $3.80 \leq R \leq 4.80$ a.u. in intervals of 0.1 a.u.The asterisk denotes the location of the potential minimum at each R-value.

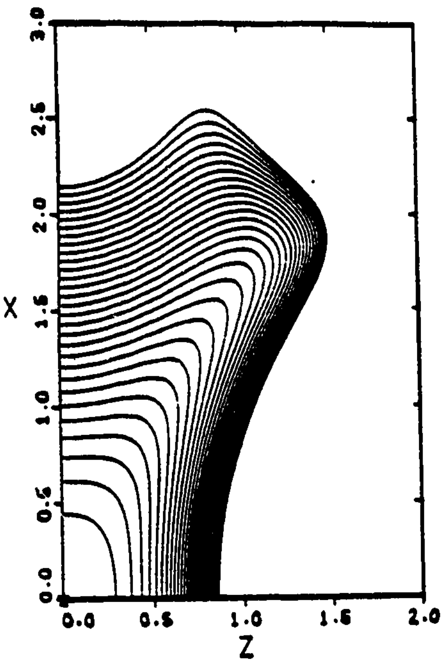

Equipotential contours for R = 4.20

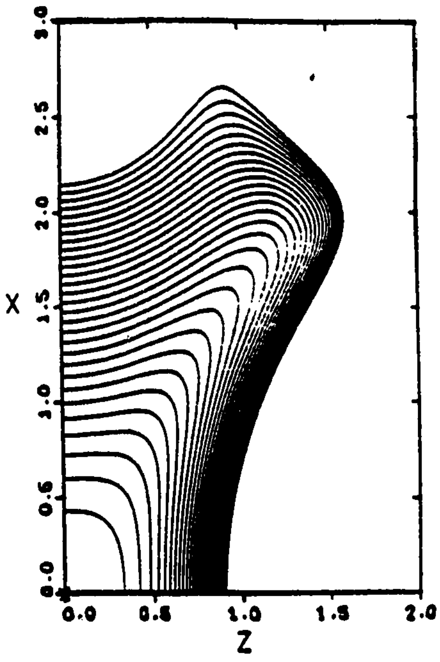

Equipotential contours for R = 4.30

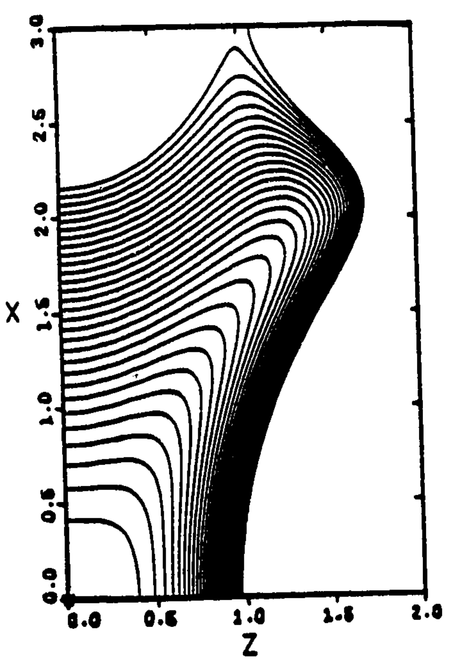

Equipotential contours for R = 4.40

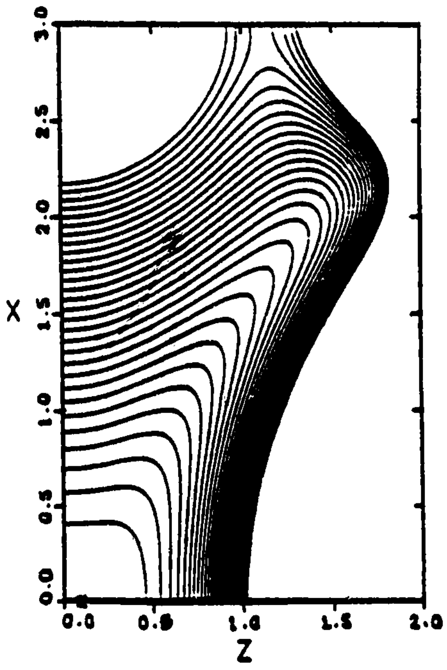

Equipotential contours for R = 4.50

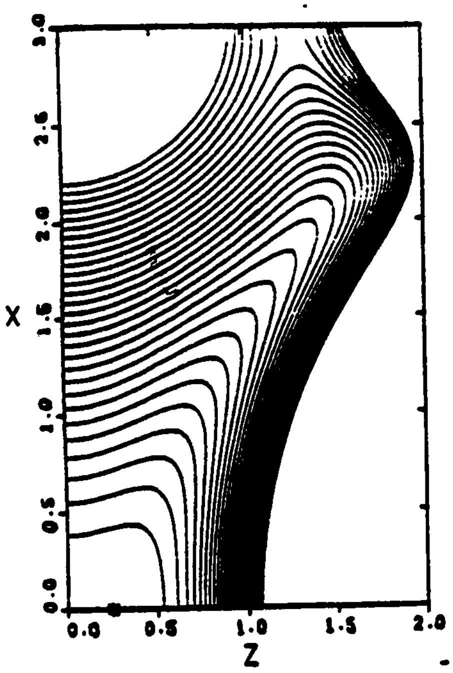

Equipotential contours for R = 4.60

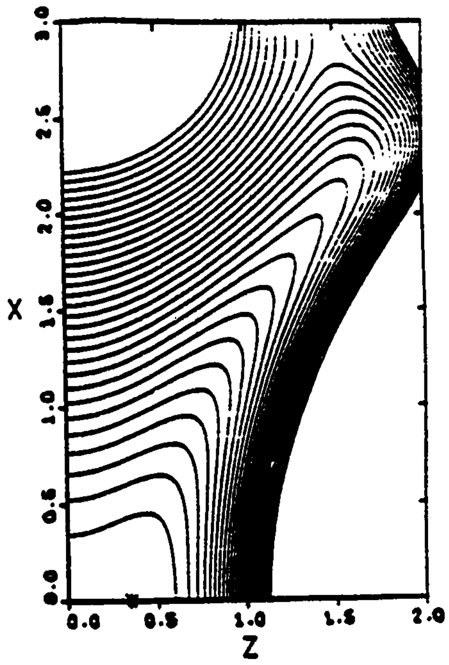

Equipotential contours for R = 4.70

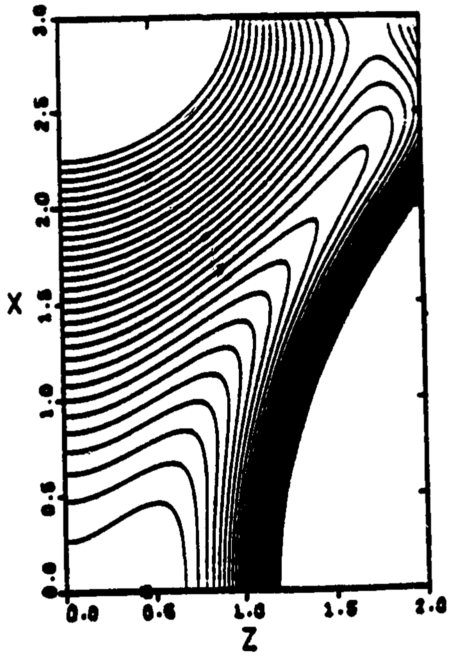

Equipotential contours for R = 4.80

Examination of these contour maps provides some physical insight into the vibrational dynamics treated in this study. The double well structure seen in the $[FHF]^-$ surface begins to appear for $R \geq 4.5$ a.u., but is strongly distorted by the "warp" mapping for the higher contours. Since the relevance of classical dynamics to the double well region of the potential surface is at best dubious, we did not extend present studies beyond $R \approx 4.6$ a.u. The "pass" appearing at large x for the highest contours near $R \geq 4.4$ a.u. also appears on the original $[FHF]^-$ surface where it corresponds to a physically unrealistic rotation of dipolar HF away from its equilibrium orientation toward the F^- ion by more than 90 degrees; note that the energies at which it appears are always more than 35,000 cm^{-1} above the potential minimum. The Cartesian model does preserve the strongly nonharmonic and nonseparable features of the original $[FHF]^-$ surface. Motion in the x-direction is more nearly harmonic than in the z-direction at all values of R; the potential for z-motion also varies more rapidly as R changes so that the fundamental frequencies of motion vary strongly with respect to one another both as energy and R change. The most prominent feature is above all the strongly pronounced "corner" in the surface which corresponds in $[FHF]^-$ to the incipient formation of the valley for libration of dipolar HF. We shall see that this feature has an especially strong influence on the classical dynamics of the system, even at the lowest energies studied. At all R-values there is a strongly stable periodic orbit ("attractor") which tends to organize the motion in the direction of this corner and strongly disrupts modal motion in the original x and z degrees of freedom under certain circumstances. While this effect eventually makes its presence known in the quantum mechanics of the system, the disruption appears at relatively much higher energies. A major part of this study is aimed at comparing classical dynamics and other descriptions of the system in the presence of this feature.

1.3 Outline of the Thesis

The thesis will discuss first the quantum mechanics and supporting methods for the analysis of the quantum energy levels and wavefunctions as developed in the series of papers published previously by this laboratory [1,2,3]. The quantum self-consistent field and configuration interaction procedures will be developed for and applied to the new two-dimensional cartesian model potential surface, $V(x, z; R)$, and the resulting eigenstates will be presented for discussion. The positions of the narrow avoided crossings in the energy level spectrum are located and the contributing states are identified. This is done to introduce the general concepts important to SCF theory and to illustrate the extent of state mixing evident in the quantum wavefunctions. It also allows the description of the phase space in terms of well developed theories.

A semiclassical self-consistent field theory is developed and applied to the same realistic model potential surface with qualitative and quantitative comparisons to the quantum results. The classical phase space is explored in a naive separable approximation even though the potential is technically nonseparable.

The analysis of the classical trajectories obtained by integration of Hamilton's equations will follow with comparative references to the preceding theories. The action-angle methods used to analyze these representations of the complete classical Hamiltonian will be developed and tested for accuracy and precision. Determination of the fundamental frequencies, integration of the classical actions, and identification of the Fourier components of the motions are the primary investigative techniques. The types of trajectories that are encountered in the exploration of the phase space are presented and the specifics of their analysis are detailed. Once this information is displayed, it is possible to begin investigations into the global dynamics. The identification of structures in the phase space is accomplished by understanding the interactions between the frequencies, the actions, the energies, and the coordinate tracks.

The classical self-consistent field Hamiltonians are used as the zero-order Hamiltonians for a classical perturbation theory based on coordinate expansions. The theory improves the separable approximation by incorporating the inherent coordinate correlation removed by the SCF procedure in much the same way that the CI procedure corrected the quantum SCF eigenstates. The effectiveness of this combination of methods will be tested in the different regions of the phase space. Finally, all of the classical methods are compared. The effectiveness of the classical SCF and perturbation procedure is tested in the light of the classical trajectory analysis. Attempts are made to improve the theories with more appropriate coordinate systems. The correspondence between the classical phase space structure and the quantum eigenvalue spectrum is discussed with a hope of illuminating future methods of investigation.

Chapter 2

Quantum Mechanical Calculations

2.1 Introduction

Quantum mechanical eigenstates for the two-dimensional model system have been computed for values of the F–F separation parameter R between 3.80 a.u. and 4.70 a.u. If energy is expressed in c.e.u., the classical Hamiltonian has the form

$$H = p_x^2 + p_z^2 + V(x, z; R) \qquad [2.1]$$

and the corresponding Schrödinger equation $H\Psi = E\Psi$ has eigenstates

$$\left[-\left(\frac{\partial^2}{\partial x^2} \right) - \left(\frac{\partial^2}{\partial z^2} \right) + V(x, z; R) \right] \Psi_{ns}(x, z; R) = E_{ns}(R) \Psi_{ns}(x, z; R). \qquad [2.2]$$

The subscripts s and n denote, respectively, the symmetry type of the state and its ordering with energy starting with the lowest at $n = 0$. C_{2v} symmetries are A_1 (invariant), A_2 (transforms like xz), B_1 (transforms like z), and B_2 (transforms like x).

For each symmetry, solutions to equation [2.2] are constructed as expansions in an adequate set of zero-order states of that symmetry. Here, as in the treatment of the $[\mathrm{FHF}]^-$ system by Epa and Thorson [2], the zero-order states used as expansion basis are the *Self-Consistent Field* (SCF) eigenstates. Such a procedure is called *Configuration Interaction* (CI) in analogy with common usage in quantum chemistry, although there are some technical differences. Sections 2.2 and 2.3 discuss the SCF equations for vibrational states and numerical methods used to solve them. In Section 2.4, results of the SCF calculations are presented and discussed. In Section 2.5, details of the CI computation are briefly discussed and Section 2.6 presents the results of calculations.

2.2 SCF Approximation in Vibrational Dynamics

The essential idea in the SCF approximation for any dynamical system is that the motion in each individual degree of freedom, for an appropriate coordinate system, is (1) approximately independent of (*i.e.* *separable* from) the detailed motion in other degrees of freedom, and (2) is determined by a suitably chosen average of the system Hamiltonian over all other degrees of freedom. Self-consistency is the requirement that equations of motion in each degree of freedom and the averages over the resulting motions which produce them are mutually consistent.

In quantum mechanics, the SCF approximation to a time-independent Schrödinger equation $H\Psi = E\Psi$ is generated by applying the Rayleigh-Ritz variation principle to a trial wave function which is a product of independent components for each degree of freedom. The expectation value of the Hamiltonian is made stationary for arbitrary variations of the components subject to the usual normalization constraints. This procedure leads to a set of one-dimensional Schrödinger equations whose solutions are the required optimum factors and determine the effective Hamiltonians for these equations in a mutually self-consistent manner.

In the cases most familiar to chemists and many physicists, the SCF method is applied to a many-electron or other many-particle system to reduce the problem to a system of one-particle equations. The earliest applications, due to Hartree [9] and others, incurred very large errors since the approximation ignored the permutation symmetry requirements associated with systems of identical particles. For electrons and other fermions, the Pauli principle is fundamental to electronic structure. The method was later modified by Fock to satisfy the permutation symmetry and leads to the well known Hartree-Fock SCF equations [10].

In contrast to the many-electron case, applications of the SCF method to vibrational states of molecules are usually uncomplicated by the requirements of permutation symmetry; each degree of vibrational freedom is physically distinguishable from all others. Hence, unlike the Hartree-Fock SCF case, the SCF approximation to a vibrational stationary state is a simple product of independent factors for each degree of freedom. A distinct one-dimensional SCF equation results for each factor.

In the context of equation [2.2], SCF equations are obtained by making the approximation

$$\Psi \simeq \Phi^{SCF} = X(x;R) \cdot Z(z;R), \tag{2.3}$$

and requiring that

$$E^{SCF} = \frac{\langle \Phi^{SCF} | \hat{H} | \Phi^{SCF} \rangle}{\langle \Phi^{SCF} | \Phi^{SCF} \rangle} \tag{2.4}$$

be made stationary for arbitrary variations of the factors X and Z, subject to the normalization constraints

$$\begin{aligned} \langle X | X \rangle_x &= \int_{-\infty}^{+\infty} X^2(x;R)dx = 1, \\ \langle Z | Z \rangle_z &= \int_{-\infty}^{+\infty} Z^2(z;R)dz = 1. \end{aligned} \tag{2.5}$$

The resulting SCF equations in cartesian coordinates are

$$\begin{aligned} \left[-\left(\frac{d^2}{dx^2} \right) + V_x^{SCF}(x;R) - E_x \right] X(x;R) &= 0, \\ \left[-\left(\frac{d^2}{dz^2} \right) + V_z^{SCF}(z;R) - E_z \right] Z(z;R) &= 0, \end{aligned} \tag{2.6}$$

where the effective potentials are defined as SCF averages of the true potential $V(x,z;R)$,

$$\begin{aligned} V_x^{SCF}(x;R) &= \langle V(x,z;R) \rangle_z = \int_{-\infty}^{+\infty} V(x,z;R) Z^2(z;R)dz, \\ V_z^{SCF}(z;R) &= \langle V(x,z;R) \rangle_x = \int_{-\infty}^{+\infty} V(x,z;R) X^2(x;R)dx. \end{aligned} \tag{2.7}$$

Self-consistency requires that

$$\begin{aligned}\langle\langle V(x,z;R)\rangle\rangle &= \langle V_x^{SCF}(x;R)\rangle_x = \langle V_z^{SCF}(z;R)\rangle_z, \\ &= \int_{-\infty}^{+\infty}\int_{-\infty}^{+\infty} V(x,z;R)\Phi^2(x,z;R)dxdz. \end{aligned} \quad [2.8]$$

Solutions of the SCF equations [2.6] to [2.8] may be characterized by the nodal quantum numbers (n_x, n_z). The separable approximate Hamiltonian having the solution Φ_{n_x,n_z} as an eigenstate is given by

$$H^{SCF} = \left[-\left(\frac{d^2}{dx^2}\right) + V_x^{SCF}(x;R)\right] + \left[-\left(\frac{d^2}{dz^2}\right) + V_z^{SCF}(z;R)\right] - \langle\langle V(x,z;R)\rangle\rangle_{n_x,n_z}, \quad [2.9]$$

and the corresponding approximation to the total energy is

$$E^{SCF}_{n_x,n_z} = E_x(n_x,n_z;R) + E_z(n_x,n_z;R) - \langle\langle V(x,z;R)\rangle\rangle_{n_x,n_z}. \quad [2.10]$$

As the notation in equations [2.9] and [2.10] implies, the SCF effective potentials, the SCF Hamiltonians H^{SCF} and the corresponding eigenvalue problems posed by equation [2.6] are all distinct for each choice of the quantum numbers (n_x, n_z). As a consequence, the eigenstates $\{\Phi_{n_x,n_z}\}$ do not form an orthogonal set of functions, and there is also no formal guarantee that the set is complete. Symmetries of the SCF eigenstates are determined by the parities of (n_x, n_z): A_1 if both are even, A_2 if both are odd; B_1 if n_z is odd and n_x is even, and B_2 if n_x is odd and n_z even. In practice, two SCF states Φ_{n_x,n_z} and $\Phi_{n'_x,n'_z}$ with the same symmetry but different quantum numbers will be nearly orthogonal.

For a given set of quantum numbers, the SCF equations are solved by

1. guessing initial values of expectation values to compute an effective SCF potential for one degree of freedom (for example, $V_z^{SCF}(z;R)$);
2. solving the resulting SCF equation (in this case, $Z_{n_z}(z;R)$);

3. computing expectation values to determine the effective SCF potential for the other degree of freedom (here, $V_x^{SCF}(x;R)$);
4. solving the resulting SCF equation ($X_{n_x}(x;R)$);
5. computing expectation values to recompute the first effective SCF potential ($V_z^{SCF}(z;R)$);
6. iterating steps (2) to (5) until all eigenvalues and expectation values are converged to within the desired accuracy.

While there is no guarantee that this procedure is necessarily convergent or that the solutions are unique, our computations always converged provided that care was taken to ensure precise determination of expectation values. Solutions obtained do not depend on the initial sequence ordering of the two degrees of freedom in the iterative process. For computational feasibility, it is essential that the potential function $V(x,z;R)$ have the form of a finite sum of simple products of functions of each coordinate (x or z): the model potential has such a form.

The connection to a *Classical* Self-Consistent Field (CSCF) method is made by recognizing that an SCF problem is defined by establishing values for the action variables. Associated with each (assumed separable) one-dimensional motion in the chosen coordinate system, the actions are strictly analogous to the concept of a nodal quantum number and its relation to a corresponding *quantal action.* Definitions of the resulting CSCF equations of motion and classical averages of dynamical variables over the SCF motions may then be contrived in a fashion strictly analogous to their counterparts in quantum mechanics.

The use of the quantum mechanical SCF method to form approximate molecular vibrational eigenstates for comparison with accurate eigenstates has been explored by Bowman and a few other workers [11]. With the exception of the $[FHF]^-$ study by Epa and Thorson [2] in this laboratory, most systems studied have been more nearly harmonic or more nearly separable in some obvious sense. In addition, the methods used to solve the one-dimensional SCF equations have usually employed expansions in basis sets of suitably chosen harmonic oscillator functions. The computations done here used rapid numerical methods to solve the SCF equations [2.6] "exactly".

2.3 Rapid Numerical Solution of SCF Equations

As was done by Epa and Thorson [2] for [FHF]$^-$, the SCF equations [2.6] were solved using the *quantal momentum* scheme (a modification of Milne's method [14]). Both equations have the form

$$\frac{d^2F(u)}{du^2} + k^2(u)F(u) = 0, \qquad -\infty \le u \le +\infty. \qquad [2.11]$$

For the one-dimensional problem with given mode energy E, the square of the classical momentum, $k^2(u)$, has positive values in one or more domains of its argument u. Acceptable solutions exist only for discrete eigenvalues E_n with corresponding bound state eigenfunctions $F_n(u)$. Because $k^2(u)$ is an even function of u, only two cases occur:

(a) $k^2(u)$ is positive in a single domain with zeroes located at classical turning points $\pm u_1$, and has a maximum at $u_0 = 0$ (single-well potential with a minimum at the origin); or,

(b) $k^2(u)$ has two symmetrically placed maxima at $\pm u_0$ and a local minimum at $u = 0$ (double-well potential with minima at $\pm u_0$ and a barrier maximum at the origin). For sufficiently high energy, $k^2(u)$ has a single positive domain and only two turning points at $\pm u_1$; for energies below the top of the barrier at $u = 0$, it has two symmetrically placed positive domains bounded by zeroes at outer and inner turning points $(\pm u_1, \pm u_2)$.

For simplicity, only the first case is discussed in detail. Let a pair of solutions to equation [2.11] be defined with the form

$$F_\pm(u) = exp\left[\pm i \int^u q_\pm(u')du'\right]. \qquad [2.12]$$

Substitution into equation [2.11] provides the Riccati equations

$$\pm i\frac{dq_{\pm}(u)}{du} - q_{\pm}^2(u) + k^2(u) = 0, \qquad [2.13]$$

and putting $q_{\pm}(u) = q_{Re}(u) \pm iq_{Im}(u)$ gives the relation

$$\begin{aligned} q_{Im}(u) &= \frac{[q_{Re}(u)]'}{2q_{Re}(u)}, \\ 0 &= -q_{Re}^2(u) + q_{Im}^2(u) - q_{Im}'(u) + k^2(u). \end{aligned} \qquad [2.14]$$

with conjugate solution pairs

$$F_{\pm}(u) = \frac{1}{\sqrt{q_{Re}(u)}} \exp\left[\pm i\int^{u} q_{Re}(u')du'\right]. \qquad [2.15]$$

These solutions are completely determined by the single real function $q_{Re}(u)$ and a general solution is a linear combination of the two. Classically forbidden domains are regions where $k^2(u) < 0$; for case(a), where $-\infty < u \leq -u_1$ or $+u_1 \leq u < +\infty$. It was shown by Milne [14] that solutions of equation [2.11] which are regular in a classically forbidden domain have the forms

$$F(u) = C\frac{1}{\sqrt{q_{Re}(u)}}\sin\Theta(u), \qquad [2.16]$$

$$\Theta(u) = \int_{\pm\infty}^{u} q_{Re}(u')du', \qquad [2.17]$$

where $q_{Re}(u)$ is *any* particular solution of equations [2.14]. Eigenvalues of equation [2.11] are determined by the quantization condition

$$\int_{-\infty}^{+\infty} q_{Re}(u)du = (n+1)\pi \; ; \qquad n = 0,1,2\ldots \qquad [2.18]$$

Efficiency of the scheme rests on the fact that one particular solution of equations [2.14], the ***quantal momentum***, is nonoscillatory and closely resembles the corresponding classical momentum function $k(u)$ in the classically allowed region where

$k^2(u)$ is positive. It can be computed efficiently in the regions where $k^2(u)$ is negative and tends strongly to zero as $u \to \pm\infty$. It can be shown [12] that classical zero-order approximations

$$q^0_{Re} = k(u_i), \qquad q^0_{Im}(u_i) = \frac{k'(u_i)}{2k(u_i)}. \qquad [2.19]$$

suffice as initial conditions to generate an extremely accurate approximation to the particular solution, $q_{Re}(u_i)$, provided that the point of initiation u_i is taken to be a local maximum of $k^2(u)$ (here, $u_0 = 0$).

The phase integral or *quantal action* function

$$S(E) \equiv \int_{-\infty}^{+\infty} q_{Re}(u)du, \qquad [2.20]$$

is a continuous, monotonically increasing function of the mode energy E and may be rapidly computed in tandem with the solution of equations [2.14] for $q_{Re}(u)$. Application of the quantum eigenvalue condition [2.18]

$$S(E_n) = (n+1)\pi \qquad [2.21]$$

then yields the mode energies and corresponding eigenfunctions defined by [2.16]. Because of bilateral symmetry, equations need only be solved on the positive axis $0 \leq u < +\infty$.

In the more complicated situations covered by case(b), an analogous procedure can be developed with the following modifications (see for example Lee and Light [13]). Initial conditions [2.19] are applied at u_0, the local maximum of $k^2(u)$, and equations [2.14] and [2.17] are integrated from u_0 outward to $+\infty$ and inward to $u = 0$. The corresponding solution [2.16] regular as $u \to +\infty$ is

$$F_R(u) = \frac{1}{\sqrt{q_{Re}(u)}} \sin \int_{\infty}^{u} q_{Re}(u')du'; \qquad [2.22]$$

there exists a mirror image solution on the $-u$ axis regular as $u \to -\infty$. Since the eigenstates are either symmetric or antisymmetric about $u = 0$:

Either,

(i) for even parity states ($n = 0, 2, 4 \ldots$), the derivative of the eigenfunction $F_n'(u) = 0$ at $u = 0$ and the eigenvalue condition is

$$\int_0^{+\infty} q_{Re}(u)du + \cot^{-1}\left[\frac{q_{Im}(0)}{q_{Re}(0)}\right] = \left(\frac{n}{2} + 1\right)\pi; \qquad [2.23]$$

or,

(ii) for odd parity states ($n = 1, 3, 5 \ldots$), the eigenfunction itself vanishes at $u = 0$, $F_n(u) = 0$ and the eigenvalue condition is

$$\int_0^{+\infty} q_{Re}(u)du = \left[\frac{n+1}{2}\right]\pi. \qquad [2.24]$$

It can be shown that case (b) eigenvalues obtained by these rules agree accurately with the results of the simpler formula for case (a) in situations where the energy E is far above the barrier. Since equations [2.14] and [2.17] can be integrated at the speed of Hamilton's equations for the corresponding classical one-dimensional problem, this method is especially efficient for states with large quantum actions.

2.4 Analysis of Quantum SCF Results

In the SCF calculations done here, all SCF states with energies less than approximately 750 c.e.u. ($\approx$ 45,000 cm^{-1}) were computed for R-values $3.80 \leq R \leq 4.50$ a.u. at intervals of 0.05 a.u. Over this domain of R, about 300 states have energies below the cutoff energy roughly occupying a domain of quantum numbers $0 \leq n_x \leq 28$ and $0 \leq n_z \leq 14$. Figure 2.1 shows a contour diagram depicting $E^{SCF}_{n_x,n_z}$ *vs.* n_x, n_z at $R = 4.30$ a.u. as a typical example. Note that simultaneous excitation of both modes tends to lower the energy, corresponding to states located in the region of the marked "valley" appearing on the potential contour maps (see Figures 1.2). For $4.55 \leq R \leq 4.70$, both the cutoff energy and the number of SCF levels decreased with increasing R since care must be taken to ensure that all states lie below the top of the unphysical "pass" or saddle seen on the potential surface at larger R-values. By $R = 4.70$ a.u., the cutoff energy has dropped to 500 c.e.u. and only 215 SCF levels were computed. The contour diagram at this R-value is plotted in Figure 2.2.

In calculations, SCF solutions for the lowest levels were determined first and these were used to provide extrapolated input guesses for the higher levels. After SCF results for three adjacent R-values were obtained, these provided very efficient extrapolated input guesses for the next R-point.

The lowest SCF energy levels plotted against R are presented in Figures 2.3 through 2.6 for each of the four C_{2v} symmetry types. These are approximately the first few levels ranked at $R_{eq} \approx 4.30$, but the sequencing of quantum numbers (n_x, n_z) listed at the right margin of each figure is in order of increasing energy at $R = 4.70$ a.u. for the first 20 states. All energies are plotted relative to the absolute minimum of the surface at R_{eq} rather than with respect to the minimum surface potential energy at each R. For $3.80 \leq R \leq 4.70$ a.u., the ground state zero-point

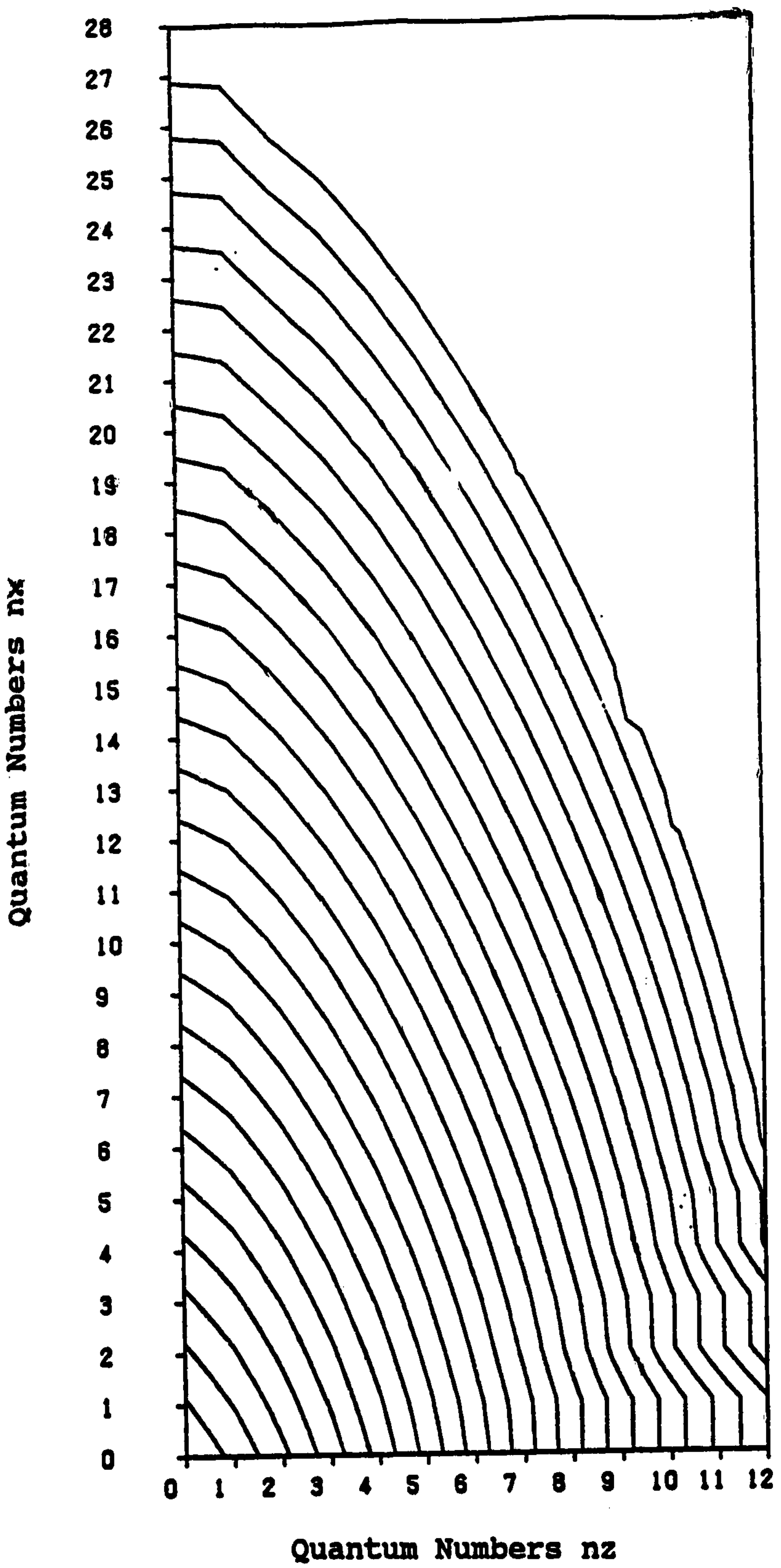

Figure 2.1: Quantum SCF energies *vs.* n_x, n_z at $R = 4.30$ a.u. with contour spacings of 50 c.e.u.

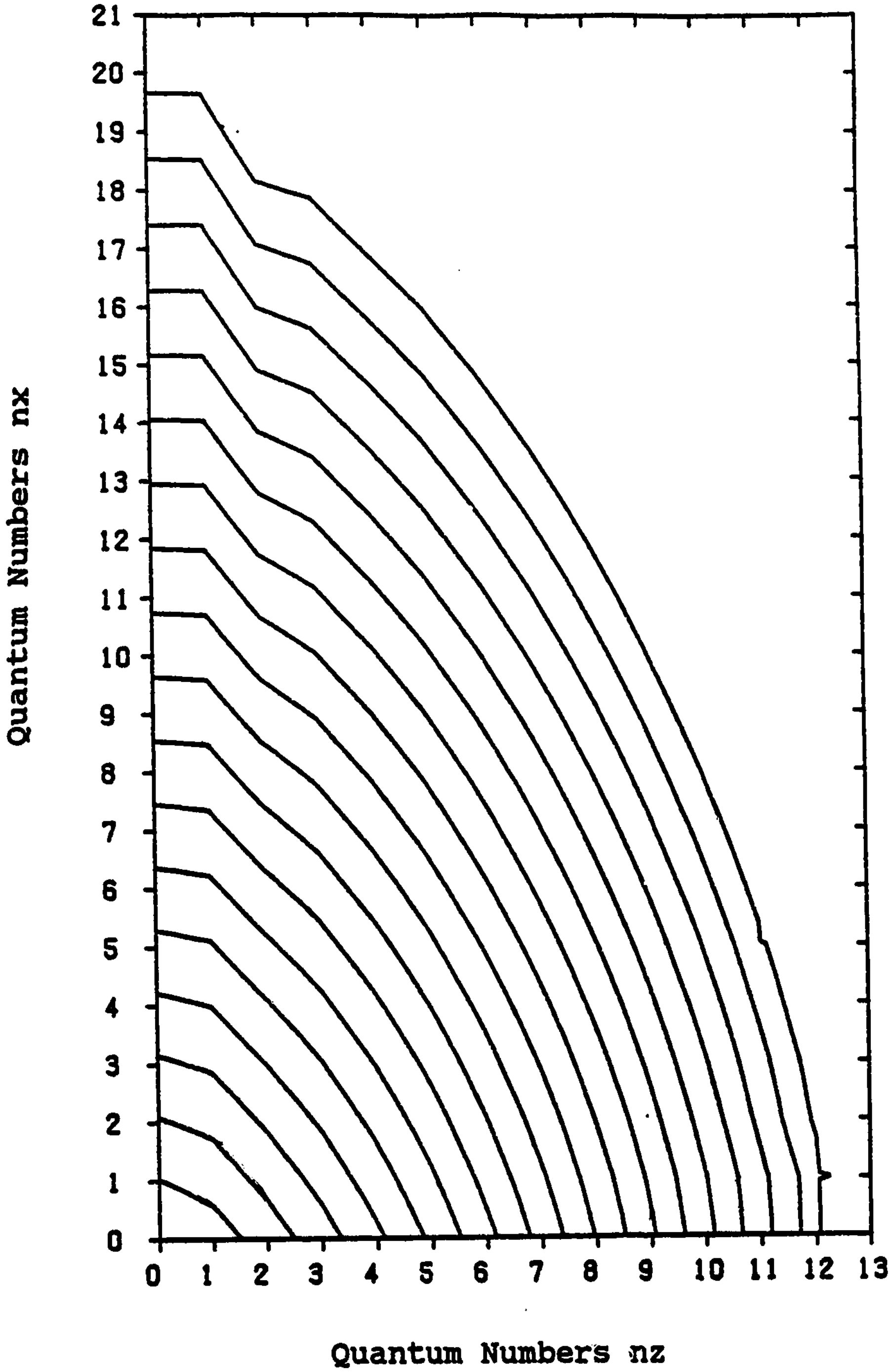

Figure 2.2: Quantum SCF energies *vs.* n_x, n_z at $R = 4.70$ a.u. with contour spacings of 50 c.e.u.

energy varies between 36. and 15. c.e.u.

The most important features in Figures 2.3–2.6 are the curve crossings involving two or more SCF levels at particular R-values. At such points, the SCF states involved will interact strongly producing *avoided crossings* of the CI energy levels and corresponding strong mixing of these SCF states in the CI eigenfunctions. Concentrating on the A_1 states in Figure 2.3 as an example, one can see that the SCF levels are organized into families of curves showing qualitatively similar behaviour against R. This grouping reflects mostly the different relative shape and R-dependence of the potential surface in the x and z directions and its influence on the corresponding mode excitation energies. Excitation energy for the z-mode varies much more strongly with R than for the x-mode. The complicated crossing structure is therefore systematic and always involves one member from each of a limited set of families. Of special interest to this thesis are the crossings involving swappings of two quanta of x-mode excitation for two quanta of z-mode excitation. The first is between (2,0) and (0,2) at $R \approx 4.50$ a.u. A family of such crossings can be observed: (4,0) with (2,2), (6,0) with (4,2), (8,0) with (6,2), etc. This structure, complicated by multiple crossings involving still other families with swapping of two or more quanta, continues to higher energy. Eventually the pattern of level crossings becomes so complex that the utility of an SCF description is obviously in question. These crossings and the strong CI mixing they produce between SCF states swapping two quanta between modes are related to phenomena in the *classical dynamics* of this model system. Classical motion is strongly affected in this region by a family of trajectories centering on a stable, periodic, and almost linear orbit lying in the direction of the potential valley or "corner" on the potential surface: this is associated directly to a 1:1 *frequency matching* or *resonance* and resulting correlated motion in x and z directions. The CI wavefunctions resulting from the mixing at such crossings display the quantum mechanical effects of the valley's powerful reorganization of the motion produced by this potential.

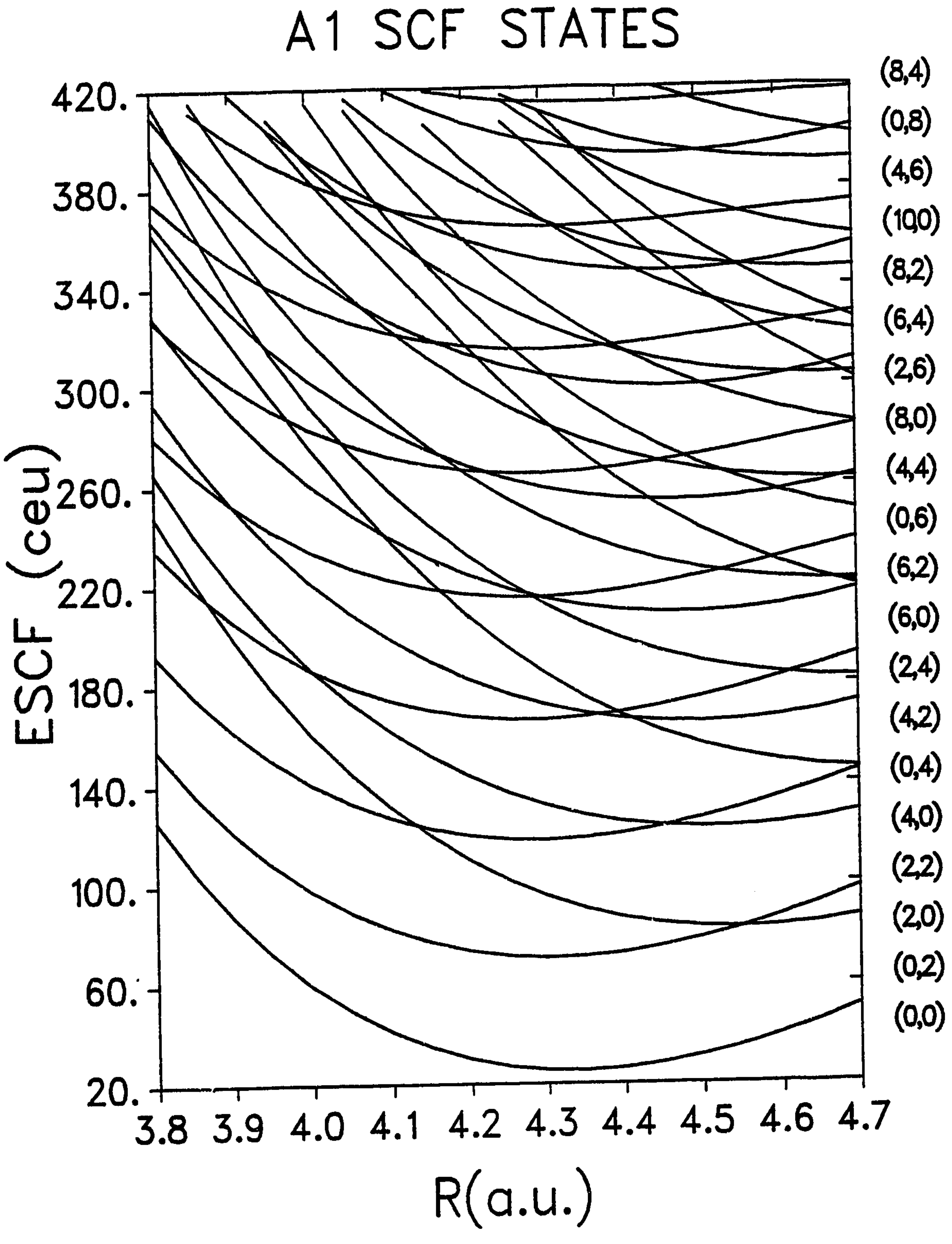

Figure 2.3: Quantum SCF energy level diagram in A_1 symmetry. Labels to the right are states listed in order of increasing energy at $R = 4.70$ a.u.

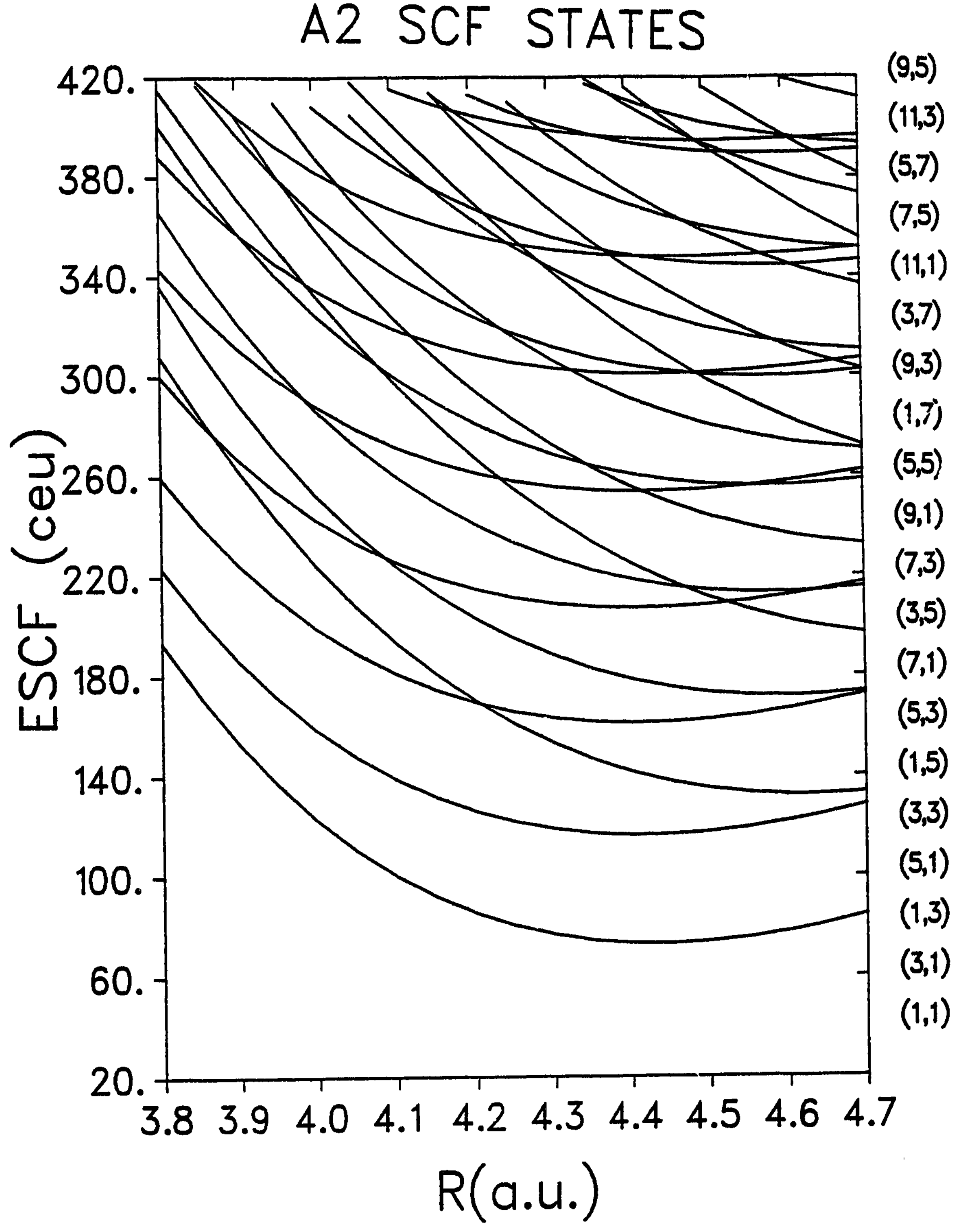

Figure 2.4: Quantum SCF energy level diagram in A_2 symmetry. Labels to the right are states listed in order of increasing energy at $R = 4.70$ a.u.

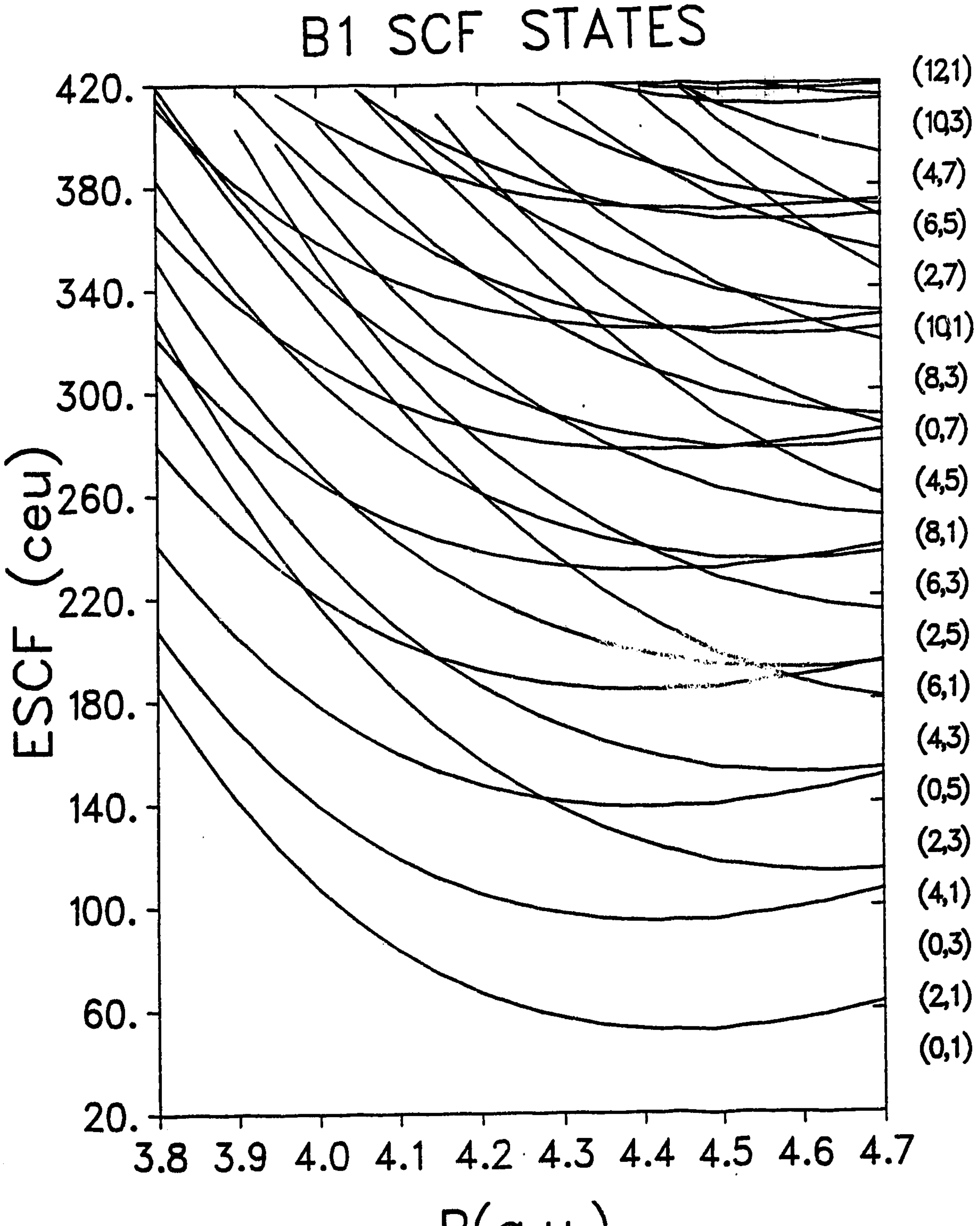

Figure 2.5: Quantum SCF energy level diagram in B_1 symmetry. Labels to the right are states listed in order of increasing energy at $R = 4.70$ a.u.

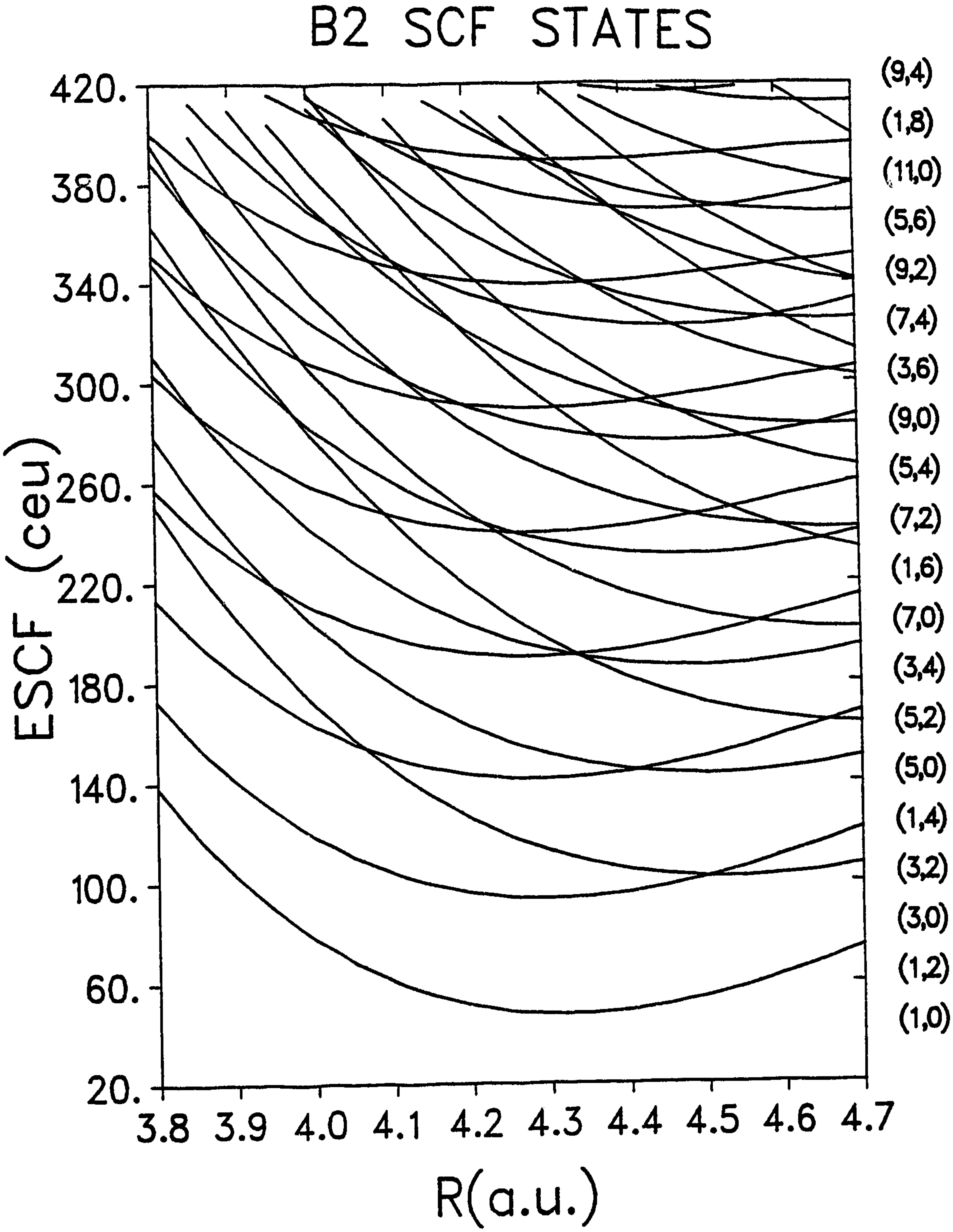

Figure 2.6: Quantum SCF energy level diagram in B_2 symmetry. Labels to the right are states listed in order of increasing energy at $R = 4.70$ a.u.

2.5 Configuration Interaction

The set of SCF eigenstates $\{\Phi_{n_x,n_z}\}$ is used as an expansion basis for solving the Schrödinger equation [2.2]. As stated earlier, this set of functions is not strictly an orthogonal set, and there is also no formal guarantee of its completeness. However, if sufficiently large basis sets are used, there is some confidence that the method may give reliable results for at least the lower lying levels. By comparison, Epa and Thorson [2] achieved sufficiently accurate results for at least the lowest five CI states with a basis of only 21 SCF states for each symmetry.

For a given symmetry s, a solution Ψ_s to equation [2.2] is expanded in the subset of SCF states $\left\{\Phi^s_{n_x,n_z}\right\}$ of that symmetry:

$$\Psi_s(x,z;R) = \sum_{n_x,n_z} C^s_{n_x,n_z}(R)\Phi^s_{n_x,n_z}(x,z;R). \qquad [2.25]$$

Substituting [2.25] into the Schrödinger equation [2.2], multiplying by $\Phi^s_{n'_x,n'_z}(x,z;R)$ and integrating over x, z yields the equations

$$\sum_{n_x,n_z} \left[H(n'_x,n'_z,n_x,n_z;R) - ES(n'_x,n'_z,n_x,n_z;R)\right] C^s_{n_x,n_z}(R) = 0, \qquad [2.26]$$

$$\text{or} \qquad [\mathbf{H} - E\mathbf{S}]\,\mathbf{C} = 0. \qquad [2.27]$$

The diagonal elements of the Hamiltonian and overlap matices **H** and **S** are defined by

$$\begin{aligned} S(n_x,n_z,n_x,n_z;R) &= 1 \\ H(n_x,n_z,n_x,n_z;R) &= E^{SCF}_{n_x,n_z}(R) \end{aligned} \qquad [2.28]$$

and the off-diagonal elements by

$$\begin{aligned} S(n'_x,n'_z,n_x,n_z;R) &= \langle X_{n'_x}|X_{n_x}\rangle_x \cdot \langle Z_{n'_z}|Z_{n_z}\rangle_z \\ = \int_{-\infty}^{+\infty} X_{n'_x}(x;R)X_{n_x}(x;R)dx &\cdot \int_{-\infty}^{+\infty} Z_{n'_z}(z;R)Z_{n_z}(z;R)dz, \end{aligned} \qquad [2.29]$$

and

$$\begin{aligned} H(n'_x, n'_z, n_x, n_z; R) &= \langle \Phi^s_{n'_x,n'_z} | H | \Phi^s_{n_x,n_z} \rangle \\ = \int_{-\infty}^{+\infty} dx \int_{-\infty}^{+\infty} dz \quad & \Phi^s_{n'_x,n'_z}(x, z; R) \left[H \Phi^s_{n_x,n_z}(x, z; R) \right]. \end{aligned} \qquad [2.30]$$

To evaluate [2.30], we used the relationship

$$\begin{aligned} H(n'_x, n'_z; n_x, n_z; R) &= S(n'_x, n'_z, n_x, n_z; R)[E^{SCF}_{n_x,n_z}(R) + \langle\langle V(x, z; R)\rangle\rangle_{n_x,n_z}] \\ &- \langle Z_{n'_z} | Z_{n_z} \rangle_z \cdot \langle X_{n'_x} | V^{SCF}_x(x; R) X_{n_x} \rangle_x \\ &+ \langle X_{n'_x} | X_{n_x} \rangle_x \cdot \langle Z_{n'_z} | V^{SCF}_z(z; R) Z_{n_z} \rangle_z \\ &+ V(n'_x, n'_z; n_x, n_z; R), \end{aligned} \qquad [2.31]$$

where

$$V(n'_x, n'_z; n_x, n_z; R) = \int_{-\infty}^{+\infty} dx \int_{-\infty}^{+\infty} dz \Phi^s_{n'_x,n'_z}(x, z; R) V(x, z; R) \Phi^s_{n_x,n_z}(x, z; R) \qquad [2.32]$$

and the SCF effective potentials $V^{SCF}_x(x; R), V^{SCF}_z(z; R)$ appearing in the third and fourth terms of equation [2.31] are those associated with the SCF state $\Phi^s_{n_x,n_z}$.

A measure of the overall precision of computations is obtained by testing the Hermiticity of the matrix **H** defined by equation [2.31]. In a survey of the precision test results at $R = 4.30$ a.u., approximately 12–15 matrix elements (in an approximately 75x75 matrix, depending on the symmetry) have a nonhermiticity capable of producing maximum precision errors of 10^{-5} in one or more eigenvectors and 10^{-7} c.e.u. in corresponding eigenvalues (estimates based on perturbation theory).

To solve equation [2.27], an adaptation of the Givens-Householder [10] method for nonorthogonal basis sets was used. Compute the matrix $\mathbf{S}^{-\frac{1}{2}}$ and define

$$\mathbf{C}' = \mathbf{S}^{\frac{1}{2}} \mathbf{C} \qquad [2.33]$$

with inverse

$$\mathbf{C} = \mathbf{S}^{-\frac{1}{2}}\mathbf{C}'. \tag{2.34}$$

Substituting **C** from [2.34] into [2.27] and multiplying on the left by $\mathbf{S}^{-\frac{1}{2}}$, one obtains

$$[\mathbf{H}' - E\mathbf{1}]\,\mathbf{C}' = 0 \tag{2.35}$$

where

$$\mathbf{H}' = \mathbf{S}^{-\frac{1}{2}}\mathbf{H}\mathbf{S}^{-\frac{1}{2}}. \tag{2.36}$$

Finally, solve equation [2.35] for eigenvalues E_{ns} and eigenvectors

$$\mathbf{C}_{ns} = \mathbf{S}^{-\frac{1}{2}}\mathbf{C}'_{ns}. \tag{2.37}$$

2.6 Analysis of CI Results

Figures 2.7 to 2.10 show the lowest CI energy levels plotted against R for each of the four symmetries. In accordance with the non-crossing rule, the crossings that appear on the SCF energy level diagrams (Figures 2.3 to 2.6) have here become avoided crossings. Note that some of these are extremely narrow indicating that the crossing states interact very weakly; this was also observed by Epa and Thorson for the $[FHF]^-$ system [2]. The lowest 4–6 states of each symmetry can still be assigned unambiguously to corresponding SCF levels. With increasing energy, this simple connection disappears, as may be expected from the high density of states and the occurrence of crossings almost everywhere.

Table 2.1 compares SCF and CI energies for the first ten levels of each symmetry at $R = 4.30$ a.u. The close correspondence found for most of these levels suggests that a comparison of the classical SCF approximation with exact classical mechanics would be of some interest.

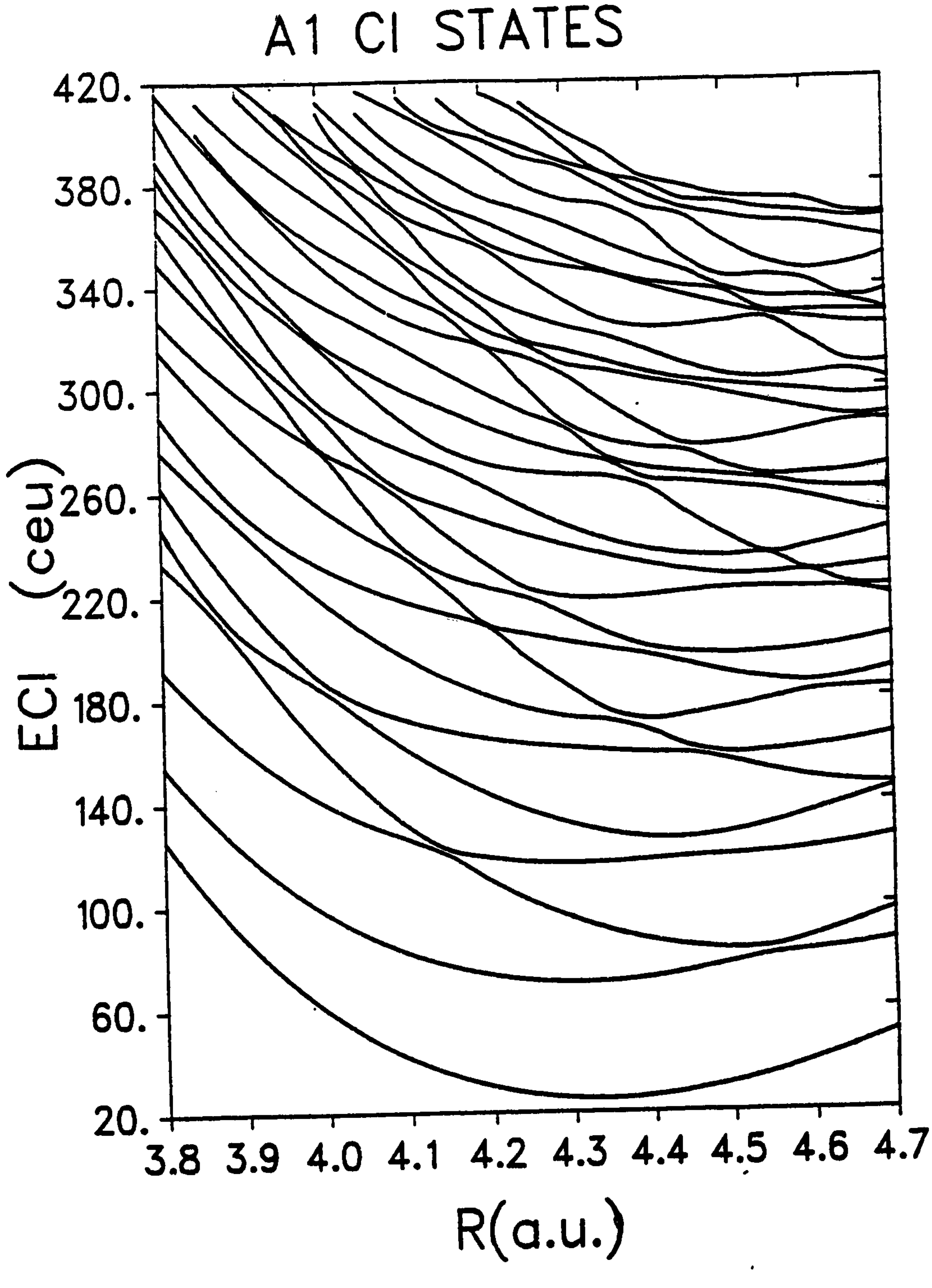

Figure 2.7: Quantum CI energy level diagram in the A_1 symmetry:

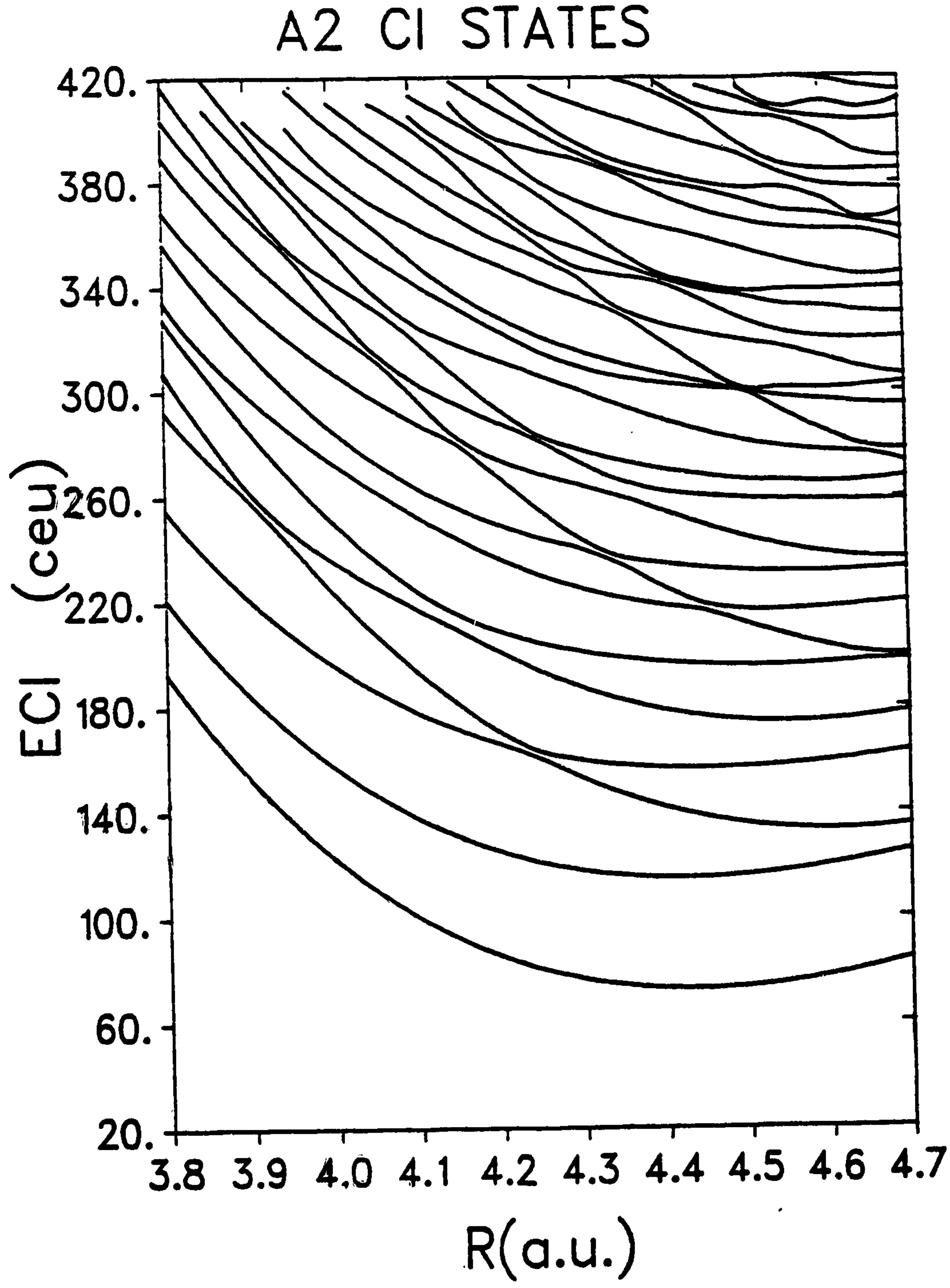

Figure 2.8: Quantum CI energy level diagram in the A_2 symmetry:

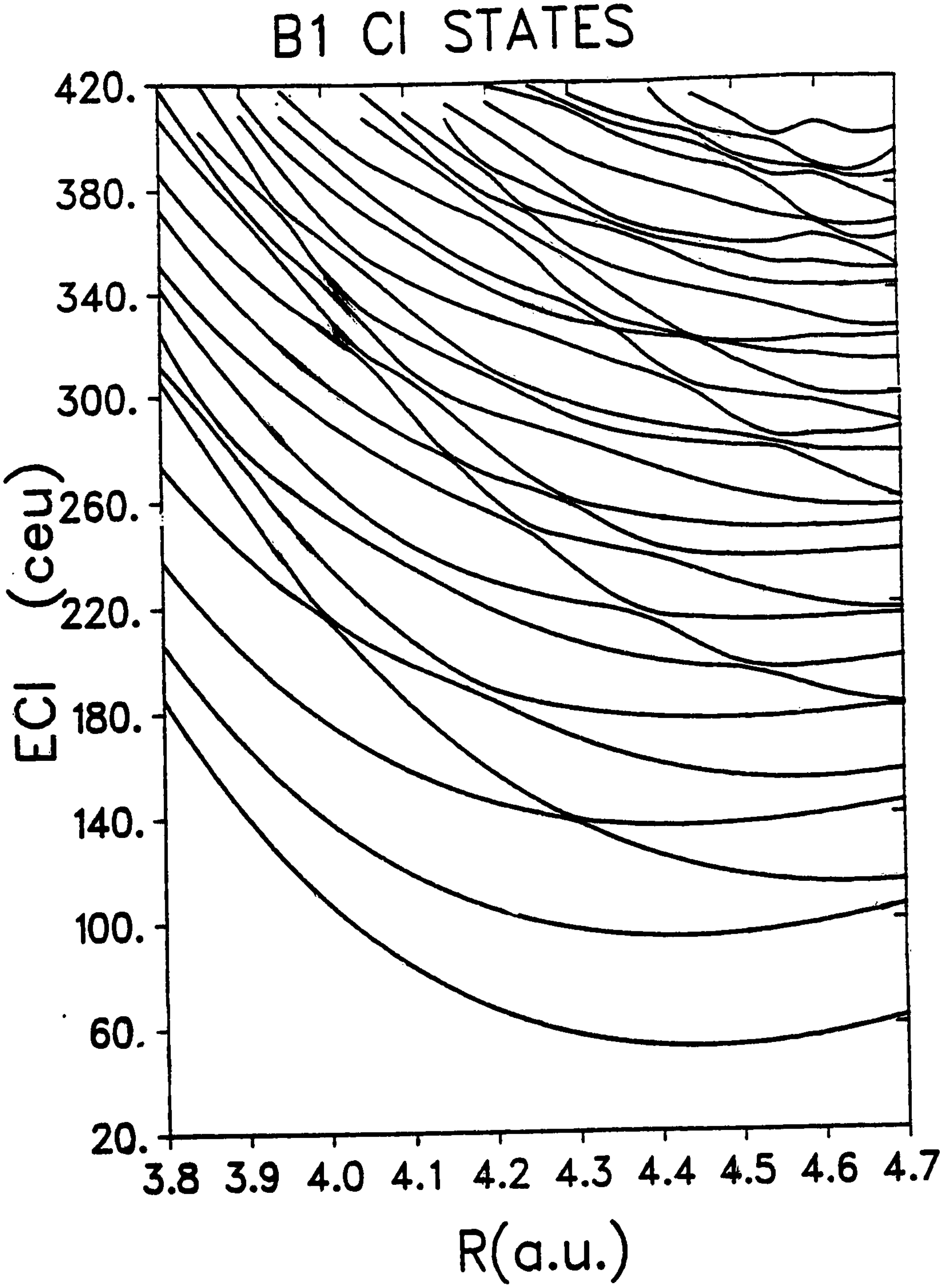

Figure 2.9: Quantum CI energy level diagram in the B_1 symmetry:

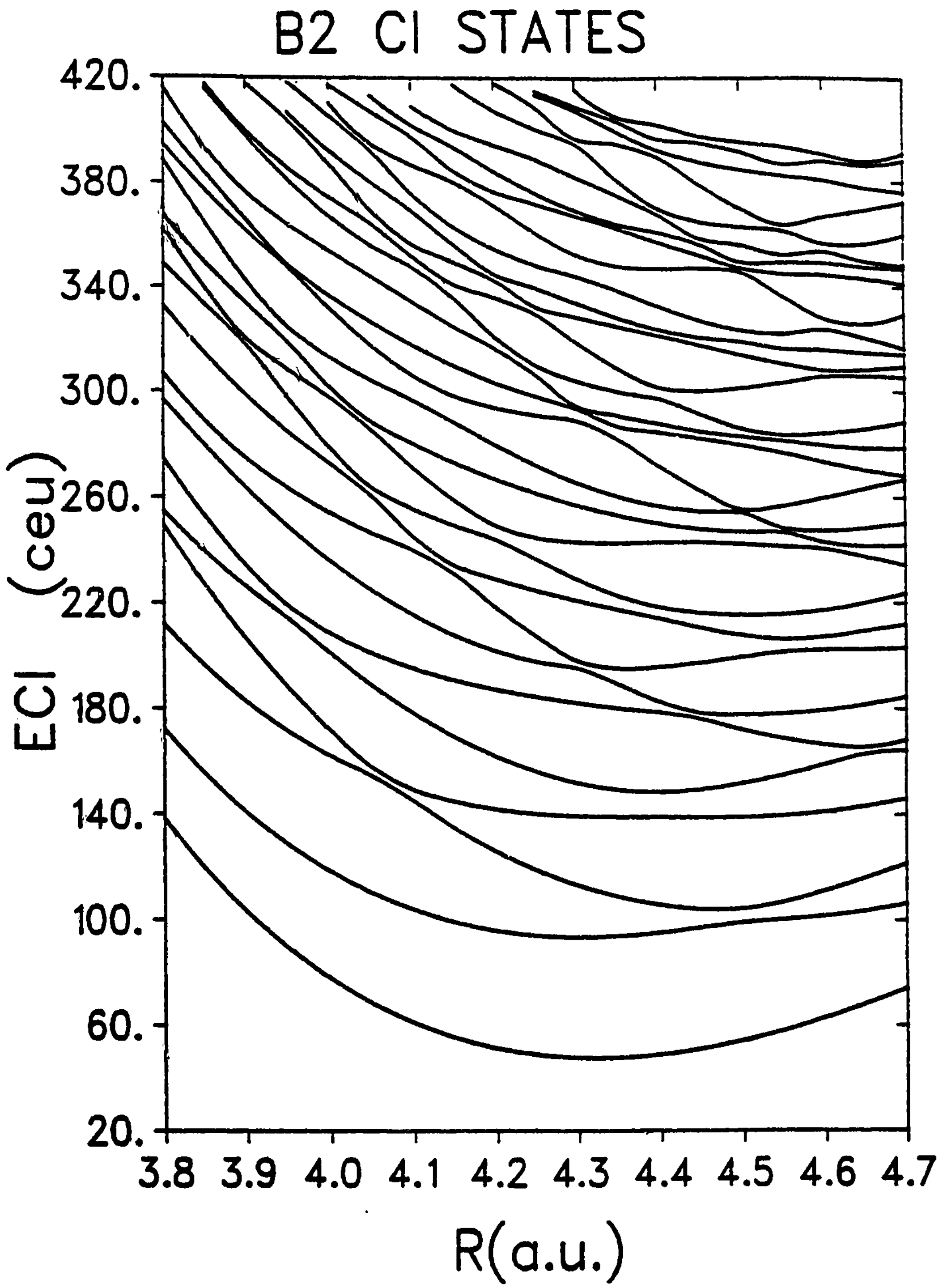

Figure 2.10: Quantum CI energy level diagram in the B_2 symmetry:

A1 #	CI Energy	n_x, n_z	SCF Energy	A2 #	CI Energy	n_x, n_z	SCF Energy
1	25.41110	0 0	25.42807	1	76.60425	1 1	76.75836
2	70.28719	2 0	70.48677	2	117.67971	3 1	118.79055
3	95.12556	0 2	95.14007	3	153.01057	1 3	153.07449
4	116.32323	4 0	117.53655	4	159.70450	5 1	163.05422
5	131.54316	2 2	131.49552	5	187.47639	3 3	188.23010
6	160.97411	6 0	165.86834	6	200.94638	7 1	208.79346
7	172.76869	4 2	171.74418	7	225.23023	5 3	227.17212
8	184.40935	0 4	184.37798	8	240.18877	1 5	243.67398
9	201.66509	2 4	212.17032	9	244.07632	9 1	255.52207
10	211.91334	6 2	214.42599	10	264.06043	3 5	272.43536

B1 #	CI Energy	n_x, n_z	SCF Energy	B2 #	CI Energy	n_x, n_z	SCF Energy
1	56.92371	0 1	56.97717	1	47.59729	1 0	47.64844
2	96.93935	2 1	97.43053	2	93.27696	3 0	93.81499
3	137.63161	0 3	137.90111	3	112.73077	1 2	112.67926
4	138.87999	4 1	140.69952	4	139.05298	5 0	141.57512
5	169.72266	2 3	170.05085	5	151.50913	3 2	151.25058
6	180.50793	6 1	185.77399	6	181.80855	7 0	190.36394
7	206.05335	4 3	207.33229	7	194.88519	5 2	192.83728
8	220.89978	8 1	232.05824	8	197.68488	1 4	196.97619
9	233.95281	0 5	233.95514	9	220.58154	3 4	228.81672
10	244.80960	6 3	247.61685	10	228.62144	7 2	236.42885

Table 2.1: Quantum CI and SCF State Energies at $R = 4.30$a.u.

Figure 2.11 shows contour plots of CI wave functions $\Psi_{n_x,n_z}(x,z;R)$ for 18 states of A_1 symmetry at R=4.30 a.u. From their nodal structure, it is evident that the first three correspond directly with the SCF states (0,0), (2,0) and (0,2); similarly states 4 and 8 correspond respectively to (4,0) and (0,4) SCF levels. Although its nodal structure appears more complex, state 5 is primarily SCF level (2,2) (95% contribution). Note the buildup of the amplitude along the two diagonal potential valleys lying at 26° to the x-axis (see potential contour plots in Figure 1.2), a feature which will become more pronounced with increasing energy. States 6 and 7 may also be regarded (at this R-value) as the daughters of the SCF states (6,0) and (4,2), respectively, but again with a buildup along the potential valleys.

We next consider Figure 2.12 which shows two CI wave function contour plots for a strong avoided crossing of SCF states (2,0) and (0,2) occurring at $R \approx$ 4.54805 a.u. At this R-value the SCF energies differ by $8.9\text{x}10^{-4}$ c.e.u. (0.05 cm^{-1}) while the two CI levels are split by 3.05 c.e.u. (187 cm^{-1}). The lower of the two states has only *radial* nodes, with pronounced buildup in the direction of the potential valleys; the upper one could be better described as having *angular* nodal character. The first distribution would correspond to a stable classical motion oriented along the potential valleys, while the second state with its resemblance to a "d-orbital" suggests a classical motion in an elliptical orbit about the origin.

Next consider the pair of wave functions given in Figure 2.13 associated with the avoided crossing of SCF states (4,0) and (2,2) at R = 4.45 a.u. This crossing is the next instance in the sequence of crossings involving "swapping" of two quanta between the two modes, initiated with the (2,0)x(0,2) crossing at $R \approx$ 4.55 a.u. In contrast with the corresponding plots for states 4 and 5 at R = 4.30 a.u. where these are dominantly the SCF states (see above), strong mixing of the two components is present. Again the lower state 4 is essentially "radial" in its nodal structure while the upper state 5 is "angular". Notice in particular for state 4, the splitting of the outer maxima into two peaks located along the potential valleys; the central maximum of the SCF state (2,2) is replaced in state 5 by a saddle point, with the result that the maxima in probability are thrust out from the origin, reminiscent of an elliptical orbital motion.

Figure 2.14 shows the wave function contours for the three CI states 6, 7, and 8 at $R = 4.40$ a.u. associated with the nearby "triple" crossing of SCF levels (6,0), (4,2) and (0,4). CI energies for these levels are 155.6, 164.1 and 168.5 c.e.u. respectively. The coefficients of the corresponding dominant SCF components are as follows:

- CI state 6: (4,2), 0.80; (6,0), 0.54; (2,4), 0.20.
- CI state 7: (0,4), 0.99.
- CI state 8: (6,0), 0.83; (4,2), 0.52; (2,4), 0.16.

Evidently, the SCF level (0,4) interacts only very weakly with the other two, which are strongly mixed and split by 791 cm^{-1}. Smaller contributions from more distant SCF states are present leading to an overall depression relative to the original SCF energies. The wave function contour plots tell the same story. State 7 is essentially the SCF state (0,4) with a very small distortion toward the valleys; again, states 6 and 8 are the radial and angular CI states seen in previous instances of the sequence of SCF crossings (n+2,0) and (n,2). Note that at $R = 4.30$ a.u. , the CI state 6 is primarily SCF state (6,0), state 7 is primarily (4,2), and 8 is almost entirely (0,4); obviously the weakly interacting states 7 and 8 have interchanged SCF character completely between 4.30 and 4.40 a.u., while the stronger interaction between SCF levels (6,0) and (4,2) is already affecting the wave functions for these states at 4.30 a.u.(see Figure 2.11).

Now return to Figure 2.11 and consider the plots for CI states 9, 10 and 11 at R = 4.30 a.u. Again these states arise from a nearby triple crossing of the SCF levels (8,0), (6,2) and (2,4). Roughly the same interpretation holds here as was given for the previous triple crossing. State 10 is mostly the SCF level (2,4); states 9 and 11 are split strongly (1074 cm^{-1}) by interaction of (8,0) and (6,2), with state 9 the radial member and state 11 the angular member of the pair as usual. Admixture from other SCF levels needed to produce this characteristic nodal structure has increased significantly; for states 9 and 11, 13 and 8 SCF coefficients have magnitudes greater than 0.05. The remaining CI wave functions ($n \geq 12$), shown in the series of 18 states at R = 4.30 a.u. (Figure 2.11), have a complex nodal structure and, with the exception of the "z-oscillation" state 17 which is dominated by SCF component (0,6), typically involve 20 or more significant SCF contributors.

We shall see that the radial and angular nodal structures seen in CI states at the avoided crossings considered here do in fact have classical analogues. In the treatment of exact classical dynamics discussed in the chapters to follow, motions which are essentially modal in x and z directions are strongly reorganized to center instead around strongly stable classical periodic orbits which move up and down the potential valleys. In the transition region where the reorganization is taking place, unstable elliptical orbits figure prominently in the trajectories. However in contrast to quantum mechanics where their effects occur widely only at higher energies, these phenomena *all* appear in classical dynamics at even the lowest energies.

Figure 2.11: The series of plots given on the following 18 pages are the lowest 18 A_1 CI eigenstates of the system at $R = 4.30$ a.u. The state number, R-value, energy, and symmetry are the physical parameters provided on each diagram along with information on the contour selections: number of contours (Nd), contour spacing (DS), maximum positive and negative contour levels (Ymax, Ymin), and the spacings of SCF wave function points selected to generate the CI wave functions (Dx, Dz). The red contours indicate negative values of the wave functions and black positive. The blue marks indicate the maximum negative (x) and positive (+) regions.

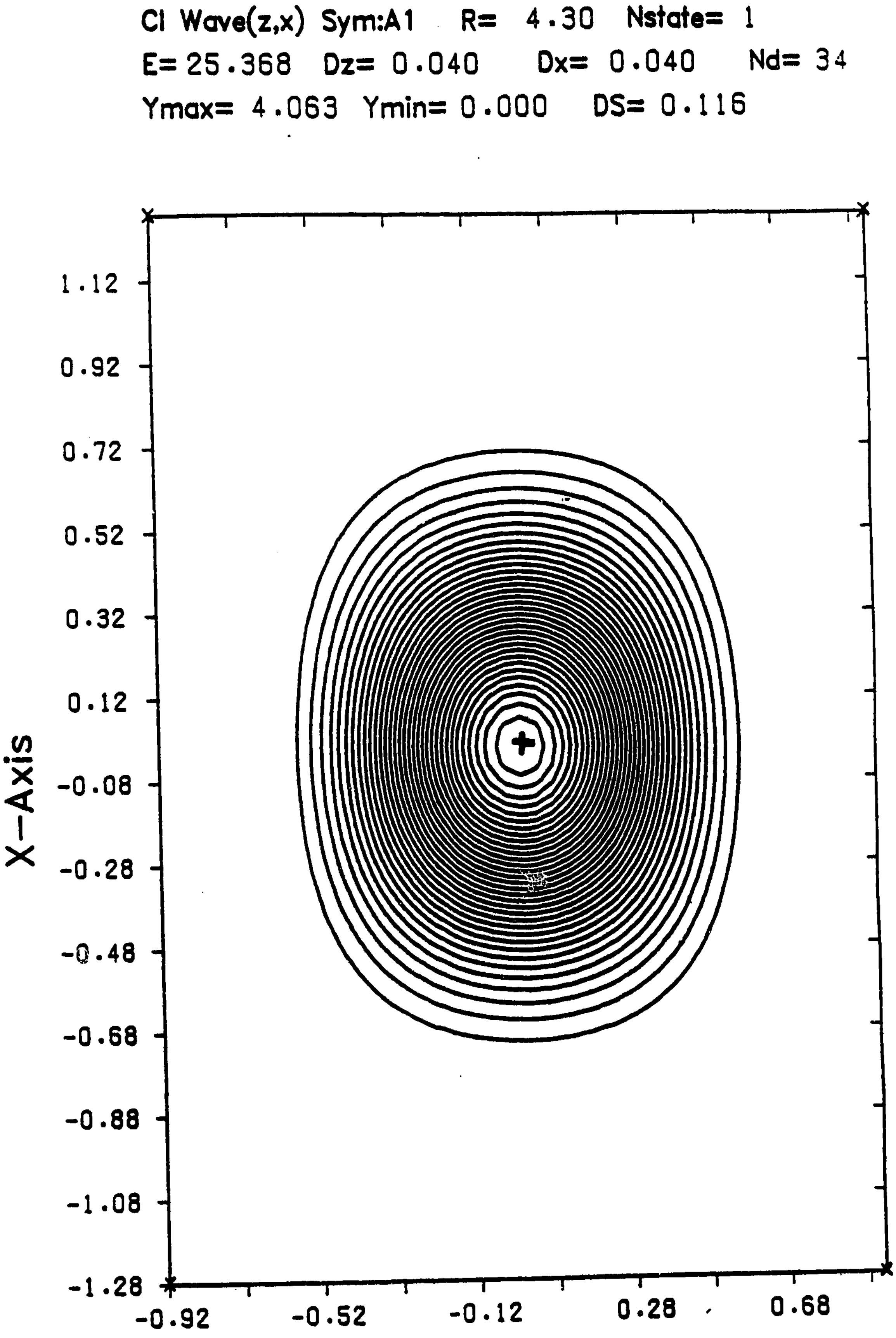
CI Wave(z,x) Sym:A1 R= 4.30 Nstate= 1
E= 25.368 Dz= 0.040 Dx= 0.040 Nd= 34
Ymax= 4.063 Ymin= 0.000 DS= 0.116
X–Axis
1.12
0.92
0.72
0.52
0.32
0.12
-0.08
-0.28
-0.48
-0.68
-0.88
-1.08
-1.28
-0.92
-0.52
-0.12
0.28
0.68

CI Wave(z,x) Sym:A1 R= 4.30 Nstate= 2
E= 70.244 Dz= 0.040 Dx= 0.040 Nd= 34
Ymax= 3.014 Ymin= -3.094 DS= 0.174

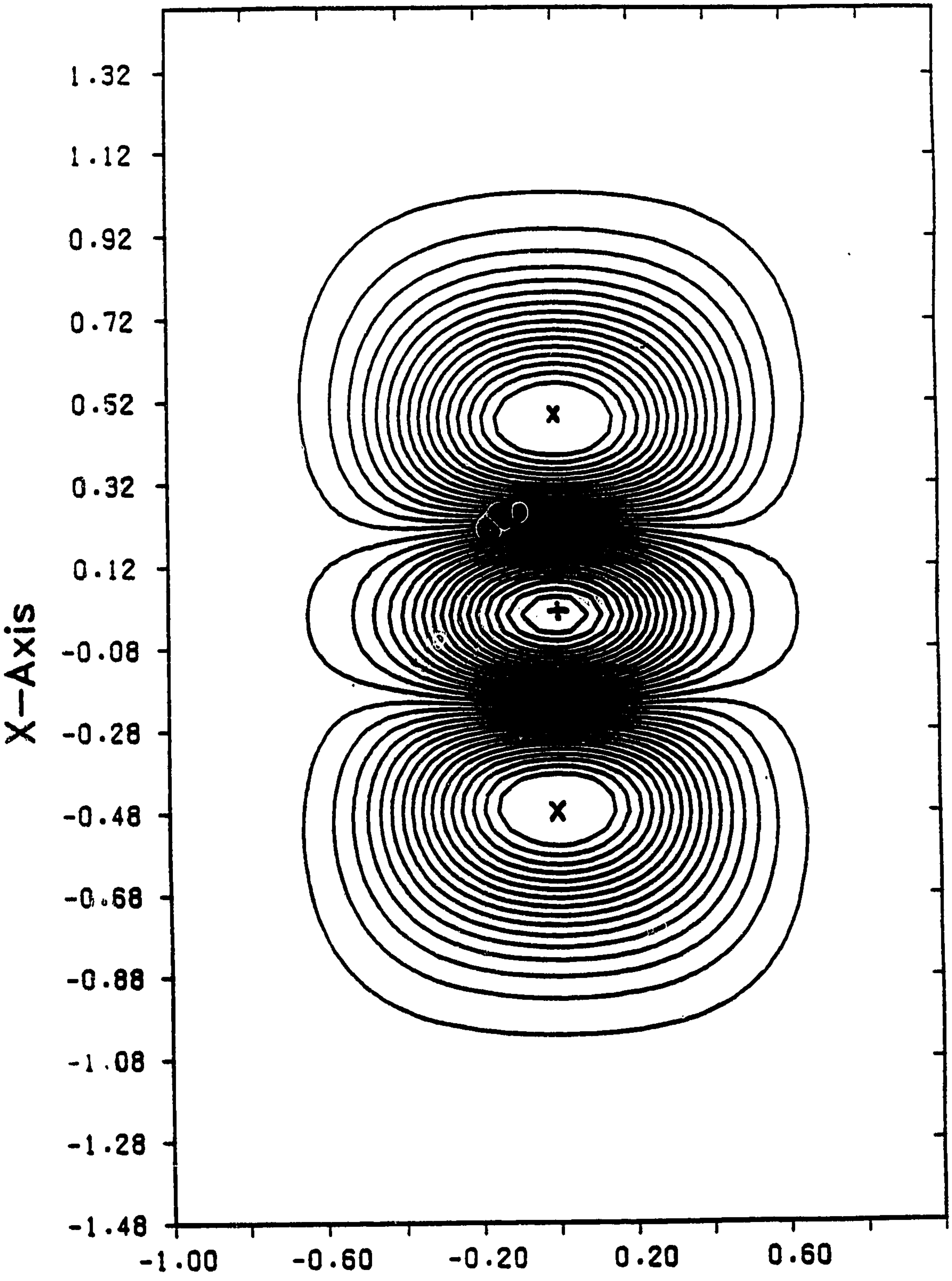

CI Wave(z,x) Sym:A1 R= 4.30 Nstate= 3
E= 95.083 Dz= 0.040 Dx= 0.040 Nd= 33
Ymax= 2.883 Ymin= -3.382 DS= 0.179

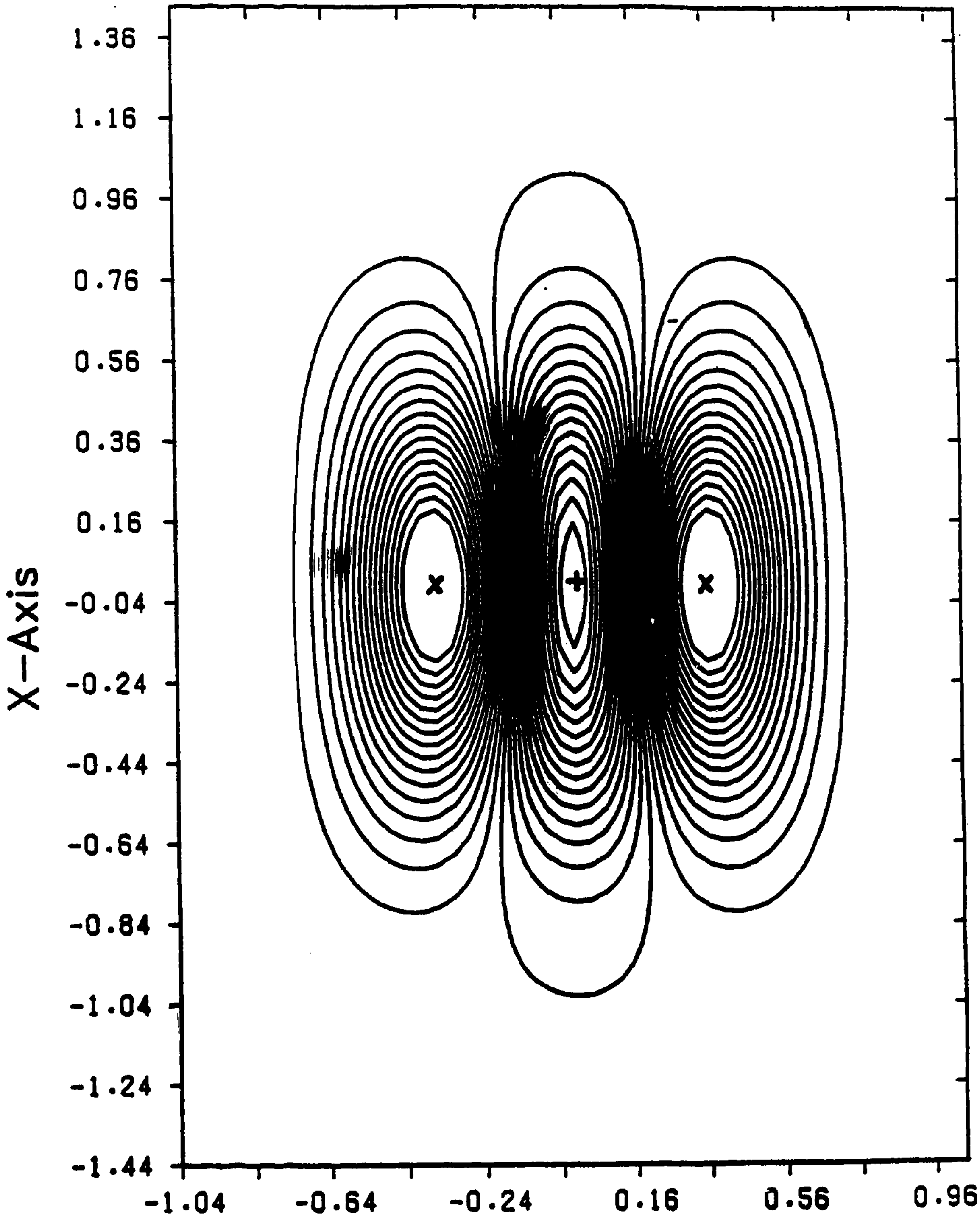

CI Wave(z,x) Sym:A1 R= 4.30 Nstate= 4
E= 116.280 Dz= 0.040 Dx= 0.040 Nd= 33
Ymax= 2.935 Ymin= -2.631 DS= 0.159

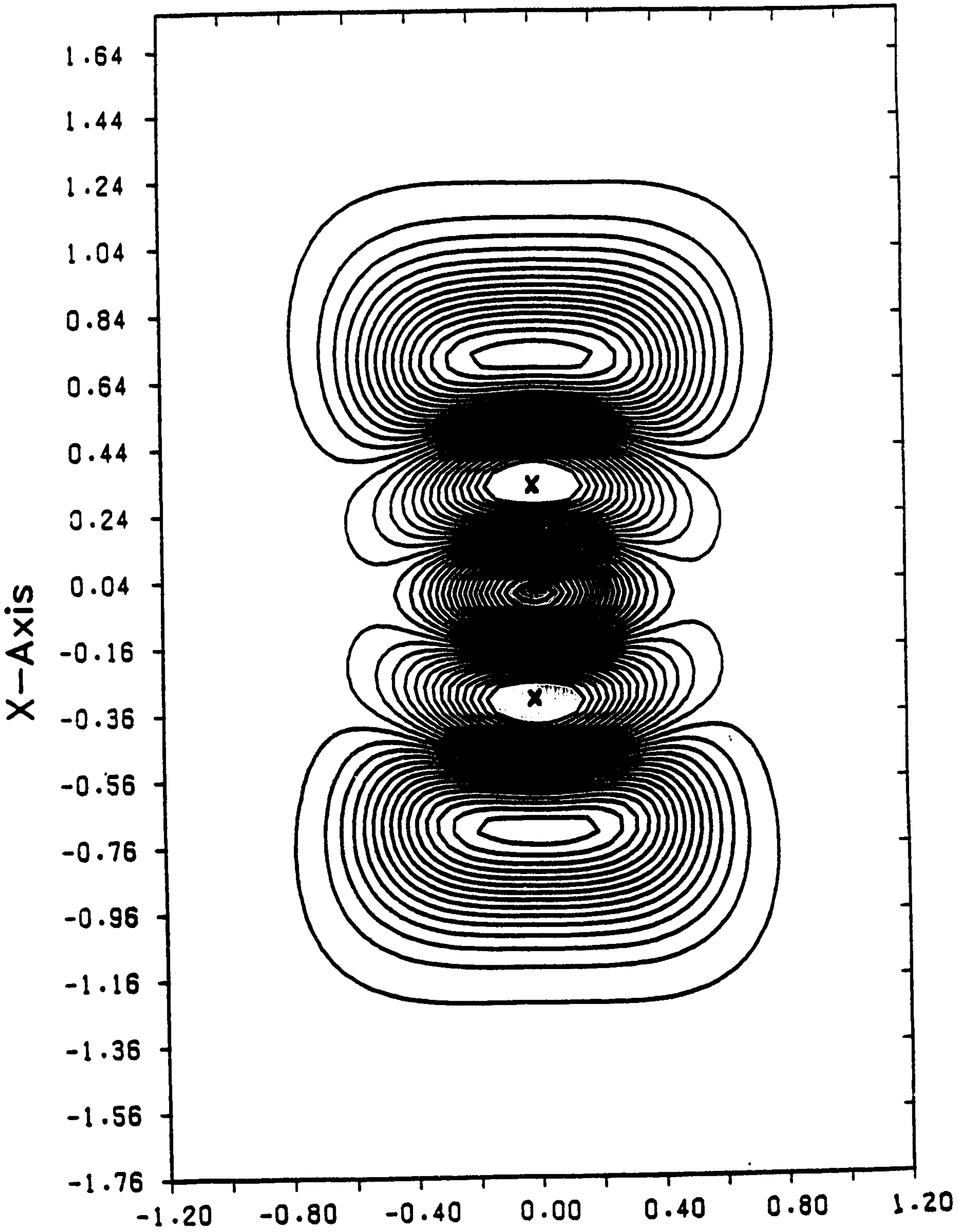

CI Wave(z,x) Sym:A1 R= 4.30 Nstate= 5
E= 131.500 Dz= 0.040 Dx= 0.040 Nd= 33
Ymax= 2.528 Ymin= -2.755 DS= 0.151

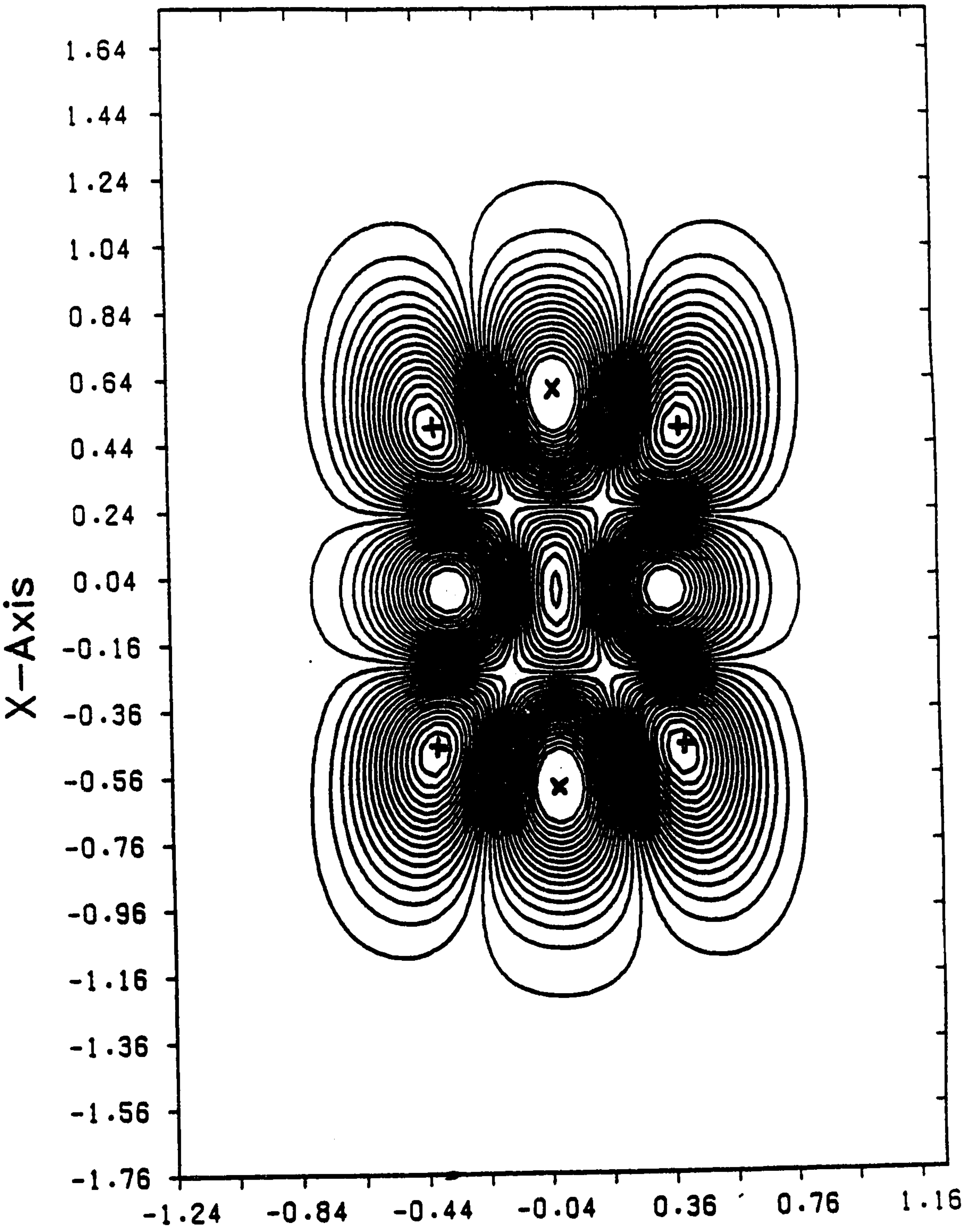

Cl Wave(z,x) Sym:A1 R= 4.30 Nstate= 6

E= 160.931 Dz= 0.040 Dx= 0.040 Nd= 33

Ymax= 3.014 Ymin= -2.679 DS= 0.163

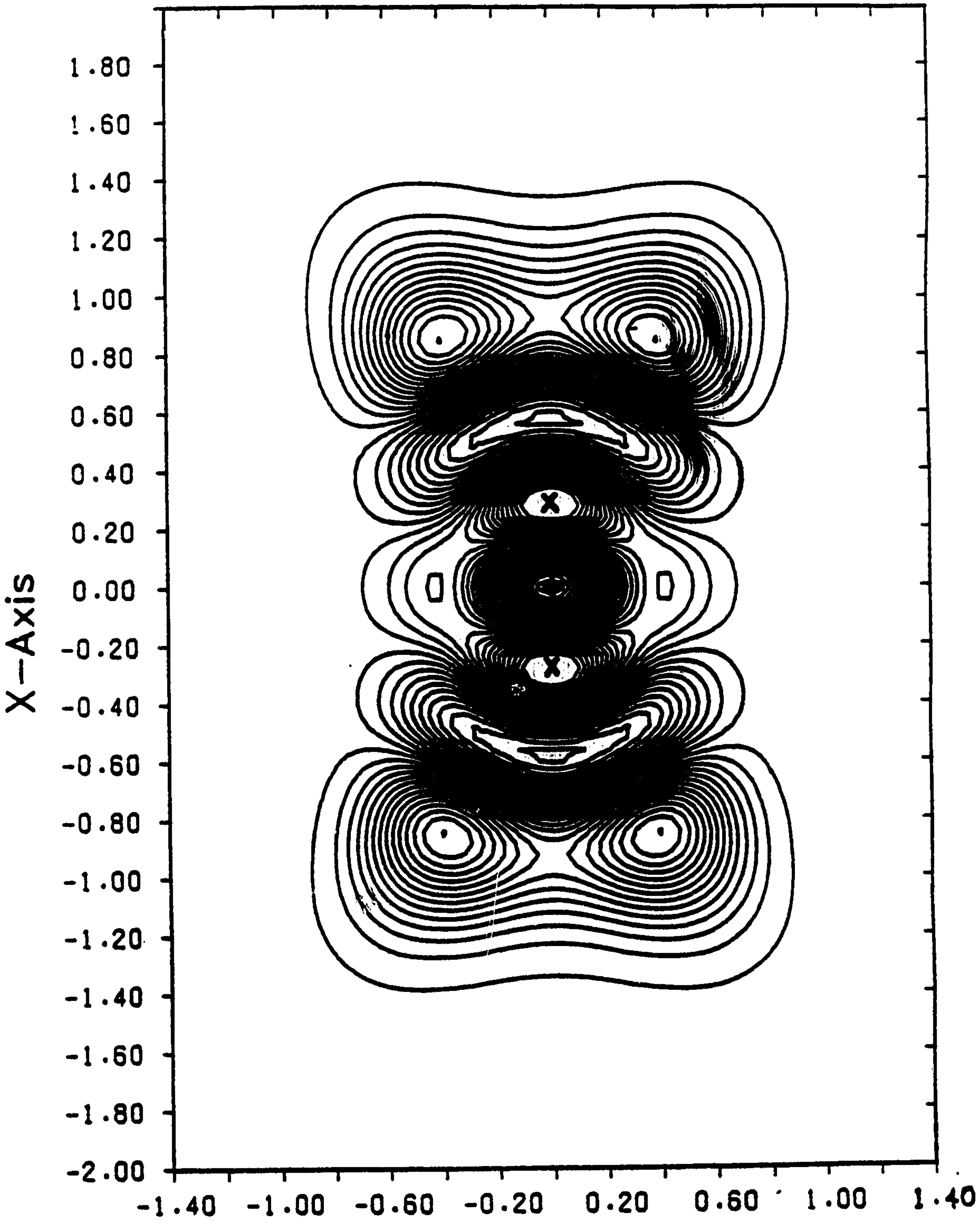

CI Wave(z,x) Sym:A1 R= 4.30 Nstate= 7
E= 172.726 Dz= 0.040 Dx= 0.040 Nd= 33
Ymax= 3.027 Ymin= -2.298 DS= 0.152

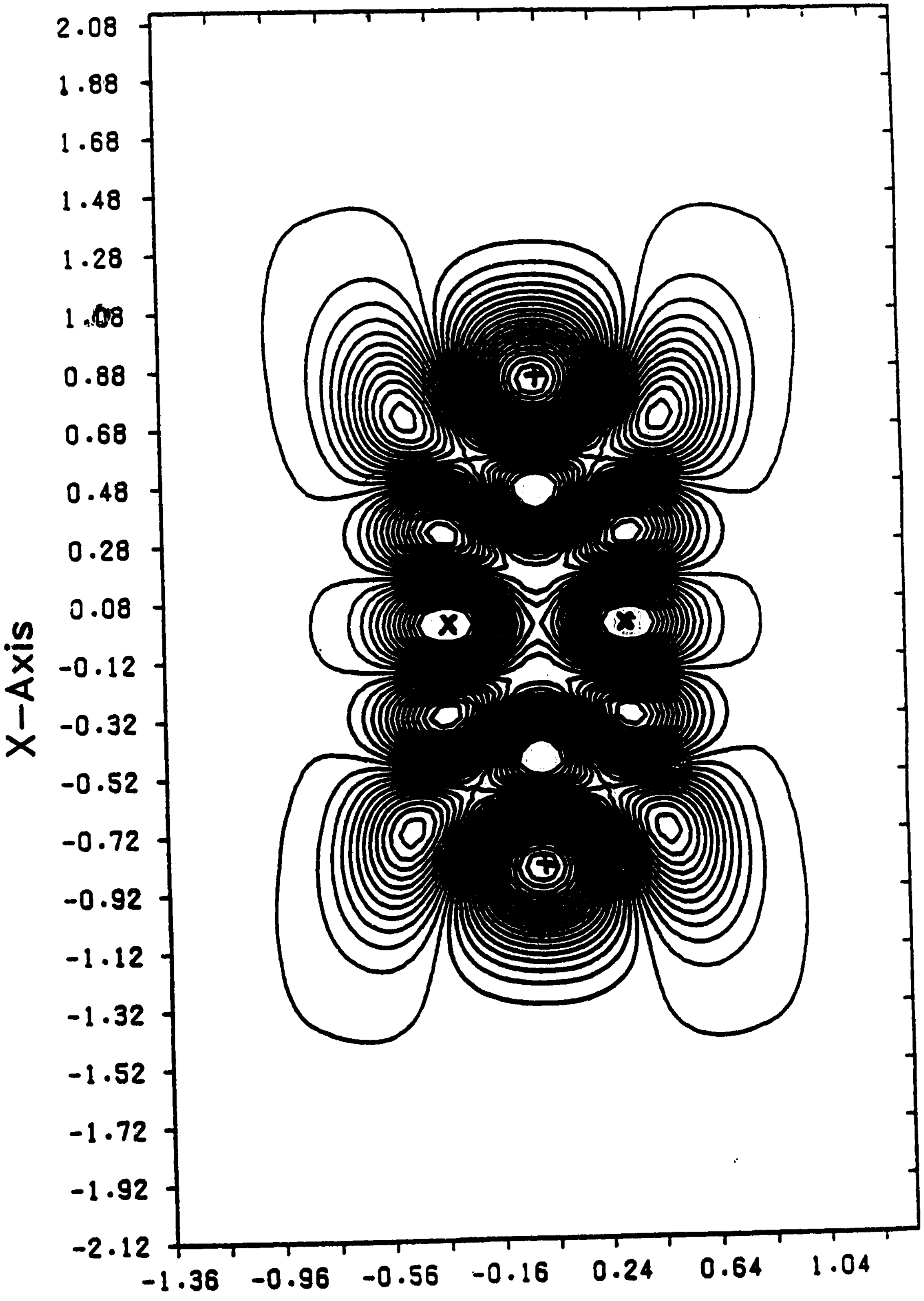

CI Wave(z,x) Sym:A1 R= 4.30 Nstate= 8
E= 184.367 Dz= 0.040 Dx= 0.040 Nd= 33
Ymax= 2.932 Ymin= -2.634 DS= 0.159

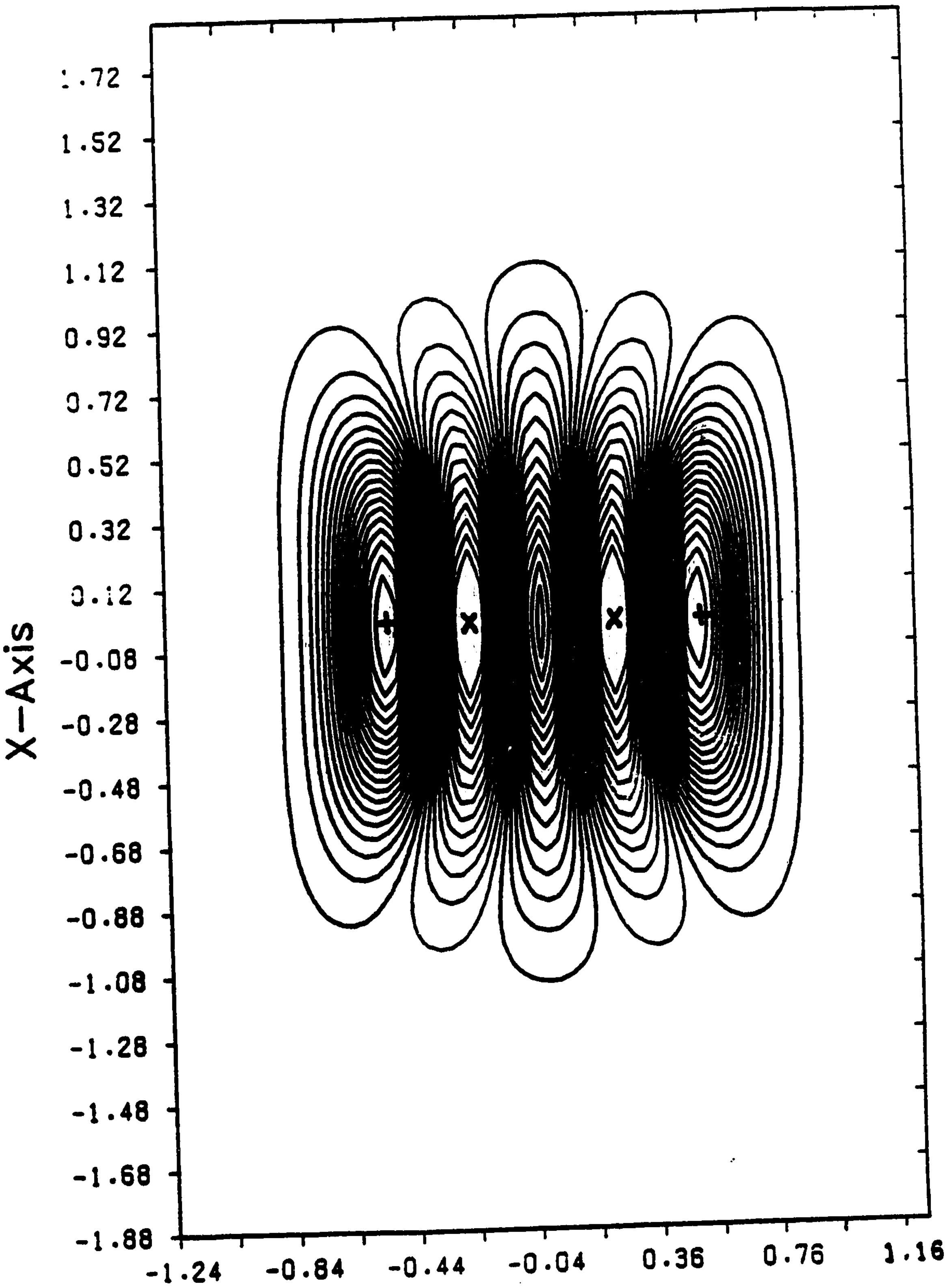

Cl Wave(z,x) Sym:A1 R= 4.30 Nstate= 9

E= 201.622 Dz= 0.040 Dx= 0.040 Nd= 33

Ymax= 2.530 Ymin= -2.509 DS= 0.144

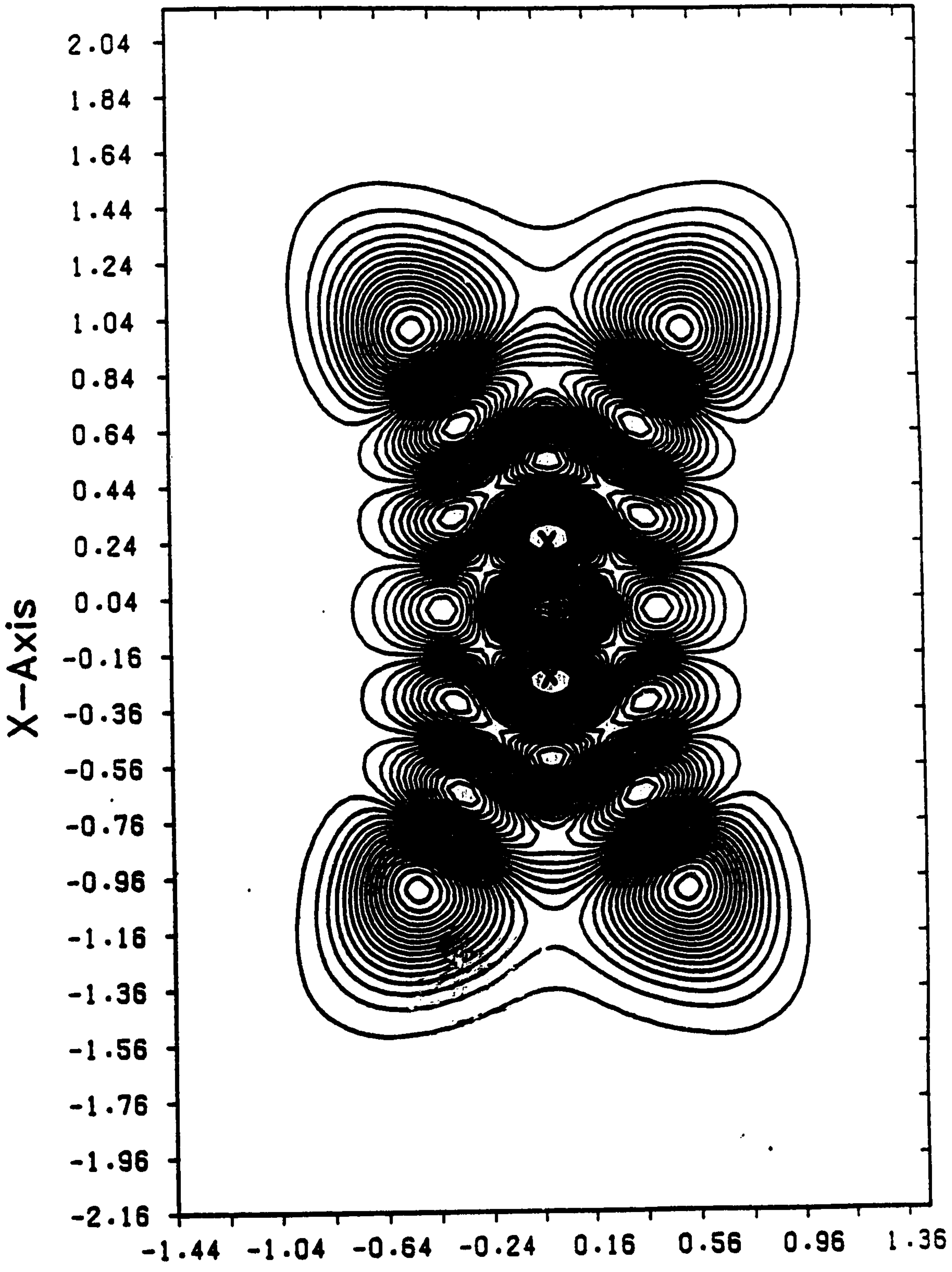

CI Wave(z,x) Sym:A1 R= 4.30 Nstate= 10
E= 211.870 Dz= 0.040 Dx= 0.040 Nd= 33
Ymax= 2.360 Ymin= -2.579 DS= 0.141

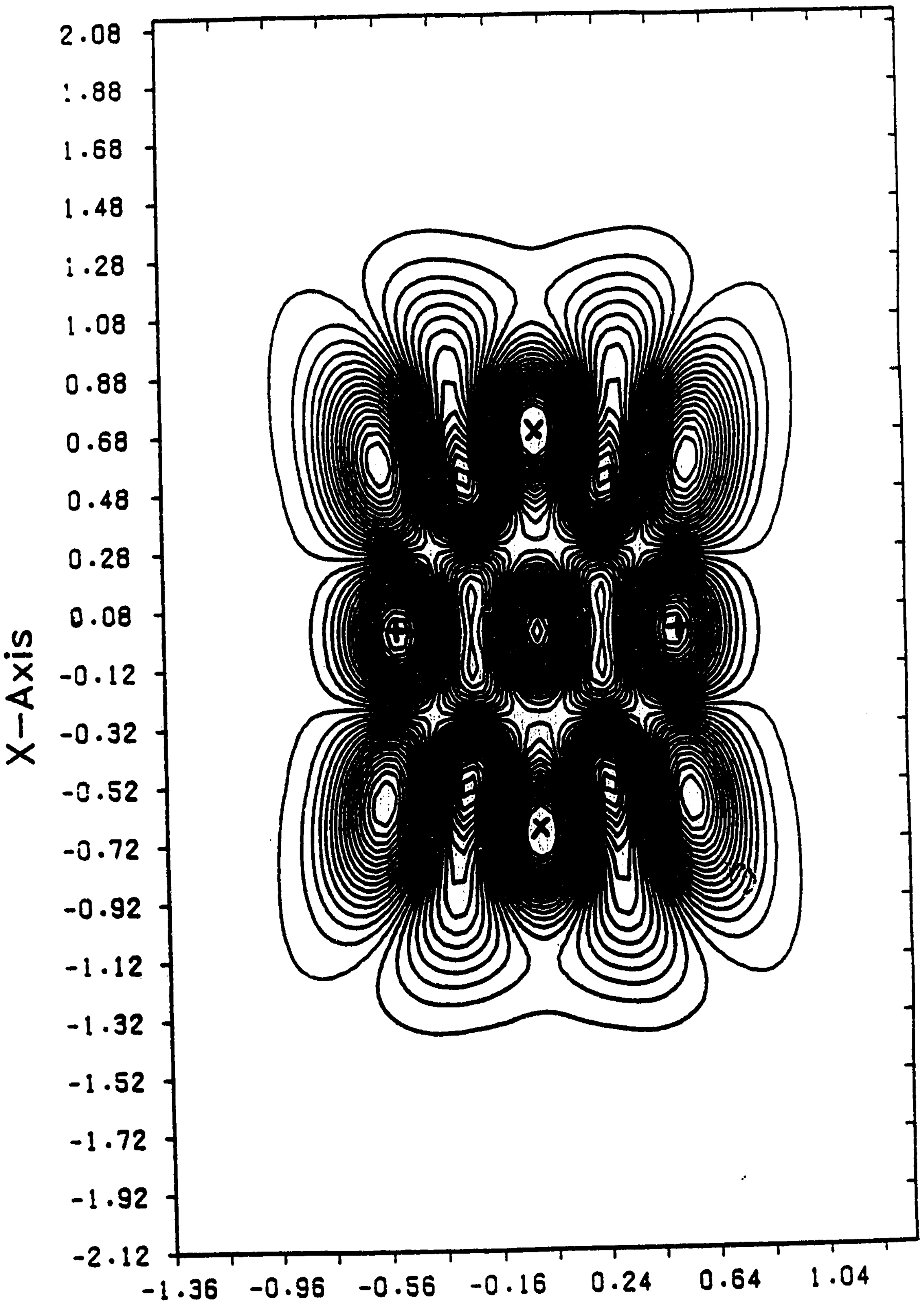

CI Wave(z,x) Sym:A1 R= 4.30 Nstate= 11
E= 219.073 Dz= 0.040 Dx= 0.040 Nd= 34
Ymax= 1.919 Ymin= -2.871 DS= 0.137

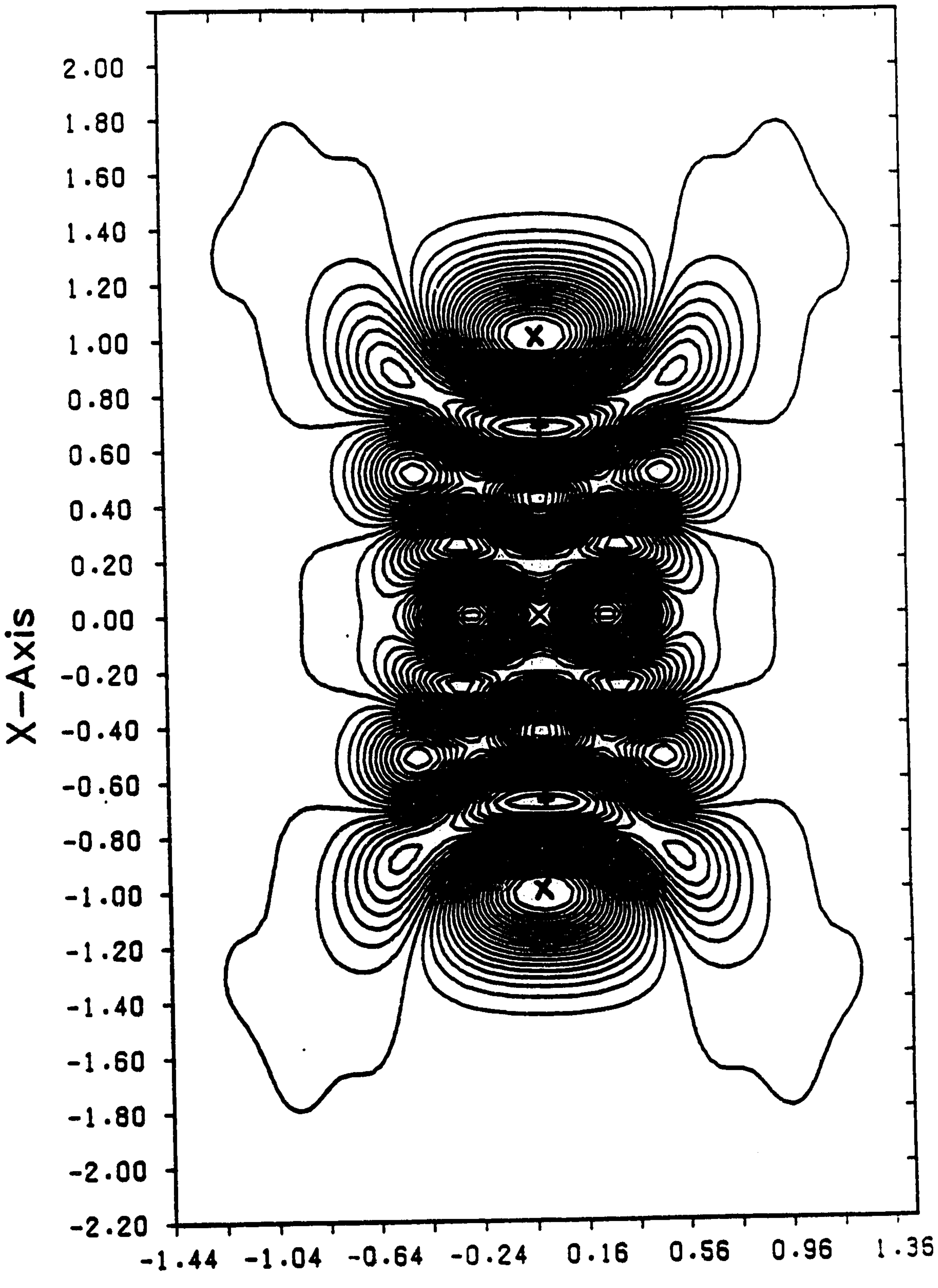

CI Wave(z,x) Sym:A1 R= 4.30 Nstate= 12
E= 238.785 Dz= 0.040 Dx= 0.040 Nd= 33
Ymax= 2.232 Ymin= -2.252 DS= 0.128

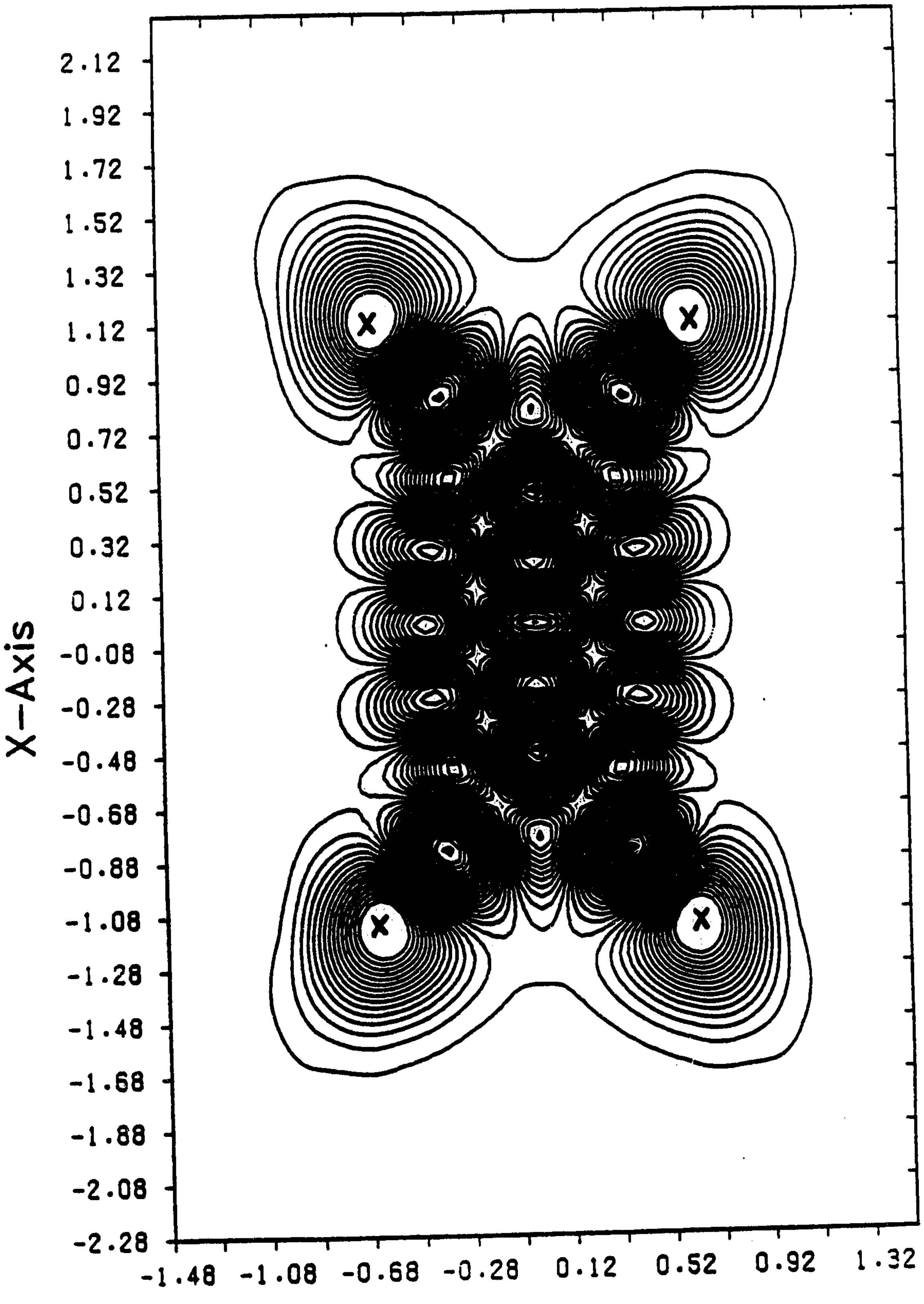

CI Wave(z,x) Sym:A1 R= 4.30 Nstate= 13
E= 246.470 Dz= 0.040 Dx= 0.040 Nd= 34
Ymax= 2.573 Ymin= -1.918 DS= 0.128

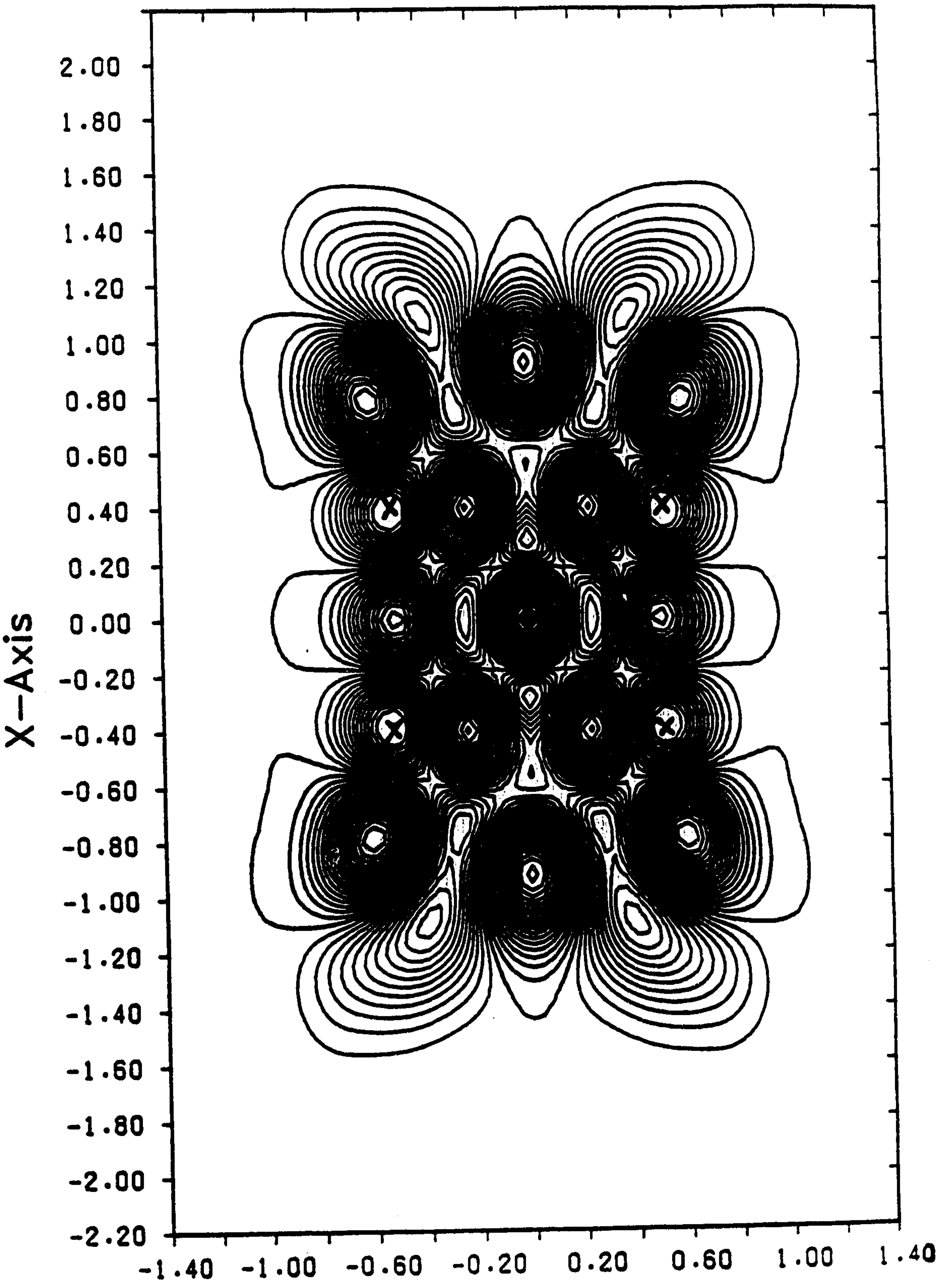

CI Wave(z,x) Sym:A1 R= 4.30 Nstate= 14
E= 266.241 Dz= 0.040 Dx= 0.040 Nd= 34
Ymax= 2.205 Ymin= -2.271 DS= 0.128

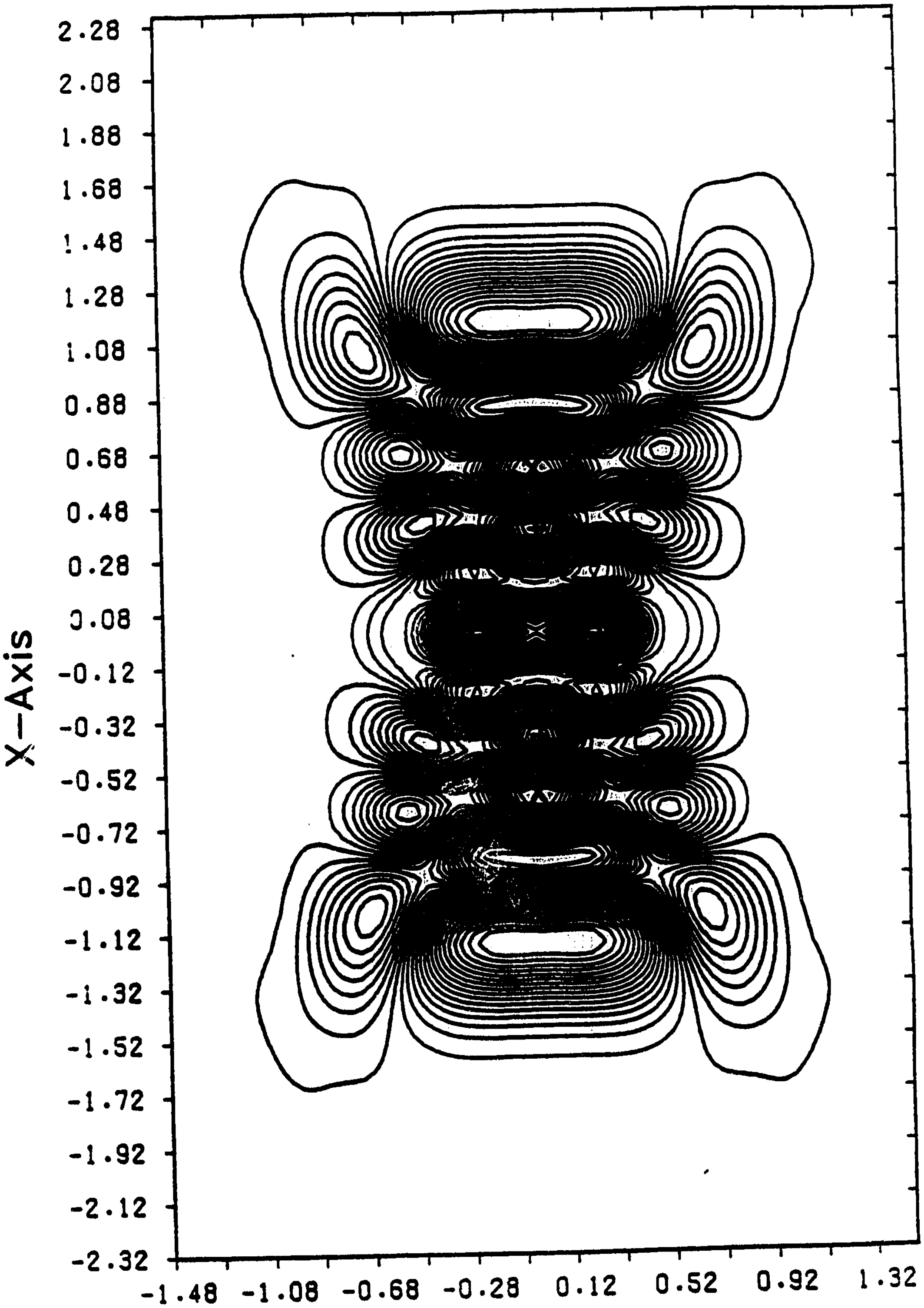

CI Wave(z,x) Sym:A1 R= 4.30 Nstate= 15

E= 274.683 Dz= 0.040 Dx= 0.040 Nd= 33

Ymax= 2.174 Ymin= -2.112 DS= 0.122

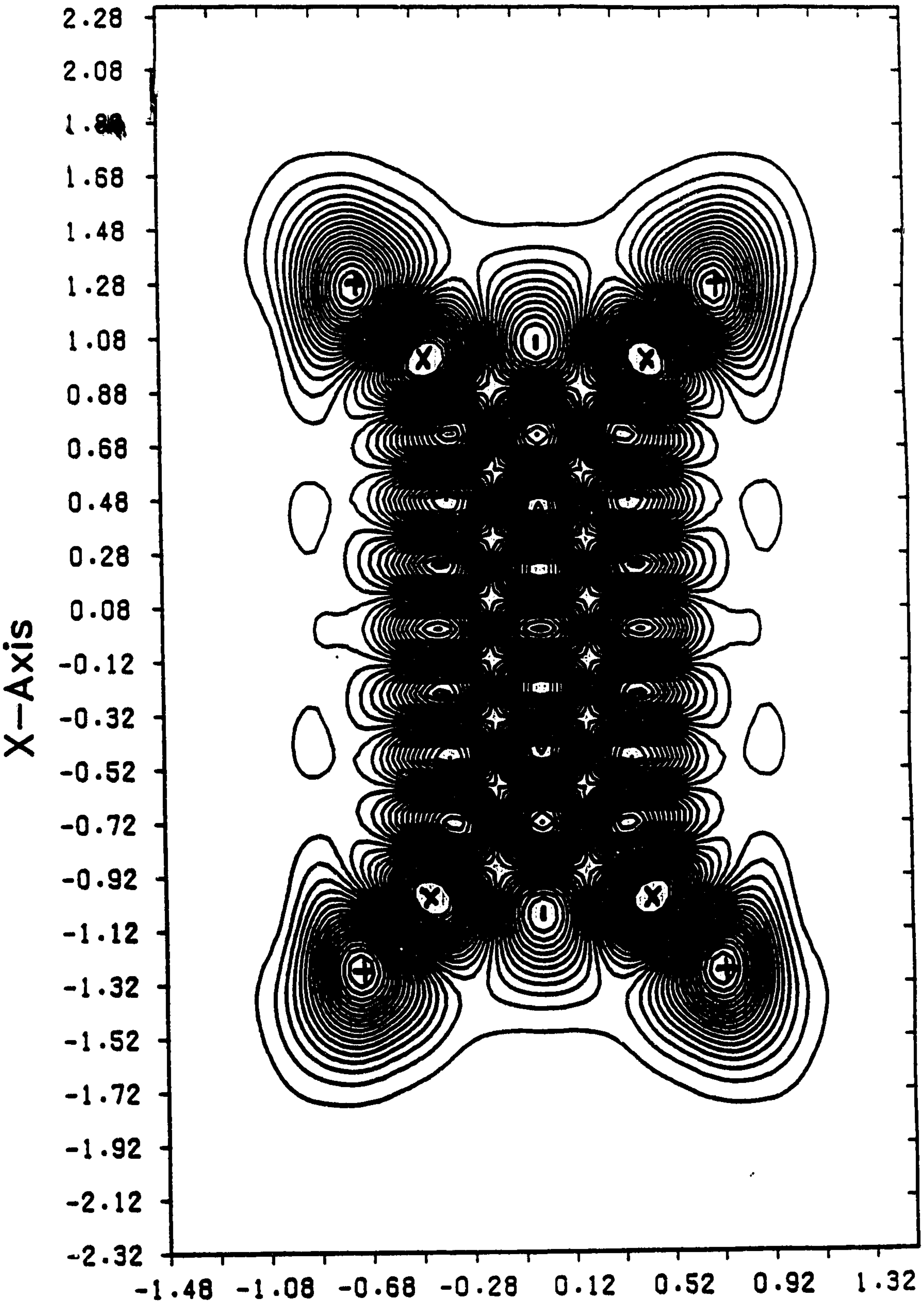

CI Wave(z,x) Sym:A1 R= 4.30 Nstate= 16

E= 284.036 Dz= 0.040 Dx= 0.040 Nd= 33

Ymax= 2.694 Ymin= -2.110 DS= 0.137

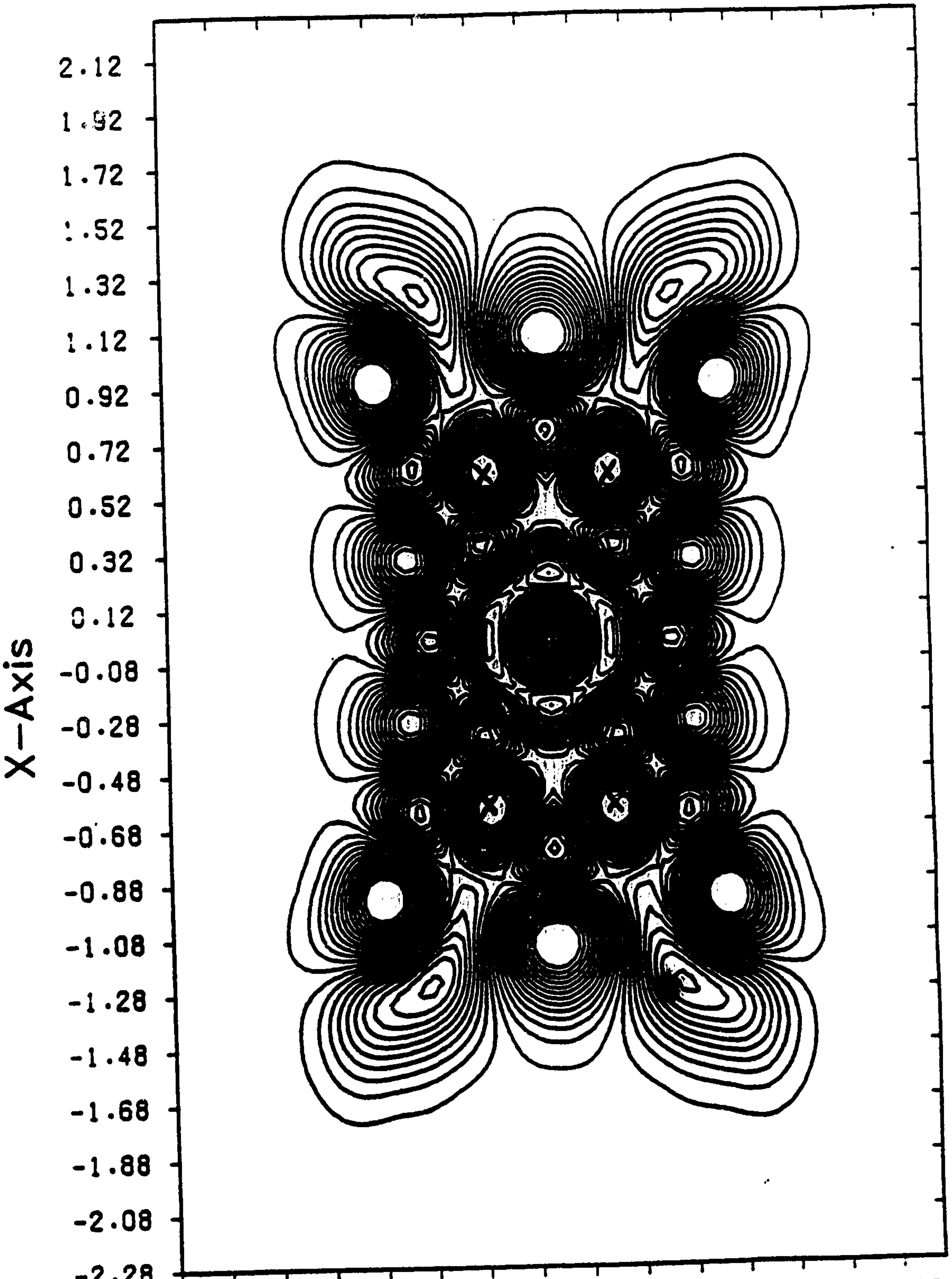

Cl Wave(z,x) Sym:A1 R= 4.30 Nstate= 17
E= 286.088 Dz= 0.040 Dx= 0.040 Nd= 33
Ymax= 2.182 Ymin= -2.701 DS= 0.139

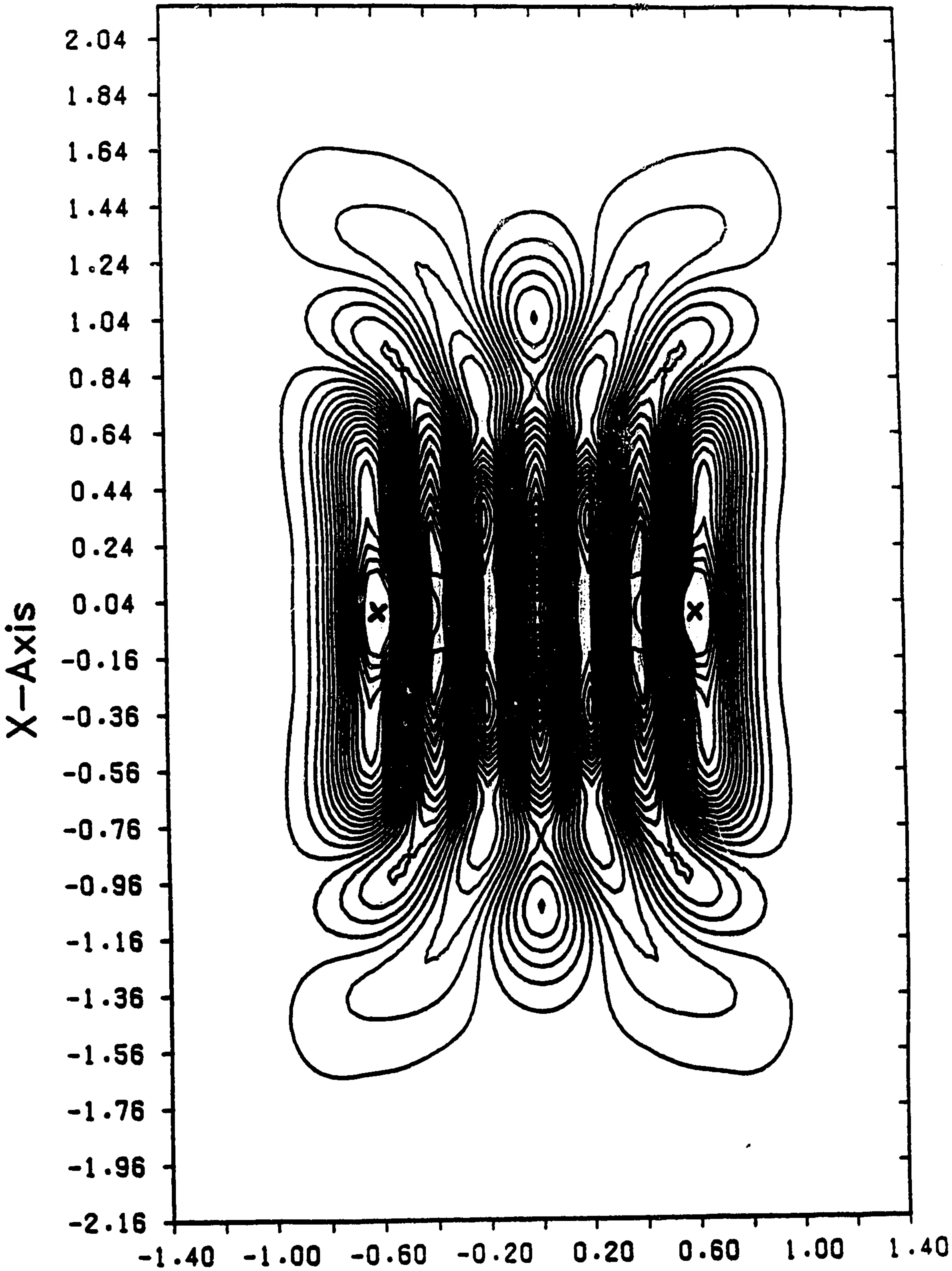

CI Wave(z,x) Sym:A1 R= 4.30 Nstate= 18
E= 304.466 Dz= 0.040 Dx= 0.040 Nd= 33
Ymax= 2.205 Ymin= -2.055 DS= 0.122

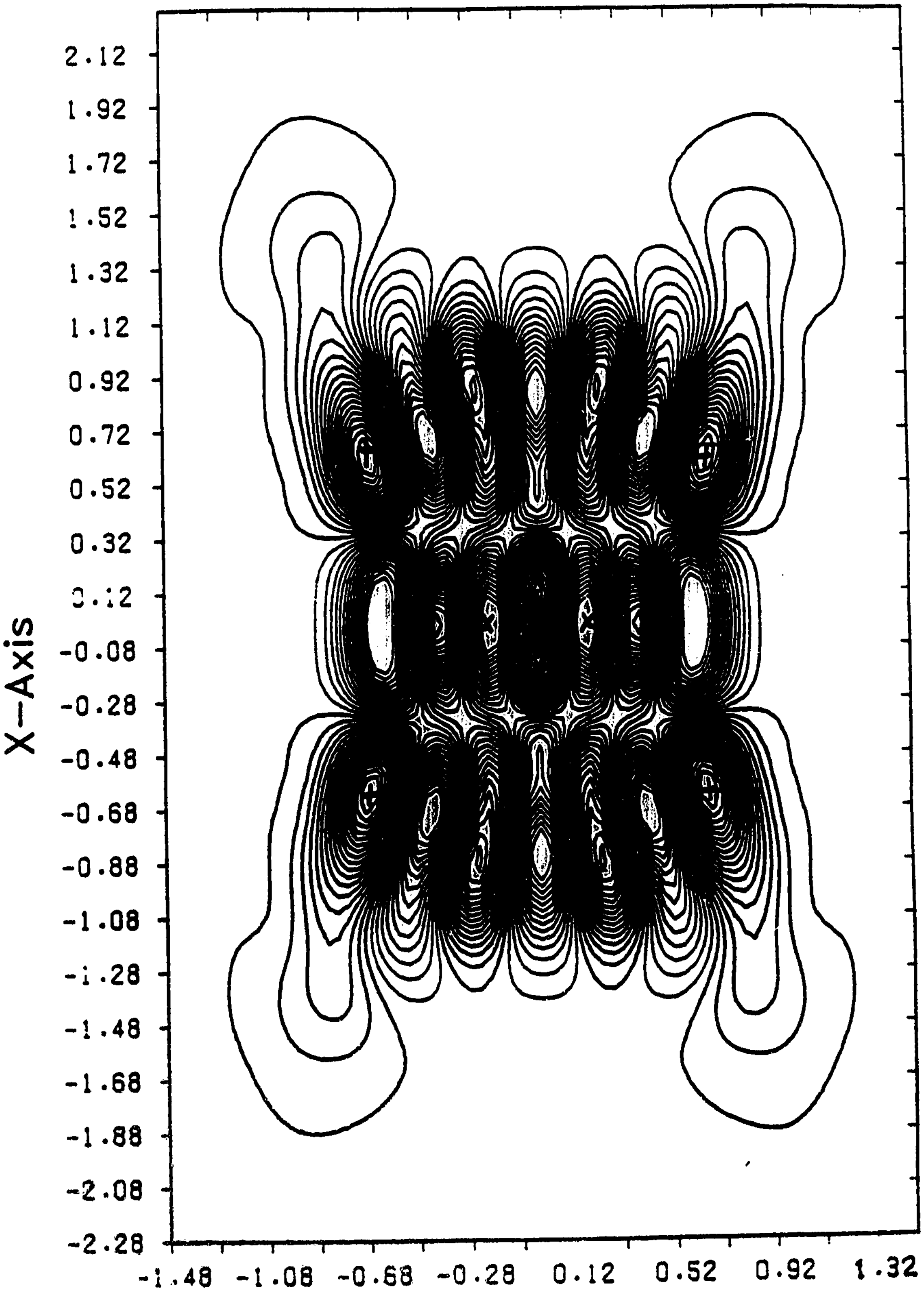

Figure 2.12: The notation used in this set of plots is the same as that described in Figure 2.11. Displayed here are the quantum CI wave functions at the narrow avoided crossing of SCF states (2,0) and (0,2) at $R = 4.54805$ a.u. The energy splitting in the SCF domain is 8.910^{-4} c.e.u. = 0.05 cm^{-1}; the energy splitting in the CI states is 3.05 c.e.u. or 187 cm^{-1}.

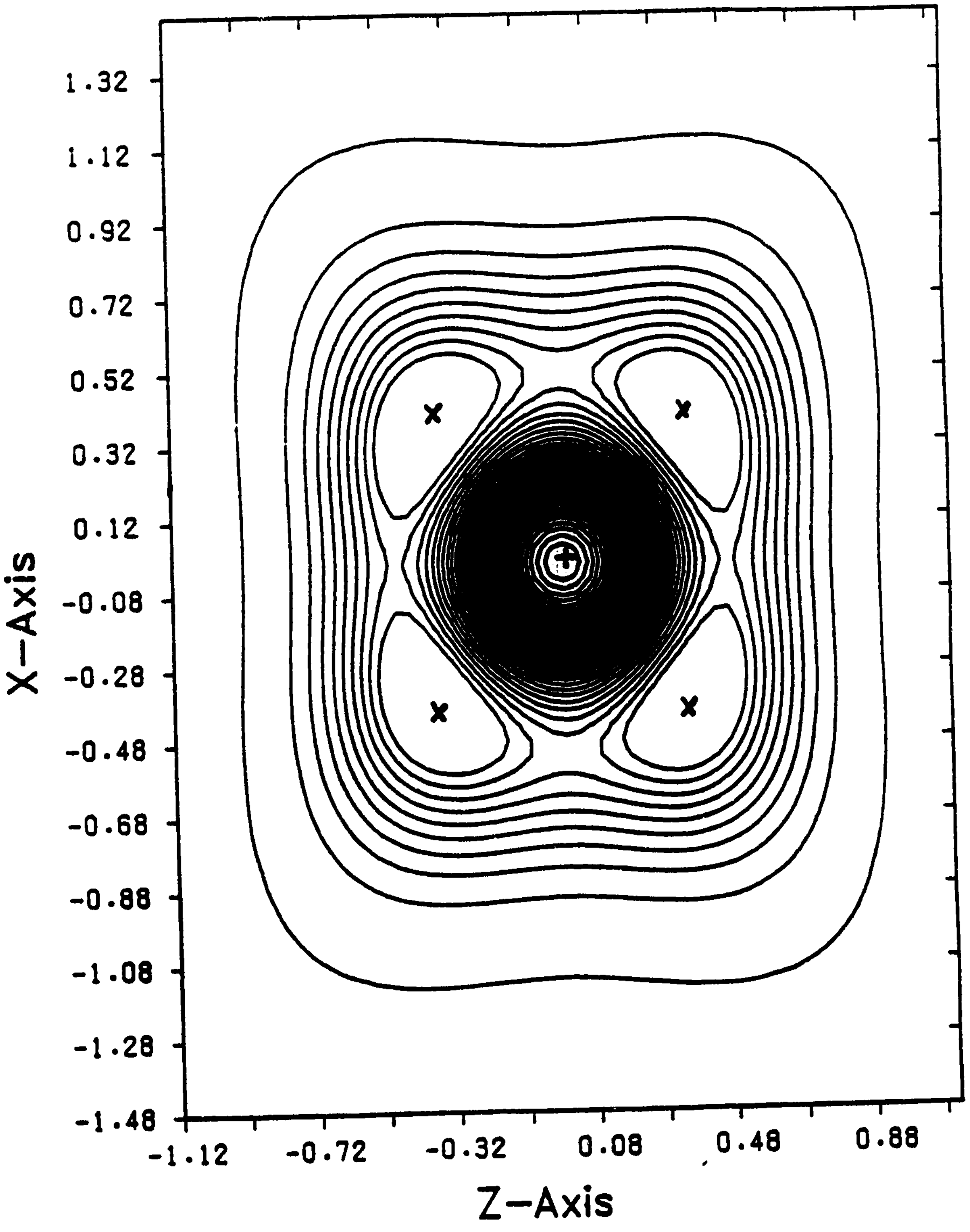

CI Wave(z,x) Sym:A1 R= 4.55 Nstate= 2
E= 64.915 Dz= 0.040 Dx= 0.040 Nd= 33
Ymax= 3.873 Ymin= -2.050 DS= 0.169

CI Wave(z,x) Sym:A1 R= 4.55 Nstate= 3
E= 67.966 Dz= 0.040 Dx= 0.040 Nd= 33
Ymax= 2.768 Ymin= -3.178 DS= 0.170

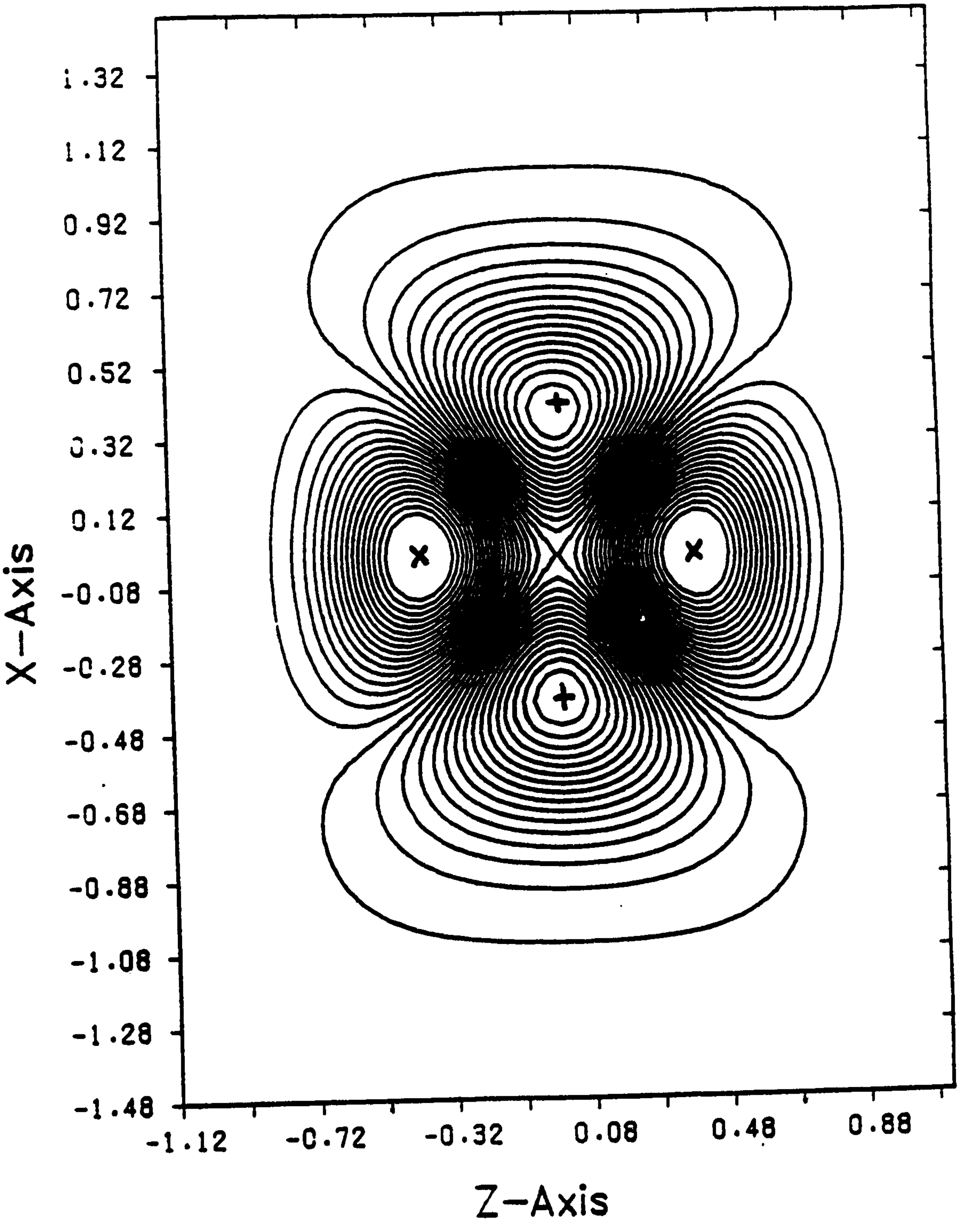

Figure 2.13: The notation used in this set of plots is the same as that described in Figure 2.11. Displayed here are the quantum CI wave functions near the narrow avoided crossing of SCF states (4,0) and (2,2) at $R = 4.45$ a.u.

CI Wave(z,x) Sym:A1 R= 4.45 Nstate= 4
E= 111.910 Dz= 0.040 Dx= 0.040 Nd= 33
Ymax= 3.208 Ymin= -2.587 DS= 0.166

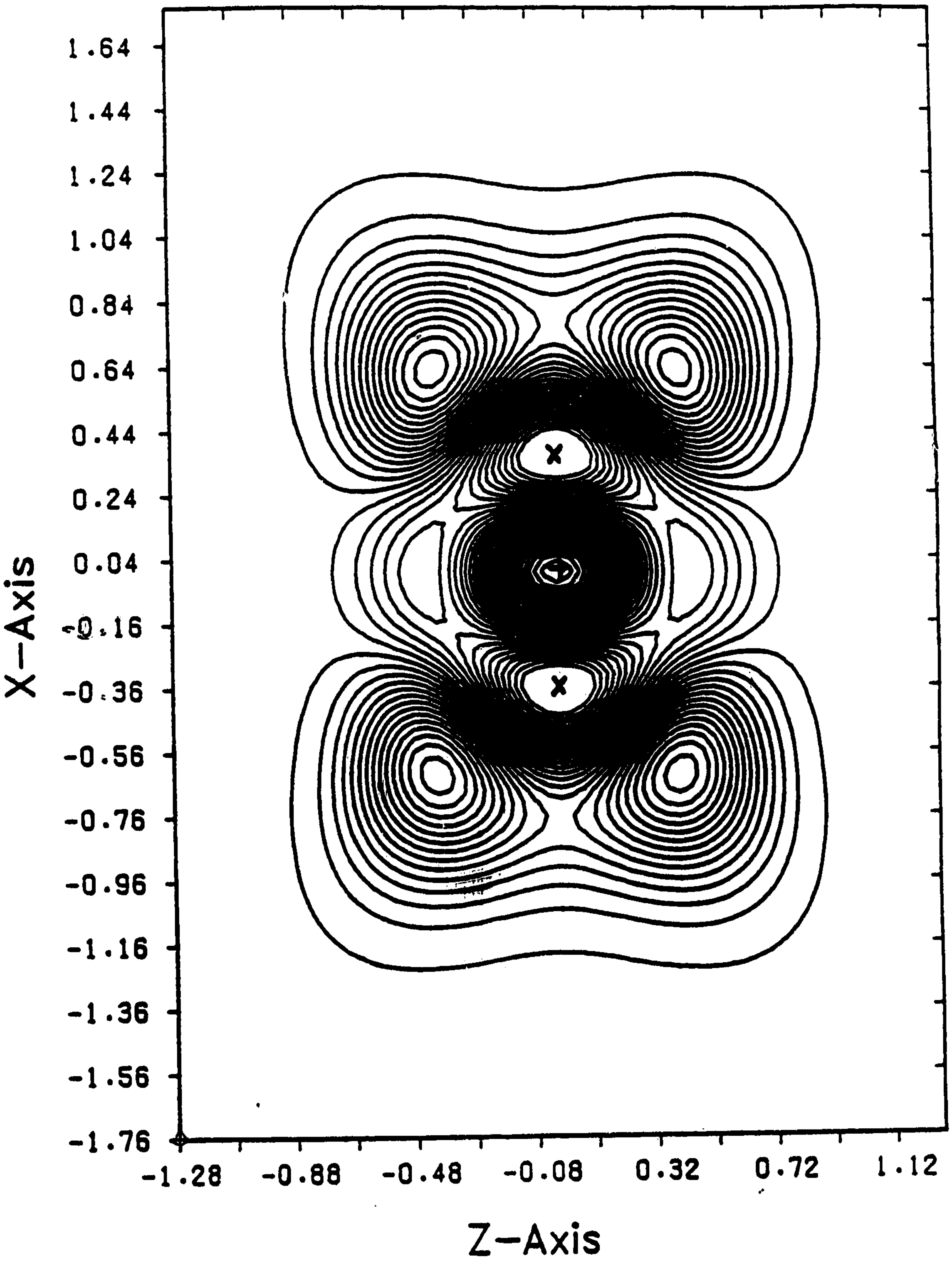

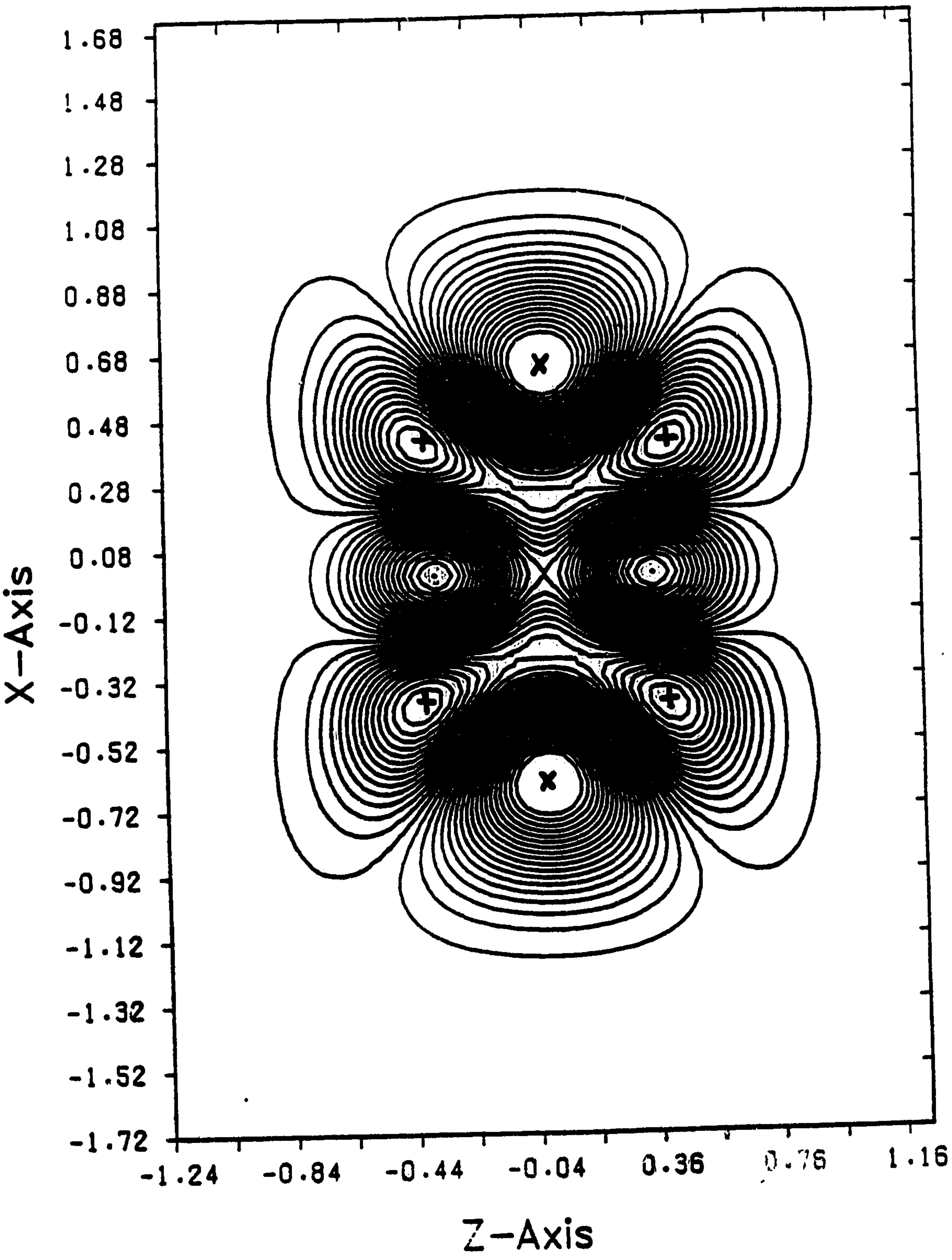

CI Wave(z,x) Sym:A1 R= 4.45 Nstate= 5
E= 119.373 Dz= 0.040 Dx= 0.040 Nd= 33
Ymax= 2.120 Ymin= -3.085 DS= 0.149

Figure 2.14: The notation used in this set of plots is the same as that described in Figure 2.11. Displayed here are the quantum CI wave functions near the narrow avoided crossing of SCF states (6,0), (4,2) and (0,4) at R = 4.40 a.u. The states (6,0) and (4,2) are split by a greater amount than (0,4) is from either indicating a stronger CI interaction between the former two. For further comparison, consider the states 9 through 11 in the R = 4.30 a.u. series of figures. These states are associated with the triple crossing between (8,0), (6,2) and (2,4) and contain the same trends as indicated at this R-value.

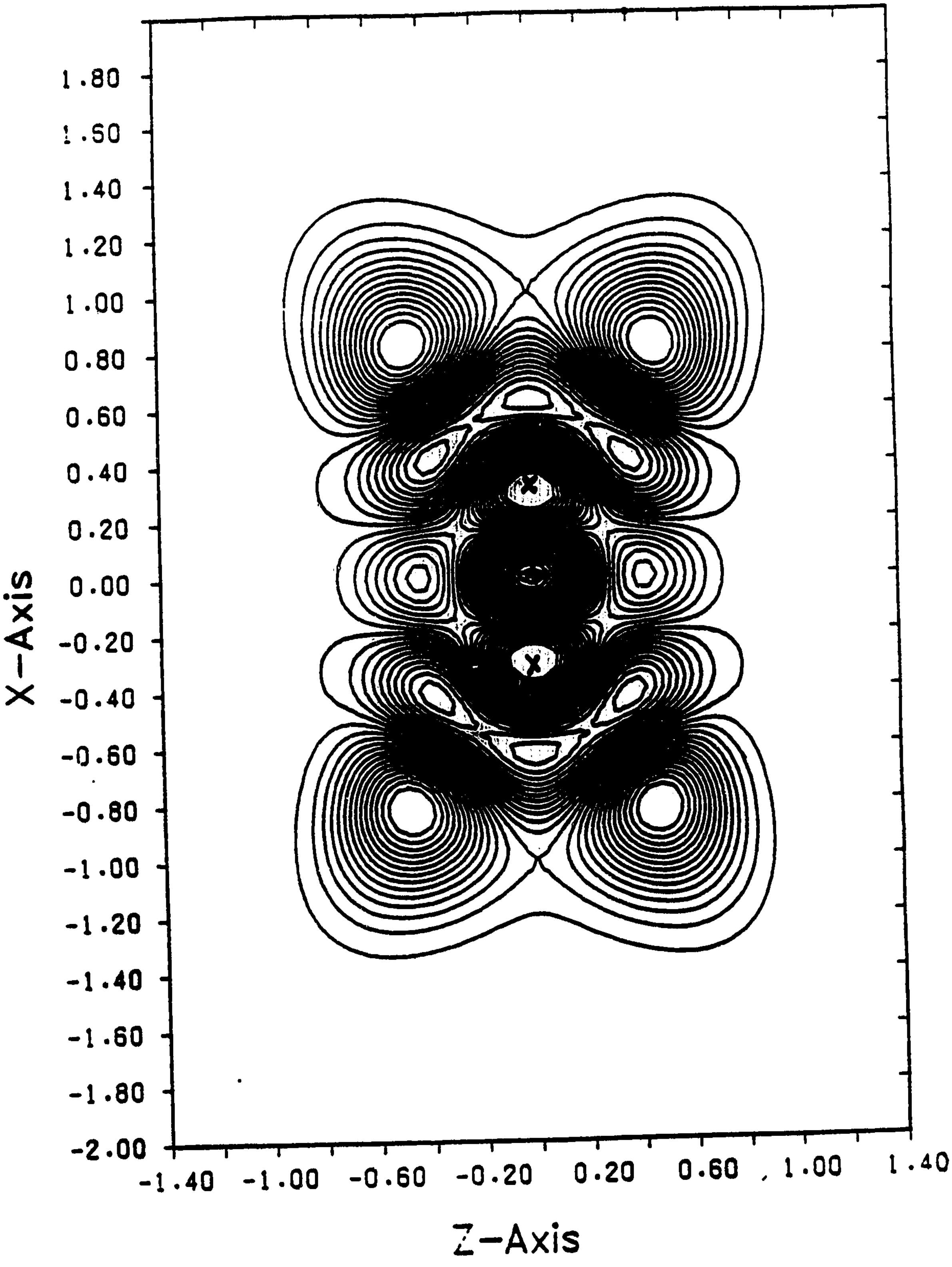

CI Wave(z,x) Sym:A1 R= 4.40 Nstate= 6
E= 155.629 Dz= 0.040 Dx= 0.040 Nd= 33
Ymax= 2.819 Ymin= -2.594 DS= 0.155

CI Wave(z,x) Sym:A1 R= 4.40 Nstate= 7
E= 164.083 Dz= 0.040 Dx= 0.040 Nd= 33
Ymax= 3.056 Ymin= -2.405 DS= 0.156

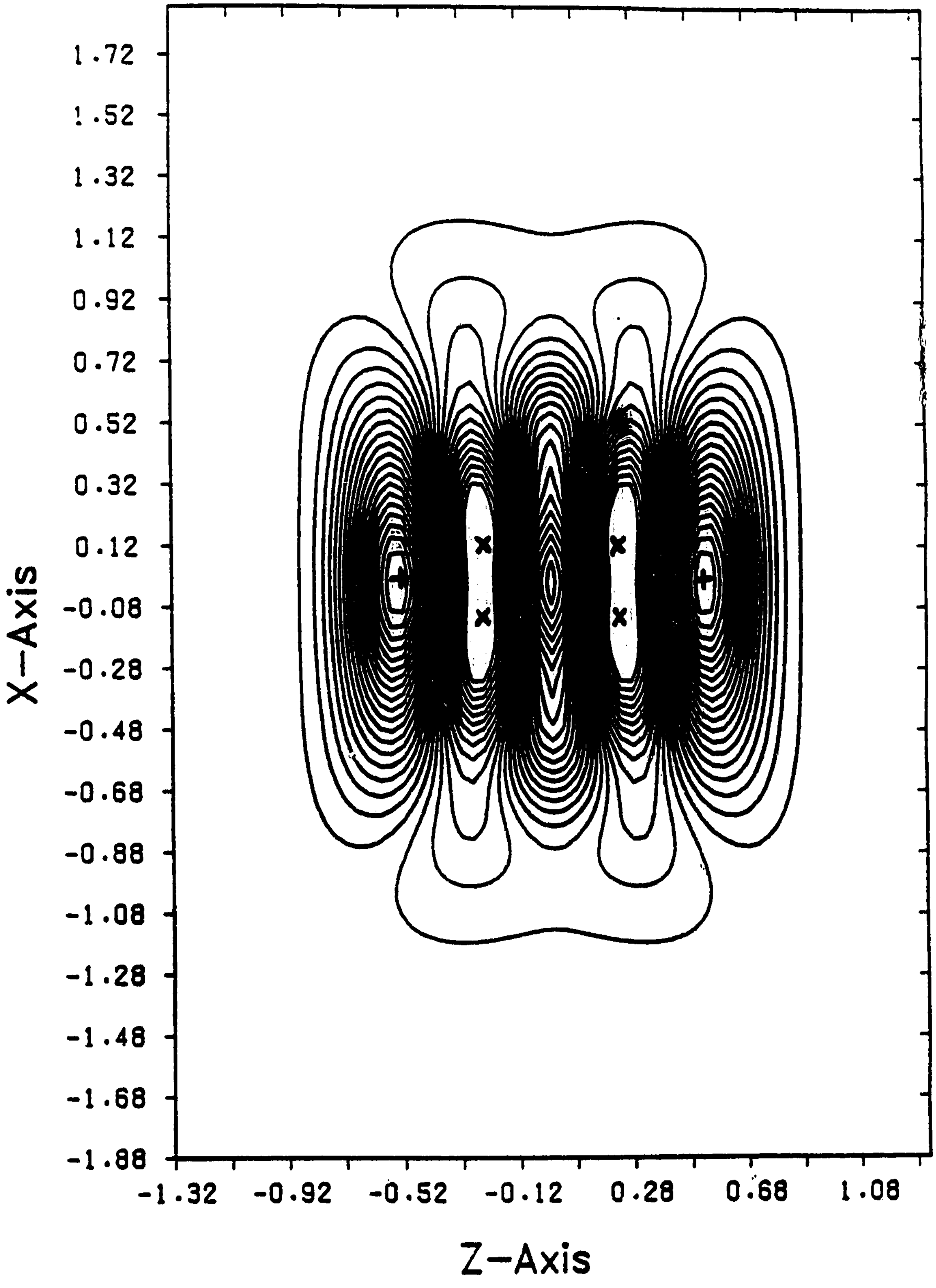

CI Wave(z,x) Sym:A1 R= 4.40 Nstate= 8
E= 168.504 Dz= 0.040 Dx= 0.040 Nd= 33
Ymax= 2.370 Ymin= -2.963 DS= 0.152

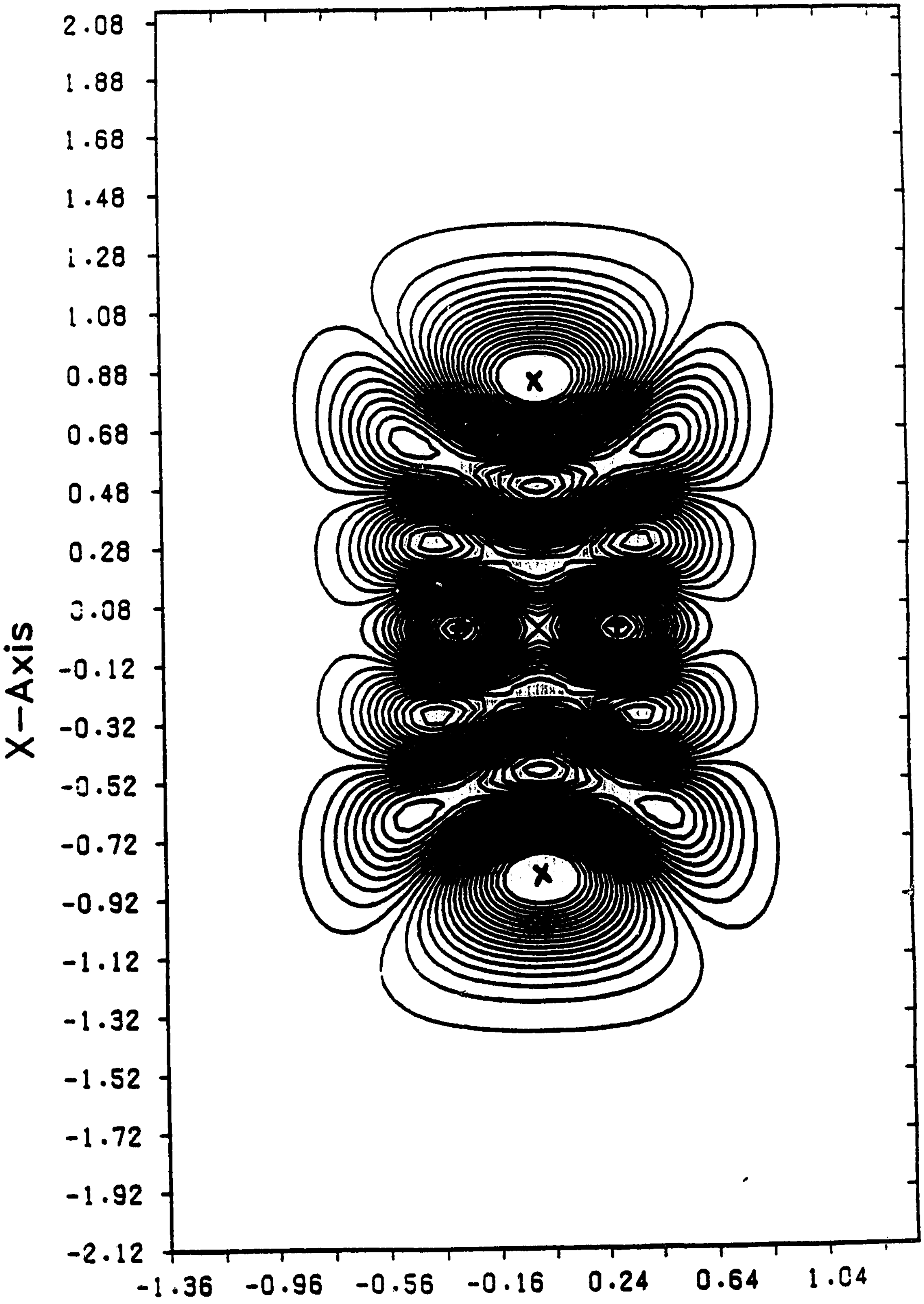

Chapter 3

Semiclassical SCF Theory

3.1 Introduction

The Self-Consistent Field (SCF) approximation replaces the actual Hamiltonian for a system by an approximate Hamiltonian which is separable in the selected coordinates. Hence, it is not difficult to construct a *Classical Self-Consistent Field* (CSCF) approximation [15]. Such an approximation to motion in a system with N degrees of freedom is defined by specifying the set of actions associated with the particular chosen coordinates $\{q_i\}$,

$$J_i = \frac{1}{2\pi} \oint p_i dq_i, \qquad i = 1, \ldots N. \qquad [3.1]$$

Each integral is associated with a one-dimensional motion and is taken over a complete period T_i of that degree of freedom,

$$T_i \equiv \oint dt = \oint \frac{dq_i}{\dot{q}_i}, \qquad i = 1, \ldots N. \qquad [3.2]$$

Given the SCF effective potential $V_i^{SCF}(q_i)$ and a value for the associated separation constant E_i, the momentum p_i conjugate to q_i is determined by the classical analogue of the corresponding one-dimensional Schrödinger equation for the quantum SCF problem,

$$p_i = \sqrt{E_i - V_i^{SCF}(q_i)} \qquad i = 1, \ldots N. \qquad [3.3]$$

The average value for a dynamical variable, $F(q_i)$, may be defined as a time-average over a period,

$$\langle F(q_i)\rangle_i = \frac{1}{T_i}\oint \frac{F(q_i)dq_i}{\dot{q}_i}, \qquad [3.4]$$

(except at critical points where T_i may be infinite). With this apparatus, iterative procedures like those described in the previous chapter may be used to determine CSCF approximations.

Particular semiclassical approximations to the energies of quantum SCF states are obtained if semiclassical quantization rules are used like those of one-dimensional JWKB theory, which assign classical actions $\{J_i\}$ to each nodal quantum number $\{n_i\}$. Obviously, the accuracy of semiclassical SCF is limited by the errors inherent in the JWKB approximation as well as by anomalies in the definition of *classical* average values (such as arise for motion near a critical point).

The Classical SCF approximation has been used by Gerber and Ratner [16] to compute semiclassical approximations to the energies of quantum SCF states for molecular vibrational systems, mostly in cases with nearly harmonic potentials. Their work always assumed semiclassical quantization of actions according to the JWKB method and results were compared with other computations of quantum energy levels. They did not consider the comparisons between CSCF theory and true classical dynamics which are a focus of this study.

This chapter describes application of the CSCF approximation to the realistic model potential used here and assesses its utility as a method for predicting quantum vibrational energy levels. As might be expected, the nonharmonic nature of the potential surface introduces significant errors because of deficiencies in the JWKB approximation, but these do not appear to be aggravated by using classical instead of quantum average values for dynamical variables. While the true potential has only a shallow double-well structure for $R < 4.70$ a.u., the one-dimensional SCF effective potentials have pronounced double-wells generated by the decided corner or valley in the potential surface; SCF energy levels of interest may lie above or below the barrier separating the two wells. There are technical problems regarding continuity of classical calculations in a one-dimensional double-well at energies near the barrier maximum but no major difficulties arise from this provided the semiclassical quantization rules are suitably adapted for the double-well problem.

2

PM-1 3½"x4" PHOTOGRAPHIC MICROCOPY TARGET
NBS 1010a ANSI/ISO #2 EQUIVALENT

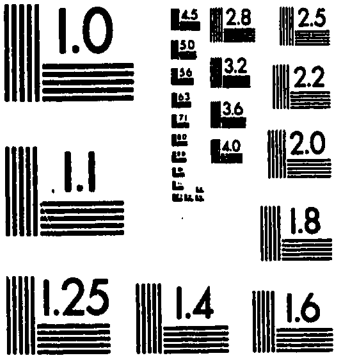
1.0
4.5
2.8
2.5
5.0
5.6
3.2
2.2
6.3
3.6
7.1
4.0
2.0
1.1
1.8
1.25
1.4
1.6

PRECISION℠ RESOLUTION TARGETS

PIONEERS IN METHYLENE BLUE TESTING SINCE 1974

Micro-D INTERNATIONAL

15000 COUNTY ROAD 5, BURNSVILLE, MN 55337, USA
TEL: 612 435 7867 FAX: 612 435 7887 TLX: 5106009486

3.2 Classical SCF Equations

For this model system, the classical SCF equations analogous to equation 2.6 are

$$\begin{aligned} p_x^2 + V_x^{SCF}(x;R) &= E_x, \\ p_z^2 + V_z^{SCF}(z;R) &= E_z. \end{aligned} \qquad [3.5]$$

Since $\dot{q}_i = 2p_i$, the SCF effective potentials are given by

$$\begin{aligned} V_x^{SCF}(x;R) = \langle V(x,z;R)\rangle_z &= \frac{1}{2T_z}\oint \frac{V(x,z;R)}{p_z}dz, \\ V_z^{SCF}(z;R) = \langle V(x,z;R)\rangle_x &= \frac{1}{2T_x}\oint \frac{V(x,z;R)}{p_x}dx. \end{aligned} \qquad [3.6]$$

Self-consistency requires as before that

$$\langle\langle V(x,z;R)\rangle\rangle = \langle V_x^{SCF}(x;R)\rangle_x = \langle V_z^{SCF}(z;R)\rangle_z. \qquad [3.7]$$

To determine a particular CSCF solution, values are assigned to the actions (J_x, J_z) and one follows the classical analogue to the SCF iteration procedure outlined in Section 2.2.

As before, the SCF effective potentials $V_i^{SCF}(q_i)$ are symmetric functions of their arguments and either have a single minimum or a double-well form with a barrier maximum E_c at $q_i = 0$. With reference to Figure 3.1, the two cases are discussed below.

Case (a):

$V_i^{SCF}(q_i)$ has a single minimum at $q_i = 0$ and p_i^2 defined by [3.5] has zeroes at $\pm q_1$ (classical turning points). The action J_i is given by the integral

$$J_i = \frac{2}{\pi}\int_0^{q_1} p_i dq_i. \qquad [3.8]$$

The value of E_i corresponding to a specified value of J_i is to be determined. The period integral and average values for dynamical variables are defined as

$$T_i = 2\int_0^{q_1} \frac{dq_i}{p_i} \qquad [3.9]$$

and

$$\langle F(q_i)\rangle_i = \frac{2}{T_i}\int_0^{q_1} \frac{F(q_i)dq_i}{p_i}. \qquad [3.10]$$

The associated classical SCF frequency is defined as $\omega_i \equiv 2\pi/T_i$.

Case (b):

$V_i^{SCF}(q_i)$ has a double-well with minima at $q_i = \pm q_0$ and a barrier maximum at $q_i = 0$. The energy associated with a particular choice of action may lie above or below the critical energy E_c:

(1) If $E_i > E_c$ (above barrier maximum), there are just two turning points at $\pm q_1$ and the action, period, and average values are defined as in Case (a) above.

(2) If $E_i < E_c$ (below barrier maximum), the motion is restricted to either the left or the right well with outer ($\pm q_1$) and inner ($\pm q_2$) classical turning points. In this case, one should normally define the action as an integral over a period of motion in a single well, but to maintain continuity at E_c we define it here as having *twice* that value:

$$J_i = \frac{2}{\pi}\int_{q_2}^{q_1} p_i dq_i. \qquad [3.11]$$

The true period of motion changes by a factor of 2 from the value it has just above the barrier; for convenience, we define T_i as *twice* the actual period of motion in a single well,

$$T_i = 2\int_{q_2}^{q_1} \frac{dq_i}{p_i}. \qquad [3.12]$$

Averages of dynamical variables are given by

$$\langle F(q_i)\rangle_i = \frac{2}{T_i}\int_{q_2}^{q_1} \frac{F(q_i)dq_i}{p_i}, \qquad [3.13]$$

but their values are independent of the convention used for T_i since the factor of 2 divides out in normalization. The only quantities which appear in Classical SCF computations are the actions $\{J_i\}$ and average values $\langle F(q_i)\rangle_i$; these quantities are continuous across E_c.

We now consider the behaviour of the action and average value integrals in the neighbourhood of E_c.

The action J_i as defined by equations [3.8] and [3.11] is a continuously increasing function of the energy E_i across the critical point at the barrier top, $E_i = E_c$. From the definitions it is obviously an increasing function. However, its behaviour near E_c is not analytic. If we approximate the potential $V_i^{SCF}(q_i)$ near the top of the barrier by a Taylor expansion about $q_i = 0$ then

$$V_i^{SCF}(q_i) \approx E_c - V_1^0 q_i^2 + V_2^0 q_i^4 + \ldots, \qquad [3.14]$$

where

$$\begin{aligned} V_1^0 &= -\frac{1}{2}\frac{d^2V_i^{SCF}(q_i)}{dq_i^2}\bigg|_{q_i=0} > 0, \\ V_2^0 &= +\frac{1}{24}\frac{d^4V_i^{SCF}(q_i)}{dq_i^4}\bigg|_{q_i=0}, \qquad \text{etc.} \end{aligned} \qquad [3.15]$$

Analytical expressions can be derived for the action in the neighbourhood of $E_i \approx E_c$. If $E_i = E_c + \delta$, the action can be shown to have the form

$$J_i(E_i) \approx J_i(E_c) - \left[\frac{\delta}{4\sqrt{V_1^0}} + O(\delta^2)\right] \ln\left[\frac{|\delta|}{\delta_c}\right] + S_1\delta + O(\delta^2) \qquad [3.16]$$

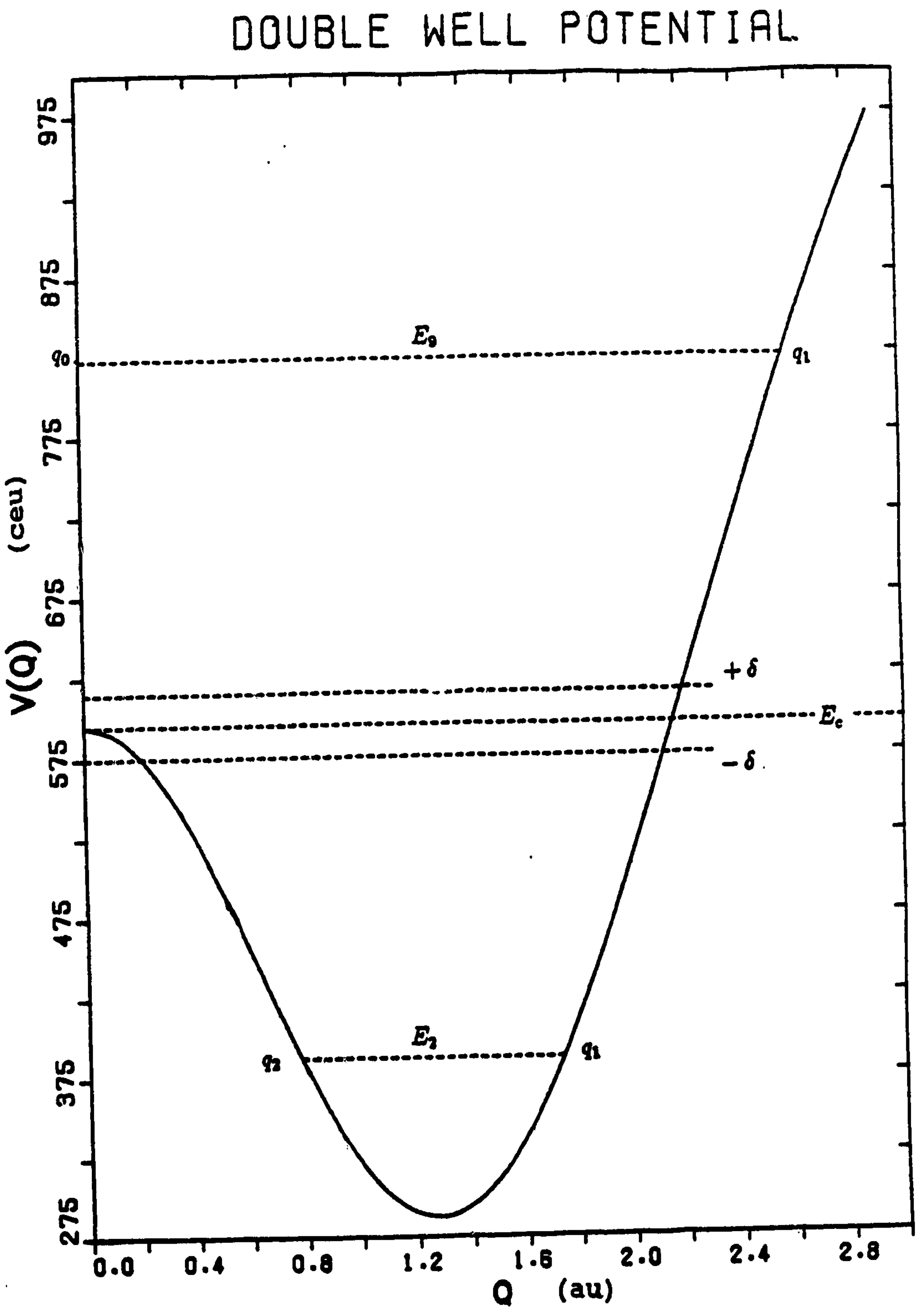

Figure 3.1: Diagramatic representation of a typical double well situation for a one-dimensional potential surface.

where corrections not given explicitly are expressible as analytic Taylor series in δ. δ_c is a parameter determining the range of energies over which the effects of the logarithmic term are significant and has a magnitude of the order of 0.01 c.e.u. ($\approx$ 1 cm^{-1}). While the derivative $[dJ_i(E_i)/dE_i]$ is singular at E_c, the action itself is continuous, and the coefficient S_1 is sufficiently large and positive that the action is uniformly increasing.

Since the top of the barrier is a critical point for the classical motion, the period integral diverges logarithmically there (it is essentially equal to the derivative $[dJ_i(E_i)/dE_i]$). Correspondingly, the classical average value of a dynamical variable $F(q_i)$ as defined by equations [3.10] and [3.13] exhibits a cusp-like behaviour near the barrier energy E_c with the cusp value at E_c itself equal to $F(0)$. Figure 3.2 depicts the behaviour of the classical average $\langle q_i^2\rangle$ in the neighbourhood of E_c for a representative double-well potential. It can be seen that significant effects of the barrier appear for a moderate range of energies on either side of E_c. Such a dip in average values when $E_i \approx E_c$ is a real physical effect that can also be seen in some quantum SCF eigenstates we computed; it is associated with long dwell times at $q_i \approx 0$. In quantum mechanics, the cusp singularity appearing for a classical average is smoothed out by the finite width of the quantum probability distribution.

There remains the question of the actual effect of the sharp cusp itself on the convergence and stability of classical SCF calculations; one might suppose that an unfortunate choice of actions and corresponding SCF effective potentials could lead to a case where iteration of the SCF computational cycle would fail to converge to a stable result. As is perhaps implied by Figure 3.2, the neighbourhood of the cusp proper is extremely narrow (given that similar dips in quantum mechanics are on the order of 25–50% of the depth) and we found that this problem never actually occurred in any of the hundreds of CSCF states computed. Empirically,

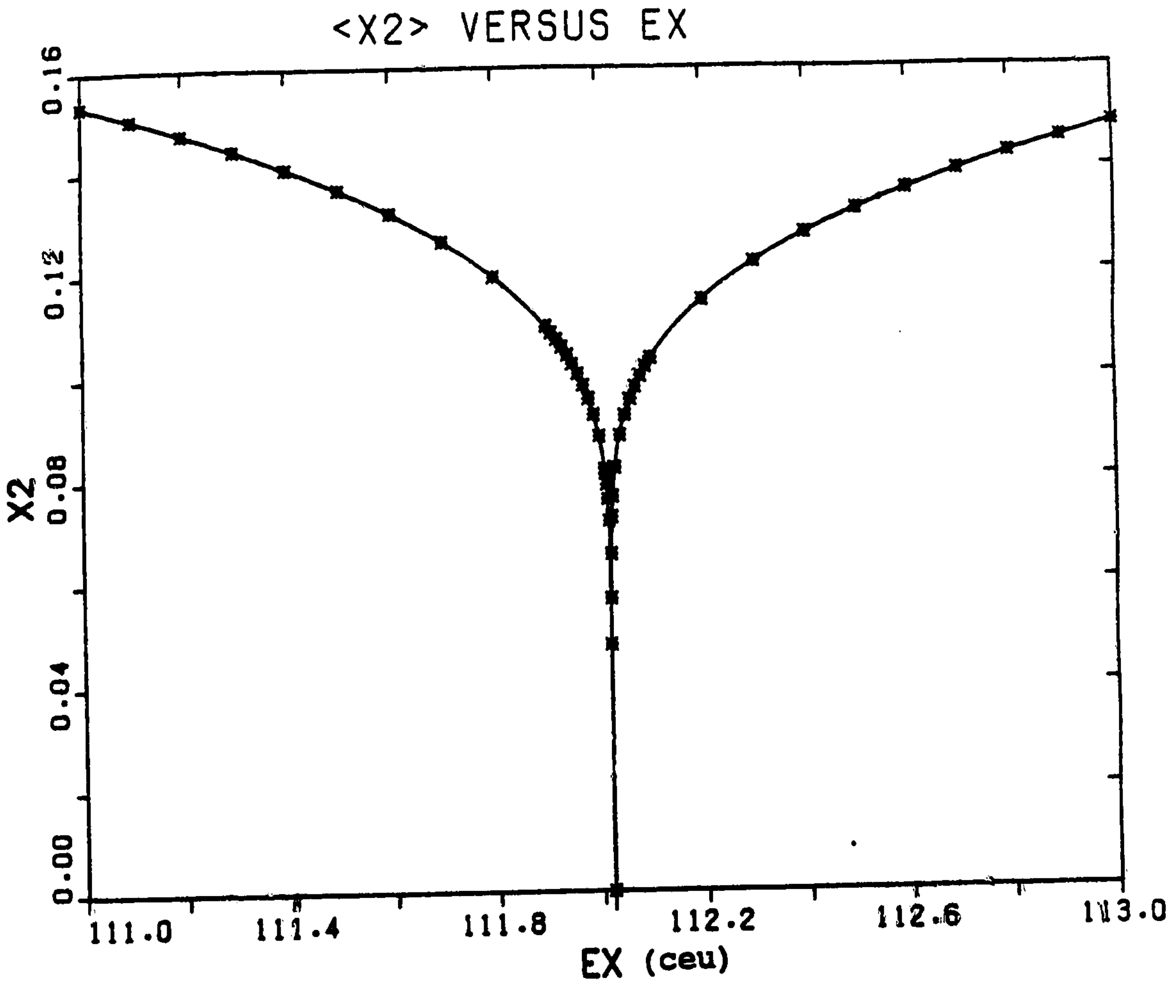

Figure 3.2: Typical behaviour of classical expectation value $< q_i^2 >$ for energies in the neighbourhood of the barrier top E_c (here $E_c \approx 112$ c.e.u.).

we found that the CSCF procedure appears to be just as stable and convergent as its quantum counterpart; at first, both procedures showed some minor convergence problems arising from the dip in average values for $E_i \approx E_c$, but these were easily avoided in either case by recognizing the existence of the effect and reducing its influence on the iteration process.

3.3 Comparison of SCF Theories

For comparison with quantum SCF results, semiclassical SCF energies can be computed provided a consistent set of quantization rules can be invoked to define the classical action J_i corresponding to a quantum energy level with nodal quantum number n_i. Gerber and Ratner [16] followed such a procedure for the nearly harmonic model systems they studied, using semiclassical quantization rules defined by the usual JWKB approximation for motion in a single potential well [10,17].

This procedure is developed here for a one-dimensional Schrödinger equation of the form

$$\frac{d^2 f(x)}{dx^2} = -p^2(x) f(x) \qquad -\infty < x < +\infty. \tag{3.17}$$

First assume that the conditions for Case (a) of the preceeding section are satisfied; that is, $p^2(x) \geq 0$ in only a single domain $a \leq x \leq b$, and $p^2(x) < 0$ and unbounded as $x \to \pm\infty$. In the classically forbidden regions where $p^2(x)$ is negative, there are two solutions of [3.17] which are *regular* as $x \to \pm\infty$ having semiclassical JWKB approximations given by

$$\begin{aligned} f_L(x) &\approx C\left[\kappa(x)\right]^{-1/2} \exp\left[+\int_a^x \kappa(x')dx'\right], \qquad -\infty < x \leq a, \\ f_R(x) &\approx C\left[\kappa(x)\right]^{-1/2} \exp\left[-\int_b^x \kappa(x')dx'\right], \qquad b \leq x < +\infty, \end{aligned} \tag{3.18}$$

where $\kappa^2 \equiv -p^2$. In the classically allowed region where $p^2(x)$ is positive, the well-known JWKB turning-point connection formulas [17] prescribe semiclassical approximations to the analytic continuations of equations [3.18]. These two solutions have the forms:

$$\begin{aligned} f_L(x) &\approx C'\left[p(x)\right]^{-1/2} \cos\left[+\int_a^x p(x')dx' - \frac{\pi}{4}\right], \\ f_R(x) &\approx C'\left[p(x)\right]^{-1/2} \cos\left[-\int_b^x p(x')dx' + \frac{\pi}{4}\right]. \end{aligned} \tag{3.19}$$

The eigenvalue condition that these solutions be the same yields the well-known formula

$$J_i\pi = \int_a^b p_i(x)dx = \left(n_i + \frac{1}{2}\right)\pi \qquad n_i = 0, 1, 2, \ldots \qquad [3.20]$$

Hence, the semiclassical quantization rule must be $J_i = n_i + \frac{1}{2}$ for Case (a) and also for Case (b) if $E_i \gg E_c$.

When the JWKB approximation is applied to motion deep within a double-well, corresponding to Case (b) with energy far below the barrier $E_i \ll E_c$, the argument above may be used again in *one* of the symmetrically equivalent wells. With the action J_i defined by equation [3.11], the quantization rule is

$$J_i = 2\left(m_i + \frac{1}{2}\right), \qquad m_i = \frac{n_i}{2} \quad \text{(integer truncation);} \qquad [3.21]$$

this yields degenerate level pairs for $n_i = (0, 1); (2, 3);$ *etc.* The problem, of course, is the discontinuity between this rule and that obtained for $E_i \gg E_c$.

JWKB connection formulas valid for reflection/transmission coefficients near the barrier top have been derived by Connor [18] (see also Child [19]). The discussion is based on asymptotic properties of parabolic cylinder functions and assumes that the shape of the barrier is approximately parabolic near its maximum. Based on these relations, semiclassical quantization rules valid for the symmetrical double-well problem can be obtained for energies $E_i \approx E_c$ both below and above the barrier. If the classical action J_i is defined as before by [3.11], these rules are as follows:

For n_i ***even*** (symmetrical eigenstates),

$$J_i = \left(n_i + \frac{1}{2}\right) + \left[\phi_0(\epsilon) + \chi_0(\epsilon)\right]/\pi; \qquad [3.22]$$

for n_i ***odd*** (antisymmetrical eigenstates),

$$J_i = \left(n_i + \frac{1}{2}\right) + \left[\phi_0(\epsilon) - \chi_0(\epsilon)\right]/\pi. \qquad [3.23]$$

The barrier phase corrections, ϕ_0 and χ_0, are defined by

$$\begin{aligned} \phi_0(\epsilon) &\equiv \epsilon - \epsilon \ln \mid \epsilon \mid + \arg\left[\Gamma\left(\frac{1}{2} + i\epsilon\right)\right], \\ \chi_0 &\equiv \arctan\left[e^{(-\pi\epsilon)}\right] \qquad 0 < \chi_0 < \frac{\pi}{2}. \end{aligned} \qquad [3.24]$$

The parameter ϵ is positive for $E_i > E_c$ and negative for $E_i < E_c$. It is defined for energies below and above the barrier, respectively, by

$$\begin{aligned} \pi\epsilon &= -2\int_0^{q_2} \kappa(q)dq \qquad \delta = E_i - E_c < 0, \\ \pi\epsilon &= +2\int_0^{a} \mid p(iy) \mid dy \qquad \delta = E_i - E_c > 0. \end{aligned} \qquad [3.25]$$

The integration limits are q_2, the inner turning point defined previously for Case (b), and a which is a zero of $p^2(iy)$, the analytic continuation of $p^2(q)$ on the positive imaginary axis. In particular, if the barrier is parabolic,

$$V(q) = E_c - V_1^0 q^2, \qquad \epsilon = \frac{\delta}{2\sqrt{V_1^0}}. \qquad [3.26]$$

At the expense of the additional quadrature in one of equations [3.25] needed to determine these phase corrections, the CSCF method can be used to obtain semiclassical SCF energy levels which are consistent across the critical point at E_c.

Consistency is maintained as follows: The phase correction ϕ_0 is zero at $E_i = E_c$ and tends to zero when $\mid \delta \mid = \mid E_i - E_c \mid \rightarrow \infty$. It has a maximum magnitude of about 0.15 when $\epsilon \approx 0.2$. Hence,

- For $E_i >> E_c$, $\chi_0 \rightarrow 0$ and [3.22] and [3.23] are consistent with [3.11];
- For $E_i << E_c$, $\chi_0 \rightarrow \pi/2$ and [3.22] and [3.23] are consistent with [3.8].

At the critical point itself, χ_0 takes the interpolating value $\pi/4$; it is interesting that in this neighbourhood the logarithmic term in the classical action (see equation [3.16]) is matched by an exactly corresponding term in ϕ_0.

We have computed semiclassical SCF approximations to about 300 SCF energy levels for $R = 4.30$ a.u. Figure 3.3 provides the semiclassical energy level contour map that corresponds to the quantum SCF map shown previously in Chapter 2; they are virtually indistinguishable. The error in the semiclassical value is usually less than 0.2–0.3 c.e.u.(12–20 cm^{-1}) and is always less than 2.5 c.e.u.(150 cm^{-1}). The cases where larger errors occur are of two types. Levels where one SCF mode has $n_i = 0$ or 1 produce errors due mainly to the JWKB approximation for anharmonic potentials although these are normally less than 1.0 c.e.u.Larger errors occur for states in which a mode energy E_i happens to fall close to E_c. We attribute these mostly to errors in the "cusp" behaviour of the resulting classical average values, relative to their quantum counterparts, which are amplified in the SCF effective potentials dependent on such average values.

Such extensive semiclassical SCF energy level calculations were not carried out at other R-values. Although the semiclassical SCF scheme is about an order of magnitude faster computationally than the corresponding quantum computation, it offers no further useful information for energies where configuration interaction is widespread and the SCF description is a poor one anyway. As shown in Chapter 2, this is *always* true for SCF levels beyond the first 10–12 states of each symmetry. Figures 3.4–3.7 show the first few semiclassical SCF energy levels as a function of R for each symmetry type. As expected, these compare closely with the corresponding quantum SCF levels, exhibiting the same curve crossing structure. In cases where SCF description is generally valid, the semiclassical SCF energies do correctly anticipate the locations of avoided crossings where it is expected to fail.

In the remainder of this work, we concentrate mainly on comparisons between the classical SCF approximation and the corresponding exact classical dy-

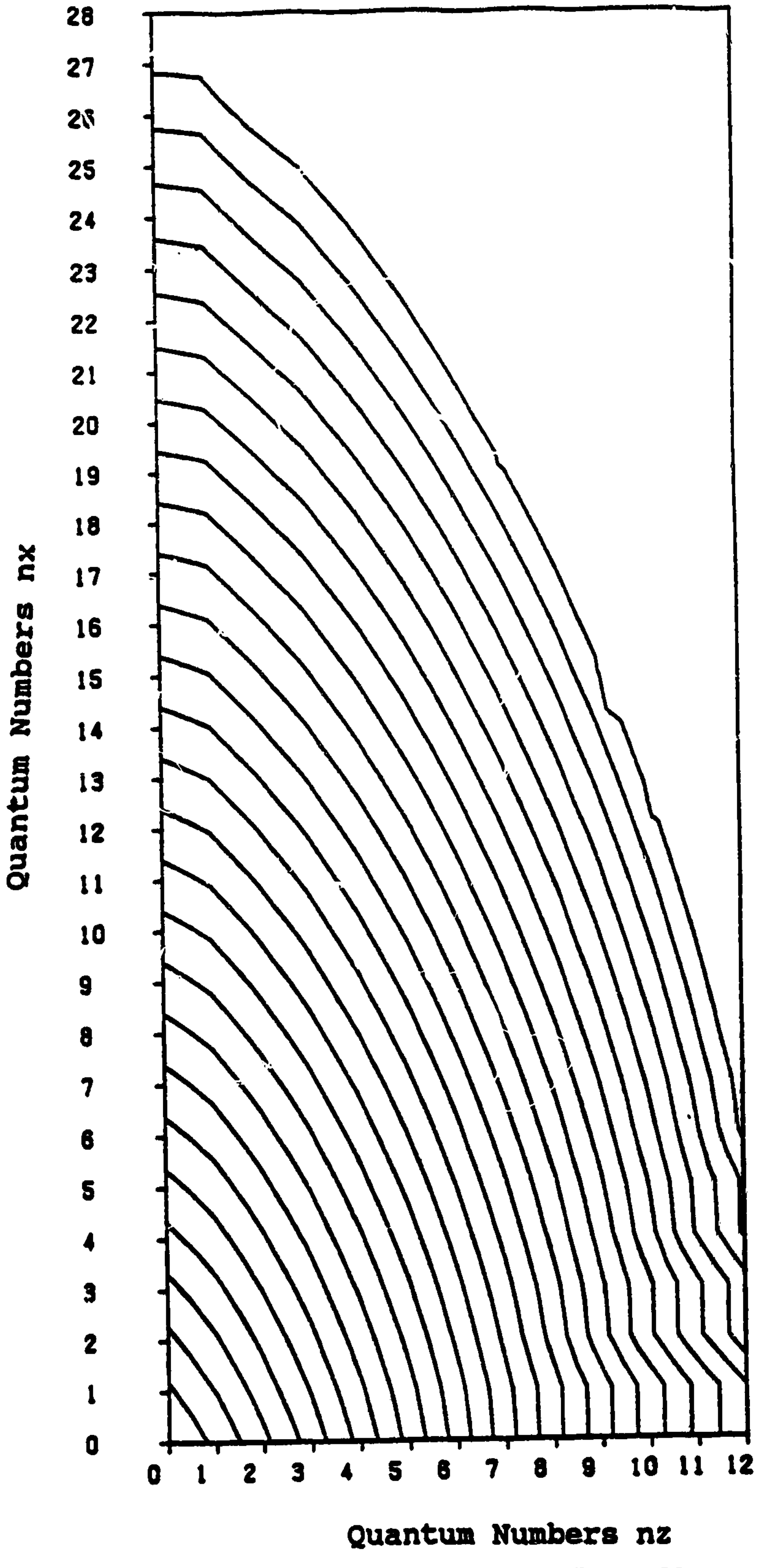

Figure 3.3: Semiclassical SCF energy surface at $R = 4.30$ a.u. plotted at pairs of n_x, n_z with contour spacings of 50 c.e.u.

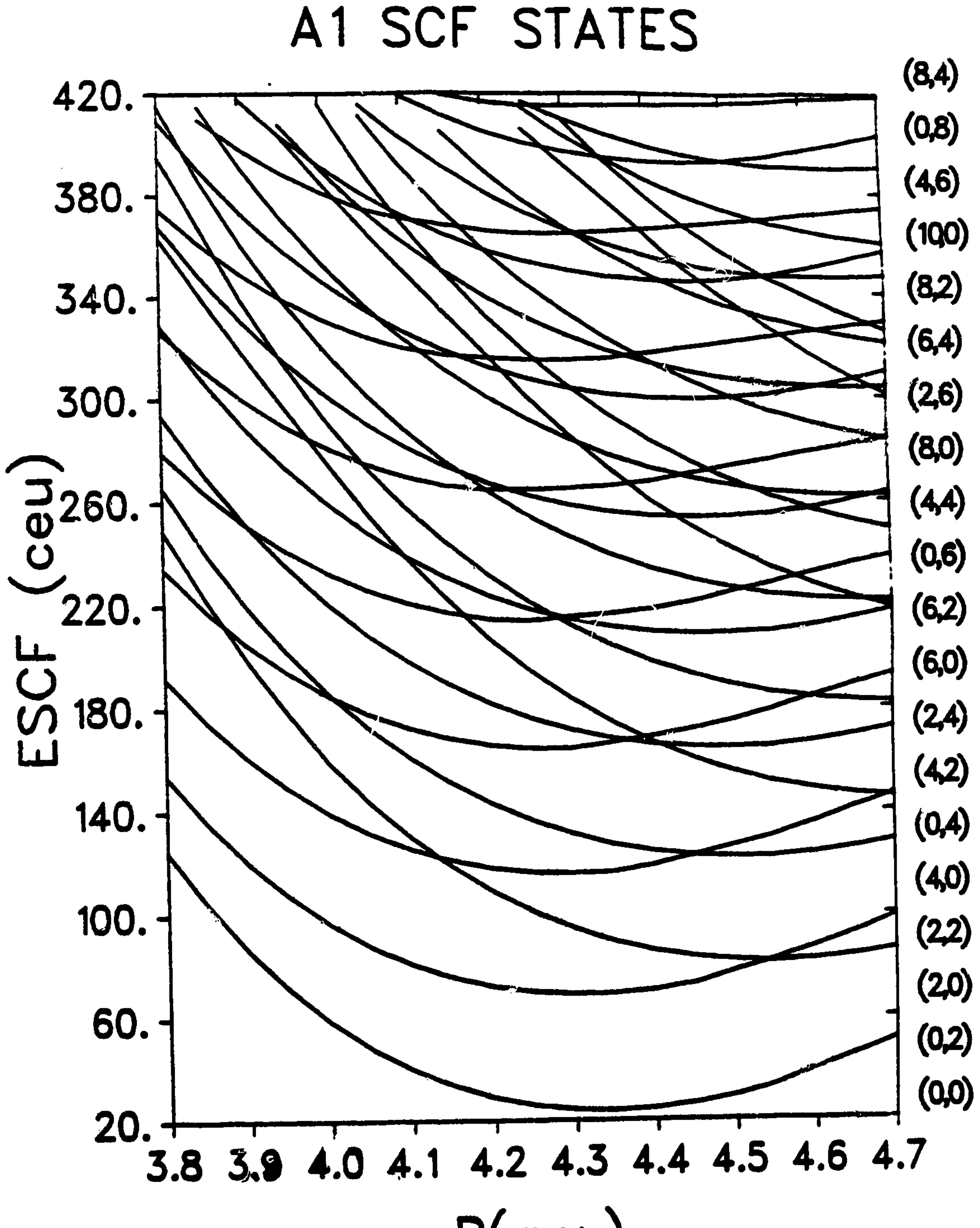

Figure 3.4: Semiclassical SCF energy levels in the A_1 symmetry are plotted against R.

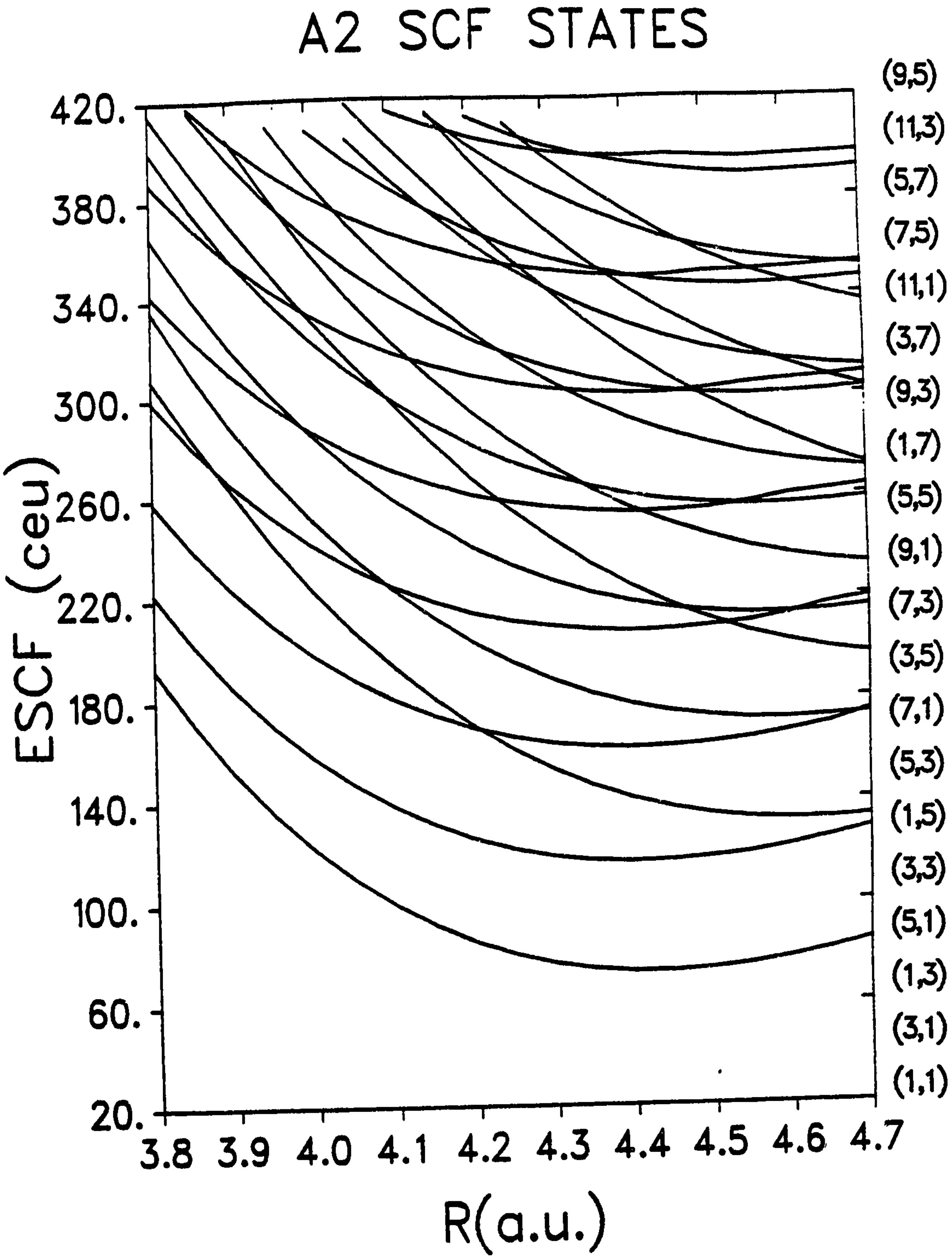

Figure 3.5: Semiclassical SCF energy levels in the A_2 symmetry are plotted against R.

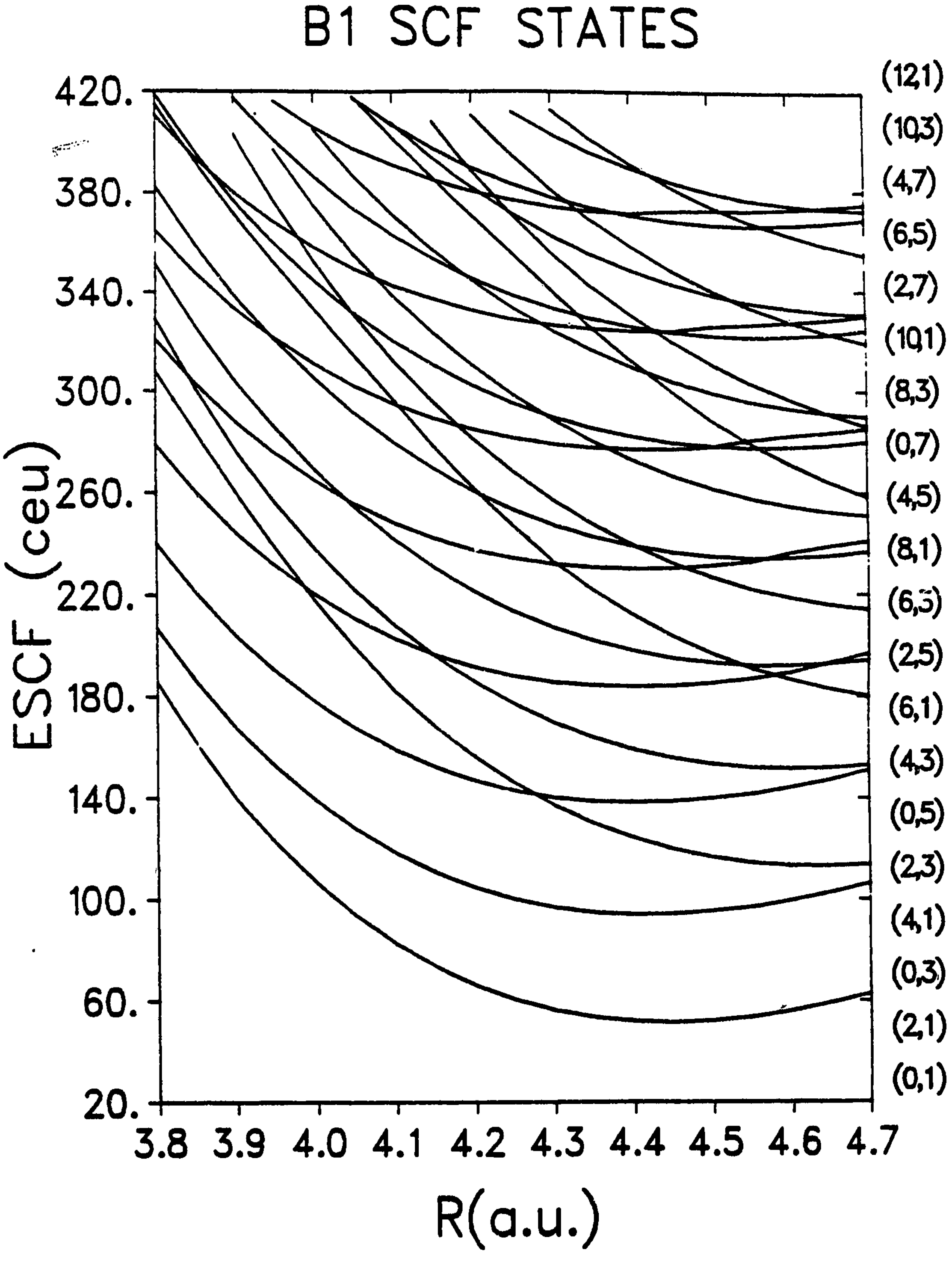

Figure 3.6: Semiclassical SCF energy levels in the B_1 symmetry are plotted against *R*.

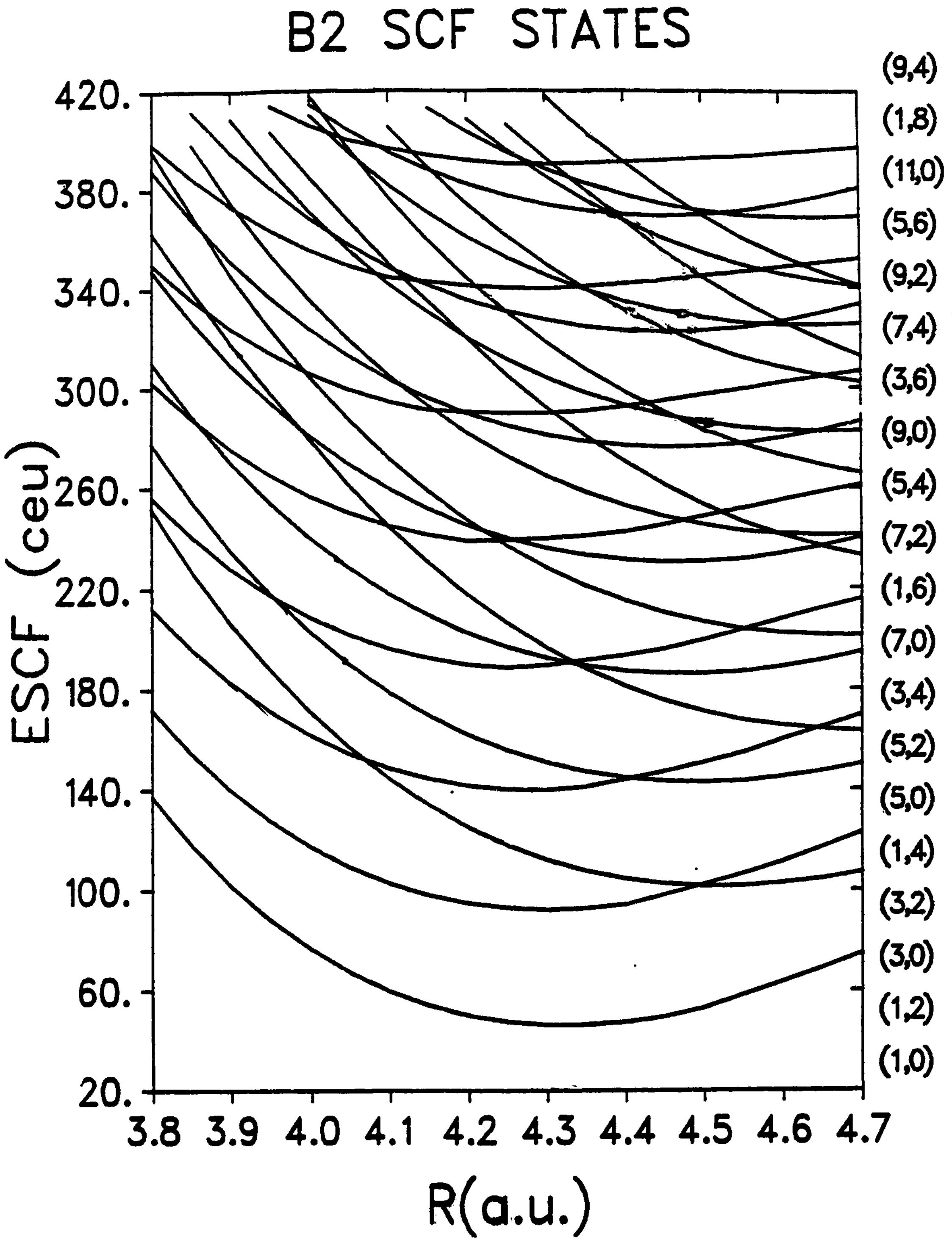

Figure 3.7: Semiclassical SCF energy levels in the B_2 symmetry are plotted against R.

namics for the same system. It was seen in Chapter 2 that for the lower states of each symmetry, the quantum SCF approximation offers a surprisingly accurate description of the "exact" quantum states of this system, except at isolated curve crossings; similar comparisons in classical dynamics appeared to merit further study. In such comparisons, semiclassical quantization is not of primary interest and is not, in fact, used. Our particular interest is the capacity of the SCF approximation to sustain a description of the motion which is closer in many cases to the actual behaviour of the quantum system than the exact classical mechanical description. This occurs because the latter is "chaotically" disrupted by system perturbations at energies far below those at which corresponding effects are observable in quantum mechanics.

Chapter 4

Classical Vibrational Dynamics

4.1 Introduction

In this chapter we study the classical dynamics of this model potential system; that is, Hamilton's equations are solved numerically and information is obtained from resulting classical trajectories. Attention is focussed on cases involving regular (quasiperiodic or periodic) motion and the associated constants of the motion.

A dynamical system with N degrees of freedom can be described with canonical coordinates $\{q_i\}$ and the conjugate momenta $\{p_i\}$, $i = 1, \ldots N$. In the present case, $N = 2$ and the coordinates and momenta are (x, z) and (p_x, p_z). The state of the system at any time t is fully defined by specifying the set (q_i, p_i), $i = 1, \ldots N$, and is represented as a point moving in the $2N$-dimensional *phase space* for the system. A solution of Hamilton's equations (which defines the coordinates and momenta as functions of time) with a given set of initial values $\{q_i^0, p_i^0\}$ constructs a phase-space *trajectory*. If, as is the case here, the Hamiltonian function $H(q_i, p_i)$ does not depend explicitly on time t, the system is said to be *conservative* and its energy $E \equiv H(q_i, p_i)$ is a constant of the motion.

Near the turn of the century, Poincaré [20] and other celestial mechanicians had observed that a conservative system of coupled oscillators exhibits regions of very different dynamical motions: *regular* and *irregular*. For regular motion, the system has N distinct constants of the motion, one for each degree of freedom. This restricts the trajectory in the $2N$-dimensional phase space to an N-dimensional surface called an *invariant torus*. In irregular motion, N constants of the motion do not exist and the phase-space trajectory is correspondingly unrestricted. For example, for $N = 2$, irregular motion is restricted only by energy conservation.

The formal apparatus of Hamilton-Jacobi theory is directed precisely at the case of regular motion [see, for example, H. Goldstein "Classical Mechanics", Chapters 8–10]. The Hamilton-Jacobi partial differential equation arises from the condition that there exist a canonical transformation from old dynamical variables $\{q_i, p_i\}$ to new dynamical variables $\{Q_i, P_i\}$ such that the N new momenta are all constants of the motion. In fact, the existence of a complete solution to the Hamilton-Jacobi partial differential equation is equivalent to the existence of N constants of the motion. The new momenta and coordinates are called *action* and *angle* variables, respectively; they exist if and only if the motion is regular. No practical use of the Hamilton-Jacobi formalism is made here and the details of the theory are not presented, but regular motions in this work are described using action-angle variables. We will introduce these variables in the context of separable systems. They play the role of parameters describing the invariant torus which is always associated with regular motion.

In the past two decades, these concepts of classical mechanics have been extensively applied to the study of molecular vibrations. Initially most studies focussed on the quantization of regular classical motions to obtain information about quantum energy levels ("classical bound state theory"). More recent work has included irregular or "chaotic" motion and its relation, if any, to quantum behaviour. The general background theory of classical mechanics is well presented in the text by

Herbert Goldstein [21] which will be often cited here where relevant. Aspects of the subject especially relevant to this study have been reviewed by Noid, Koszykowski, and Marcus [22] which covers work on both quasiperiodic and irregular motions in molecular dynamics to about 1980, and a second review by Noid and Marcus [23] covers work current to 1986. A useful review relevant to bound state theory in particular has been given by Percival [24]. As the present work focusses primarily on regular motion, these sources and the references they cite describe most concepts and methods used in this thesis, but some of the major points will be covered for completeness. As emphasized in Chapter 1, the model system studied here is strongly anharmonic, much more so than most systems studied previously. Comparisons with classical SCF theory (discussed in Chapter 5) are an entirely novel aspect of the present work.

Section 4.2 presents the basic theoretical elements of the classical methods used in this work and Section 4.3 summarizes the associated computational methods used to determine dynamical quantities of interest. The main results of these computations will then be presented and discussed in Section 4.4 by illustrating specific examples of trajectories important to this system. A deeper appreciation can be given only in Chapter 6, following the application of canonical perturbation theory to the classical SCF approximation, which is developed in Chapter 5.

4.2 Classical Theory

The Hamiltonian of this system ($N = 2$) has the form

$$H(x, z, p_x, p_z; R) = E_{total} = p_x^2 + p_z^2 + V(x, z; R), \qquad [4.1]$$

where the parameter R is fixed. A trajectory is obtained by integrating Hamilton's equations of motion [21],

$$\begin{aligned} \dot{x} &= \frac{\partial H}{\partial p_x} = 2p_x, & \dot{p}_x &= -\frac{\partial H}{\partial x} = -\frac{\partial V(x, z; R)}{\partial x}; \\ \dot{z} &= \frac{\partial H}{\partial p_z} = 2p_z, & \dot{p}_z &= -\frac{\partial H}{\partial z} = -\frac{\partial V(x, z; R)}{\partial z}, \end{aligned} \qquad [4.2]$$

for a given set of initial conditions.

As an introduction to action-angle variables, consider a one-dimensional oscillator with coordinate q, momentum p and Hamiltonian

$$H(q, p) = p^2 + V(q). \qquad [4.3]$$

Define the orbit of the system in (q,p) phase space by expressing the momentum as a function of q at a specified constant $H = E$:

$$p = \sqrt{E - V(q)} = p(q; E). \qquad [4.4]$$

For $V(q)$ with $p^2 \geq 0$ in a finite domain bounded by classical turning points (q_1, q_2), the orbit is a closed curve and both q and p are periodic functions of time. This is called ***librational*** motion and the action integral,

$$J \equiv \frac{1}{2\pi} \oint p dq, \qquad [4.5]$$

is performed over a complete period of motion. The action is obviously a constant of the motion depending only on E; conversely, $E = E(J)$. The problem posed by Hamilton-Jacobi theory is that of finding a canonical transformation to new momentum and coordinate such that the new momentum is a constant of the motion and the transformed Hamiltonian does not depend on the new coordinate, but only on the momentum. (see Goldstein [21], especially Sections 9.1–9.3 and 10.1–10.5). These are the action and angle variables J, θ, respectively. Since Hamilton's equations of motion remain true in the transformed coordinates,

$$\dot{J} = -\frac{\partial \tilde{H}(J)}{\partial \theta} = 0; \qquad \dot{\theta} = \frac{\partial \tilde{H}(J)}{\partial J} = \omega = \text{constant.} \tag{4.6}$$

The angle coordinate θ simply increases linearly with time,

$$\theta = \omega t + \text{constant.} \tag{4.7}$$

The utility of such a representation lies in the fact that as q and p move through one complete period of motion, the angle θ changes by 2π ; hence, the period of motion is $T = 2\pi/\omega$. ω is called the *frequency* of the motion.

Consider next a two-dimensional case where $V(x, z; R)$is separable,

$$V(x, z; R) = V_x(x; R) + V_z(z; R), \tag{4.8}$$

giving the Hamiltonian a form

$$H = H_x(x, p_x; R) + H_z(z, p_x; R) = E_x + E_z, \tag{4.9}$$

where, by equations [4.2], E_x and E_z are each independently constants of the motion. As before, the solution of the Hamilton-Jacobi problem leads to action-angle variables labelled here as $(J_x, J_z, \theta_x, \theta_z)$. The actions are defined as before by

$$J_x = \frac{1}{2\pi} \oint p_x dx, \qquad J_z = \frac{1}{2\pi} \oint p_z dz. \tag{4.10}$$

with angles, periods and frequencies as given earlier.

The constants of the motion (J_x, J_z) restrict the motion of the trajectory of the system in phase space. If phase space is described in action-angle variables instead of the original coordinates, the motion of the system is clearly limited to a two-dimensional manifold characterized by the constant actions but allowing the variation with time of the angles θ_x, θ_z. This two-dimensional manifold on which regular motion occurs is called the *invariant toroid* associated with the motion. In the four-dimensional phase space it is topologically equivalent to a torus in three-dimensional space, as depicted in Figure 4.1. To describe the location of any point on a torus in 3-space (assuming the orientation and centre of the torus are given), one need only specify the two constant radii characterizing the two topologically distinct circles on the torus (C_1, C_2 in the Figure) and the angle of rotation along each circle. For the invariant toroid, the constants of the motion J_1, J_2 (here, J_x, J_z) specify the circle radii (more strictly, the *areas* of the circles), while the angle variables θ_1, θ_2 specify the location of the moving system on its trajectory through phase space.

Regular motion on a torus is called *quasiperiodic* (or *multiply periodic*) since any dynamical variable, and the old coordinates and momenta (x, z, p_x, p_z) in particular, can be expressed as multiple Fourier series in the two angles ($\theta_1 = \theta_x$, $\theta_2 = \theta_z$):

$$\begin{aligned} q_j &= \sum_{k_1=-\infty}^{\infty} \sum_{k_2=-\infty}^{\infty} a^{(j)}_{k_1,k_2}\, e^{i(k_1\theta_1+k_2\theta_2)}, \\ p_j &= \sum_{k_1=-\infty}^{\infty} \sum_{k_2=-\infty}^{\infty} b^{(j)}_{k_1,k_2}\, e^{i(k_1\theta_1+k_2\theta_2)}, \end{aligned} \qquad [4.11]$$

where Hamilton's equations $\dot{q}_i = 2p_i$ imply that

$$b^{(j)}_{k_1,k_2} = \frac{i}{2}\left(k_1\omega_1 + k_2\omega_2\right) a^{(j)}_{k_1,k_2}. \qquad [4.12]$$

Complex Fourier series are employed to indicate the general series structure, although the variables (q_i, p_i) are necessarily real. The term *quasi*periodic, rather than periodic, is used because in general the two frequencies ω_1, ω_2 are rationally

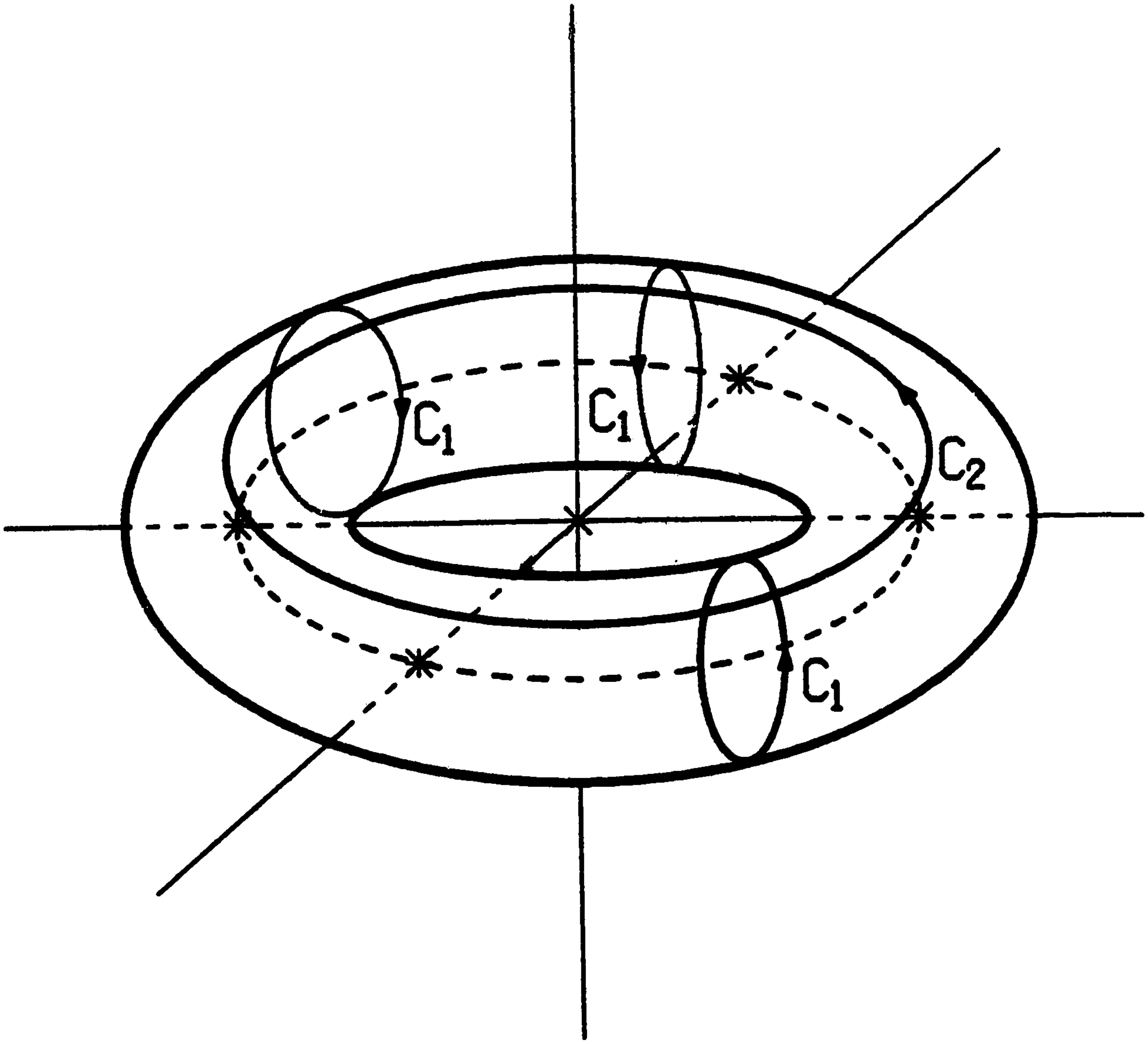

Figure 4.1: Invariant torus pictured in 3-space. C_1 and C_2 indicate the two topologically distinct circles associated with the constant actions J_1, J_2 and the angles θ_1 and θ_2.

incommensurate. That is, there is no pair of integers m_1, m_2 such that

$$m_1\omega_1 = m_2\omega_2, \qquad [4.13]$$

and the system trajectory will never exactly return to its position on the toroid at $t = 0$. Over time, it will eventually cover a path which covers every point on the toroid and will return *arbitrarily closely* to its position at $t = 0$ after a sufficiently long time. Cases where a relation of the form [4.13] holds are truly *periodic* since the trajectory will return *exactly* to its position at $t = 0$ after a recurrence time given by $\tau = m_1T_2 = m_2T_1$; in this case, it will trace out a restricted path on the toroid which does not cover every point on its surface. Of course, since the set of rational numbers is embedded in the set of all points on a line in an intimate manner, any particular quasiperiodic trajectory is arbitrarily close to some simply periodic one. The distinction between them in a computational study is ultimately not relevant unless the rational relation [4.13] involves integers m_1, m_2 that are *small*. For a system which is nearly but not quite separable, such periodic *resonances* may play a strongly disruptive part in the classical motion of a system even at very low energies. In many cases, the role of the resonance is largely irrelevant to the behaviour of the corresponding quantum mechanical system, at least at low energies.

We have discussed the case of an exactly separable potential here primarily to introduce the ideas of action-angle variables, quasiperiodic and periodic regular motion and the associated invariant toroids. This is an extremely simple example and there are more complex cases of fully separable systems where the formal apparatus of Hamilton-Jacobi theory may be used to derive a transformation to action-angle variables. Of special interest to this thesis is that the classical SCF approximation always generates a strictly separable approximation to the potential $V(x, z; R)$ and the motion it creates is *always* regular; in that sense, it is a *toroid-preserving* approximation.

The concepts of action-angle variables remain applicable even to truly nonseparable systems such as the one studied here because such systems exhibit regular motion of some kind over a wide domain of dynamical conditions, even though the Hamilton-Jacobi equation cannot be fully solved via a general separability of some kind. The motion may have fewer than N constants of the motion, classifying it as irregular. Irregular motion does occur but it is by no means dominant for at least some domains.

While Poincaré and other mathematicians concerned with coupled oscillator systems in classical dynamics observed very early (1900–1910) that regular motion appears in such systems, during the first half of the present century the prevailing view was that irregular motion is the dominant behaviour expected in a nonseparable system. This general perspective was profoundly altered by more recent work and, above all, by the theorem proved (independently) by Kolmogorov, Arnold and Moser (KAM) [25,26,27]. (For some appreciation of the implications of the KAM results, see [24].) While the level of presentation of KAM is highly mathematical and certainly well beyond the scope of this work, the essential point of the theorem for this study is that regular motion is more frequent in a nonseparable problem than was previously thought. KAM consider nonseparable systems whose Hamiltonians consist of an unperturbed part H_0 with only quasiperiodic trajectories and a general nonseparable perturbation H_1. They prove that, for "sufficiently small" perturbations, most of the regular trajectories of the unperturbed system persist as regular trajectories in the perturbed system. While irregular trajectories occur, they are "outnumbered" by the regular ones. For larger perturbations (or, in molecular systems, at higher energies), irregular trajectories increase in number and eventually dominate the phase space. It is not clear what is meant by a "small" perturbation but numerical studies by many authors [28] have verified this general feature of nonseparable system dynamics. In particular, Marcus and others [29] interested in molecular vibrations have observed that molecular vibrational systems that deviate only slightly from harmonicity have perturbations that are small in the KAM sense; regular motion is common at lower energies and irregular motion is not widespread for energies near the lower lying vibrational levels. As emphasized in Chapter 1 of this thesis, the system studied here is an adaptation of a realistic vibrational potential surface for the hydrogen-bonded $[FHF]^-$ ion. It is both nonseparable and strongly nonharmonic in comparison with the great majority of molecular systems treated previously; this formed part of the motivation for this work.

Hence, it may occur that regular motion is encountered in a nonseparable system but there is no obvious relation between the action-angle variables and the physical coordinates used for the system. Understanding of the dynamics can begin by observing the two-dimensional coordinate (or momentum) space projection of the trajectory as time passes. If the relation between the toroid and the physical coordinates, (x, z) say, is simple, the projection will be in the shape of a "box", as is seen for this system in the example in Figure 4.2. It is possible to visualize that the toroid has been flattened onto the projection plane, and the trajectory winding endlessly around it now appears as lines repeatedly crossing from one side of the box to the other. The four sides of the box where one of the momenta will be identically zero are called the *caustic curves* and are reminiscent of the turning points in the classical description of a one-dimensional well. Accordingly, the four corners of the box lying exactly on the equipotential curve correspond to the only points at which both momenta are zero. Other trajectory points are constrained to lie within these toroidal boundaries at this energy. Obviously, the action-angle variables for this case are appropriately labelled $(J_x, J_z, \theta_x, \theta_z)$. A more complicated, but still quasiperiodic, motion is illustrated in Figure 4.3. The directions of basic motion have been rotated relative to the physical coordinates (x, z). The true caustics are not simply related to the outlines of the figure. It is no longer obvious what relation exists between the action-angle variables and the working coordinates and momenta. Far more complicated trajectory projections are obtained in still other situations such as those associated with degenerate systems [23].

In this work, the Poincaré surface-of-section method [30,31,32] is used to compute the actions associated with the regular motions studied. This method relies on a fact pointed out by Einstein [33]; on the surface of any invariant toroid, the differential quantity

$$\sum_i p_i dq_i = \sum_k J_k d\theta_k \qquad [4.14]$$

is a canonical invariant. The integral of this quantity around *any* closed curve on the invariant toroid is then a constant of the motion *even if the curve is not a trajectory.* In the surface-of-section method, a particular set of closed curves is selected so that each cuts the torus in a manner topologically equivalent to one of its distinct invariant circles C_k as previously illustrated in Figure 4.1. The resulting constants must be the associated actions:

$$J_k = \frac{1}{2\pi} \oint_{C_k} \sum_i p_i dq_i. \qquad [4.15]$$

For simple boxes like the one in Figure 4.2, the planes $x = 0$ and $z = 0$ achieve this with curves along which the integrals [4.15] can be conveniently evaluated.

Numerical construction of these curves takes place as a trajectory unfolds in time; the values of p_z and z are recorded each time the point passes through the plane $x = 0$ with a given direction ($p_x > 0$, say). These points are then plotted on the (z, p_z) plane resulting in a surface-of-section plot. A similar procedure

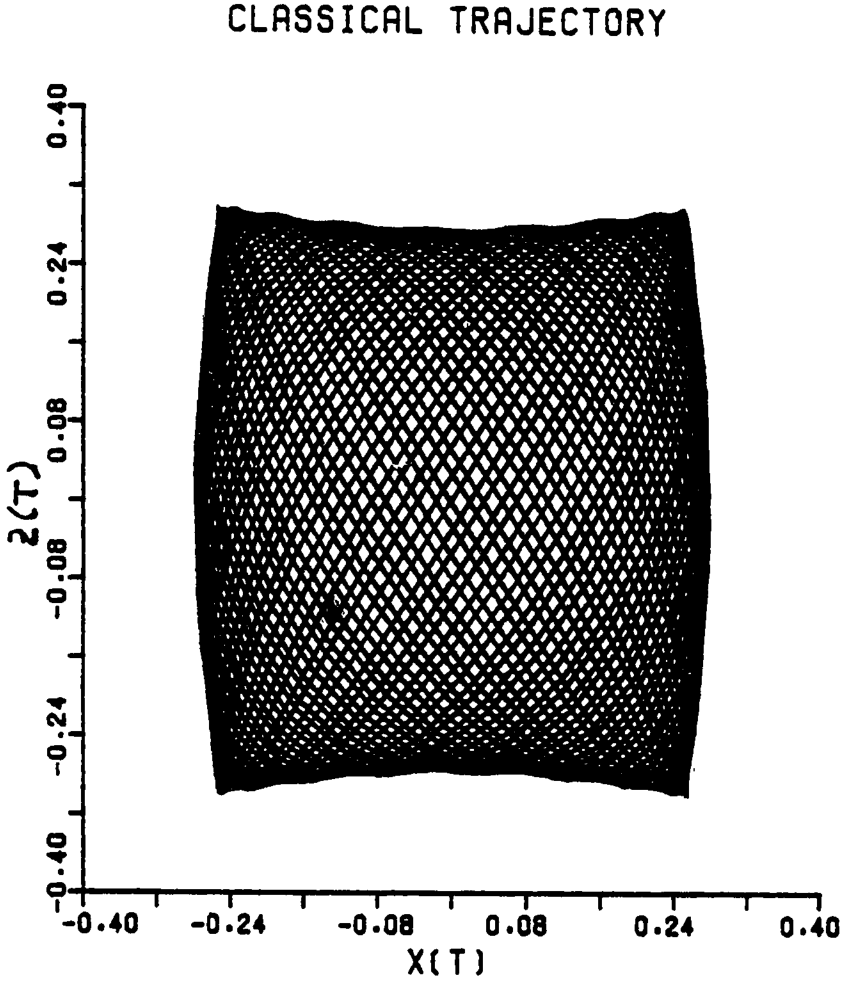

Figure 4.2: A typical boxlike trajectory is plotted for $E = 24.0$ c.e.u. $\approx 1470\ \mathrm{cm}^{-1}$ and $f_x = 0.3$. See Section 4.3 for a definition of f_x.

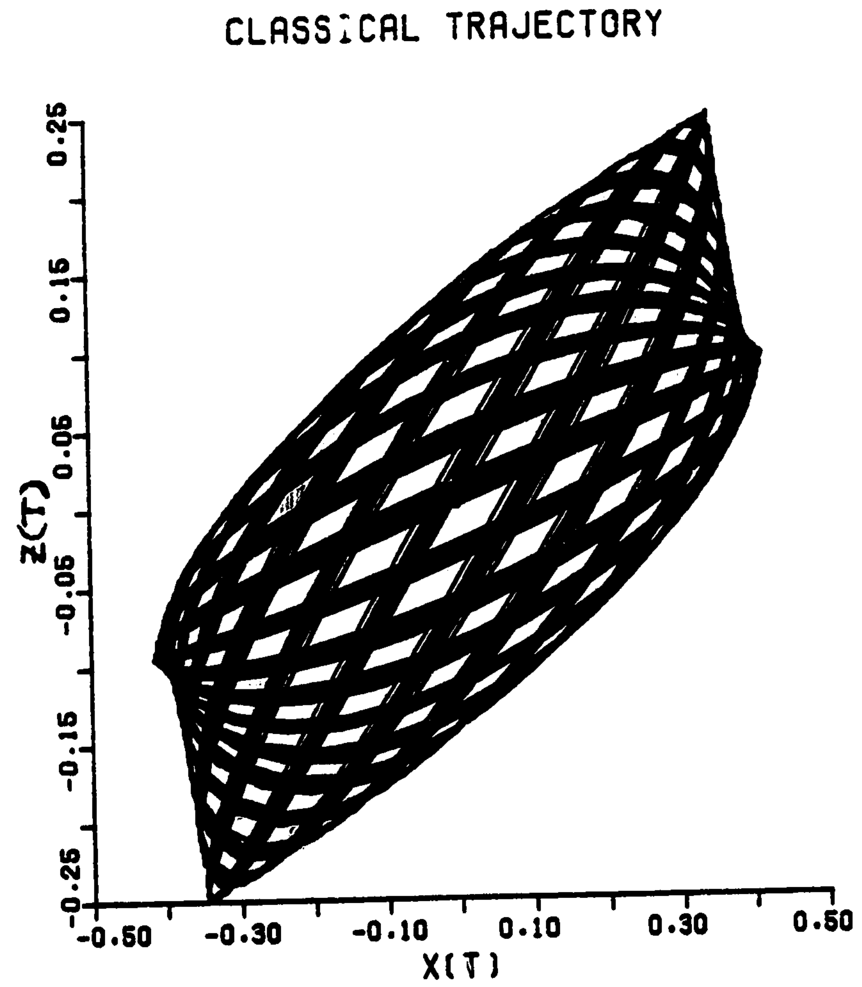

Figure 4.3: A typical 1:1 resonant family trajectory is plotted for $E = 24.0$ c.e.u. $\approx 1470\ \mathrm{cm}^{-1}$ and $f_x = 0.6$. See Section 4.3 for a definition of f_x.

is carried out for the $z = 0$ plane. For a quasiperiodic box-like trajectory, the corresponding surface-of-section points eventually delineate a closed curve on each (q, p) plane; if the motion is exactly periodic, the points are isolated. Figure 4.4 and the composite diagrams of Figure 4.6, shown for the sequence of trajectories paraded in Figure 4.5, illustrate the types of closed curves that can be generated. More complicated trajectory projections have correspondingly more complicated surface-of-section curves. In simple box cases, actions are calculated by applying [4.15] to the closed curve on each surface; for example, at $x = 0$ the section points (z, p_z) form a curve C_z with $dx = 0$ so that

$$J_z = \frac{1}{2\pi} \oint_{C_z} p_z dz. \qquad [4.16]$$

The integral is the area enclosed by the curve. Irregular motion is characterized by surface-of-section points that no longer lie on a single closed curve but form a "shotgun" pattern that can no longer be accurately integrated; Einstein's invariant [4.14] does not hold and constants of the motion do not exist.

Marcus and coworkers [29] have shown that in more complicated cases it is often possible to select surfaces-of-section such that the closed curves are simple and the associated actions can be conveniently calculated. In all cases where actions have been determined in this thesis, the surface-of-section method is used successfully by cutting the toroid with suitably chosen planes passing through the origin.

In principle, as Equations [4.11] imply, the frequencies of motion ω_k can be found from Fourier transform spectra of dynamical variables. Ezra and coworkers [34] have used the Fast Fourier Transform (FFT) method on trajectory data to illustrate how the Fourier spectrum changes when a transition to irregular motion occurs. While we were able to use the FFT method to obtain frequencies in this manner, we found that they are most reliably determined by a method using surface-of-section data, and also provide thereby an important criterion for selecting distinct toroidal sections.

4.3 Technical Methods

Hamilton's equations [4.2] were solved by numerical integration starting from specified inital conditions (q_i^0, p_i^0). Essentially all trajectories studied here were initiated at the origin $(x, z = 0, 0)$. While there are trajectories which never pass through the origin, they are not included within the scope of this work. At the zero of the potential, the total energy is simply the sum of the momenta squared,

$$E_{total} = \left(p_x^0\right)^2 + \left(p_z^0\right)^2, \qquad [4.17]$$

so that fixing the energy and one other parameter will suffice to specify the trajectory and the constants of the motion completely. This parameter is chosen, as suggested by Marcus *et al* [31], to be the initial fraction of the kinetic energy in the x-oscillator,

$$f_x = \frac{p_{x_0}^2}{E_{total}}. \qquad [4.18]$$

The parameter f_x, of course, is not a constant of the motion but is oscillatory over the trajectory's path. The initial momenta (p_x^0, p_z^0) are chosen non-negative.

The differential integrator used for this purpose is based on the extrapolation predictor/corrector algorithm developed by Bulirsch and Stoer [36] to solve coupled first-order differential equations (FORTRAN subroutine DIFSYS). This routine is able to vary the local step-size in response to the behaviour of the equations being solved. We use it to integrate from one fixed time-point to the next with spacings of 0.01 or 0.02 time units ($\approx$ 20–40 points over a typical period of motion in either coordinate; frequencies ω_k usually lie between 15.0 and 35.0). Precision errors in the sequential values of (q_i, p_i) were controlled by a parameter in the program and maintained at a relative value of $1\text{x}10^{-9}$. Poincaré surface-of-section data were generated by establishing the planes of intersection and integrating the equations of motion from the nearest logged trajectory data point to the point at which the surface of interest was crossed. The guaranteed tolerance of error in the distance from the plane was less than $1\text{x}10^{-9}$ distance units ($1\text{x}10^{-10}$ time units or better). The transit time of the intersection and the momentum and coordinate (q, p) in the section plane were then recorded as data.

Following the procedures of Ezra *et al* [34], we at first employed the Fast Fourier Transform (FFT) method [35] to determine the frequencies of motion from the trajectory data. However, these were subject to significant error due to "windowing" and "biasing" errors inherent in the FFT algorithm. In fact, the precision error in the fundamental frequencies for regular motion obtained by FFT methods was no better than that obtained by running the trajectory for the same period, locating all surface-of-section transit times, and averaging these *without weighting.* Much more accurate estimates of the period of motion are obtained by selecting only those transits which return close to the origin with momenta near their initial values at $t = 0$ — hence, corresponding to near-recurrences on the toroid. The total time elapsed at a transit is divided by the number of complete cycles through the surface of interest to give an estimate of the period transverse to it. Weighted averages of these values provide associated frequencies with relative errors between $5\text{x}10^{-7}$ to $1\text{x}10^{-9}$, usually 2–3 orders of magnitude better than the result obtained by FFT. Since all of the data used are also required for computing actions, frequencies are obtained at little extra cost and, in addition, provide a convenient test that the surfaces used are indeed topologically distinct sections of the torus. Frequencies determined by this procedure are sufficiently accurate that further refinement of their values is not required though, in principle, an additional improvement could be obtained if Fourier series expansions for the dynamical variables are also known.

Figure 4.4 shows two characteristic types of Poincaré surfaces encountered in this work. The first closed curve (a) is bilaterally symmetric about both $q = 0$ and $p = 0$. This is an $x = 0$ surface-of-section from the simple box trajectory given in Figure 4.2 which also shows two mirror planes. The second curve (b) is one section from the complex trajectory of Figure 4.3 with only a centre of symmetry. The plane of section is normal to a vector oriented at an angle of 26° to the x-axis which is essentially the direction of the pronounced valley on the potential surface maps shown in Chapter 1. The resulting closed curve is bilaterally symmetric about $q = 0$ but not about $p = 0$. *Two* closed curves are actually seen; the second is a mirror image of the first and is made up of data collected for transits of the section plane in the reverse direction; after reflection about $p = 0$ it serves to augment the data base for the first.

In both cases, the integral [4.15] to be computed is proportional to the enclosed area; this integration proceeds as described below.

(1) It is important to normalize the input data by dividing with the maximal values since the magnitudes of the two axes are very different; hence, $\tilde{q} = q/q_{max}$ and $\tilde{p} = p/p_{max}$.

(2) If the curve is of type (b) such that it shows a mirror image, all points are reflected into the single curve taking full advantage of available data. As both types of curves have reflection symmetry about $\tilde{q} = 0$, surface data is folded across the coordinate axis. Further folding (across the momentum axis) is performed for curves of type (a).

(3) Since the data (q, p) will not come from the integrator in any arranged order, the next step is to sort the points with respect to some continuous variable. For each scaled point, $(\tilde{q}, \tilde{p})$, an angle $\vartheta = \arctan[\tilde{q}/\tilde{p}]$ is computed which runs $0 \leq \vartheta \leq \pi/2$ for type (a)

POINCARE AT X=0

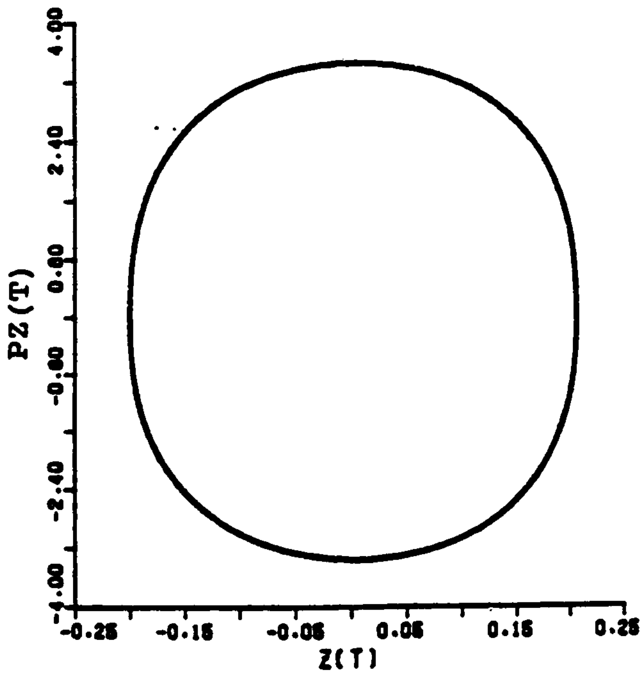

POINCARE AT Q1 = 0

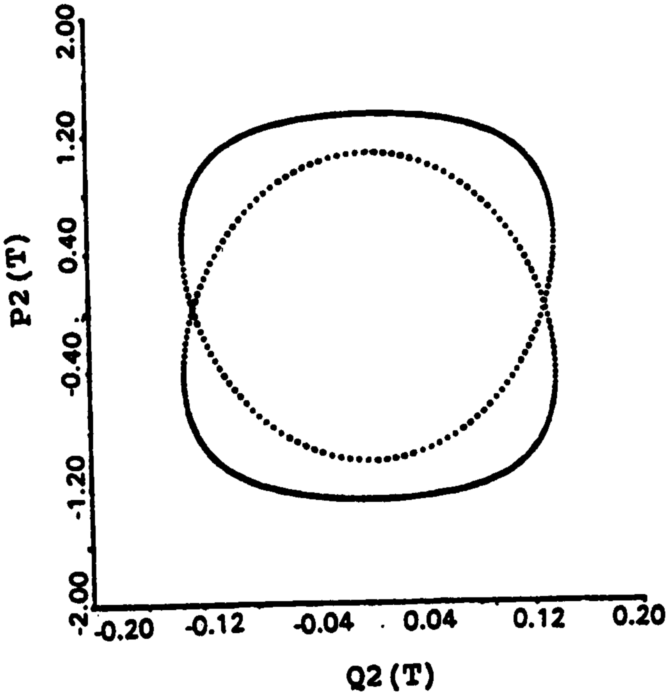

Figure 4.4: Typical forms of Poincaré surfaces-of-section encountered in this study–(a) $x = 0$ plane for a boxlike trajectory, (b) rotated $q_1 = 0$ plane for a resonant trajectory.

and $0 \leq \vartheta \leq \pi$ for type (b). A scaled square radius $\rho^2 = \tilde{p}^2 + \tilde{q}^2$ is also computed.

(4) It is necessary to ensure that a point is fixed at each limit. Since the trajectory is started at the origin, the point at $q = 0$ with $p > 0$ is known precisely as the initial condition data for both types, but the point $q > 0, p = 0$ for type (a) or $q = 0, p < 0$ for type (b) needs to be determined numerically. A restricted set of data points about the needed point is fit to a low-order power series and interpolation provides the new data point. It is then inserted as the first point of the ϑ ordered set.

(5) Scaled sets of $\tilde{q}$ and $\tilde{p}$ data are fit to Fourier series appropriate for their symmetry properties in ϑ and the integral is evaluated analytically. Another independent method that should yield the same result for the action is to fit the scaled radius ρ^2 as a Fourier series in ϑ to extract the constant term as the area enclosed. Comparison of these methods provides a measure of the precision of the computation which lies normally between 5x10^{-8} and 1x10^{-9}, though this can vary with the magnitude of the action and the orientation of the section plane. Cases of irregular motion can be readily identified by the poor quality of the Fourier fits above.

The Fourier series [4.11] for the variables (x, z, p_x, p_z) were constructed as a useful tool for comparison of trajectories obtained by other methods (such as the canonical perturbation treatment of SCF trajectories described in Chapter 5). If precise frequencies are known, this can be accomplished for any dynamical variable. For each data point on a sufficiently long trajectory run, determine the angle variables

$$\theta_1 = \omega_1 t; \qquad \theta_2 = \omega_2 t \qquad (\mathrm{mod}\ 2\pi). \qquad [4.16]$$

A set of expansion indices (k_1, k_2), adequate for the symmetry and complexity of the trajectory, are selected. The coefficients are then fit to the data by the method of linear least squares. Systematic errors in the frequencies will cause the data points later in time to be less reliable and usually a set of 4000-8000 points at most is best; the r.m.s. deviation in the fit clearly deteriorates when more are used. The precision error is estimated by the r.m.s. error in canonicity measured by the comparison of an actual fit to the momentum variable with the form calculated by equation [4.12]. A further check on the significance of the expansion coefficients is obtained by computing the actions J_1, J_2 analytically by equation [4.14]. Both criteria were well satisfied. In most cases, the resulting coefficients fit the canonicity requirement to better than $1\mathrm{x}10^{-7}$ and actions typically agree with those obtained by the surface-of-section method to $5\mathrm{x}10^{-8}$ or better. The relative uncertainty in the Fourier expansion coefficients themselves ranges from $5\mathrm{x}10^{-4}$ down to about $1\mathrm{x}10^{-5}$ or even $5\mathrm{x}10^{-6}$ in highly favourable cases.

For any continuous domain of regular motion for which actions exist, there is a relationship between the trajectory's initial conditions E, f_x and the set of actions J_1, J_2 such that values may be interpolated from known points. An iterative method allows a trajectory specific for a given set of actions to be determined to any desired accuracy for regular motions.

4.4 Trajectory Analysis

This study of classical dynamics originated in an attempt to use methods of classical bound state theory to compute vibrational eigenvalues for the proton motion in the $[FHF]^-$ model system. The quantum mechanical calculations of Epa and Thorson [2] had shown that the SCF approximation yields eigenvalues for the first few energy levels which very closely approximate the true eigenvalues, indicating that the system might be in some sense "separable" for these low-lying energies. Perhaps naively, we therefore expected that the methods reviewed by Marcus *et. al.* [22,23] would allow the determination of the ground state and first few excited states before the essential nonseparability of the system would produce widespread irregular motion. While the simple boxlike quasiperiodic trajectories discussed in the above literature did appear in a fragmented way, new families of quasiperiodic trajectories involving strong reorganizations of the motion also appeared. Moreover, irregular motion emerged prominently at very much lower energies than expected. To study these phenomena in their simplest terms, we decided to avoid the complications introduced in the $[FHF]^-$ system, by the azimuthal angular momentum and prolate pheroidal coordinates, by simplifying the model problem to the two-dimensional Cartesian model $H(x,z;R)$. As expected, the simplified model shows essentially the same phenomena as follows:

> In a study of the ground state, which is so obviously identifiable as the SCF level $(n_x,n_z) = (0,0)$ in quantum calculations, classical bound state methods were applied successfully for a continuous range of values $3.80 \leq R \leq 4.35$ by the usual rules ($J_i = n_i + 1/2$; $i = x, z$). Eigenvalues agree very closely (1–2 cm^{-1}) with those found by the Classical SCF (CSCF) method with semiclassical quantization, developed in Chapter

3. The differences are of the same magnitude as corresponding differences between exact quantum eigenvalues and quantum SCF eigenvalues for the same state. This tends to support the idea that the motion is somehow separable. However, for $R \geq 4.40$, it is impossible to determine classical bound state eigenvalues, even for the ground state, because box-like trajectories with required values $(J_x, J_z) = (1/2, 1/2)$ *do not exist.* Instead, the motion is completely reorganized in one of the prominent potential valleys lying at 26° to the x-axis. In addition, a region of irregular motion surrounding the "seam" or *bifurcation* between the two types of motion begins to spread as R increases.

Attempts to study the first and second excited states (which correspond closely with the SCF levels (1,0) and (0,1) in quantum calculations) are even more disappointing. At small R-values, there are additional strong reorganizations of the motion (apparently associated with higher order resonances) at energies close to the first excited level. While there remain isolated domains in R where quantization of box-like trajectories yields eigenvalues for these levels, they are interrupted frequently by these resonances, by the reorganized 1:1 motion already seen at the ground state energy, and by associated seams of irregular behaviour at boundaries separating distinct motions. At energies above that of the second excited state, the motion is so disrupted by chaos that no coherent results can be obtained.

This unexpected result makes clear the first conclusion to be drawn from this study, which is that classical bound state methods have little practical utility as a scheme for computing vibrational eigenvalues for molecules with significantly anharmonic *and* nonseparable potential surfaces. In fact, not even the ground state can be located effectively. This is in sharp contrast with Classical SCF calculations of semiclassical eigenvalues for such systems which (as shown in Chapter 3) give a good qualitative account of at least the low-lying energy levels of the system. It appears that classical bound state methods may be less effective for molecular vibrational systems showing strong anharmonicity and nonseparability if the present system is at all representative.

Therefore the remainder of this study is aimed at understanding this very different behaviour of classical dynamics and, if possible, relating it to corresponding phenomena in the quantum mechanics of the same system. Hence interest focusses not on the quantization of trajectories or the rules for doing so, but on the dynamics itself and its relation to other descriptions, both classical and quantum mechanical. We will pay particular attention to the strong reorganization of the motion about the potential surface valley, which is found even at the energy of the ground state, and its relation to curve-crossings or Fermi resonance phenomena seen at much higher energies in the quantum mechanics of the system. While the entire region below $E \approx 70$ c.e.u. has been broadly surveyed for $3.80 \leq R \leq 4.50$, detailed investigations have been done mainly for $R = 4.30$ a.u. and for energies near to the lowest three CSCF energy levels: $E^{00} \approx 24.0$ c.e.u., $\mathrm{E}^{10} \approx 46.0$ c.e.u., $\mathrm{E}^{01} \approx 56.0$ c.e.u. All the phenomena of specific interest to this study are adequately displayed by these samplings.

Previous sections of this chapter have emphasized analytical understanding of regular motion. However, as has been stressed by several authors [37], conceptual understanding has been greatly accelerated by computer graphics display of trajectories and other pictures arising from them. Through modern computer graphics, the trajectory may be observed *as it unfolds in time*, and the characteristics and limiting properties of the motion can be inspected *visually*. Correspondingly, a pictorial presentation of results rather than a focus on formal, analytical information can convey most effectively an understanding of essential aspects of the problem, and also provides a framework for deeper appreciation. Still further insights are provided by a *dynamical* generation of trajectories which cannot be easily visualized in the static "snap-shot" presentations. It is impossible to share these fully in context of a written document; in such cases, we shall have to rely on a combination of pictorial and analytical information with text commentary.

Figure 4.5 presents a sequence of trajectory projections on the (x, z) plane for $R = 4.30$ a.u. and $E = 24.0$ c.e.u. (near the CSCF ground state). The chosen trajectories all pass through the origin (0,0) and are shown with increasing parameter f_x, the fraction of initial kinetic energy in the x-oscillator $(0 \leq f_x \leq 1)$. For $f_x = 0$, the trajectory (not shown) corresponds simply to periodic oscillation on the z-axis; for $0 < f_x < 0.56$, a series of boxlike quasiperiodic trajectories appears. Even though they exhibit an increasing distortion of the caustics into a "butterfly" shape, all retain two mirror planes $(x = 0, z = 0)$ and exhibit full C_{2v} symmetry. At $f_x \approx 0.5678$, a complete change called a *bifurcation* occurs and a strongly reorganized family of trajectories appears in the region $0.56 < f_x < 0.98$, which is quasiperiodic but not related to the box family in any obvious way. We call this the 1:1 resonant family of regular motions; at its centre lies a simple periodic trajectory with $f_x \approx 0.795$ which corresponds to a resonant, in-phase oscillation in both x and z. The resonant trajectory is nearly a straight line and lies almost exactly in the direction of the pronounced potential surface valley at 26° to the x-axis. Finally, another bifurcation (not seen in the figure) occurs at $f_x \approx 0.983$ and simple boxlike trajectories reappear in the rest of the region, ending with periodic oscillation on the x-axis for $f_x = 1.00$.

Figure 4.5: Classical trajectories at $R = 4.30$ a.u. and $E = 24.0$ c.e.u. for a series of f_x values (0.05 to 0.80 in 0.05 steps) on the (x, z) plane.

fx = 0.05
CLASSICAL TRAJECTORY

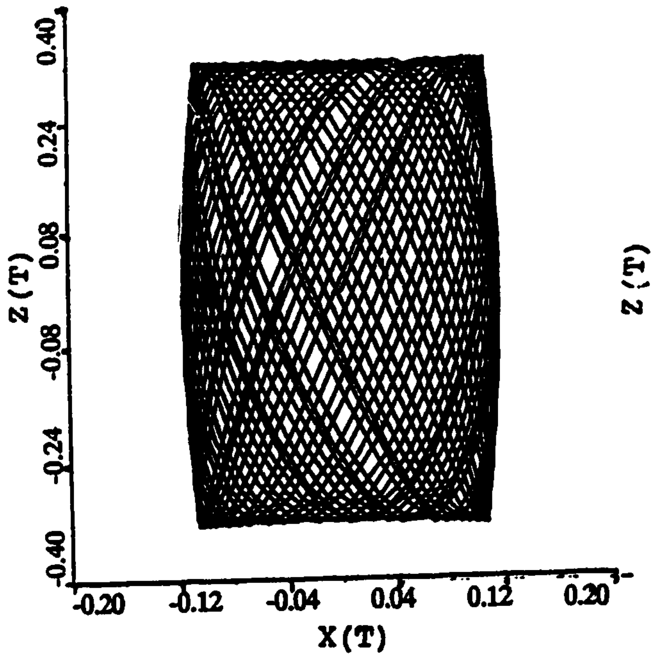

fx = 0.10
CLASSICAL TRAJECTORY

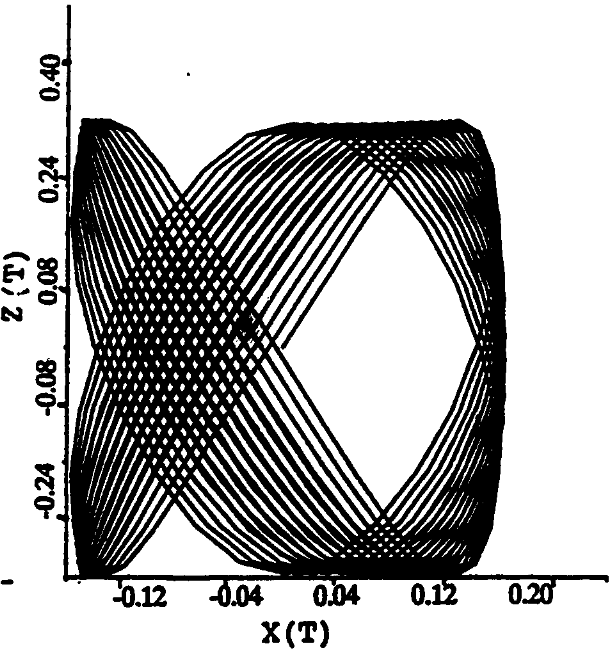

fx = 0.15
CLASSICAL TRAJECTORY

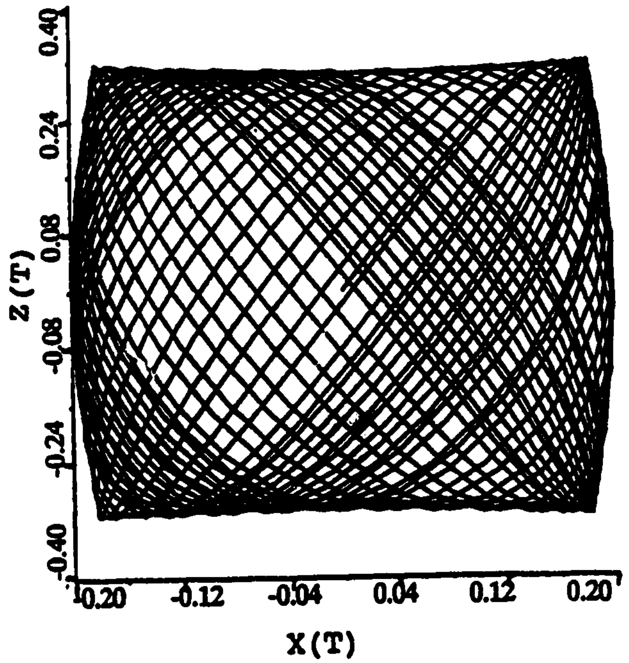

fx = 0.20
CLASSICAL TRAJECTORY

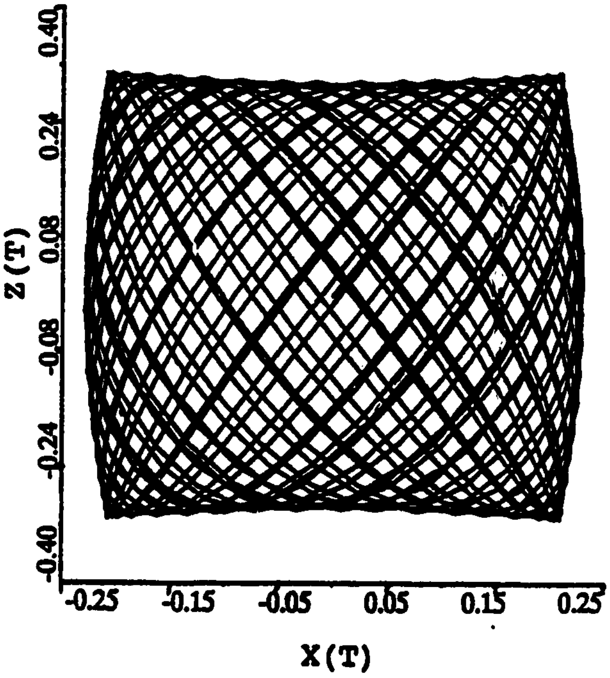

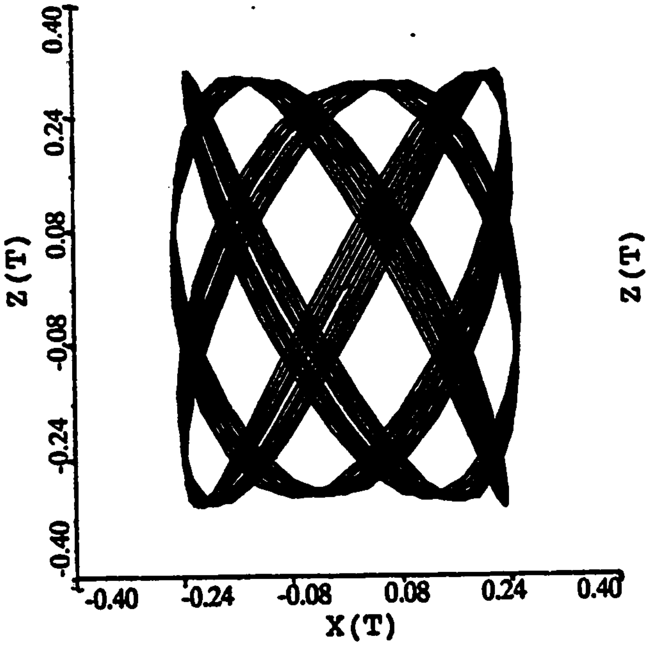

fx = 0.25
CLASSICAL TRAJECTORY

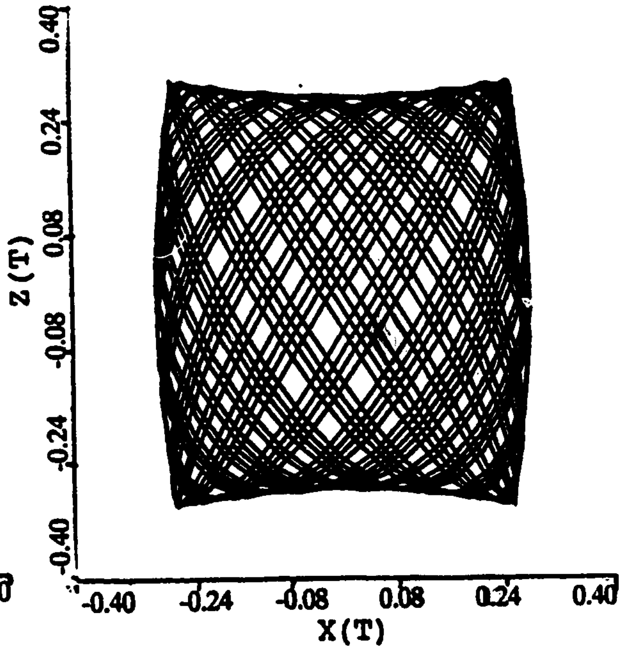

fx = 0.30
CLASSICAL TRAJECTORY

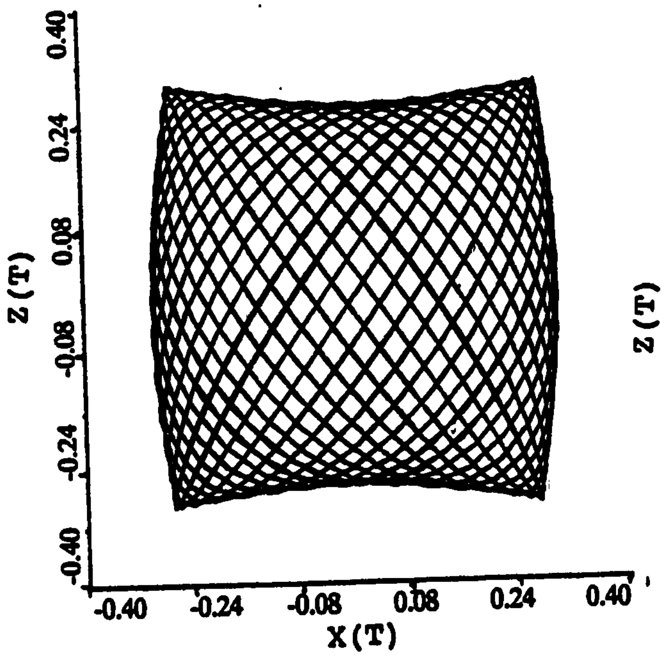

fx = 0.35
CLASSICAL TRAJECTORY

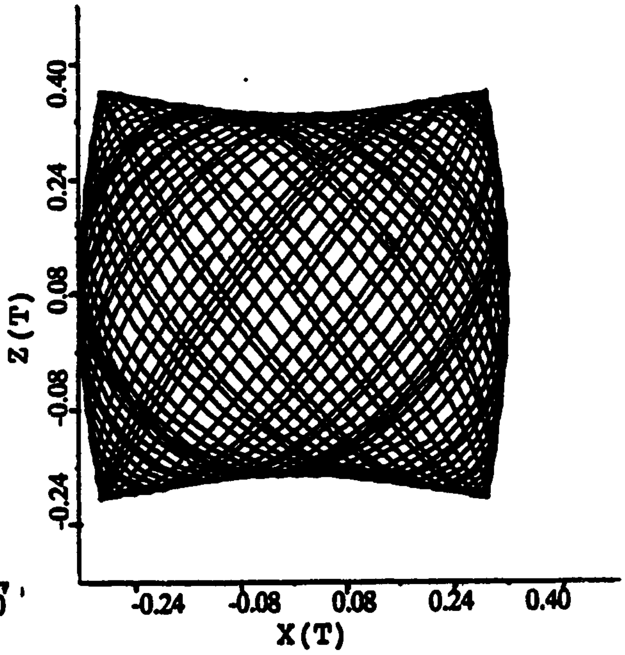

fx = 0.40
CLASSICAL TRAJECTORY

fx = 0.45
CLASSICAL TRAJECTORY

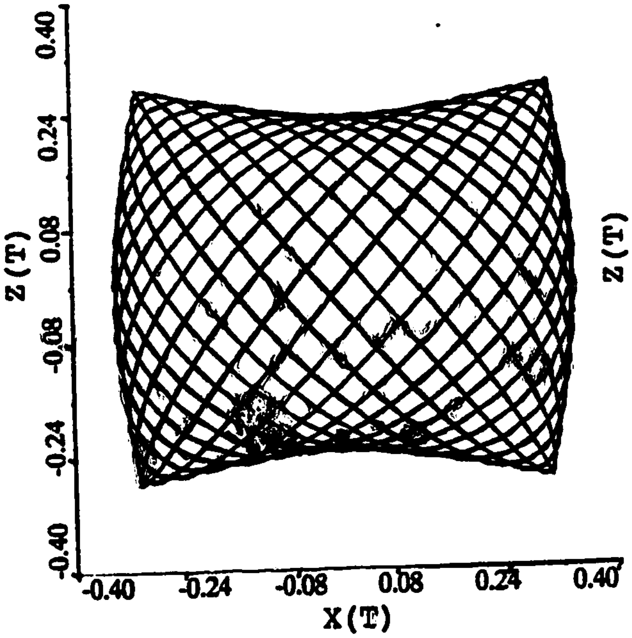

fx = 0.50
CLASSICAL TRAJECTORY

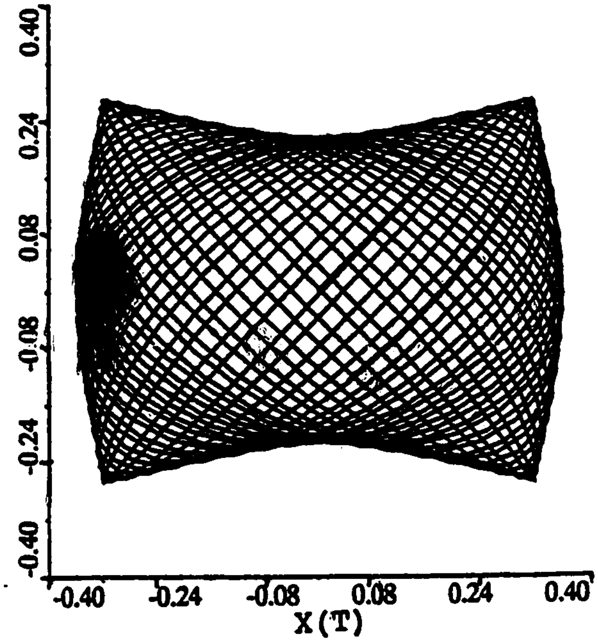

fx = 0.55
CLASSICAL TRAJECTORY

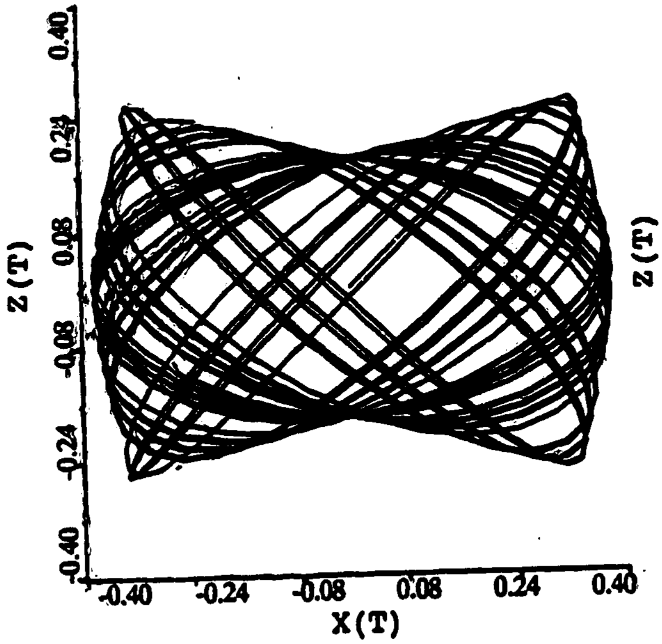

fx = 0.60
CLASSICAL TRAJECTORY

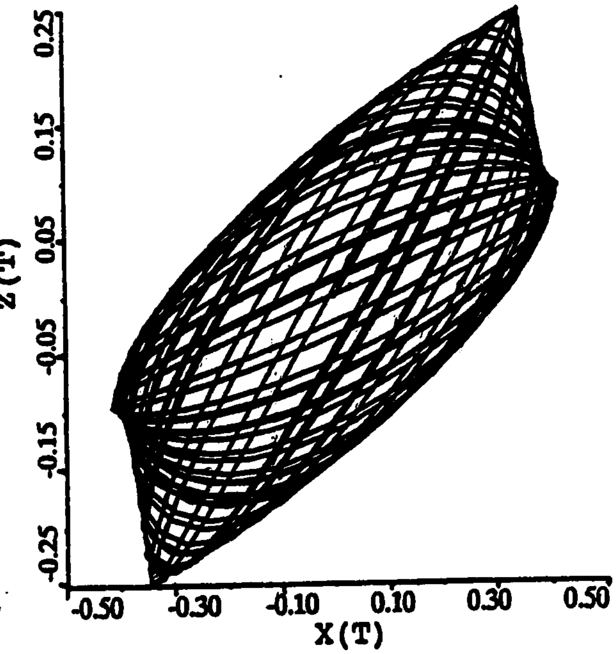

fx = 0.65

CLASSICAL TRAJECTORY

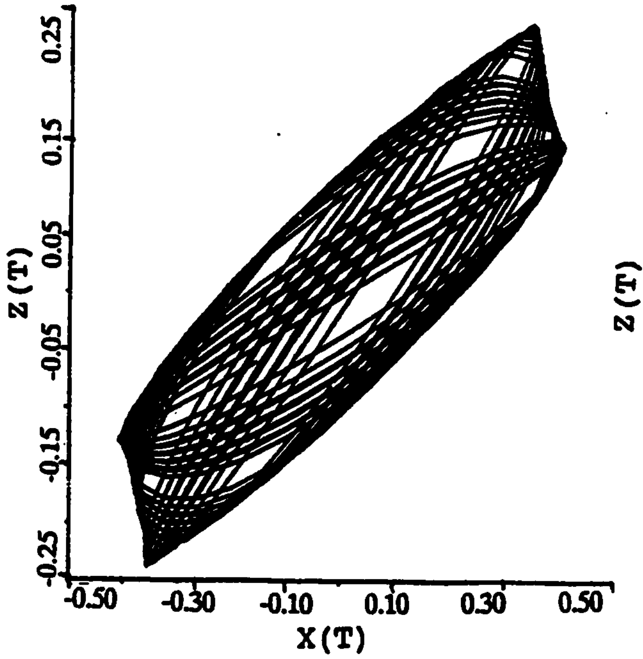

fx = 0.70

CLASSICAL TRAJECTORY

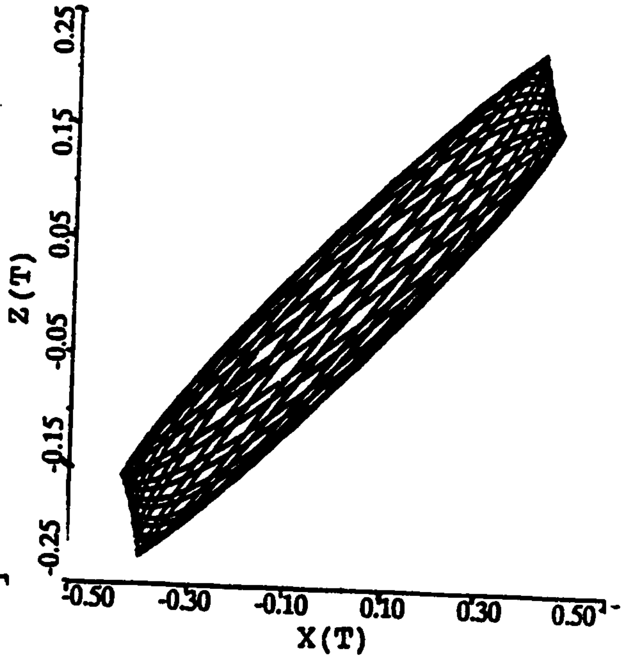

fx = 0.75

CLASSICAL TRAJECTORY

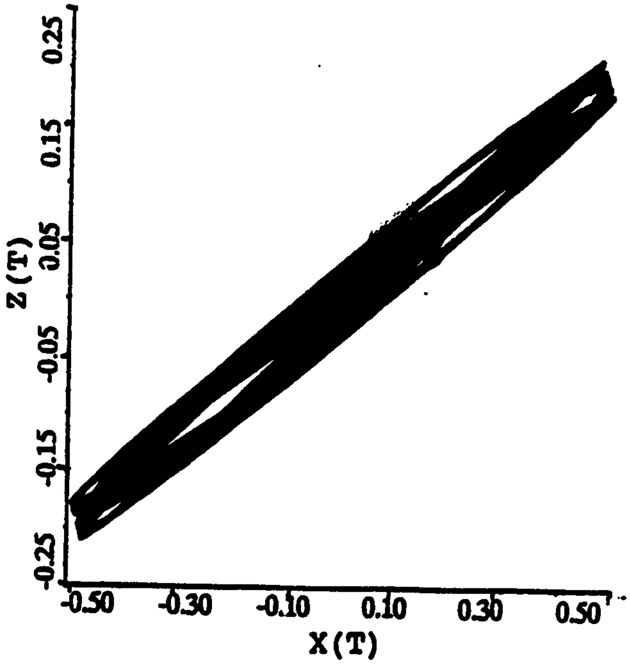

fx = 0.80

CLASSICAL TRAJECTORY

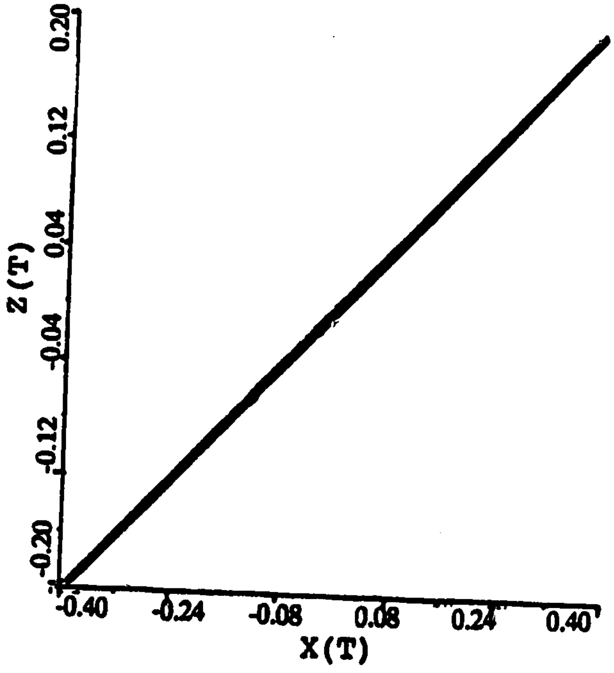

Poincaré surfaces-of-section for the planes $x = 0$ and $z = 0$ are shown in Figure [4.6] for the series of trajectories described above. This composite diagram contains sections from all of the families introduced through the series. The boxlike trajectories have cross-sections that possess mirror symmetry about both $q_i = 0$ and $p_i = 0$, and the planes present topologically distinct sections of the toroid for this family. This is confirmed by the distinct frequencies computed from transit times for near returns to the origin. Sections for boxlike trajectories with $f_x > 0.983$ are not seen in the plot but show the same behaviour and same symmetry characteristics. In these, cases, the areas enclosed by the surface-of-section curves for each plane determine the values of the actions; the area enclosed on the plane $x = 0$ provides J_z while that for $z = 0$ provides J_x. The notation (J_x, J_z) is clearly appropriate and there is a one-to-one relation between the specifying parameters (E, f_x) and the constants of the motion.

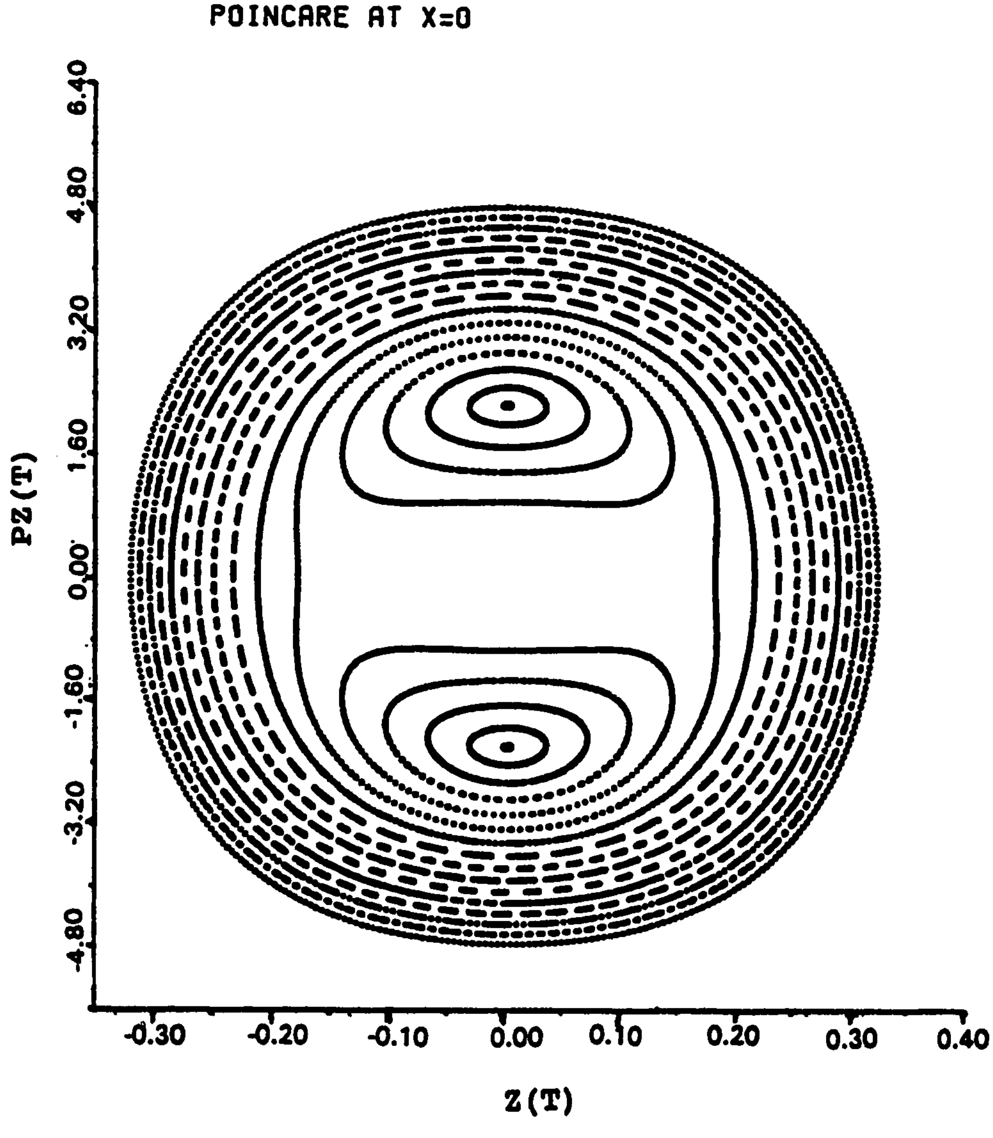

Figure 4.6: Poincaré surfaces-of-section are plotted in composite form for the series of trajectories in Figure 4.5 at R = 4.30 a.u. and E = 24.0 c.e.u. with $0.05 \leq f_x \leq 0.80$.Cross-sections are taken on the $x = 0$ and $z = 0$ planes.

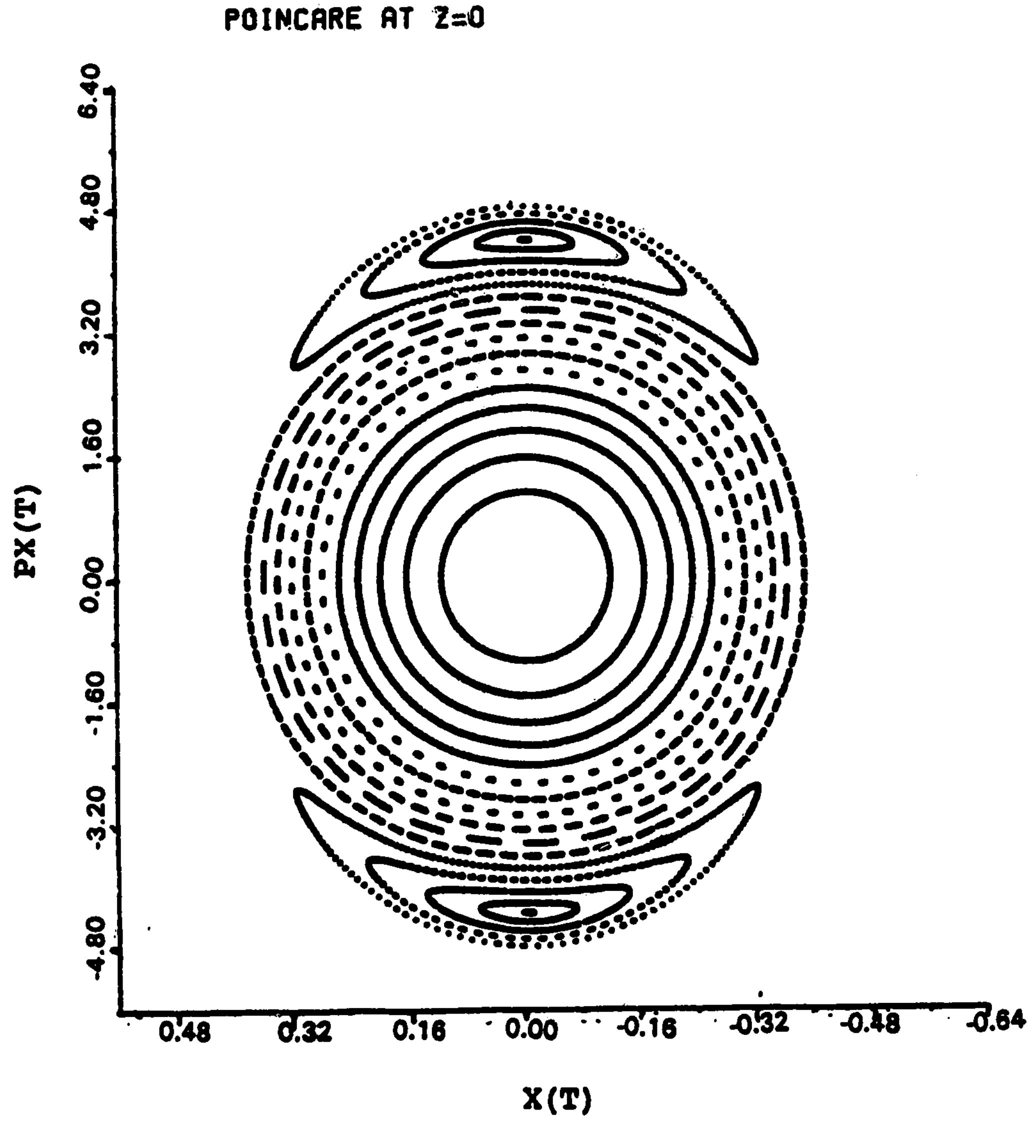
POINCARE AT Z=0
PX(T)
6.40
4.80
3.20
1.60
0.00
-1.60
-3.20
-4.80
0.48
0.32
0.16
0.00
-0.16
-0.32
-0.48
-0.64
X(T)

In the regions where motion belongs to the 1:1 resonant family, the Poincaré surface-of-section curves have been split into two libes which are mirror images of each other. One of them corresponds to transits of the plane in a positive sense and the other in a negative sense. Strictly speaking, therefore, only one of the pair should be considered. We shall see that the planes $x = 0$ and $z = 0$ do not present topologically distinct surfaces-of-section for the 1:1 resonant family of motions.

Fourier analysis of the dynamical variables (x, z, p_x, p_z) clearly reveals the characteristic symmetry of the boxlike family of motions. This symmetry is displayed in the coefficients shown in Tables 4.1 and 4.2 for the case $f_z = 0.3$. For x and p_x, k_x is odd and k_z is even, while the reverse holds for z and p_z. The strongly distorted "butterfly" trajectories seen near the bifurcation are still a part of the boxlike family. If the only terms present in the Fourier series were those with even index equal zero, the resulting trajectory projection would be a rectangular box on the (x, z) plane. The distortion to a butterfly shape is produced by substantial terms in which neither index is zero. It is useful to compare the magnitudes of coefficients in Tables 4.3 and 4.4 with those given for more rectangular boxlike motions. For all the boxlike trajectories, actions computed using Poincaré surface-of-section data are reconfirmed to an accuracy of accuracy of 1x10^{-8} to 1x10^{-9} by explicit calculation from the Fourier coefficients. Values for both calculations are given in Table 4.5. It is interesting that, while the Fourier fits show a r.m.s deviation of about 1x10^{-5}, the actions are known so precisely. This is analogous to the well known fact in quantum mechanics that energy eigenvalues are always known to higher accuracy than the associated wavefunctions.

We now discuss the 1:1 resonant family of quasiperiodic motions. Poincaré surfaces-of-section for $x = 0, z = 0$ do not form topologically distinct sections of the toroid (as frequencies obtained from near returns to the origin agree within

X	Z	2D – Coefficients	X	Z	2D – Coefficients
1	0	$3.03665958 \times 10^{-1}$	5	2	$3.86591912 \times 10^{-8}$
3	0	$-3.23586780 \times 10^{-4}$	5	4	$-4.11127671 \times 10^{-9}$
5	0	$2.41553576 \times 10^{-6}$	5	6	$-5.23696008 \times 10^{-10}$
7	0	$1.87204141 \times 10^{-8}$	5	8	$-6.50517039 \times 10^{-10}$
9	0	$-5.60406539 \times 10^{-10}$	5	−2	$-3.07060660 \times 10^{-5}$
11	0	$1.59663589 \times 10^{-10}$	5	−4	$1.91413273 \times 10^{-4}$
1	2	$1.91215661 \times 10^{-3}$	5	−6	$1.73411050 \times 10^{-5}$
1	4	$-3.19202319 \times 10^{-5}$	5	−8	$-3.54143542 \times 10^{-7}$
1	6	$6.59283717 \times 10^{-7}$	7	2	$8.33484319 \times 10^{-10}$
1	8	$-1.45614504 \times 10^{-8}$	7	4	$7.95905761 \times 10^{-10}$
1	10	$2.79718898 \times 10^{-10}$	7	6	$6.33881557 \times 10^{-10}$
1	12	$-1.00067187 \times 10^{-10}$	7	−2	$5.84458007 \times 10^{-7}$
1	−2	$1.74293418 \times 10^{-2}$	7	−4	$-7.17608372 \times 10^{-6}$
1	−4	$-9.21186820 \times 10^{-5}$	7	−6	$2.53783850 \times 10^{-5}$
1	−6	$2.64191155 \times 10^{-6}$	9	2	[illegible] $\times 10^{-10}$
1	−8	$-8.15727604 \times 10^{-8}$	9	4	$-4.51370676 \times 10^{-10}$
1	−10	$2.89634030 \times 10^{-9}$	9	−2	$-6.01638103 \times 10^{-9}$
1	−12	$2.34370491 \times 10^{-10}$	9	−4	$4.00273000 \times 10^{-7}$
3	2	$2.00076123 \times 10^{-5}$	11	2	$1.37074564 \times 10^{-10}$
3	4	$-5.85542905 \times 10^{-7}$	11	−2	$-3.73917356 \times 10^{-10}$
3	6	$1.33907678 \times 10^{-8}$			
3	8	$-1.26930273 \times 10^{-10}$			
3	10	$4.73694950 \times 10^{-10}$			
3	−2	$3.81624635 \times 10^{-3}$			
3	−4	$4.89130197 \times 10^{-4}$			
3	−6	$-5.66334364 \times 10^{-6}$			
3	−8	$1.80240709 \times 10^{-7}$			
3	−10	$-7.81829760 \times 10^{-9}$			

Table 4.1: 48 X-oscillator 2D-coefficients at $E = 24.0$ c.e.u., R = 4.30 a.u., $f_x = 0.3$:
Fundamental Frequencies: $\omega_x = 21.803706292$; $\omega_z = 28.069912655$
at r.m.s.= 5.0672610^{-5} with maximum deviation= 1.4402210^{-4}

X	Z	2D – Coefficient	X	Z	2D – Coefficients
0	1	$2.64667703 \times 10^{-1}$	2	5	$2.40180538 \times 10^{-6}$
0	3	$-5.07032822 \times 10^{-3}$	4	5	$1.81811708 \times 10^{-8}$
0	5	$1.01696915 \times 10^{-4}$	6	5	$1.40544459 \times 10^{-9}$
0	7	$-2.15065537 \times 10^{-6}$	8	5	$-1.70679598 \times 10^{-9}$
0	9	$5.00901546 \times 10^{-8}$	−2	5	$-3.58010657 \times 10^{-4}$
0	11	$2.37041920 \times 10^{-9}$	−4	5	$2.49555473 \times 10^{-4}$
0	13	$2.62369402 \times 10^{-9}$	−6	5	$-3.48387157 \times 10^{-5}$
2	1	$2.06474930 \times 10^{-3}$	−8	5	$-3.01305757 \times 10^{-5}$
4	1	$-8.01561329 \times 10^{-7}$	2	7	$-7.31142044 \times 10^{-8}$
6	1	$-5.67866614 \times 10^{-8}$	4	7	$1.49876604 \times 10^{-10}$
8	1	$-4.92710273 \times 10^{-9}$	6	7	$-6.26747189 \times 10^{-10}$
10	1	$3.48394796 \times 10^{-9}$	−2	7	$1.18455459 \times 10^{-5}$
−2	1	$-1.06140087 \times 10^{-2}$	−4	7	$-1.84487770 \times 10^{-5}$
−4	1	$-2.64276750 \times 10^{-4}$	−6	7	$1.00412424 \times 10^{-5}$
−6	1	$5.74406834 \times 10^{-7}$	2	9	$-8.16202266 \times 10^{-10}$
−8	1	$-1.65881414 \times 10^{-8}$	4	9	$2.73890652 \times 10^{-9}$
−10	1	$-3.47107619 \times 10^{-9}$	−2	9	$-3.65028119 \times 10^{-7}$
2	3	$-7.50968665 \times 10^{-5}$	−4	9	$8.74256146 \times 10^{-7}$
4	3	$-2.87532859 \times 10^{-7}$	2	11	$-3.53155992 \times 10^{-9}$
6	3	$5.32174364 \times 10^{-9}$	−2	11	$7.22887301 \times 10^{-9}$
8	3	$-3.15923183 \times 10^{-9}$	−4	11	$-3.13190236 \times 10^{-8}$
10	3	$3.21874396 \times 10^{-9}$	−2	13	$-2.56912691 \times 10^{-9}$
−2	3	$7.78750257 \times 10^{-3}$			
−4	3	$-3.49388544 \times 10^{-4}$			
−6	3	$-4.29074437 \times 10^{-5}$			
−8	3	$1.34317852 \times 10^{-6}$			
−10	3	$1.62216266 \times 10^{-8}$			

Table 4.2: 49 Z-oscillator 2D-coefficients at $E = 24.0$ c.e.u., R = 4.30 a.u., $\mathrm{f}_x \simeq 0.3$: Fundamental Frequencies: $\omega_x = 21.803706292$; $\omega_z = 28.069912655$ at r.m.s.= 1.8642310^{-5} with maximum deviation= 5.5610610^{-4}

X	Z	2D – Coefficients	X	Z	2D – Coefficients
1	0	$3.60358950 \times 10^{-1}$	5	2	$8.82044318 \times 10^{-9}$
3	0	$-5.14351002 \times 10^{-4}$	5	4	$1.07702975 \times 10^{-7}$
5	0	$3.12438939 \times 10^{-6}$	5	6	$-1.01350357 \times 10^{-7}$
7	0	$-7.08855684 \times 10^{-9}$	5	8	$6.65601796 \times 10^{-8}$
9	0	$-1.03912268 \times 10^{-7}$	5	−2	$-8.13785085 \times 10^{-5}$
11	0	$-1.08948741 \times 10^{-7}$	5	−4	$1.84597031 \times 10^{-3}$
1	2	$1.71068550 \times 10^{-3}$	5	−6	$6.23005583 \times 10^{-4}$
1	4	$-1.91948606 \times 10^{-5}$	5	−8	$-1.08503980 \times 10^{-5}$
1	6	$1.64586471 \times 10^{-7}$	7	2	$-1.70349076 \times 10^{-8}$
1	8	$-5.42036008 \times 10^{-8}$	7	4	$6.94101083 \times 10^{-8}$
1	10	$9.20548238 \times 10^{-8}$	7	6	$-9.95980500 \times 10^{-8}$
1	12	$-1.04080821 \times 10^{-7}$	7	−2	$1.33722401 \times 10^{-6}$
1	−2	$3.70469430 \times 10^{-2}$	7	−4	$-2.16243752 \times 10^{-5}$
1	−4	$-3.16839001 \times 10^{-4}$	7	−6	$3.07596139 \times 10^{-4}$
1	−6	$3.62172845 \times 10^{-6}$	9	2	$4.84814297 \times 10^{-8}$
1	−8	$-7.11106061 \times 10^{-8}$	9	4	$1.09231030 \times 10^{-8}$
1	−10	$-1.08939172 \times 10^{-7}$	9	−2	$1.63846971 \times 10^{-7}$
1	−12	$8.19043489 \times 10^{-8}$	9	−4	$2.43566373 \times 10^{-7}$
3	2	$2.38942246 \times 10^{-5}$	11	2	$9.16467129 \times 10^{-8}$
3	4	$-4.40777653 \times 10^{-7}$	11	−2	$9.97578143 \times 10^{-8}$
3	6	$-5.95017103 \times 10^{-8}$			
3	8	$1.02247440 \times 10^{-8}$			
3	10	$4.78290716 \times 10^{-8}$			
3	−2	$1.41065593 \times 10^{-2}$			
3	−4	$4.38789432 \times 10^{-3}$			
3	−6	$-5.79037750 \times 10^{-5}$			
3	−8	$2.61902616 \times 10^{-6}$			
3	−10	$-1.78897556 \times 10^{-7}$			

Table 4.3: 48 X-oscillator 2D-coefficients at $E = 24.0$ c.e.u., R = 4.30 a.u., $f_x = 0.55$: Fundamental Frequencies: $\omega_x = 22.536420579$; $\omega_z = 25.418120155$ at r.m.s.= 3.0515410^{-4} with maximum deviation= 1.1120110^{-3}

X	Z	2D – Coefficient	X	Z	2D – Coefficients
0	1	$2.10938447 \times 10^{-1}$	2	5	$1.65953764 \times 10^{-6}$
0	3	$-3.15320836 \times 10^{-3}$	4	5	$3.31631020 \times 10^{-8}$
0	5	$3.29776024 \times 10^{-4}$	6	5	$-1.59647752 \times 10^{-8}$
0	7	$-1.01552374 \times 10^{-7}$	8	5	$-3.49162544 \times 10^{-8}$
0	9	$1.80177105 \times 10^{-8}$	−2	5	$-1.18017505 \times 10^{-3}$
0	11	$2.11375637 \times 10^{-9}$	−4	5	$4.43780397 \times 10^{-3}$
0	13	$-2.86117598 \times 10^{-8}$	−6	5	$-3.10609687 \times 10^{-4}$
2	1	$2.49169521 \times 10^{-3}$	−8	5	$-3.32072531 \times 10^{-5}$
4	1	$5.61262454 \times 10^{-6}$	2	7	$-7.98093301 \times 10^{-8}$
6	1	$-1.70624744 \times 10^{-7}$	4	7	$-3.46351801 \times 10^{-8}$
8	1	$-4.42624545 \times 10^{-8}$	6	7	$-1.28503812 \times 10^{-8}$
10	1	$-1.98306850 \times 10^{-8}$	−2	7	$2.71385010 \times 10^{-5}$
−2	1	$-1.05805347 \times 10^{-2}$	−4	7	$-3.03050954 \times 10^{-4}$
−4	1	$-4.15780911 \times 10^{-4}$	−6	7	$6.70792181 \times 10^{-4}$
−6	1	$-9.56880588 \times 10^{-7}$	2	9	$4.20133034 \times 10^{-8}$
−8	1	$2.54889988 \times 10^{-8}$	4	9	$4.47389917 \times 10^{-8}$
−10	1	$1.27251754 \times 10^{-8}$	−2	9	$-4.63247283 \times 10^{-7}$
2	3	$-7.05661147 \times 10^{-5}$	−4	9	$1.08041867 \times 10^{-5}$
4	3	$-5.10624707 \times 10^{-7}$	2	11	$-2.13382059 \times 10^{-8}$
6	3	$4.58622717 \times 10^{-8}$	−2	11	$3.19220486 \times 10^{-8}$
8	3	$4.69722806 \times 10^{-8}$	−4	11	$-2.40181554 \times 10^{-7}$
10	3	$3.95717987 \times 10^{-8}$	−2	13	$-4.24366018 \times 10^{-8}$
−2	3	$3.00177840 \times 10^{-2}$			
−4	3	$-1.71537525 \times 10^{-3}$			
−6	3	$-1.09506349 \times 10^{-4}$			
−8	3	$-2.19882867 \times 10^{-7}$			
−10	3	$-4.85263976 \times 10^{-8}$			

Table 4.4: 49 Z-oscillator 2D-coefficients at $E = 24.0$ c.e.u., $\mathrm{R} = 4.30$ a.u., $\mathrm{f}_x = 0.55$:
Fundamental Frequencies: $\omega_x = 22.536420579$; $\omega_z = 25.418120155$
at r.m.s.= 1.5982610^{-4} with maximum deviation= 9.9097310^{-4}

f_x	J_x^{PSS}	J_z^{PSS}	ω_x^{PSS}	ω_z^{PSS}
0.050	0.0639095265	0.80589902600	20.664350000	31.900410000
0.100	0.1273187130	0.76433970500	20.826500000	31.402600000
0.150	0.1908368730	0.72170050800	20.989730000	30.887120000
0.200	0.2537478200	0.67841472400	21.151930000	30.358250000
0.250	0.3164434490	0.63416522300	21.314170000	29.809170000
0.300	0.3789958770	0.58883129000	21.480190000	29.237440000
0.350	0.4419693510	0.54190036600	21.648810000	28.632380000
0.400	0.5049008770	0.49358834400	21.823570000	27.992270000
0.450	0.5691846730	0.44262476000	22.012010000	27.293740000
0.500	0.6359473840	0.38773522800	22.224400000	26.497140000
0.550	0.7105322070	0.32352222500	22.537450000	25.416950000
0.555	0.7192532060	0.31575698900	22.589200000	25.252760000
0.560	0.7285452130	0.30740146200	22.659380000	25.051090000
0.565	0.7389378900	0.29791489900	22.768010000	24.753090000
0.567	0.7437864610	0.29336817900	22.860541794	24.513605186
0.984	0.0999866660	0.37415091400	23.415980929	21.733051608
0.985	1.0029347700	0.34078876200	23.434555544	21.374299951
0.990	1.0145973800	0.21036882100	23.485085617	20.656759211
0.995	1.0241502400	0.10049498000	23.523933156	20.226333417

f_x	$J_x^{Fourier}$	$J_z^{Fourier}$
0.100	0.127318642	0.764339661
0.200	0.253747828	0.678414695
0.300	0.378995409	0.588831485
0.400	0.504900341	0.493588064
0.500	0.635947418	0.387735007
0.520	0.664120021	0.363886378

Table 4.5: Actions determined by Poincaré surface-of-section integration and by explicit calculation from the Fourier series for a series of boxlike trajectories near the ground state are compared. The associated frequencies are also provided.

statistical error). It also would follow that the area enclosed by one of the lobes (as shown in Figure 4.6), for either plane, would give the same constant of motion. To obtain topologically distinct sections of the toroids for this family, we rotated the planes of section to a plane ($q_1 = 0$) normal to the periodic 1:1 trajectory at $f_x \approx 0.795$, and a plane ($q_2 = 0$) at right angles to the first one. Poincaré surfaces-of-section are shown for the planes $q_1 = 0, q_2 = 0$ in Figure 4.7 for the trajectory with $f_x = 0.6$. The two closed curves shown correspond, respectively, to transits of each plane in positive and negative senses. Only one curve in each case should be used to evaluate the actions as the enclosed areas. We denoted the action obtained from the plane $q_1 = 0$ as J_2 and from the plane $q_2 = 0$ as J_1.

The asymmetry seen in the closed curves of Figure 4.7 implies that a single trajectory possesses two distinct momentum vectors ($\vec{p}, \vec{p}\,'$) passing through the origin with positive components (p_x, p_z) and (p'_x, p'_z). This means that one and the same trajectory corresponds to *two* values of the parameter f_x, one on each side of the 1:1 periodic trajectory at $f_x \approx 0.795$. For $f_x = 0.6$, for example, the alternative f_x value is 0.9612. Thus, f_x is not a single-valued function of the constants of motion (J_1, J_2), which makes it inappropriate as a parametric variable for this family. Table 4.6 shows the actions J_1, J_2 and frequencies ω_1, ω_2 as a function of f_x for the region $0.568 < f_x < 0.983$.

The difficulty in using the f_x parameter as a running variable across the phase space at a given energy is illustrated in Figure 4.8. This shows the classical action data from Tables 4.5 and 4.6 for $E = 24.0$ c.e.u. and $R = 4.30$ a.u. as a function of the parameter f_x. Actions J_1, J_2 for the 1:1 resonant family must be sharply distinguished from the actions J_x, J_z appropriate to the box family. Data for corresponding frequencies are displayed in Figure 4.9. The double-valuedness in

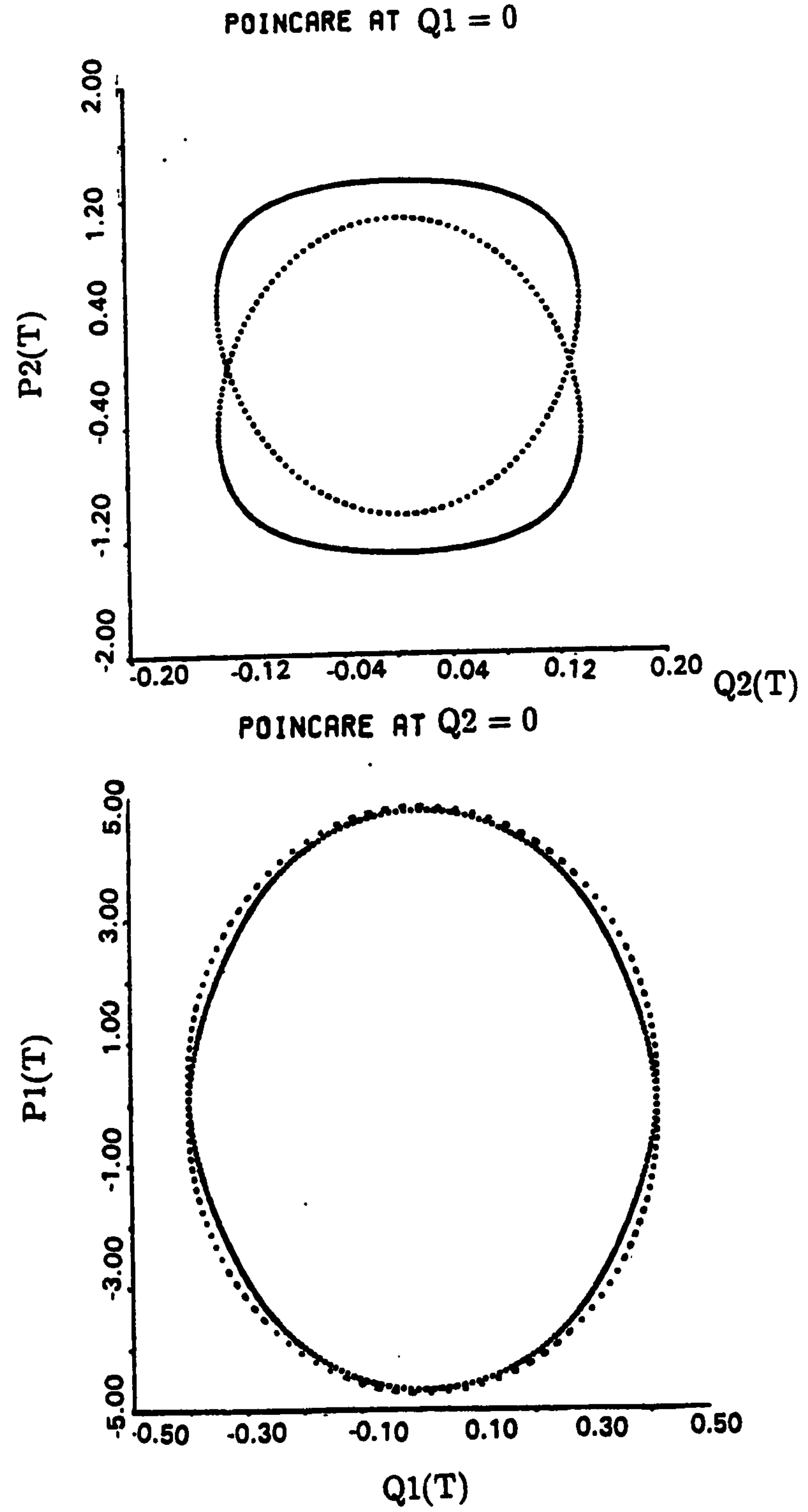

Figure 4.7: The Poincaré surfaces-of-section from a rotated coordinate axis frame for a resonant quasiperiodic trajectory at $R = 4.30$ a.u., $E = 24.0$ c.e.u., and $f_x = 0.6$.

f_x	$J_{z_1}^{PSS}$	$J_{z_2}^{PSS}$	$\omega_{z_1}^{PSS}$	$\omega_{z_2}^{PSS}$
0.568	0.9126290657	0.12418897400	23.178342602	24.502518620
0.570	0.9170318500	0.12036383700	23.086254156	25.066392964
0.600	0.9622086100	0.08063843790	22.806347683	26.413373524
0.650	1.0081862200	0.04174373760	22.595865038	27.224392039
0.700	1.0375270300	0.01765418510	22.472451726	27.651964189
0.750	1.0543625900	0.00404871783	22.403961287	27.877660557
0.800	1.0593570700	0.00004110019	22.383904251	27.942386198
0.850	1.0514480400	0.00639332918	22.415727150	27.839640121
0.900	1.0274617600	0.02586202340	22.514132365	27.510532290
0.950	0.0978931089	0.06627392250	22.726222558	26.736118932
0.960	0.0964300968	0.07879579380	22.795923284	26.456487342
0.970	0.0946656426	0.09409666050	22.886328112	26.068966404
0.980	0.0923621132	0.11447143200	23.028633784	25.382708513
0.981	0.0920764773	0.11702291800	23.051399504	25.261080153
0.982	0.0917622037	0.11983371100	23.080157635	25.101163209
0.983	0.0914099385	0.12298309200	23.123369912	24.847087021

f_x	$J_{z_1}^{Fourier}$	$J_{z_2}^{Fourier}$
0.600	0.962208881	0.0806378080
0.700	1.037527650	0.0176540225

Table 4.6: Actions and frequencies are given for the 1:1 resonant family at $E = 24.0$ c.e.u., R = 4.30 a.u. and over a range $0.568 < f_x < 0.983$.

f_x is evident. Note that the two frequencies ω_1, ω_2 take their extreme values at the periodic attractor. The bifurcation point is indicated by the apparent discontinuities of both actions and frequencies. This discontinuity shows that the two sets of constants of the motion are *not* simply related. On the other hand, it is observed in the figure that the sum of the actions $J_x + J_z$ or $J_1 + J_2$ is continuous across the bifurcation.

As is shown in Figure 4.5, the 1:1 resonant family of motion has trajectory projections with a lower symmetry; they are centro-symmetric but have lost the full C_{2v} symmetry of the box family. There is an exactly equivalent set of 1:1 trajectories which are mirror images of those shown in the figures and correspond to motion in the mirror image potential valley. Accordingly, the Fourier series for dynamical variables x, z, p_x, p_z show reduced symmetry properties. While the sum of the indices k_1, k_2 is necessarily odd to preserve central symmetry, there is no longer any parity restriction on either index alone. Tables 4.7 and 4.8 show the coefficients for $f_x = 0.6$. Again, the actions J_1, J_2 obtained explicitly from the Fourier series agree with the Poincaré surface-of-section area calculations (to within $1\text{x}10^{-7}$).

An interesting way of depicting the reduced symmetry of this family is to construct "correlation tracks". An average of the variables x and z over either angle (θ_1, θ_2) leads to two tracks in the (x, z) plane defined respectively by $(<x>_{\theta_1}, <z>_{\theta_1})$ or $(<x>_{\theta_2}, <z>_{\theta_2})$. For the boxlike family, these tracks are identically the x and z axes, which is a result of the symmetry of the Fourier series. Figure 4.10 shows the tracks for the trajectory at $f_x = 0.6$. They are neither orthogonal nor are they exactly straight lines.

The region in the neighbourhood of the bifurcation between boxlike and 1:1 trajectories is of particular interest to this work. Figure 4.11 shows a series

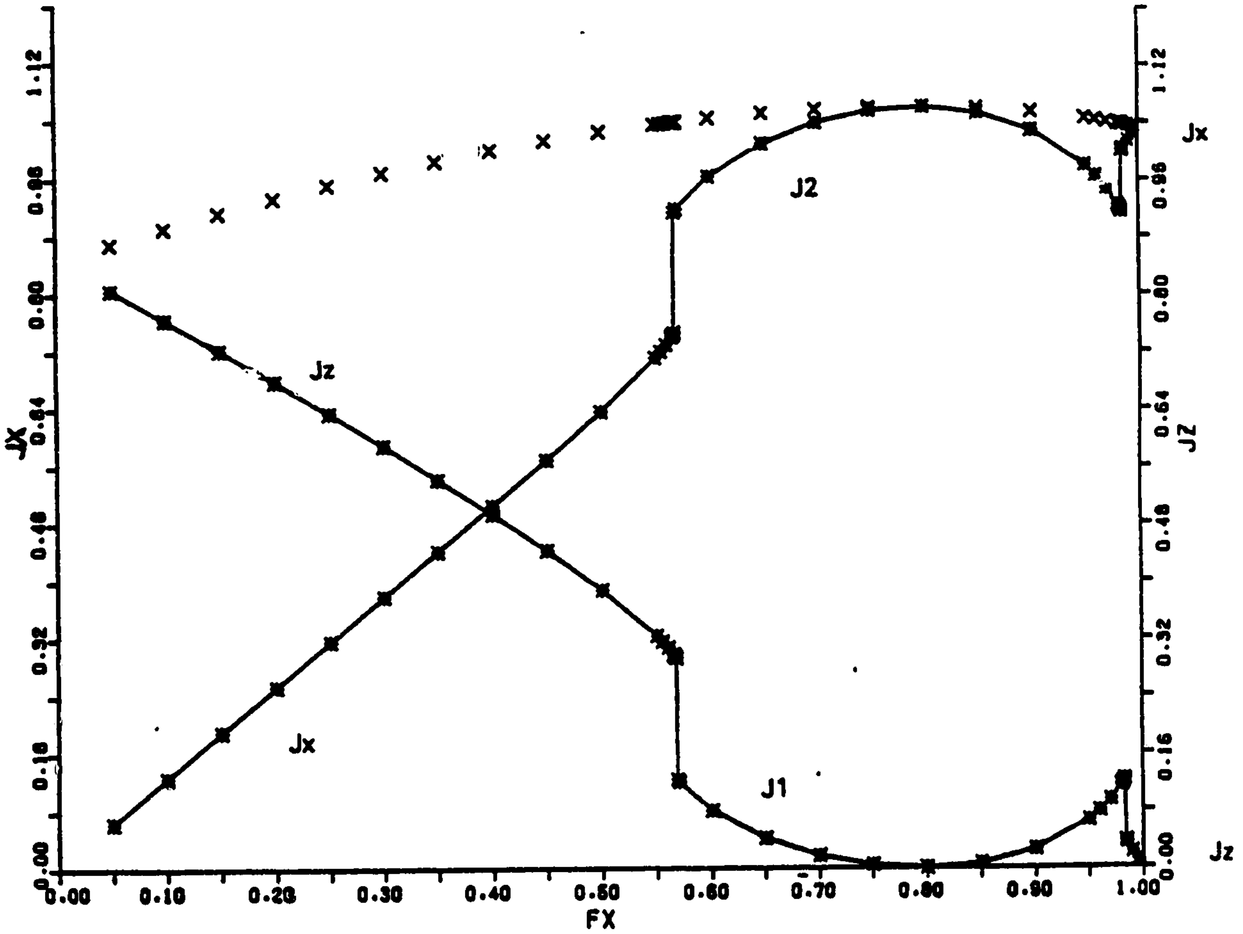

Figure 4.8: Classical actions J_x and J_z plotted against $f_x = (0,1)$ at $R = 4.30$ a.u., $E = 24.0$ c.e.u. The points marked with an 'X' indicate the sum of actions $(J_1 + J_2)$ or $(J_x + J_z)$ which appears to be continuous across the bifurcation.

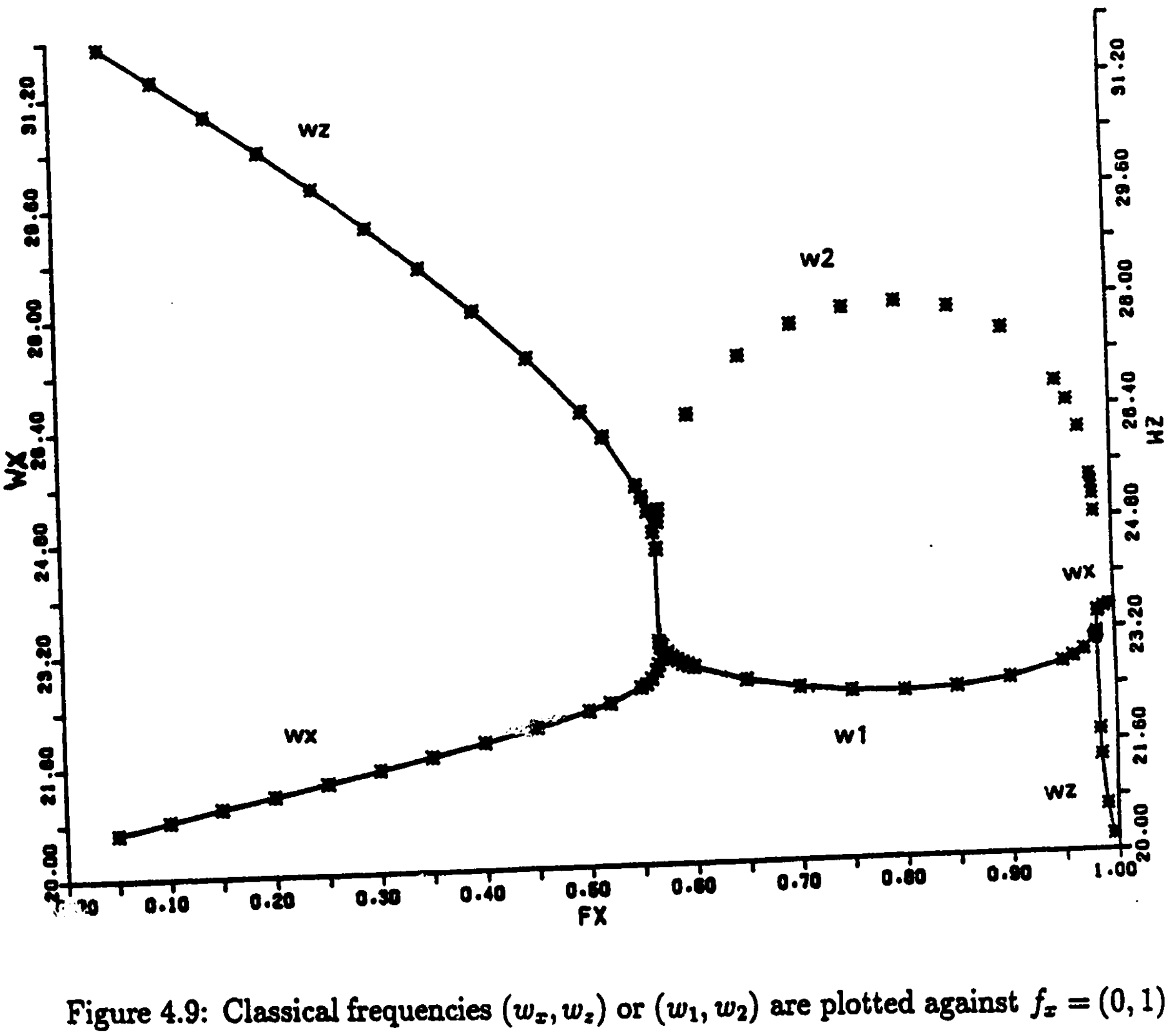

Figure 4.9: Classical frequencies (w_x, w_z) or (w_1, w_2) are plotted against $f_x = (0,1)$ at $R = 4.30$ a.u., $E = 24.0$ c.e.u.

X	Z	2D – Coefficients	X	Z	2D – Coefficients
1	0	$4.06941088 \times 10^{-1}$	4	1	$-7.81788783 \times 10^{-6}$
3	0	$8.91415964 \times 10^{-4}$	4	3	$2.18572868 \times 10^{-7}$
5	0	$1.17166340 \times 10^{-5}$	4	5	$-1.28189668 \times 10^{-8}$
7	0	$-1.02385206 \times 10^{-8}$	4	7	$-4.96642999 \times 10^{-9}$
9	0	$-1.59743094 \times 10^{-8}$	4	−1	$-1.93800998 \times 10^{-4}$
0	1	$-5.58074685 \times 10^{-3}$	4	−3	$8.01768295 \times 10^{-4}$
0	3	$-2.65163425 \times 10^{-4}$	4	−5	$-5.75769217 \times 10^{-5}$
0	5	$2.93170517 \times 10^{-6}$	4	−7	$6.89920292 \times 10^{-6}$
0	7	$-2.05780857 \times 10^{-8}$	4	−9	$-1.49579799 \times 10^{-7}$
0	9	$-2.40616551 \times 10^{-9}$	5	2	$5.03908817 \times 10^{-8}$
1	2	$-3.28034671 \times 10^{-4}$	5	4	$-1.34376095 \times 10^{-8}$
1	4	$3.14348656 \times 10^{-6}$	5	6	$-3.21419402 \times 10^{-9}$
1	6	$-1.72893029 \times 10^{-8}$	5	8	$1.20998546 \times 10^{-8}$
1	8	$-4.45359816 \times 10^{-9}$	5	−2	$2.47591438 \times 10^{-5}$
1	−2	$-2.20519292 \times 10^{-3}$	5	−4	$4.86342430 \times 10^{-4}$
1	−4	$1.29523876 \times 10^{-4}$	5	−6	$-1.70016652 \times 10^{-5}$
1	−6	$-1.77125908 \times 10^{-6}$	5	−8	$2.32546474 \times 10^{-6}$
1	−8	$1.04283313 \times 10^{-8}$	5	−10	$-4.82359098 \times 10^{-8}$
2	1	$7.48897280 \times 10^{-4}$	6	1	$-2.14718630 \times 10^{-7}$
2	3	$-1.14134362 \times 10^{-6}$	6	3	$-1.04295312 \times 10^{-8}$
2	5	$2.76487209 \times 10^{-8}$	6	5	$-1.41901153 \times 10^{-9}$
2	7	$-6.92254846 \times 10^{-9}$	6	7	$1.18662319 \times 10^{-8}$
2	−1	$8.59880536 \times 10^{-3}$	6	−1	$2.65375297 \times 10^{-6}$
2	−3	$-5.96268726 \times 10^{-4}$	6	−3	$8.57857708 \times 10^{-6}$
2	−5	$5.29455739 \times 10^{-5}$	6	−5	$9.52914227 \times 10^{-5}$
2	−7	$-8.79236460 \times 10^{-7}$	6	−7	$-4.78395937 \times 10^{-6}$
2	−9	$6.77907329 \times 10^{-10}$	6	−9	$7.58288612 \times 10^{-7}$
3	2	$-1.24797635 \times 10^{-5}$	7	2	$-8.63573548 \times 10^{-9}$
3	4	$1.34333396 \times 10^{-7}$	7	4	$4.02367982 \times 10^{-10}$
3	6	$-9.93906471 \times 10^{-9}$	7	6	$1.13657018 \times 10^{-8}$
3	8	$-6.61350557 \times 10^{-9}$	7	8	$-7.85771710 \times 10^{-9}$
3	−2	$7.70467794 \times 10^{-3}$	7	−2	$-1.38177112 \times 10^{-7}$
3	−4	$-2.12673762 \times 10^{-4}$	7	−4	$3.33469494 \times 10^{-7}$
3	−6	$1.96696097 \times 10^{-5}$	7	−6	$4.41587676 \times 10^{-5}$
3	−8	$-3.84468293 \times 10^{-7}$	7	−8	$-1.39732274 \times 10^{-6}$
			7	−10	$2.43163117 \times 10^{-7}$

Table 4.7: 71 X-oscillator 2D-coefficients at $E = 24.0$ e.u., R = 4.30 a.u., $f_x = 0.6$:
Fundamental Frequencies: $\omega_x = 22.806343215$; $\omega_z = 26.413337926$
at r.m.s.= $7.66378 10^{-5}$ with maximum deviation= $2.99307 10^{-4}$

X	Z	2D – Coefficients	X	Z	2D – Coefficients
0	1	$1.07739256 \times 10^{-1}$	1	4	$1.56002391 \times 10^{-5}$
0	3	$-8.12222640 \times 10^{-4}$	3	4	$-2.78178271 \times 10^{-8}$
0	5	$9.99100642 \times 10^{-6}$	5	4	$4.42106849 \times 10^{-8}$
0	7	$-2.05427719 \times 10^{-7}$	7	4	$-3.74580929 \times 10^{-9}$
0	9	$1.76864742 \times 10^{-8}$	−1	4	$-3.46409501 \times 10^{-4}$
0	11	$4.70152634 \times 10^{-6}$	−3	4	$1.71667646 \times 10^{-5}$
1	0	$-4.55819693 \times 10^{-2}$	−5	4	$-1.08046000 \times 10^{-4}$
3	0	$1.91817689 \times 10^{-3}$	−7	4	$1.04591391 \times 10^{-6}$
5	0	$-6.99968645 \times 10^{-6}$	−9	4	$-2.19854988 \times 10^{-8}$
7	0	$-3.98618631 \times 10^{-7}$	2	5	$-2.36923662 \times 10^{-7}$
9	0	$6.32246019 \times 10^{-8}$	4	5	$4.20589539 \times 10^{-6}$
11	0	$-3.67758294 \times 10^{-8}$	6	5	$5.11869461 \times 10^{-9}$
2	1	$-1.22740696 \times 10^{-3}$	8	5	$-4.88283725 \times 10^{-8}$
4	1	$-3.68877819 \times 10^{-5}$	−2	5	$-1.32878648 \times 10^{-4}$
6	1	$-9.94303533 \times 10^{-8}$	−4	5	$4.81244298 \times 10^{-4}$
8	1	$7.25000499 \times 10^{-8}$	−6	5	$3.21187365 \times 10^{-5}$
10	1	$-2.92044529 \times 10^{-8}$	−8	5	$-1.56934714 \times 10^{-5}$
−2	1	$3.05852723 \times 10^{-2}$	−10	5	$2.69637602 \times 10^{-7}$
−4	1	$-4.86998539 \times 10^{-4}$	1	6	$-2.57891626 \times 10^{-7}$
−6	1	$-7.56690024 \times 10^{-6}$	3	6	$4.00755822 \times 10^{-8}$
−8	1	$2.96805957 \times 10^{-8}$	5	6	$1.36779331 \times 10^{-8}$
−10	1	$-6.27276722 \times 10^{-8}$	7	6	$-5.16078167 \times 10^{-8}$
1	2	$-1.58744517 \times 10^{-3}$	−1	6	$5.22472934 \times 10^{-6}$
3	2	$-6.96085256 \times 10^{-6}$	−3	6	$-4.79596559 \times 10^{-5}$
5	2	$5.12067158 \times 10^{-7}$	−5	6	$1.33440164 \times 10^{-4}$
7	2	$6.89603263 \times 10^{-8}$	−7	6	$-6.94753511 \times 10^{-6}$
9	2	$-2.13423596 \times 10^{-8}$	−9	6	$-2.53005688 \times 10^{-6}$
−1	2	$2.26878106 \times 10^{-2}$	2	7	$3.49374451 \times 10^{-8}$
−3	2	$-2.95806516 \times 10^{-3}$	4	7	$2.17686578 \times 10^{-8}$
−5	2	$4.86392394 \times 10^{-5}$	6	7	$-5.45463189 \times 10^{-8}$
−7	2	$1.98084725 \times 10^{-6}$	8	7	$4.07125419 \times 10^{-8}$
−9	2	$1.54982481 \times 10^{-8}$	−2	7	$2.44446719 \times 10^{-6}$
2	3	$1.52029354 \times 10^{-5}$	−4	7	$-1.66055325 \times 10^{-5}$
4	3	$3.78807083 \times 10^{-7}$	−6	7	$3.79278446 \times 10^{-5}$
6	3	$5.35871506 \times 10^{-8}$	−8	7	$6.31897710 \times 10^{-7}$
8	3	$-1.21456862 \times 10^{-8}$			
10	3	$-3.81363961 \times 10^{-8}$			
−2	3	$6.45299969 \times 10^{-3}$			
−4	3	$8.16469867 \times 10^{-4}$			
−6	3	$-1.08722452 \times 10^{-4}$			
−8	3	$2.02464601 \times 10^{-7}$			
−10	3	$3.39507521 \times 10^{-8}$			

Table 4.8: 77 Z-oscillator 2D-coefficients at $E = 24.0$ c.e.u., R = 4.30 a.u., $f_x = 0.6$: Fundamental Frequencies: $\omega_z = 22.806343215$; $\omega_x = 26.413337926$ at r.m.s.= 1.4604510^{-4} with maximum deviation= 6.2538810^{-4}

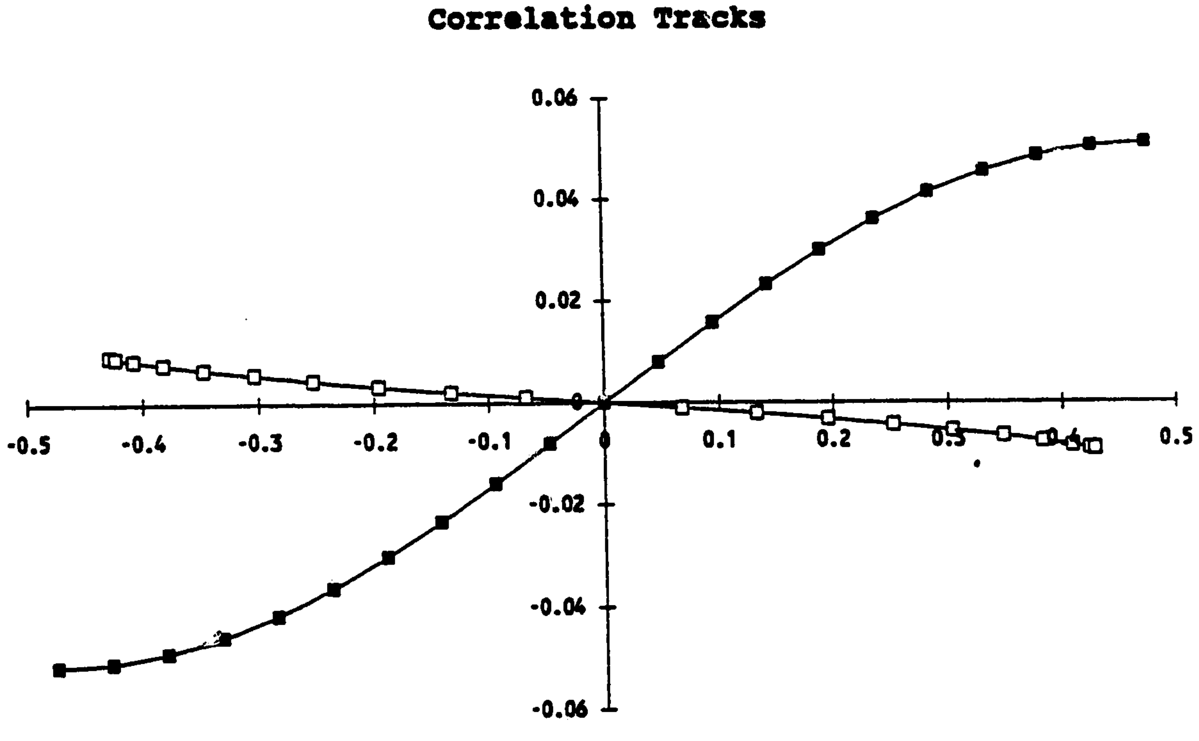

Figure 4.10: A depiction of the nonorthogonal average tracks obtained at $R = 4.30$ a.u., $E = 24.0$ c.e.u., and $f_x = 0.6$.

of trajectory plots near the bifurcation at $f_x \approx 0.5687$ for $E = 24.0$ c.e.u. and $R = 4.30$ a.u.. While it is known from general theory [38] that at least a seam of irregular or chaotic motion must exist at the bifurcation between two distinct quasiperiodic families, this seam was undetectable here, with a width in f_x smaller than 10^{-8}. In the neighbourhood of the bifurcation, the dynamics undergoes a sequence of changes that can be observed statically in Figure 4.11, but are best seen dynamically (using computer display). A relatively large proportion of the trajectory (in time) is concentrated in an elliptical motion about the origin, which appears prominently in trajectory plots on *either* side of the bifurcation. In this region we used Fast Fourier Transforms (FFT's) of the dynamical variables (x, z) to see if the results show any evidence of this elliptical motion. Table 4.9 present FFT frequencies and associated peak heights for trajectories with f_x values lying on either side of the bifurcation and near to it. Numerous smaller peaks and the broadening of the "fundamentals" seem to appear only in the neighbourhood of the bifurcation where the elliptical motion is also prominent. This elliptical motion is an important transitional motion between the two stable quasiperiodic families of motion. Further clarification of its meaning will be given after the discussion of work presented in Chapter 5.

Figure 4.11: Classical trajectories at $R = 4.30$ a.u., $E = 24.0$ c.e.u. for a series of f_x values between 0.5 and 0.6 on the (x, z) plane.

fx = 0.52

CLASSICAL TRAJECTORY

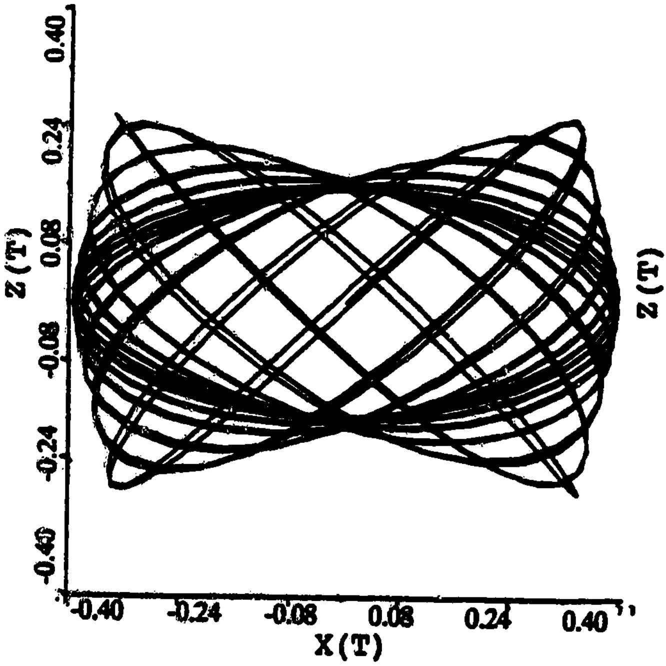

fx = 0.54

CLASSICAL TRAJECTORY

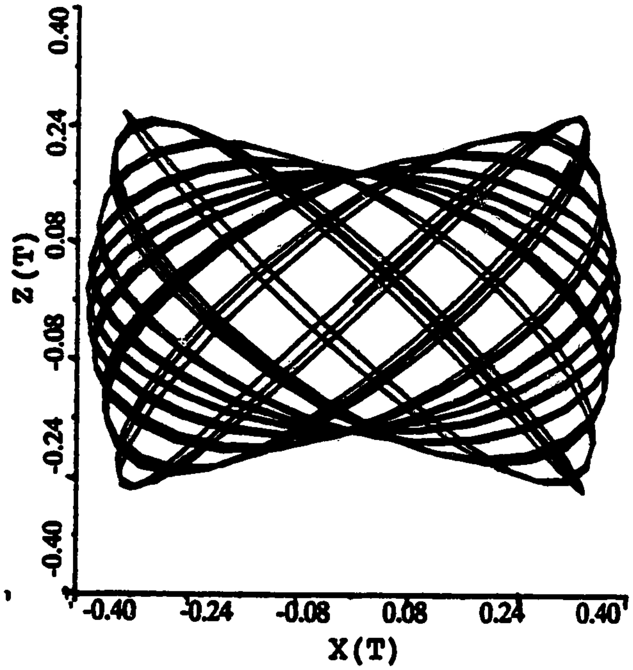

CLASSICAL TRAJECTORY

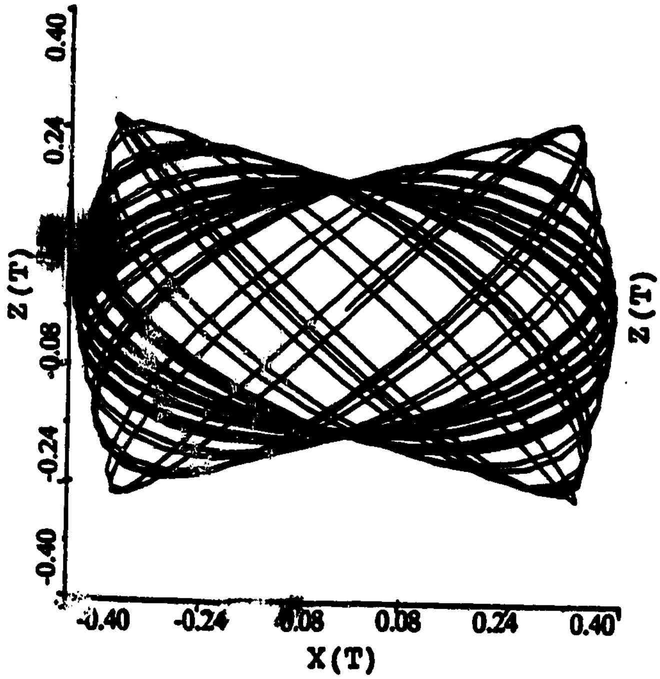

fx = 0.56

CLASSICAL TRAJECTORY

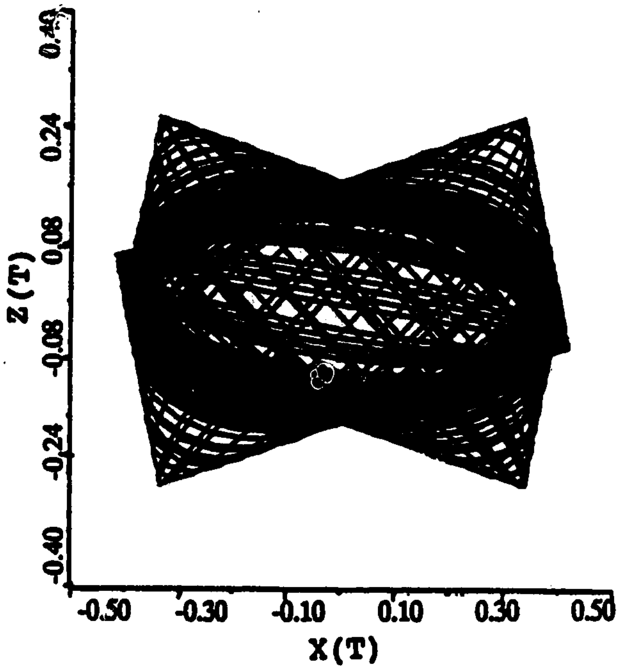

fx = 0.567

fx = 0.57

CLASSICAL TRAJECTORY

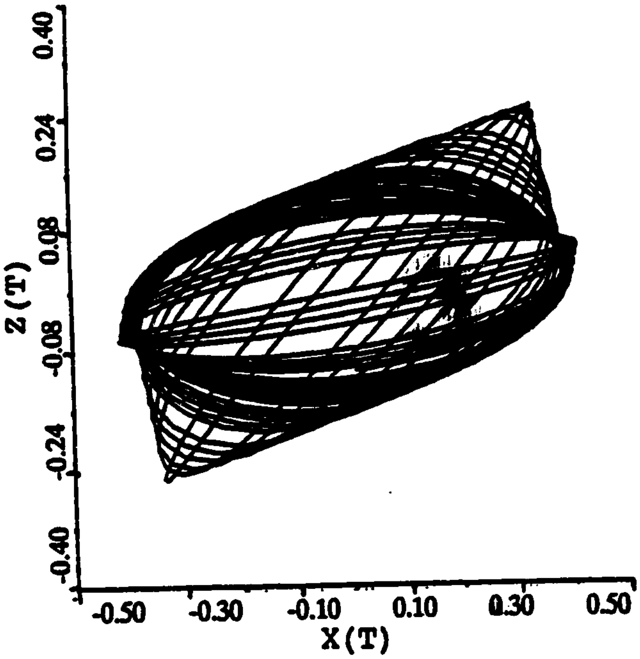

fx = 0.58

CLASSICAL TRAJECTORY

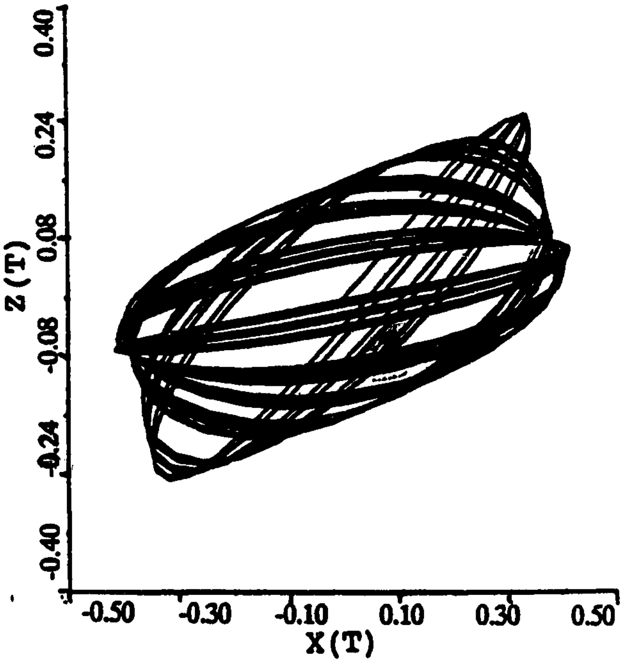

CLASSICAL TRAJECTORY

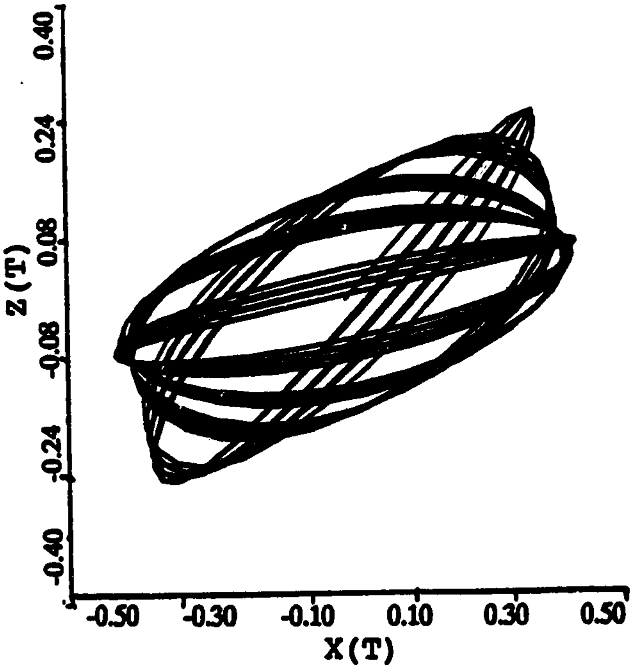

fx = 0.59

Examination of this transitional behaviour is not as feasible at higher energies or larger R-values than 4.30 a.u. because the seam of chaotic or irregular motion at the bifurcation expands rapidly. For $R = 4.30$ a.u., the seam has a width $\Delta f_x \approx 0.05$ by $E = 46.0$ c.e.u. and $\Delta f_x \approx 0.1$ at 56.0 c.e.u.; at 70.0 c.e.u. this has grown to more than 0.30. Figure 4.12 maps out domains of boxlike and 1:1 quasiperiodic motions and chaos on the (E, f_x) plane at $R = 4.30$ a.u.; note that the portion of the region occupied by the 1:1 resonant family expands as E increase, the bifurcation moving to lower f_x values. In general, even at low energy the chaotic seam also expands rapidly for R-values increasing beyond approximately 4.40 a.u.; this may be an effect associated with the development of a double-well structure in the potential for $R \geq 4.45$ a.u.

In conclusion we emphasize that classical bound state theory has little utility for determining semiclassical vibrational eigenvalues in anharmonic, nonseparable systems like the model studied here. As has been shown in many previous studies, it does work well for nearly harmonic systems. But since there are many other means by which nearly harmonic cases may easily be analyzed, the utility of classical bound state methods in general remains questionable. Perhaps this is the tacit reason for the rapid decline of interest in eigenvalue computations by this method in recent literature. An understanding of the classical dynamics for its own sake (at energies low enough to avoid swamping by chaotic motions) does offer some indirect comparisons to be made with quantum mechanical behaviour in the same system, and this has been the main focus of the studies of classical dynamics made here.

In Chapter 5, we further develop the description of the same system via Classical Self-Consistent Field theory. Using canonical perturbation theory we show that the CSCF approximation offers some important insights into the classical dy-

f_x	ω_x	$x-peak$	Notes	ω_z	$z-peak$	Notes
0.555	3.5400	0.014		3.9795	0.014	
	3.5645	0.045		4.0039	0.093	
	3.5889	1.078	}	4.0283	0.272	}
	3.6133	0.130		4.0527	0.019	
	3.6377	0.023		4.0771	0.007	
	4.4434	0.018	—			
0.560	3.5400	0.012		3.9307	0.006	
	3.5645	0.031		3.9551	0.017	
	3.5889	0.183		3.9795	0.288	}
	3.6133	1.016	}	4.0039	0.064	
	3.6377	0.053		4.0283	0.010	
	3.6621	0.017				
	3.6865	0.008				
	4.3701	0.017	—			
0.565	3.5400	0.011		3.3818	0.005	
	3.5645	0.022		3.9063	0.016	
	3.5889	0.066		3.9307	0.237	}
	3.6133	0.759		3.9551	0.070	
	3.6377	0.397	}	3.9795	0.011	
	3.6621	0.054				
	3.6865	0.020				
	3.7109	0.011				
	4.2480	0.022	—			
0.5678	3.5645	0.024	—	3.8086	0.029	
	3.6133	0.020		3.8330	0.097	}
	3.6377	0.025		3.8574	0.026	
	3.6621	0.081		4.1504	0.014	—
	3.6852	1.137	}			
	3.7109	0.140				
	3.7354	0.044				
	3.8330	0.011	}			
	3.8818	0.012				
	4.0039	0.014	—			

f_x	ω_1	q_1-peak	Notes	ω_2	q_2-peak	Notes
0.570	3.5889	0.012		3.3691	0.014	—
	3.6133	0.024		3.6377	0.002	
	3.6377	0.068		3.6621	0.028	}
	3.6621	0.616		3.6865	0.038	
	3.6865	0.617	}	3.7109	0.006	
	3.7109	0.069		3.9551	0.010	
	3.7354	0.025		3.9795	0.100	}
	3.7598	0.013		4.0039	0.039	
				4.0283	0.005	
				4.2969	0.011	}
				4.3213	0.003	
0.575	3.6377	0.002		3.2471	0.003	}
	3.6621	1.570	}	3.2715	0.012	
	3.6865	0.002		3.6621	0.036	—
				4.0283	0.006	
				4.0527	0.119	}
				4.0772	0.019	
				4.1016	0.003	
0.580	3.5645	0.011		3.6133	0.001	
	3.5889	0.021		3.6377	0.010	
	3.6133	0.035		3.6621	0.027	}
	3.6377	0.381	}	3.6865	0.002	
	3.6621	0.958		4.1016	0.148	—
	3.6865	0.074				
	3.7109	0.025				

Table 4.9: Discrete FFT frequencies are provided for a number of trajectories on either side of the bifurcation at $f_x = 0.5678$ with $E = 24.0$ c.e.u. and $R = 4.30$ a.u.. Broad peaks are indicated with brackets. (These values are divided by 2π from other notation in the text.)

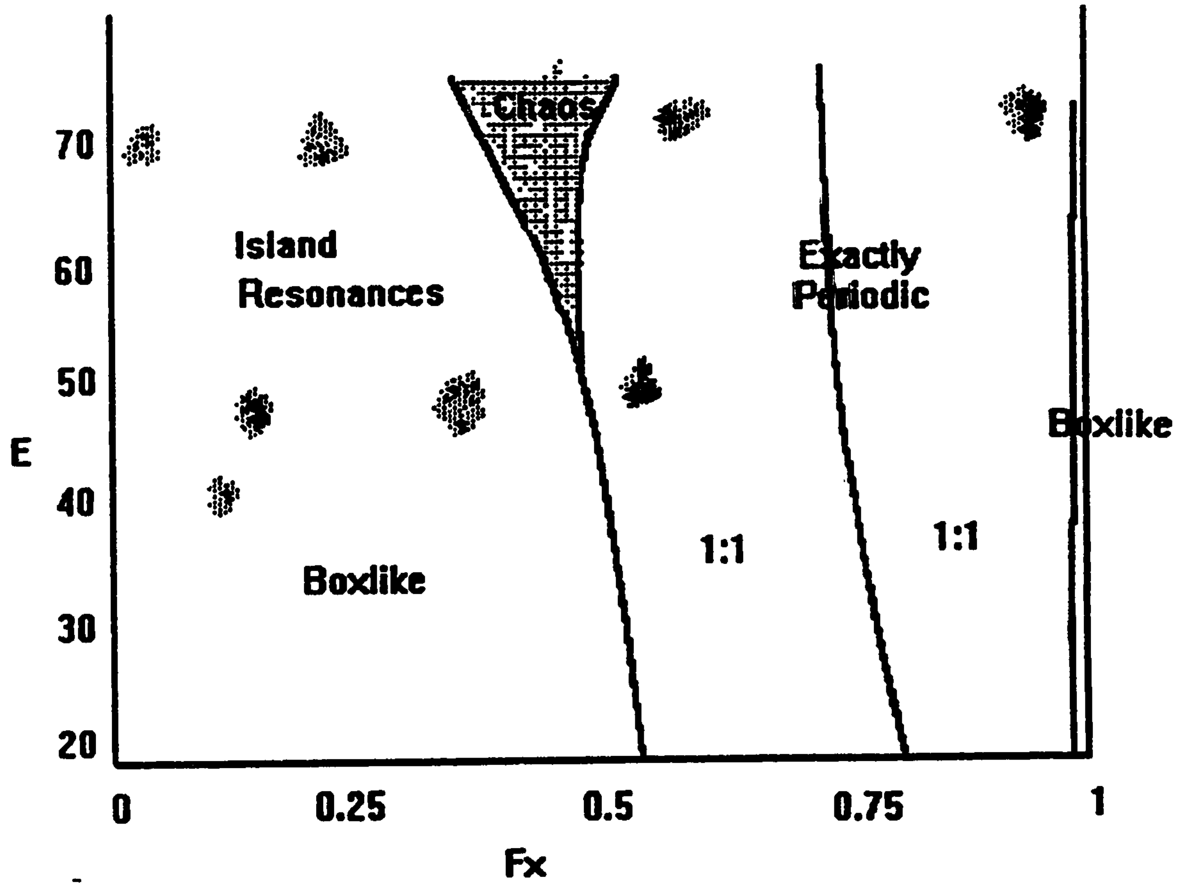

Figure 4.12: A depiction of global behavious as a function of energy and initial conditions f_x at $R = 4.30$ a.u. Regions of boxlike and 1:1 resonant regular motions are indicated as well as chaotic domains and points of higher order periodic resonances.

namics studied in this chapter.

Chapter 5

Canonical Perturbation Theory

5.1 Introduction

The Classical Self-Consistent Field (CSCF) approximation was introduced in Chapter 3 where it was used to obtain semiclassical approximations to quantum SCF energy levels. The total Hamiltonian of a system is replaced by an approximation which is *exactly separable* in the chosen coordinates $\{q_i\}$. The actions $\{J_i\}$, one associated with each degree of freedom, are the constants of the motion for the system and are defined by

$$J_i \equiv \frac{1}{2\pi} \oint p_i dq_i, \qquad (i = 1, 2). \tag{5.1}$$

The conjugate momentum p_i is defined as a function of q_i in the classical SCF equation for that degree of freedom. The actions $\{J_i\}$ determine the energy parameters E_i associated with the classical SCF equations through equation [5.1] and, therefore, the resulting SCF Hamiltonian depends functionally on the actions.

From the perspective of the classical dynamics presented in Chapter 4, the classical SCF method defines a class of *regular* motions for the systems approximated. Because the separated Hamiltonians are derived from the true Hamiltonian by the SCF averaging procedure, the constants of the motion are linked in a one-to-one fashion with a specific set of coordinates. Although there is no formal proof that a solution to the CSCF problem always exists or that it is unique, the broad range of experience shows that it is as "robust" as the quantum SCF approximation with respect to existence, uniqueness and stability. It appears that the CSCF approximation defines a *continuous* (or piecewise continuous) set of invariant toroids for the phase space. Associated quasiperiodic motions for the system are obtained as a function of the defining actions. It remains to determine how these are related to the true classical motion of the system.

It was found in Chapter 2 that lower quantum states of this system are extremely well approximated by their quantum SCF counterparts. Furthermore, in Chapter 3 it was shown that, except for the errors inherent in the one-dimensional JWKB approximation, semi-classical quantization of the classical SCF approximation gave a reasonable account of the corresponding quantum SCF behaviour. Hence, it is at least plausible that a close approximation to the true *classical* dynamics of the system may be provided by the classical SCF approximation in cases where (J_x, J_z) appear to be appropriate labels for the constants of regular motion. As illustrated in Chapter 4, the class of regular motions characterized by box or butterfly trajectories occurred in a situation where the actions *are* legitimately labelled (J_x, J_z). We shall show that this type of motion is indeed described well by the classical SCF approximation.

If the Hamiltonian for the system is represented as the sum of the separable Classical SCF (CSCF) Hamiltonian plus a "small" perturbation, classical canonical perturbation theory may be used to compute the influence of the perturbation on the motion and the energy of the system. Since the action-angle variables generated by the CSCF approximation are necessarily canonical, they provide a starting point for a succession of canonical transformations to the *true* action-angle variables at least in those cases where the zero-order CSCF description is "close" to the corresponding true motion. The sequence of successively higher order corrections to the energy and trajectory of the system is analogous to successive perturbative corrections to the energy and wave function of a nondegenerate quantum mechanical stationary state [17]. The first-order correction to the motion and second-order correction to the energy are not hard to carry out on the classical SCF motion for this system; these perturbative calculations are compared with the true motion and energies and, as expected, the comparison is extremely close in favourable cases.

Perhaps more intriguing is that we also find that even when the canonically perturbed SCF results do *not* closely simulate the true classical motion, relevant features of the system dynamics are retained. In particular, in cases where the classical motion is disrupted by *weak* periodic resonances, the first-order perturbed CSCF motion retains a motion associated with the original invariant toroid while suppressing the effects of such weak disturbances. In addition, at the bifurcation associated with the strong reorganization of motion about the periodic resonant trajectory moving in the direction of a potential valley at 26° to the x-axis in this system, the first-order perturbed CSCF trajectory clearly "signals" the bifurcation in certain ways even though it continues to describe motion related to the original toroid. These and other aspects of the comparison between perturbed SCF motion and the true classical dynamics are presented here.

The canonical time-independent pertubation theory is developed in Section 5.2 using the CSCF approximation as the zero-order description of the system; the presentation is essentially parallel to the general development given by Goldstein [21] (Sections 11.4–11.5). Following in Section 5.3 is a general comparison of perturbed CSCF with classical dynamics. Broader questions raised by these results and other aspects of this work are discussed later in Chapter 6.

5.2 Perturbation Calculations

Time-independent canonical perturbation theory in classical mechanics is designed to treat the case of stable regular motion in a conservative system whose Hamiltonian has the form

$$H(\{q_i, p_i\}) = H_0(\{q_i, p_i\}) + \epsilon H_c(\{q_i, p_i\}) + \dots, \tag{5.2}$$

where the motion for a system with the Hamiltonian H_0 alone is fully integrable and the perturbation term H_c is in some relevant sense small. Normally, as is the case here, the zero-order problem is exactly separable; the theory assumes the *perturbed* motion remains regular. In particular, a one-to-one correspondence is assumed between the action-angle variables describing the zero-order motion and the true action-angle variables describing the actual regular motion. The analogous situation in quantum mechanics is the application of time-independent perturbation theory to a nondegenerate stationary state.

In the present case, the unperturbed Hamiltonian H_0 is the SCF Hamiltonian and the perturbation term H_c is the difference between the true potential and that generated by the SCF calculation. All higher-order terms in ϵ are zero. However, ϵ is retained as a formal parameter which permits the assignment of first, second, etc. orders of perturbative correction; it is set equal to unity at the end.

Although essentially all applications made in this work are in the context of an SCF approximation in the original coordinates (x, z), for convenience we will formally designate coordinates as $\{q_i\}, i = 1, 2$, with conjugate momenta $\{p_i\}$. In this notation, the SCF Hamiltonian is given by

$$H_0 \equiv H^{SCF} = H_1(q_1, p_1) + H_2(q_2, p_2) - \langle\langle V \rangle\rangle. \tag{5.3}$$

The separate terms H_i for each degree of freedom (see Equations 3.5–3.7) are defined

$$H_i = p_i^2 + V_i^{SCF}(q_i) = E_i, \tag{5.4}$$

with the SCF effective potentials given by the averages of the true potential over the ignored degree of freedom:

$$\begin{aligned} V_1^{SCF}(q_1) \equiv \langle V(q_1,p_1)\rangle_{q_2} &= \frac{1}{T_2}\oint \frac{V(q_1,q_2)}{\dot{q}_2}dq_2, \\ V_2^{SCF}(q_2) \equiv \langle V(q_2,p_2)\rangle_{q_1} &= \frac{1}{T_1}\oint \frac{V(q_1,q_2)}{\dot{q}_1}dq_1, \qquad (5.5) \\ T_i &\equiv \oint \frac{dq_i}{\dot{q}_i}. \qquad (5.6) \end{aligned}$$

The integrals in each case are taken over a period of the SCF motion in the designated coordinate. The last term in [5.3] is the double average

$$\langle\langle V\rangle\rangle = \langle V_1^{SCF}(q_1)\rangle_{q_1} = \langle V_2^{SCF}(q_2)\rangle_{q_2}. \tag{5.7}$$

It follows that the perturbation or "correction potential" is given by

$$H_c \equiv V(q_1,q_2) - V_1^{SCF}(q_1) - V_2^{SCF}(q_2) + \langle\langle V\rangle\rangle, \tag{5.8}$$

and it is evident that its average value over the SCF motion is zero,

$$\langle\langle H_c\rangle\rangle \equiv 0; \tag{5.9}$$

a result which always holds for SCF approximations.

The action-angle variables $\{J_{0i},\theta_{0i}\}$ describe the zero-order SCF motion with the frequencies

$$\omega_{0i} = \frac{\partial H_c}{\partial J_{0i}}. \tag{5.10}$$

In the SCF system, the actions $\{J_{0i}\}$ are constants of the motion and the angles $\{\theta_{0i}\}$ simply increase linearly with time. Under the true Hamiltonian, however, neither condition is true although $\{J_{0i}, \theta_{0i}\}$ still form a canonical set of momenta and coordinates for the unperturbed system. Since the perturbed motion is regular, there is a *new* set of action-angle variables $\{J_i, \theta_i\}$ such that $\{J_i\}$ are constants of the motion and $\{\theta_i\}$ are cyclic coordinates. The problem is to find a canonical transformation from the old set $\{J_{0i}, \theta_{0i}\}$ to the required new set $\{J_i, \theta_i\}$. To do this, we employ the apparatus of Hamilton-Jacobi theory as outlined by Goldstein [21].

For any conservative system described by canonical variables (q_i, p_i), the problem posed by Hamilton-Jacobi theory is to find a function $W(\{q_i, p_i\})$, called *Hamilton's principal function*, which is the *generating function* of the canonical transformation to the desired set of canonical coordinates $\{Q_i, P_i\}$. If the new momenta are all constants of the motion and the new coordinates are all cyclic, then the Hamiltonian expressed in the new variables is a function only of the momenta,

$$\dot{P}_i = -\frac{\partial H}{\partial Q_i} = 0, \tag{5.11}$$

and the new coordinates simply increase linearly with time,

$$\begin{aligned} \dot{Q}_i &= \frac{\partial H}{\partial P_i} = \omega_i, \\ Q_i &= \omega_i t + constant. \end{aligned} \tag{5.12}$$

For such a transformation, the equations relating the old and new variables are

$$\begin{aligned} p_i &= \frac{\partial W}{\partial q_i}, \\ Q_i &= \frac{\partial W}{\partial P_i} = w_i t + \beta_i. \end{aligned} \tag{5.13}$$

and the generating function $W(\{q_i, p_i\})$ satisfies the time-independent Hamilton-Jacobi partial differential equation,

$$H\left(\left\{q_i, \left(\frac{\partial W}{\partial q_i}\right)\right\}\right) = E_{total}. \tag{5.14}$$

We will now apply this formalism to the two-dimensional case considered here.

In the old SCF variables, the true Hamiltonian has the form

$$H(\vec{J}_0, \vec{\theta}_0, \epsilon) = H_0(\vec{J}_0) + \epsilon H_c(\vec{J}_0, \vec{\theta}_0), \tag{5.15}$$

where $\vec{J}_0, \vec{\theta}_0$ are $N(=2)$ vectors whose components are the zero-order actions and angles, respectively. When expressed in terms of the new variables, the Hamiltonian depends only on the new momenta,

$$H = \alpha(\vec{J}, \epsilon) = \alpha_0(\vec{J}) + \epsilon\alpha_1(\vec{J}) + \epsilon^2\alpha_2(\vec{J}) + \ldots, \tag{5.16}$$

and the new frequencies are

$$\omega_i = \frac{\partial\alpha}{\partial J_i}. \tag{5.17}$$

The Hamilton's principal function for this perturbative transformation has the form

$$Y(\vec{J}, \vec{\theta}_0, \epsilon) = \vec{\theta}_0 \cdot \vec{J} + \epsilon Y_1(\vec{J}, \vec{\theta}_0) + \epsilon^2 Y_2(\vec{J}, \vec{\theta}_0) + \ldots; \tag{5.18}$$

the leading term

$$\vec{\theta}_0 \cdot \vec{J} = \sum_i \theta_{0i} J_i, \tag{5.19}$$

corresponds simply to the *identity transformation* and reflects the fact that as $\epsilon \rightarrow 0$ and the Hamiltonian reduces to the zero-order term H_0, the action-angle variables reduce to the old SCF action-angle variables.

The function Y is determined by solving the Hamilton-Jacobi equation

$$H(\vec{\theta}_0, \frac{\partial Y}{\partial \vec{\theta}_0}, \epsilon) = \alpha(\vec{J}, \epsilon). \tag{5.20}$$

This is accomplished by expanding both sides of this equation in powers of ϵ using equations [5.15] for H and [5.16] for α. Coefficients in each power of ϵ are equated to obtain expressions in successively higher order; the results are given in detail here for second-order corrections only. From the transformation equations [5.13], the old momenta can be written as

$$J_{0i} = \frac{\partial Y}{\partial \theta_{0i}} = J_i + \epsilon \frac{\partial Y_1}{\partial \theta_{0i}} + \epsilon^2 \frac{\partial Y_2}{\partial \theta_{0i}} + \ldots; \tag{5.21}$$

this can be used to expand both H_0 and H_c in a Taylor series about $\vec{J}_0 = \vec{J}$. In a compact notation and to second order only, these expansions are written:

$$\begin{aligned} H_0\left(\frac{\partial Y}{\partial \vec{\theta}_0}\right) &= H_0(\vec{J}) + \frac{\partial H_0}{\partial \vec{J}} \left[\epsilon \frac{\partial Y_1}{\partial \vec{\theta}_0} + \epsilon^2 \frac{\partial Y_2}{\partial \vec{\theta}_0}\right] \\ &+ \frac{1}{2}\left(\epsilon \frac{\partial Y_1}{\partial \vec{\theta}_0}\right) \cdot \frac{\partial^2 H_0}{\partial \vec{J} \partial \vec{J}} \cdot \left(\epsilon \frac{\partial Y_1}{\partial \vec{\theta}_0}\right), \qquad (5.22) \\ H_c\left(\vec{\theta}_0, \frac{\partial Y}{\partial \vec{\theta}_0}\right) &= H_c(\vec{\theta}_0, \vec{J}) + \epsilon \frac{\partial Y_1}{\partial \vec{\theta}_0} \cdot \frac{\partial H_c}{\partial \vec{J}}. \qquad (5.23) \end{aligned}$$

These forms are substituted into equation [5.15] and with [5.16] both are inserted into the Hamilton-Jacobi equation [5.20]. Equating terms with equal powers of ϵ, the following sequence of perturbation equations is obtained:

$$\begin{aligned} \alpha_0 &= H_0(\vec{J}), \qquad (5.24) \\ \alpha_1 &= \vec{\omega}_0 \cdot \frac{\partial Y_1}{\partial \vec{\theta}_0} + H_c(\vec{\theta}_0, \vec{J}), \qquad (5.25) \\ \alpha_2 &= \vec{\omega}_0 \cdot \frac{\partial Y_2}{\partial \vec{\theta}_0} + \Phi_2(\vec{\theta}_0, \vec{J}), \qquad (5.26) \end{aligned}$$

where

$$\Phi_2 = \frac{\partial Y_1}{\partial \vec{\theta}_0} \cdot \frac{\partial H_c}{\partial \vec{J}} + \frac{1}{2} \frac{\partial Y_1}{\partial \vec{\theta}_0} \cdot \frac{\partial^2 H_0}{\partial \vec{J} \partial \vec{J}} \cdot \frac{\partial Y_1}{\partial \vec{\theta}_0}. \tag{5.27}$$

The equations can be solved in succession to yield the first-order perturbation energy α_1, then the generating function Y_1 and next the second-order energy α_2. This is the limit of the present calculations.

The transformation equations [5.13] define the new coordinates by

$$\theta_i = \frac{\partial Y}{\partial J_i} = \theta_{0i} + \epsilon \frac{\partial Y_1}{\partial J_i} + \epsilon^2 \frac{\partial Y_2}{\partial J_i} + \ldots. \tag{5.28}$$

Since both θ_i and θ_{0i} must pass through 2π whenever the motion passes through a complete period of motion T_i, it follows that the generating functions (Y_1, Y_2,etc.) must themselves be quasiperiodic function of the angle variables $\{\theta_{0i}\}$. In particular, they cannot contain any terms which are independent of $\{\theta_{0i}\}$; that is, Y_1 must have the form

$$Y_1(\vec{\theta}_0, \vec{J}) = \sum_{\vec{k}} B_{\vec{k}}(\vec{J}) \exp(i\vec{k} \cdot \vec{\theta}_0), \tag{5.29}$$

where the coefficient for $(k_1, k_2) = (0, 0)$ vanishes.

It can be shown from equation [5.25] that the first-order perturbation energy α_1 vanishes. The terms to the right contain quasiperiodic terms arising from both components but, since no term in [5.29] can appear with $\vec{k} = (0, 0)$, any constant terms can arise only from H_c. It therefore follows that

$$\alpha_1(\vec{J}) = \overline{H_1}(\vec{\theta}_0, \vec{J}), \tag{5.30}$$

where the average is over a full period in both angles. From equation [5.9], this average is known to vanish also; hence, $\alpha = 0$.

Equation [5.25] can now be solved for Y_1. Let the correlation potential H_c be expanded in Fourier series,

$$H_c(\vec{\theta}_0, \vec{J}) = \sum_{\vec{k}} C_{\vec{k}}(\vec{J}) \exp(i\vec{k} \cdot \vec{\theta}_0). \tag{5.31}$$

Using [5.29] to compute the partial derivative term, substitution into [5.25] reveals that

$$B_{\vec{k}}(\vec{J}) = i\frac{C_{\vec{k}}(\vec{J})}{\vec{k} \cdot \vec{\omega}_0}. \tag{5.32}$$

The form of the correction potential [5.8] places restrictions on the coefficients $C_{\vec{k}}(\vec{J})$ and, hence, on the generating function Y_1. It has already been shown that there are no terms with $\vec{k} = (0, 0)$. In addition, there can be no terms with $\vec{k} = (k_1, 0)$ or $(0, k_2)$

since these are precisely the terms retained from the true potential $V(q_1, q_2)$ by the two effective SCF potentials.

Similarly, since no constant terms in [5.26] can arise from the partial derivative, the second-order perturbation energy is found to be

$$\alpha_2 = \overline{\Phi}_2^a + \overline{\Phi}_2^b, \tag{5.33}$$

where

$$\begin{aligned} \overline{\Phi}_2^a &= -2\sum_{\vec{k}} \frac{C_{\vec{k}}}{(\vec{k}\cdot\vec{\omega}_0)} \left[k_x \frac{\partial C_{\vec{k}}}{\partial J_x} + k_z \frac{\partial C_{\vec{k}}}{\partial J_z}\right], &(5.34)\\ \overline{\Phi}_2^b &= \frac{1}{2}\sum_{\vec{k}} \frac{C_{\vec{k}}^2}{(\vec{k}\cdot\vec{\omega}_0)^2} \left[k_x^2 \frac{\partial \omega_{x0}}{\partial J_x} + k_z^2 \frac{\partial \omega_{z0}}{\partial J_z} + 2k_x k_z \frac{\partial \omega_{x0}}{\partial J_z}\right]. &(5.35)\end{aligned}$$

The computation of the perturbed trajectory is not trivial and is described briefly here. All of the information needed to compute the correction to the trajectory is contained in the first-order generating function Y_1. In the zero-order approximation, the working coordinates and momenta are

$$\begin{aligned} q_i &= \sum_l Q_{il}(\vec{J}_0) \exp\left[il\theta_{0i}\right], &(5.36)\\ p_i &= \sum_l P_{il}(\vec{J}_0) \exp\left[il\theta_{0i}\right]. &(5.37)\end{aligned}$$

Using equation [5.28], the Fourier coefficients can be expanded in Taylor series about $\vec{J}_0 = \vec{J}$,

$$Q_{il}(\vec{J}_0) \approx Q_{il}(\vec{J}) + \frac{\partial Q_{il}}{\partial J_1}\frac{\partial Y_1}{\partial \theta_1} + \frac{\partial Q_{il}}{\partial J_2}\frac{\partial Y_1}{\partial \theta_2}. \tag{5.38}$$

Substituting [5.32] into equation [5.29] yields the explicit result

$$Q_{il}(\vec{J}_0) \approx Q_{il}(\vec{J}) - \sum_{\vec{k}} \frac{C_{\vec{k}}}{\vec{k}\cdot\vec{\omega}_0} \left[k_1 \frac{\partial Q_{kl}}{\partial J_1} + k_2 \frac{\partial Q_{kl}}{\partial J_2}\right] e^{i\vec{k}\cdot\vec{\theta}}, \tag{5.39}$$

and a similar expression is obtained for $P_{il}(\vec{J}_0)$.

Using equation [5.21] in [5.36], the oscillatory factors can be expressed as

$$\begin{aligned}\exp\left[il\theta_{0i}\right] &\approx \exp\left[il\theta_i\right]\left[1 - il\epsilon\frac{\partial Y_1}{\partial J_i} + O(\epsilon^2)\right] \\ &\approx \exp\left[il\theta_i\right]\left[1 + \sum_{\vec{k}} l\left[\frac{\partial C_{\vec{k}}/\partial J_i}{\vec{k}\cdot\vec{\omega}_0} - C_{\vec{k}}\frac{\vec{k}\cdot(\partial\vec{\omega}_0/\partial J_i)}{(\vec{k}\cdot\vec{\omega}_0)^2}\right] e^{i\vec{k}\cdot\vec{\theta}}\right]. \quad (5.40)\end{aligned}$$

When [5.39] and [5.40] are substituted into [5.36] and the terms are regrouped, the perturbed Fourier expansion becomes

$$q_i = \sum_{k} Q_{i\vec{k}}(\vec{J})\exp\left[i\vec{k}\cdot\theta_{0i}\right], \quad (5.41)$$

with an analogous expression for p_i. These may be compared with the expansions obtained by Fourier analysis of the true trajectory for the same set of actions (compare with equation [4.11]).

The C_{2v} symmetry of the potential surface guarantees that there are certain restricting symmetries in the Fourier expansion for H_c; in particular, the indices (k_1, k_2) in [5.31] are both *even*. It then necessarily follows that the expansions of the form [5.41] for q_1 and p_1 have $k_1 = odd$, $k_2 = even$, while the parities are reversed for q_2 and p_2. This restriction leads to an important property of the perturbed SCF trajectories when projected on the coordinate plane; namely, these trajectories *always* possess C_{2v} symmetry and can never show the asymmetry characterizing the true trajectories when the motion is reorganized into the family of quasiperiodic trajectories associated with one or the other of the potential surface valleys.

Numerically, the calculation of the second-order perturbation energy [5.33] and first-order perturbed trajectory [5.41] requires first the calculation of the CSCF solution at a particular set of actions (J_1, J_2). This must include frequencies ω_{0i} and the Fourier expansion coefficients for both H_c and the dynamical variables (q_i, p_i). In addition the partial derivatives with respect to the actions are needed for all these quantities. Centered on the point (J_1, J_2), a "cross" of CSCF calculations was performed at 17 neighbouring points $(J_1 + m\delta, J_2)$, $(J_1, J_2 + m\delta), m = \pm 1 \ldots \pm 4$; the spacing δ was normally taken to be 0.01 or 0.005. A high-order interpolation formula was then used to compute the partial derivatives from the 9 data points in each direction. We were able to show that the resulting partial derivatives are accurate to a relative error of about $1\text{x}10^{-7}$ or better in essentially every case. Since much of the time required for a CSCF calculation is spent on iterating approximate input guesses to convergence, the ability to forecast very good estimates from the data already obtained for nearby points on the cross results in faster overall computational speed for these calculations than might otherwise be expected.

5.3 Classical Perturbation Results

We first compare zero-order and perturbed Classical SCF motions with the corresponding true classical motion for representative "boxlike" trajectories where the actions (J_x, J_z) exist as constants of the motion. Figure 5.1 presents (x, z) plane trajectory projections and Poincaré surfaces-of-section computed using perturbed CSCF theory for six states of motion at $R = 4.30$ a.u. and $E = 24.0$ c.e.u. Actions characterizing each state were determined from analysis of the true dynamics for values of the parameter $f_x = 0.15$ to 0.55 at intervals of 0.05; for this energy and R-value, the bifurcation occurs at $f_x \approx 0.568$. These figures can be compared with the corresponding true trajectories shown in the sequence in Figure 4.5 and the composite Poincaré surface-of-section curves of Figure 4.6; they resemble each other very closely. The zero-order CSCF trajectory projections (not shown) are, of course, simple rectangular boxes in all cases since the x and z motions are completely independent. By contrast, the first-order corrected description is a strikingly accurate visual reproduction of the true motion–even in the case of the rather strongly deformed trajectory with $f_x = 0.55$ which lies quite close to the bifurcation. First-order perturbation theory is able to reproduce caustic and Poincaré surface-of-section curves accurately despite the fact that SCF frequencies are not exactly the classical ones.

Figure 5.1: Classical perturbation trajectories and accompanying Poincaré surfaces-of-section at $R = 4.30$ a.u. and $E = 24.0$ c.e.u. for pairs of actions in the boxlike quasiperiodic regime. Trajectories are provided near the classical f_x values of 0.05 to 0.55 in steps of 0.05.

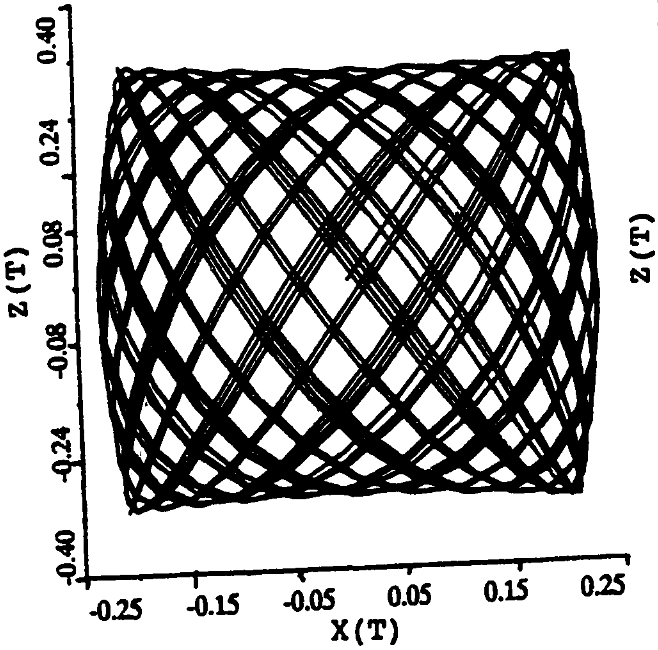

PERTURBED TRAJECTORY

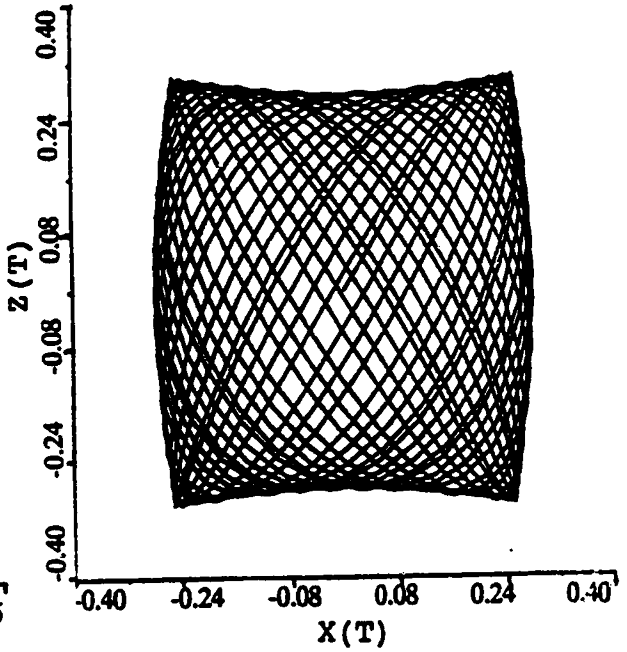

PERTURBED TRAJECTORY

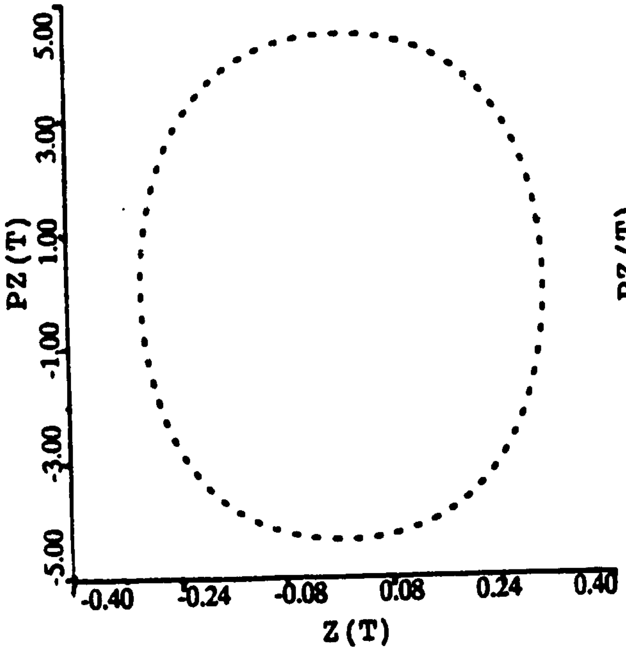

POINCARE AT X=0

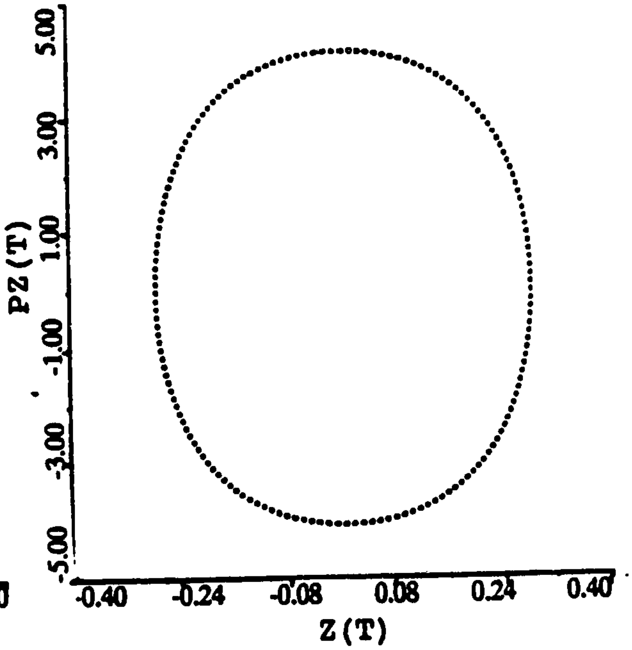

POINCARE AT X=0

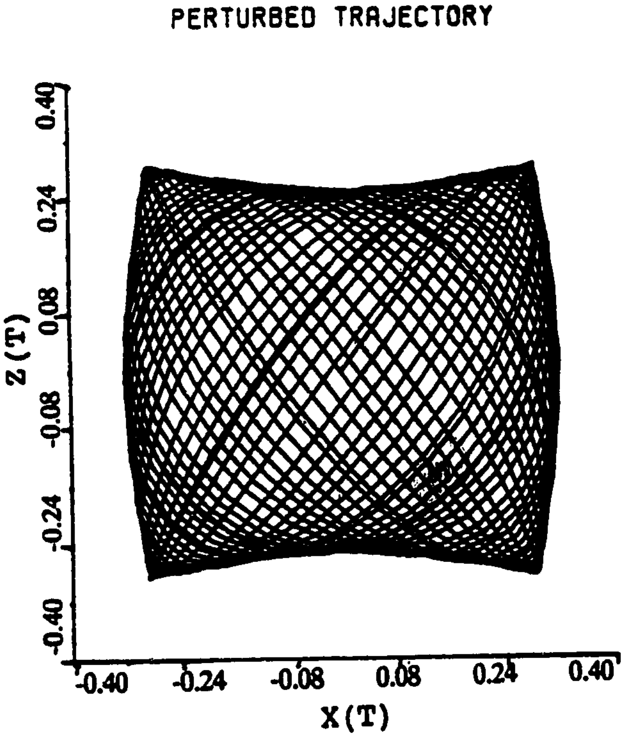
PERTURBED TRAJECTORY
Z(T)
0.40
0.24
0.08
-0.08
-0.24
-0.40
-0.40
-0.24
-0.08
0.08
0.24
0.40
X(T)

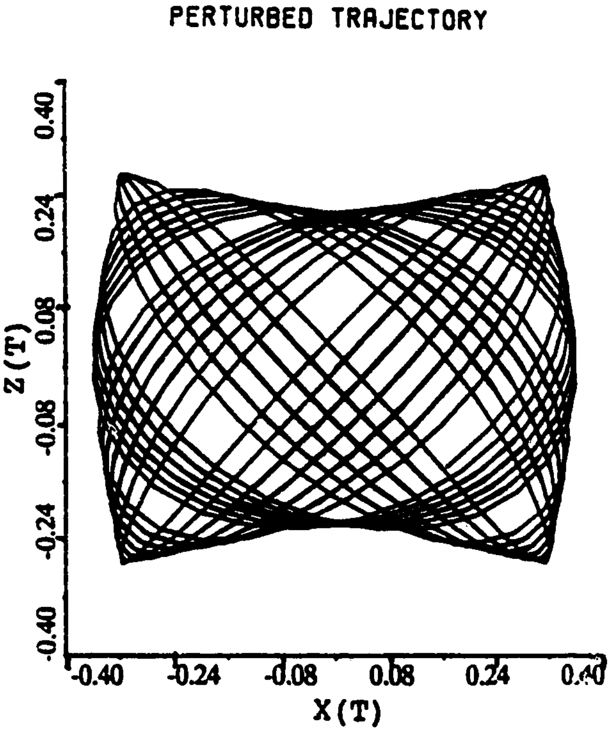
PERTURBED TRAJECTORY
Z(T)
0.40
0.24
0.08
-0.08
-0.24
-0.40
-0.40
-0.24
-0.08
0.08
0.24
0.40
X(T)

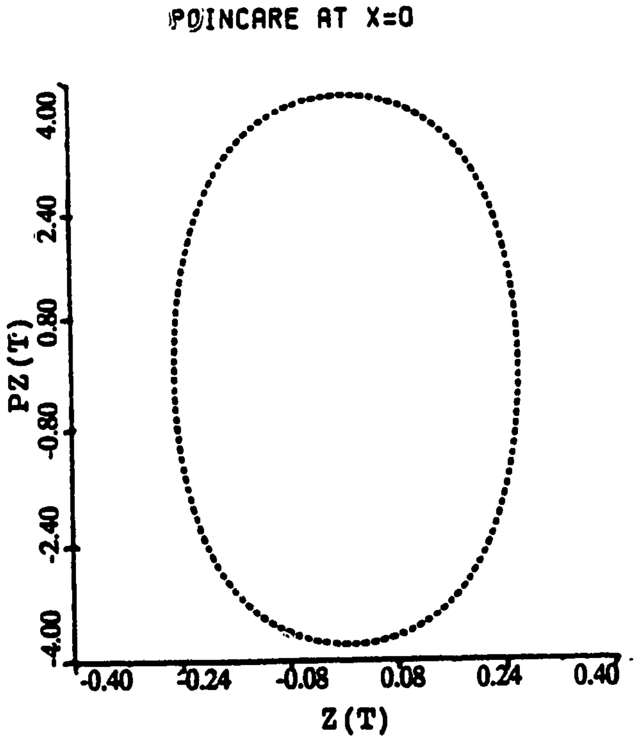
POINCARE AT X=0
PZ(T)
4.00
2.40
0.80
-0.80
-2.40
-4.00
-0.40
-0.24
-0.08
0.08
0.24
0.40
Z(T)

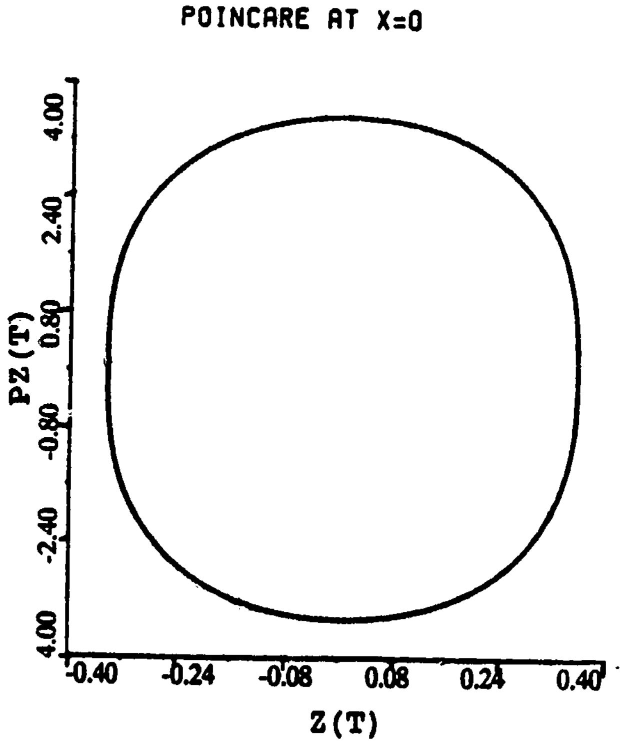
POINCARE AT X=0
PZ(T)
4.00
2.40
0.80
-0.80
-2.40
-4.00
-0.40
-0.24
-0.08
0.08
0.24
0.40
Z(T)

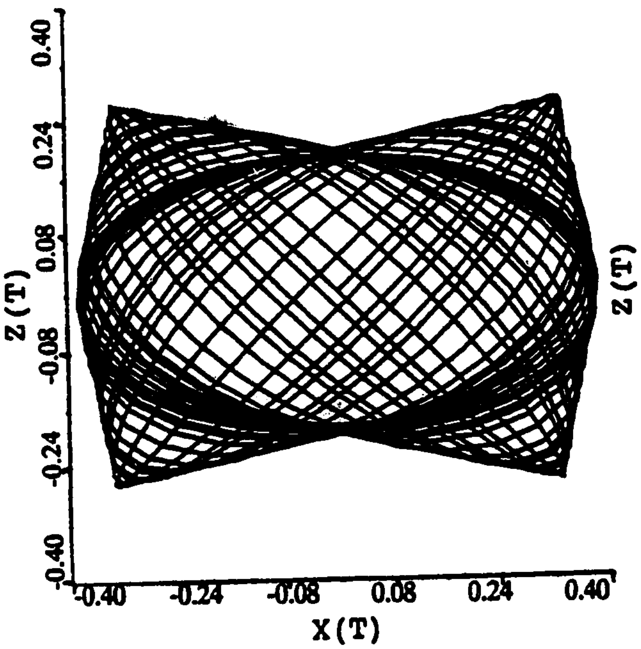

PERTURBED TRAJECTORY

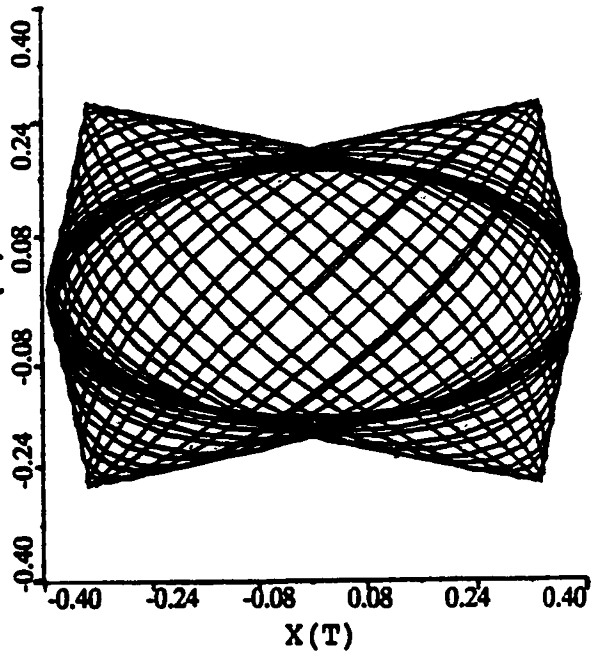

PERTURBED TRAJECTORY

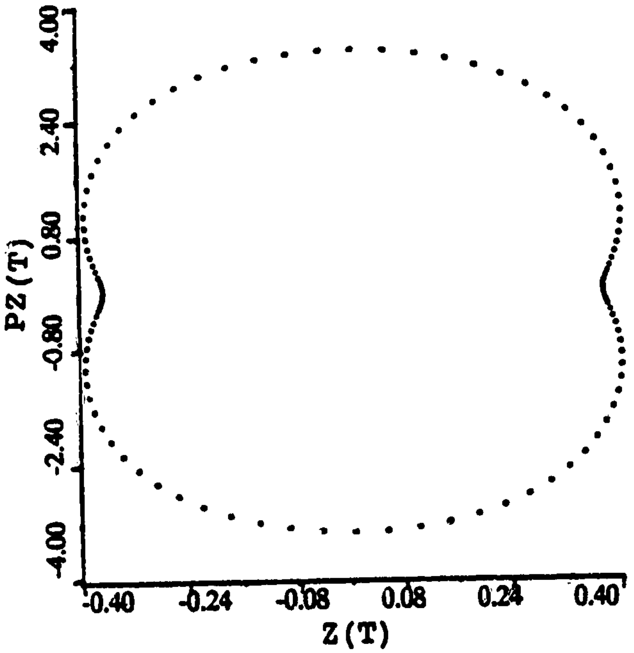

POINCARE AT X=0

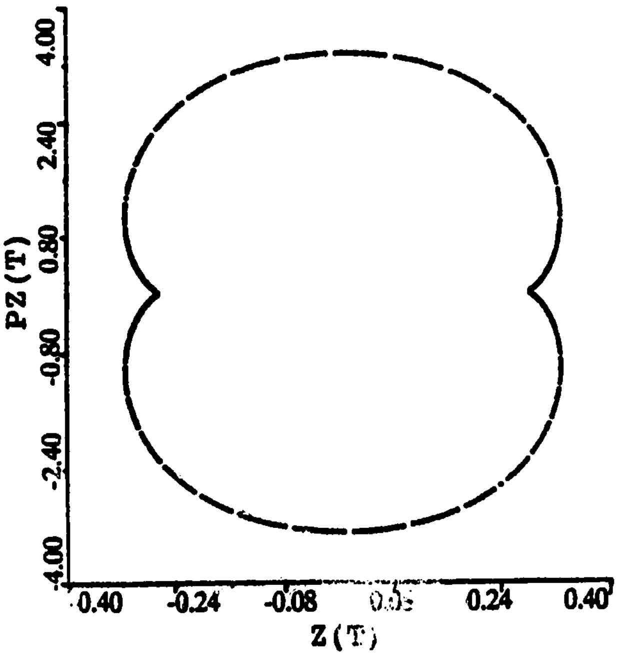

POINCARE AT X=0

Further demonstration of the accuracy of the perturbed SCF description in these cases is presented in Table 5.1. Zero-order and perturbed CSCF energies and zero-order frequencies are compared with the corresponding true values for $R =$ 4.30 a.u. and actions (J_x, J_z) determined from classical dynamics for states with $E = 24.0$, 46.0 or 56.0 c.e.u. and representative f_x values in the boxlike domain. Second-order perturbation corrections to the energy are less than 0.05 c.e.u.even for cases quite close to the bifurcation and the resulting perturbed SCF energies agree with the true classical energies to within 0.002 c.e.u. in all cases. The CSCF zero-order frequencies, which are not corrected by the perturbation calculation, approximate the actual frequencies with relative errors of 5% or less. As a final, more quantitative comparison, Fourier series coefficients for the dynamical variables (x, z) are listed in Tables 5.2 and 5.3 for two cases at $E = 24.0$ c.e.u.; one is a motion only slightly perturbed from the CSCF box ($f_x = 0.30$) and the other is strongly distorted ($f_x =$ 0.55).

The striking similarity between perturbed SCF and true classical motions is evidence that the choice of a CSCF zero-order Hamiltonian using coordinates (x, z) is appropriate in the boxlike regime where the actions (J_x, J_z) are constants of the motion; the low-order perturbed CSCF description provides a remarkably accurate representation of the motion both qualitatively and quantitatively. This is true in spite of the fact that the frequencies of SCF motion are the uncorrected zero-order values. The perturbed SCF trajectory is traced out on a different time scale from the true one but closely agrees with its phase space characteristics. The SCF perturbation results show little or no indication of the strong reorganization which occurs in the classical motion at the bifurcation point; no divergence is observed since the CSCF frequencies are still far from their 1:1 resonance.

Previously, the classical SCF approximation was described as "torus-preserving"

f_x	J_x	J_z	E^{SCF}	E^{PT}
0.100	0.12731871	0.76433971	23.993479	23.999919
0.150	0.19083687	0.72170051	23.991291	23.999841
0.200	0.25374782	0.67841472	23.989753	23.999758
0.250	0.31644345	0.63416522	23.988780	23.999685
0.300	0.37899588	0.58883129	23.988277	23.999634
0.350	0.44196935	0.54190037	23.988108	23.999622
0.400	0.50490088	0.49358834	23.988049	23.999677
0.450	0.56918467	0.44262476	23.987635	23.999852
0.500	0.63594738	0.38773523	23.985611	24.000281
0.550	0.71053221	0.32352223	23.975929	24.001123
0.555	0.71925321	0.31575699	23.973347	24.001107
0.560	0.72854521	0.30740146	23.969787	24.000870
0.565	0.73893789	0.29791490	23.963831	23.999569
0.567	0.74378646	0.29336818	23.958607	23.996968

f_x	ω_x^{CT}	ω_z^{CT}	ω_x^{SCF}	ω_z^{SCF}
0.100	20.82650	31.40260	20.780167	31.393197
0.150	20.98973	30.88712	20.950656	30.873650
0.200	21.15193	30.35825	21.119667	30.340675
0.250	21.31417	29.80917	21.288638	29.788723
0.300	21.48019	29.23744	21.458195	29.214258
0.350	21.64891	28.63238	21.630389	28.608135
0.400	21.82357	27.99227	21.804585	27.969786
0.450	22.01201	27.29374	21.985518	27.277646
0.500	22.22440	26.49714	22.177807	26.506506
0.550	22.53745	25.41695	22.400295	25.563552
0.555	22.58920	25.25276	22.427060	25.446142
0.560	22.65938	25.05109	22.455824	25.318956
0.565	22.76801	24.75309	22.488415	25.173560
0.567	22.60542	24.51361	22.503963	25.103685

Table 5.1: Classical SCF-PT energies and frequencies are presented at a series of f_x values corresponding to boxlike quasiperiodic trajectories. The actions were determined from true classical trajectories at the given low f_x initial conditions for $E_{CT} = 24.0$ and $R = 4.3$. For comparision, the frequencies from the actual trajectories and the CSCF analysis are provided.

X – Oscillator			Z – Oscillator		
X	Z	2D – Coefficients	X	Z	2D – Coefficients
1	0	$1.42941538 \times 10^{-1}$	0	1	$1.374015553 \times 10^{-1}$
3	0	$-2.39030893 \times 10^{-4}$	0	3	$-2.643922012 \times 10^{-3}$
5	0	$-4.62405886 \times 10^{-7}$	0	5	$5.563901748 \times 10^{-5}$
7	0	$1.49506128 \times 10^{-9}$	0	7	$-1.272784102 \times 10^{-6}$
1	2	$-1.02851702 \times 10^{-3}$	0	9	$3.097056777 \times 10^{-8}$
1	4	$5.76206699 \times 10^{-5}$	0	11	$-7.915756427 \times 10^{-10}$
1	6	$-2.65842529 \times 10^{-6}$	2	1	$-9.847780279 \times 10^{-4}$
1	8	$1.10994155 \times 10^{-7}$	4	1	$-2.381430636 \times 10^{-6}$
1	10	$-4.33447099 \times 10^{-9}$	6	1	$1.308204921 \times 10^{-8}$
1	−2	$9.77101497 \times 10^{-3}$	−2	1	$-2.860792504 \times 10^{-3}$
1	−4	$-1.06492492 \times 10^{-4}$	−4	1	$2.008921795 \times 10^{-5}$
1	−6	$2.82954995 \times 10^{-6}$	−6	1	$-3.878721873 \times 10^{-8}$
1	−8	$-8.39513287 \times 10^{-8}$	2	3	$4.842136713 \times 10^{-5}$
1	10	$2.55616248 \times 10^{-9}$	4	3	$4.193133196 \times 10^{-7}$
3	2	$7.52419946 \times 10^{-6}$	6	3	$4.112042012 \times 10^{-9}$
3	4	$6.35054170 \times 10^{-7}$	−2	3	$2.798900617 \times 10^{-3}$
3	6	$-5.30632949 \times 10^{-8}$	−4	3	$7.269305747 \times 10^{-6}$
3	8	$2.85440018 \times 10^{-9}$	−6	3	$2.491193824 \times 10^{-9}$
3	−2	$1.23917811 \times 10^{-3}$	2	5	$-1.972076142 \times 10^{-6}$
3	−4	$-1.73199453 \times 10^{-5}$	4	5	$-4.141888341 \times 10^{-8}$
3	−6	$6.00626462 \times 10^{-7}$	−2	5	$-1.208277162 \times 10^{-4}$
3	−8	$-2.32386613 \times 10^{-8}$	−4	5	$-1.122292420 \times 10^{-6}$
5	2	$-4.92980587 \times 10^{-7}$	−6	5	$1.302276675 \times 10^{-8}$
5	4	$3.83878935 \times 10^{-8}$	2	7	$8.646563481 \times 10^{-8}$
5	6	$-2.00773057 \times 10^{-9}$	4	7	$2.545003404 \times 10^{-9}$
5	−2	$-1.12899896 \times 10^{-5}$	−2	7	$3.766557103 \times 10^{-6}$
5	−4	$-1.56797996 \times 10^{-7}$	−4	7	$4.421435488 \times 10^{-8}$
5	−6	$-3.02115483 \times 10^{-9}$	2	9	$-3.800108136 \times 10^{-9}$
7	2	$-2.11895980 \times 10^{-9}$	−2	9	$-1.087071577 \times 10^{-7}$
7	−2	$-4.08401040 \times 10^{-9}$	−4	9	$-1.443920685 \times 10^{-9}$
7	−4	$5.01458421 \times 10^{-9}$	−2	11	$3.045184253 \times 10^{-9}$

Table 5.2: Classical SCF-Perturbation Fourier series corresponding to a boxlike quasiperiodic trajectory for $f_x = 0.30$at $E = 24.0$ c.e.u. and $R = 4.30$ a.u. $E(SCF) = 23.98810781$ c.e.u.; E(PTN) = 23.99962196 c.e.u. and $J_x = 0.44196935$ $J_z = 0.54190037$; $\omega_x = 21.63038857$ $\omega_z = 28.60813452$

X – Oscillator			Z – Oscillator		
X	Z	2D – Coefficients	X	Z	2D – Coefficients
1	0	$1.780966309 \times 10^{-1}$	1	0	$1.123749387 \times 10^{-1}$
3	0	$-3.888313642 \times 10^{-4}$	3	0	$-1.746655724 \times 10^{-3}$
5	0	$-1.409867215 \times 10^{-6}$	5	0	$2.925164374 \times 10^{-5}$
7	0	$4.020516776 \times 10^{-9}$	7	0	$-5.266064036 \times 10^{-7}$
1	2	$-1.029082854 \times 10^{-3}$	9	0	$1.002775027 \times 10^{-8}$
1	4	$5.365458038 \times 10^{-5}$	11	0	$-2.026964573 \times 10^{-10}$
1	6	$-2.037143879 \times 10^{-6}$	1	2	$-1.264680651 \times 10^{-3}$
1	8	$6.876115817 \times 10^{-8}$	1	4	$-6.976293681 \times 10^{-6}$
1	10	$-2.150033011 \times 10^{-9}$	1	6	$2.402537365 \times 10^{-8}$
1	−2	$2.040067968 \times 10^{-2}$	1	−2	$-2.778350210 \times 10^{-3}$
1	−4	$-8.010847284 \times 10^{-5}$	1	−4	$3.326485306 \times 10^{-5}$
1	−6	$1.576533091 \times 10^{-6}$	1	−6	$-5.758919573 \times 10^{-8}$
1	−8	$-3.621360261 \times 10^{-8}$	3	2	$6.164795065 \times 10^{-5}$
3	2	$7.871718635 \times 10^{-7}$	3	4	$7.014681892 \times 10^{-7}$
3	4	$1.438230741 \times 10^{-6}$	3	6	$7.940521070 \times 10^{-9}$
3	6	$-7.685264723 \times 10^{-8}$	3	−2	$1.471184026 \times 10^{-2}$
3	8	$3.038389861 \times 10^{-9}$	3	−4	$1.001125596 \times 10^{-5}$
3	−2	$6.661086582 \times 10^{-3}$	3	−6	$-1.524639707 \times 10^{-8}$
3	−4	$-2.658269121 \times 10^{-5}$	5	2	$-2.271341769 \times 10^{-6}$
3	−6	$5.870656175 \times 10^{-7}$	5	4	$-5.062107444 \times 10^{-8}$
3	−8	$-1.719216029 \times 10^{-8}$	5	−2	$-5.975445465 \times 10^{-4}$
5	2	$-9.187840838 \times 10^{-7}$	5	−4	$-3.862806398 \times 10^{-6}$
5	4	$5.784295997 \times 10^{-8}$	5	−6	$6.642275553 \times 10^{-9}$
5	6	$-2.370750255 \times 10^{-9}$	7	2	$8.221627925 \times 10^{-8}$
5	−2	$-6.327080833 \times 10^{-5}$	7	4	$2.402264903 \times 10^{-9}$
5	−4	$-1.459286586 \times 10^{-6}$	7	−2	$1.612097316 \times 10^{-5}$
7	2	$-6.800588310 \times 10^{-9}$	7	−4	$1.405953750 \times 10^{-7}$
7	−2	$-2.338778243 \times 10^{-7}$	9	2	$-2.843873396 \times 10^{-9}$
7	−4	$2.002116137 \times 10^{-8}$	9	−2	$-3.984030869 \times 10^{-7}$
9	−2	$1.793239708 \times 10^{-9}$	9	−4	$-3.728470976 \times 10^{-9}$

Table 5.3: Classical SCF-Perturbation Fourier series corresponding to a boxlike "butterfly" quasiperiodic trajectory for $f_z = 0.55$ at $E = 24.0$ c.e.u. and $R =$ 4.30 a.u. $E(SCF) = 23.97592881$ c.e.u.; Σ(PTN) = 24.00112253 c.e.u. and $J_x =$ 0.71053221 $J_z = 0.32352223$; $\omega_x = 22.40029465$ $\omega_z = 25.56355204$

since it guarantees the existence of an action associated with each chosen degree of freedom. This property can be seen in a study of its behaviour in the neighbourhood of "accidental" periodic resonances [39]. These interrupt the basic quasiperiodic motions associated with a dominant torus because of local commensurability of the frequencies, but do not depart from its essential symmetry. As an example consider the 3:5 resonance that interrupts the classical (x, z) boxlike quasiperiodic motions at $R = 4.30$ a.u. and $E = 46.0$ c.e.u. This interruption occurs for a small domain of initial conditions near $f_x = 0.20$ (width ± 0.005). True trajectories are compared in Figure 5.2 with the corresponding CSCF perturbed trajectories for three values of f_x near this domain; for the intermediate trajectory, lying inside the resonant domain, actions for the SCF calculation were determined by interpolation of (J_x, J_z) data versus f_x on either side of the disruption. A composite Poincaré surface-of-section plot is provided for both sets of trajectories in Figure 5.3. For the intermediate case, the true motion displays the isolated "islands" structure characteristic of such resonant motions, while the perturbed system maintains the single closed curve characteristic of the dominant boxlike family. Evidently, the CSCF approximation ignores this type of "weak" periodic resonance. The SCF frequencies are not in 3:5 resonance for actions in this region but even near such a high-order resonance of SCF frequencies, small magnitudes of the corresponding Fourier coefficients in the perturbation Hamiltonian severely restrict or completely suppress the effects of the resonance on perturbed SCF motion. Only those terms in the Hamiltonian which sample prominent aspects of the correction potential will tend to have strong effects.

With this idea in mind, consider next the possibility of extending the perturbed CSCF calculations into a region where the true motion has been reorganized into the 1:1 resonant family of quasiperiodic motions. A procedure similar to that described above was used to construct perturbed SCF trajectories for comparison

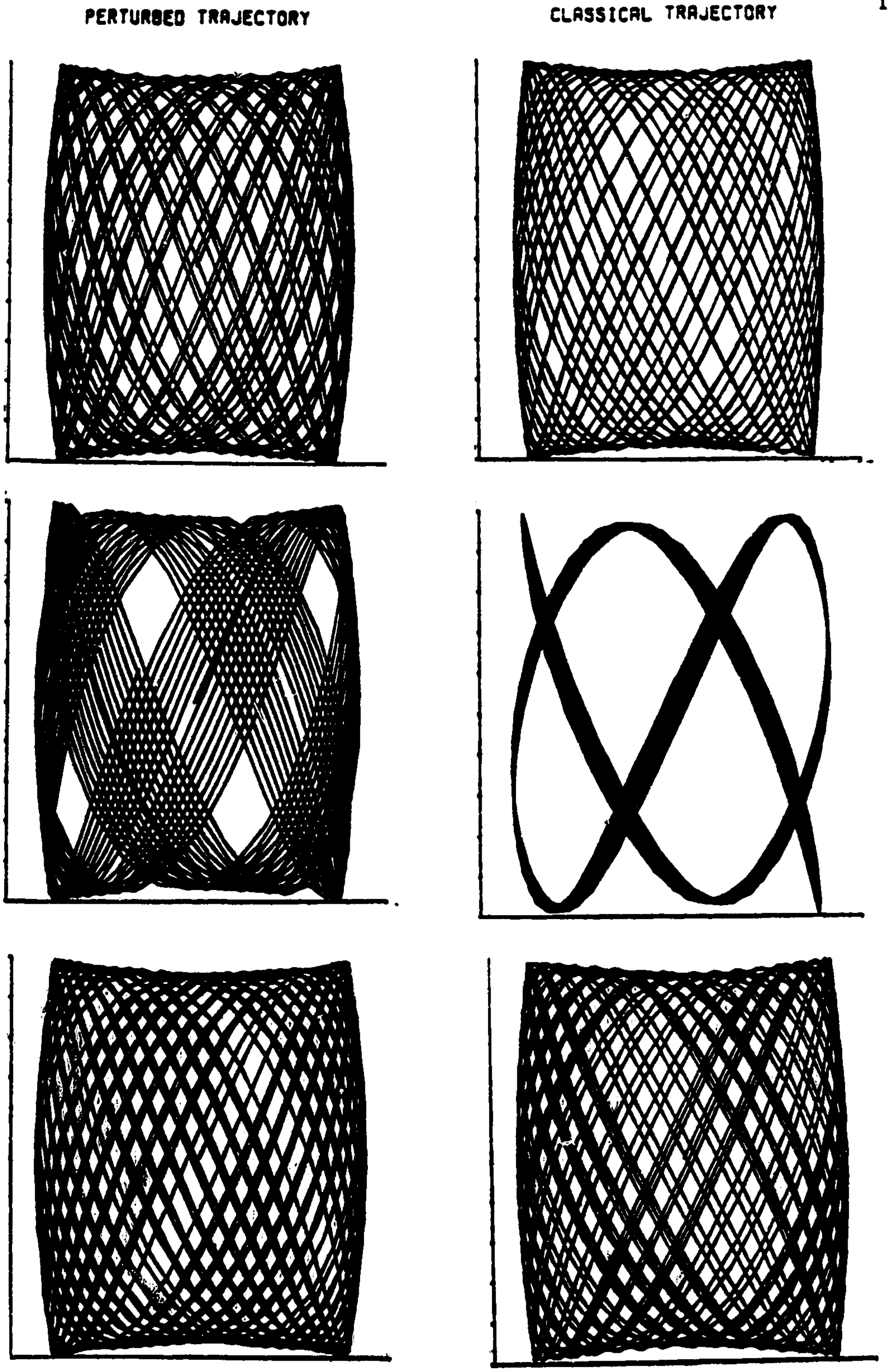

Figure 5.2: Classical and SCF perturbation trajectories are presented at three initial conditions about the accidental 3:5 resonance at $R = 4.30$ a.u. and $E = 46.0$ c.e.u.

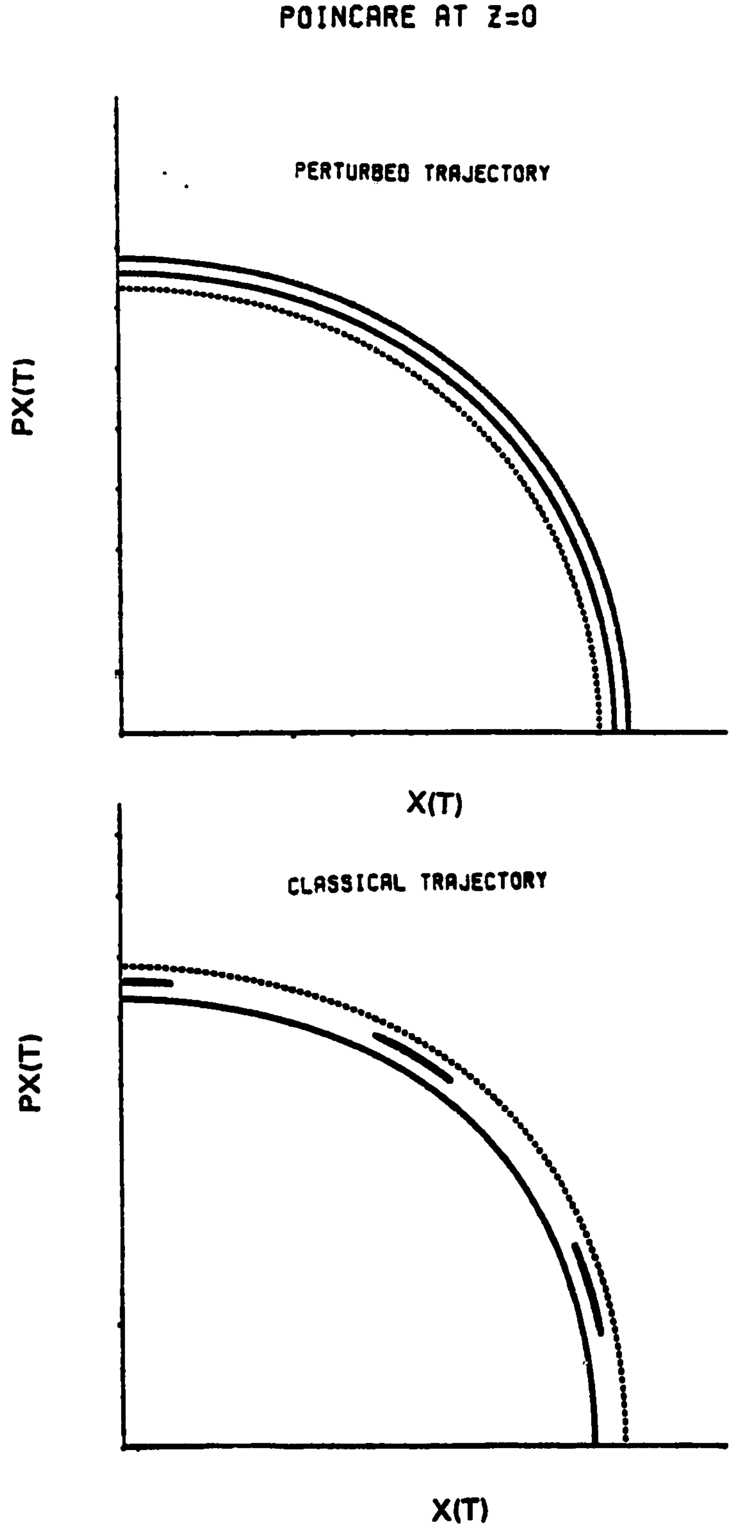

Figure 5.3: Composite Poincaré surfaces-of-section on the $z = 0$ plane for true classical and SCF perturbed motion are compared at $R = 4.30$ a.u. and $E = 46.0$ c.e.u. about a 3:5 accidental resonance.

with true motions in the resonant 1:1 region at $R = 4.30$ a.u. and $E = 24.0$ c.e.u. Previously (see Chapter 4), action pairs, either (J_x, J_z) or (J_1, J_2), were plotted as functions of f_x for the same R and E. The parameter f_x is not a single-valued function of the actions characterizing the 1:1 resonant family and distorts the mapping of the actions characterizing the boxlike families. Plotting J_z against J_x as in Figure 5.4 provides a more rational mapping procedure. The two piece-wise continuous segments on the plot are obtained from classical analysis of the two boxlike regions on either side of the 1:1 region lying within $0.568 < f_x < 0.983$. It is immediately evident that the two sections belong to a common curve. Additional constraints on the function may be obtained from the quotient relation

$$\frac{\partial J_z}{\partial J_x}_E = -\left[\frac{\partial H}{\partial J_x}\right]_{J_z} \Big/ \left[\frac{\partial H}{\partial J_z}\right]_{J_x} = -\frac{\omega_x}{\omega_z}. \tag{5.42}$$

Using a three-term polynomial all of the (J_x, J_z) data were successfully fitted by the least squares method with an r.m.s. error of less than $1\text{x}10^{-4}$ whether the data points from the smaller segment were included or not. The polynomial fit was used to generate interpolating values for the hypothetical action pairs (J_x, J_z) inside the "gap" region, where the true motion is reorganized into the 1:1 resonance and the actual constants of the motion are (J_1, J_2). Using these hypothetical values, classical SCF states of motion in the gap region were computed for comparison with the true dynamics.

A number of interesting features are evident in the results. Table 5.4 lists CSCF energies and frequencies, and the perturbation energies at the projected action pairs as the gap region is traversed. Throughout the gap region, the zero-order CSCF energies are within 0.05 c.e.u. of the projected energy $E = 24.0$ c.e.u. The second-order perturbation energy corrections increase gradually as the gap is entered, with no discontinuity or singularity as the bifurcation is crossed. As the SCF 1:1 resonance,

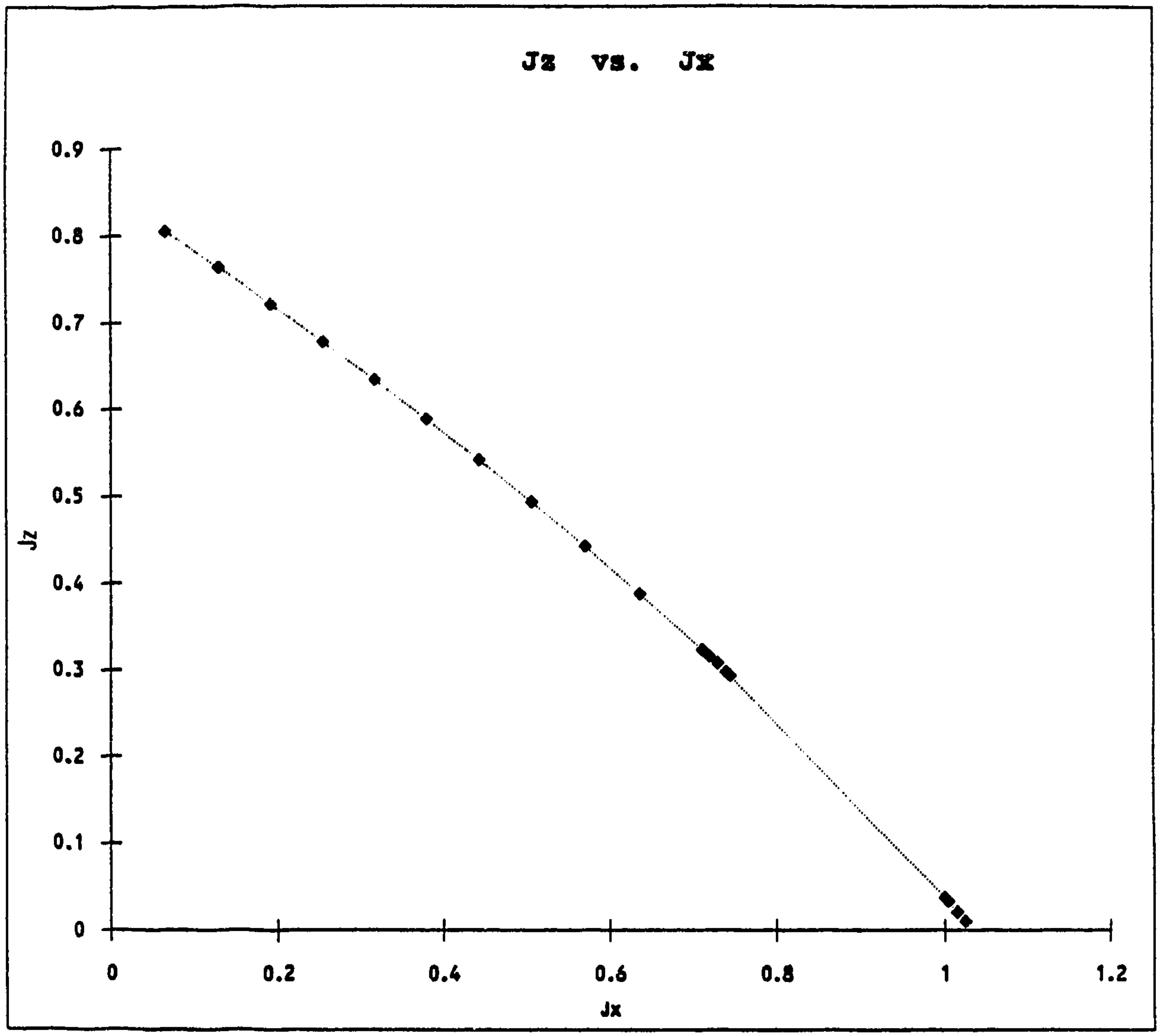

Figure 5.4: Classical actions are plotted against each other at R = 4.30 a.u. and $E = 24.0$ c.e.u..

at $(J_x, J_z) \approx (0.8710, 0.1734)$, is approached, small divisors in the perturbation energy expression produce the expected divergence in a small neighbourhood about the resonance. On the other side of the resonance, the second-order corrections again decrease and gradually approach the small values found in boxlike regions as the second bifurcation is passed. This behaviour is completely in accord with the predictions of the perturbation formalism, which places the source of the disturbance at the SCF 1:1 resonance. Curiously, this resonance is located almost exactly at the point on the curve where the sum of the projected actions is a maximum. For the true 1:1 periodic resonance, the sum $(J_1 + J_2)$ is *exactly* at its maximum.

It is worthwhile to compare the coordinate plane projections of perturbed SCF trajectories in the gap region with an imagined "superposition" of true classical 1:1 resonant family trajectories and their mirror images which would correspond to motion in the other potential valley. Such a superposition would retain the C_{2v} symmetry which necessarily characterizes the perturbed SCF motion. Figure 5.5 shows a sequence of perturbed and true trajectories (none with superpositions). While there is no exact relation between corresponding members in each sequence, they have been chosen at regular intervals between the bifurcation and the 1:1 resonance for each set. Given that the full C_{2v} symmetry cannot be removed from the perturbation calculation, it is remarkable that perturbation theory is able to qualitatively reproduce the distribution of the imagined superposition of the two equivalent but asymmetric true trajectories. This suggests that the perturbation terms are attempting to accomodate the effects of the two pronounced potential valleys. However, as the resonance is approached, the difference between the two descriptions becomes much greater.

J_x	J_z	$Escf$	$Eptn$	ω_x^{scf}	ω_z^{scf}
0.76610679	0.27336816	23.962733	24.017666	22.573147	24.789215
0.78777633	0.25336816	23.960035	24.044857	22.642167	24.468937
0.80910488	0.23336816	23.957579	24.103477	22.711291	24.141424
0.83009244	0.21336816	23.955470	24.254680	22.780588	23.806019
0.85073902	0.19336816	23.953832	24.836266	22.850133	23.461974
0.87104661	0.17336816	23.952849	33.641967	22.920015	23.108432
0.89100929	0.15336816	23.952546	29.802395	22.990323	22.744429
0.91067293	0.13336816	23.953239	24.698921	23.061172	22.368811
0.92991559	0.11336816	23.955093	24.220739	23.132685	21.980251
0.94885733	0.09336816	23.958348	24.085513	23.205009	21.577174

Table 5.4: Classical SCF-perturbation theory results across the "gap" at $E_{CT} = 24.0$ and $R = 4.30$ a.u.

Figure 5.5: Classical SCF perturbation trajectories and "corresponding" classical trajectories in the 1:1 resonant region at $R = 4.30$ a.u. and $E = 24.0$ c.e.u. crossing the bifurcation from the boxlike region into the resonant region or "gap".

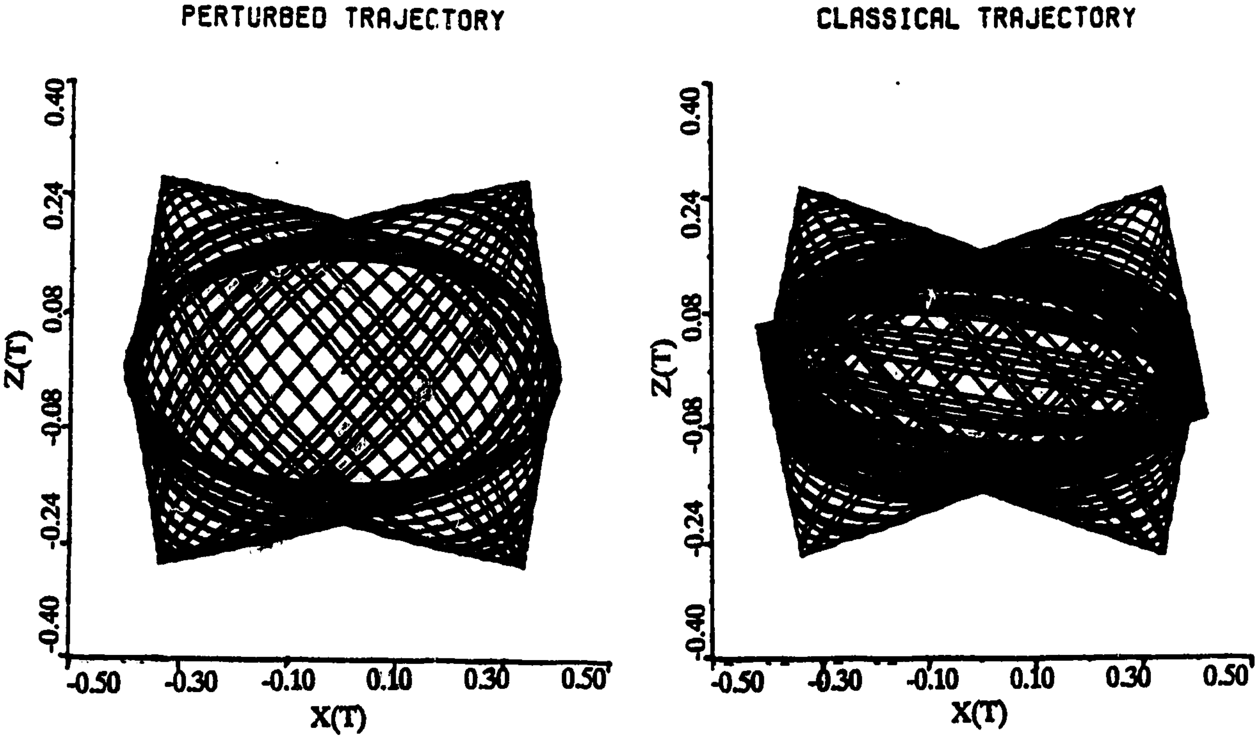

PERTURBED TRAJECTORY

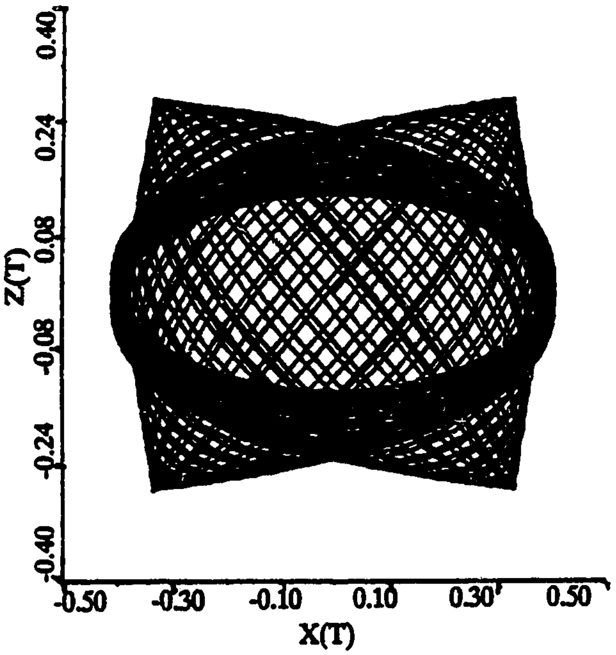

CLASSICAL TRAJECTORY

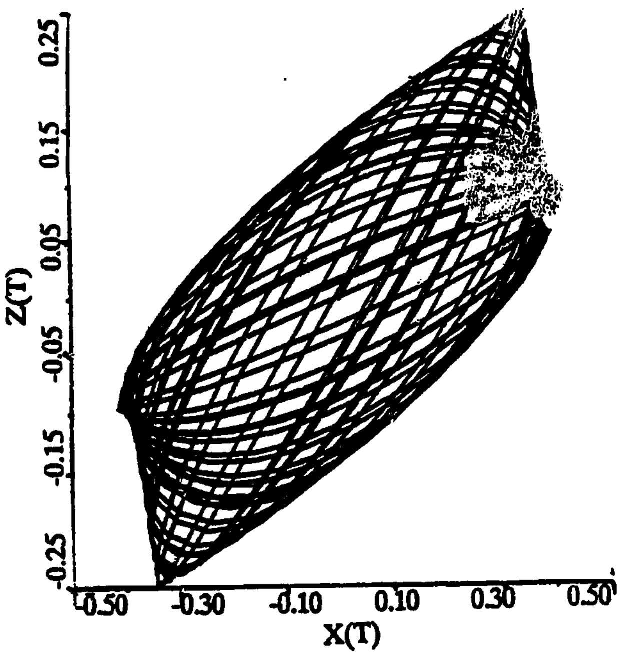

PERTURBED TRAJECTORY

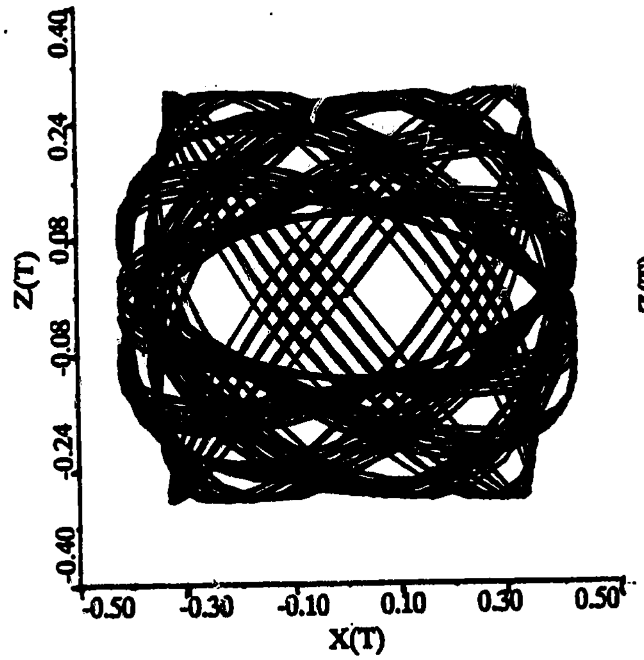

CLASSICAL TRAJECTORY

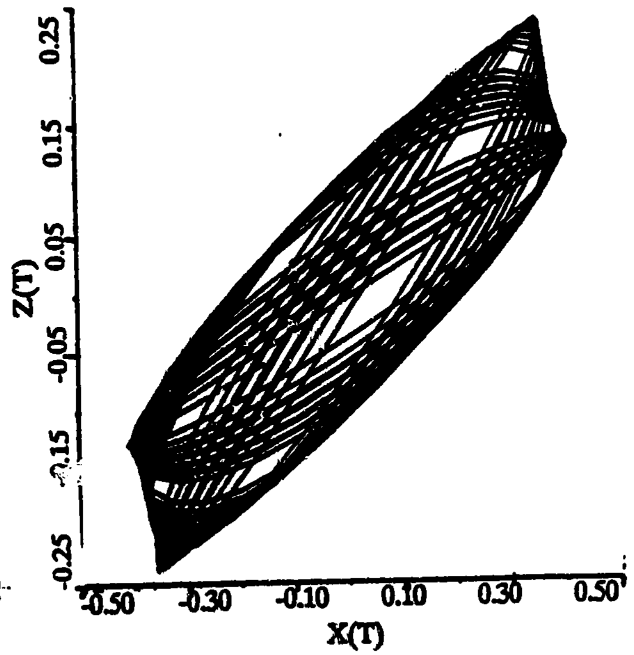

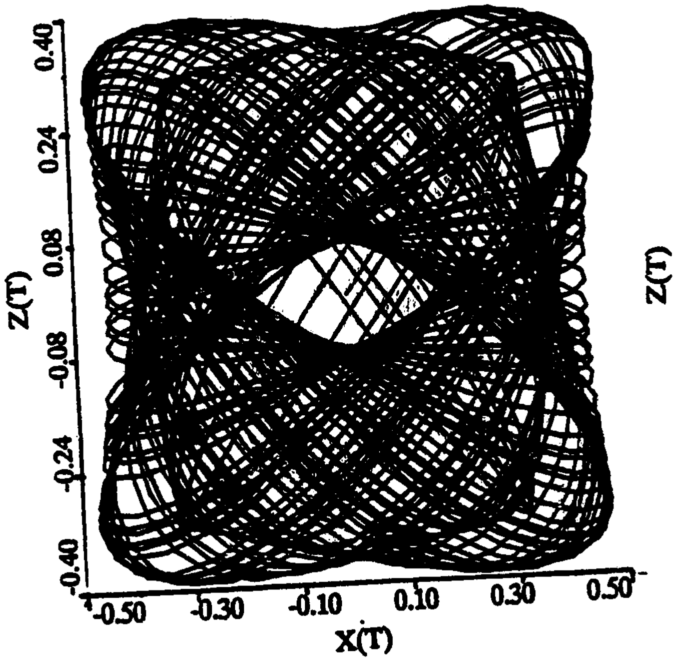

PERTURBED TRAJECTORY

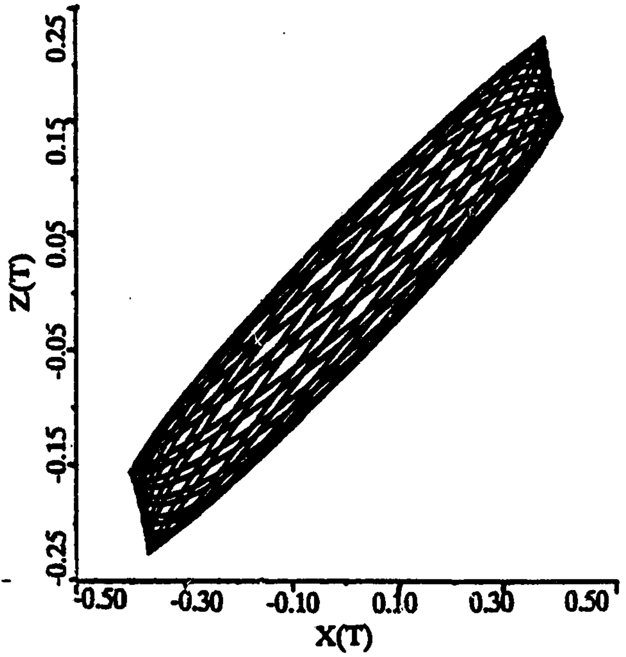

CLASSICAL TRAJECTORY

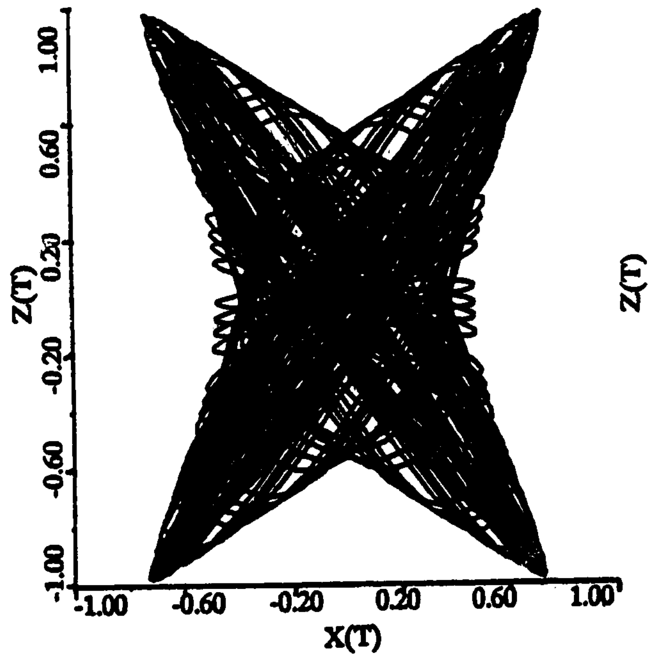

PERTURBED TRAJECTORY

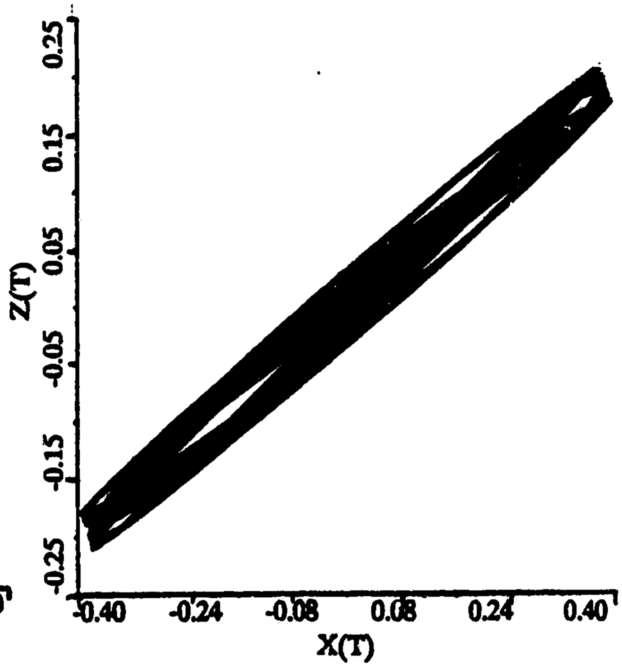

CLASSICAL TRAJECTORY

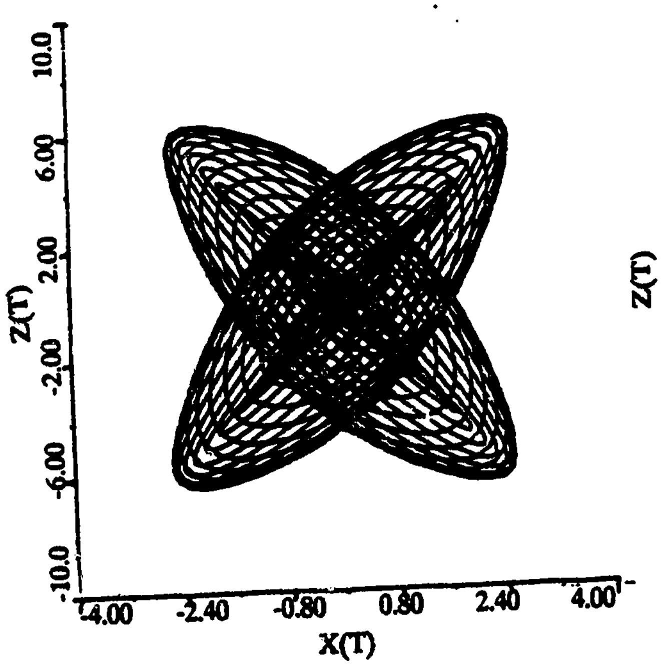
PERTURBED TRAJECTORY

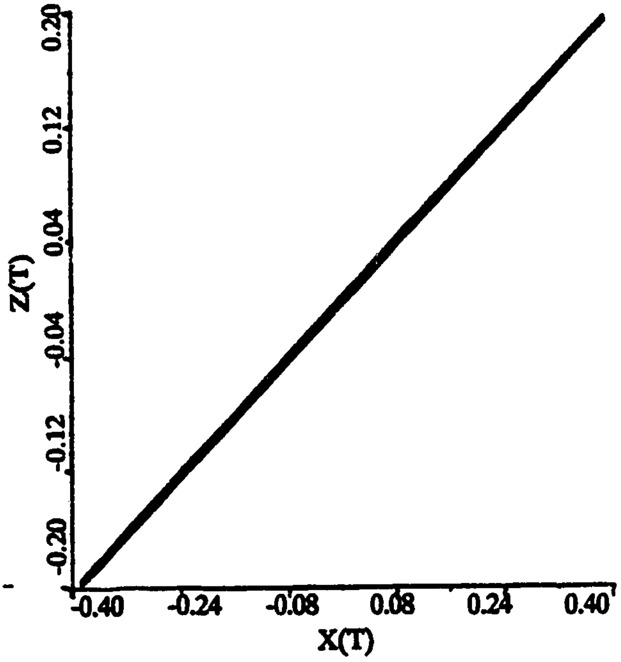
CLASSICAL TRAJECTORY

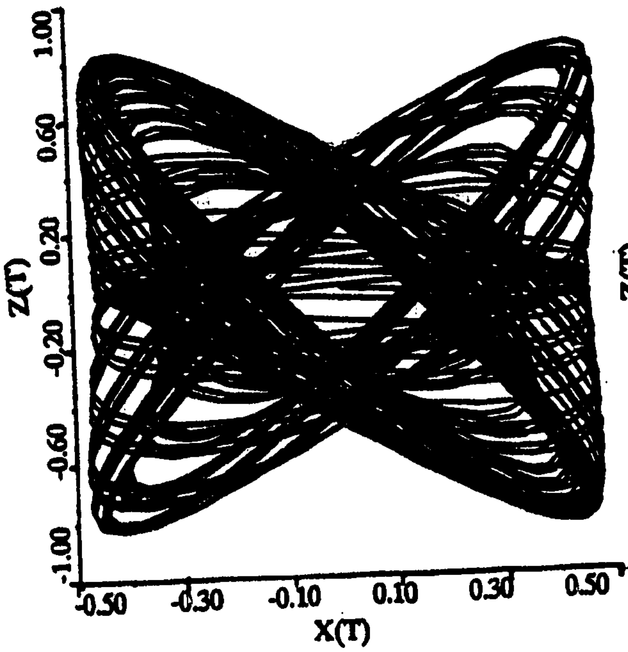
PERTURBED TRAJECTORY

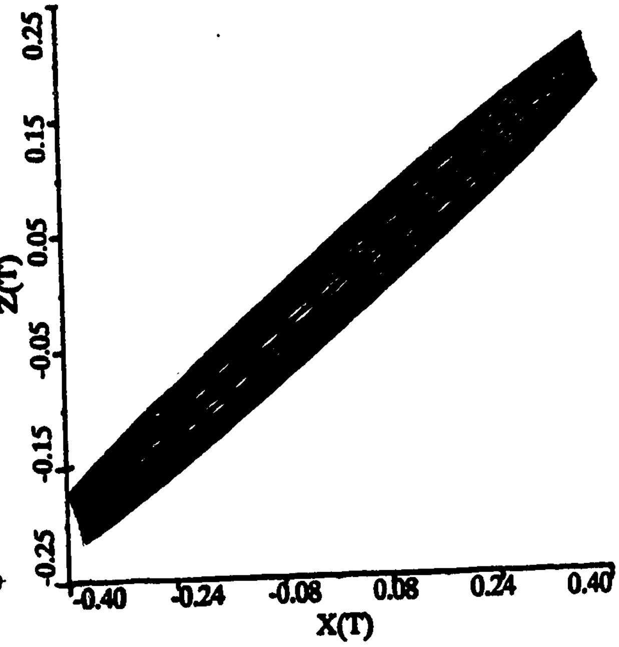
CLASSICAL TRAJECTORY

PERTURBED TRAJECTORY

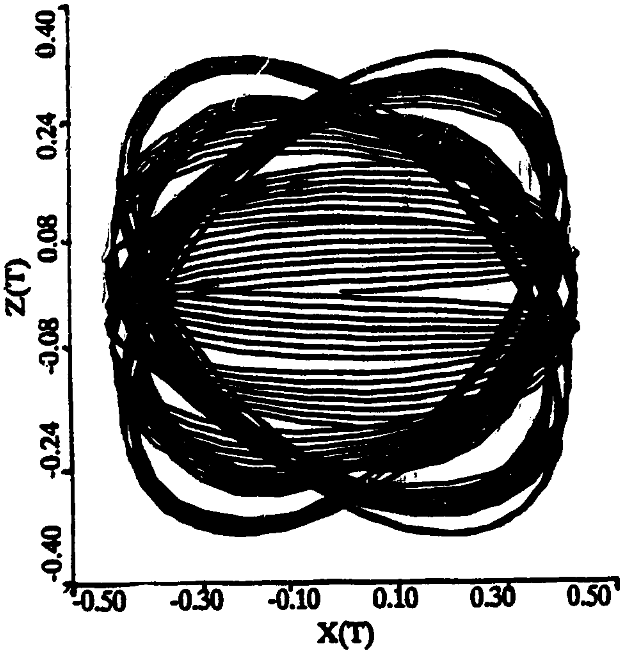

CLASSICAL TRAJECTORY

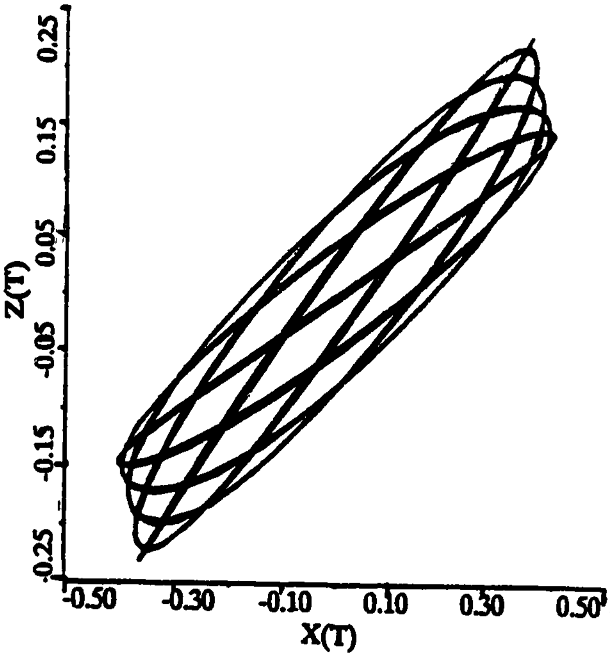

PERTURBED TRAJECTORY

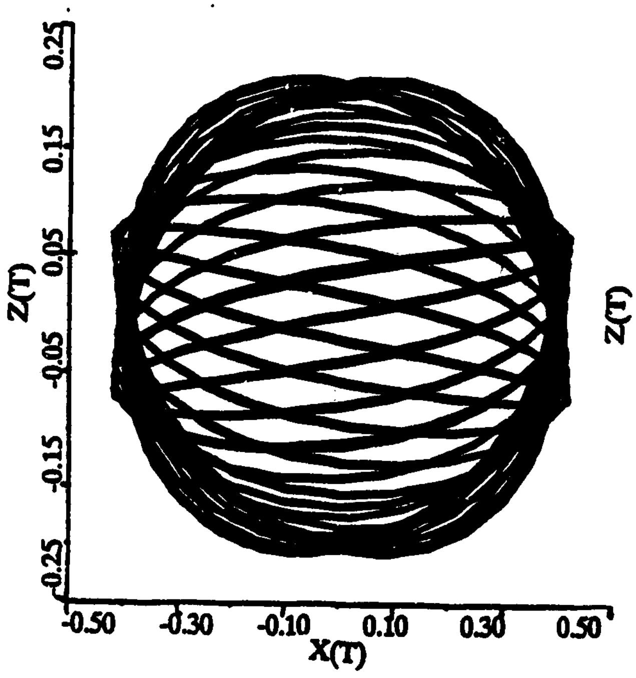

CLASSICAL TRAJECTORY

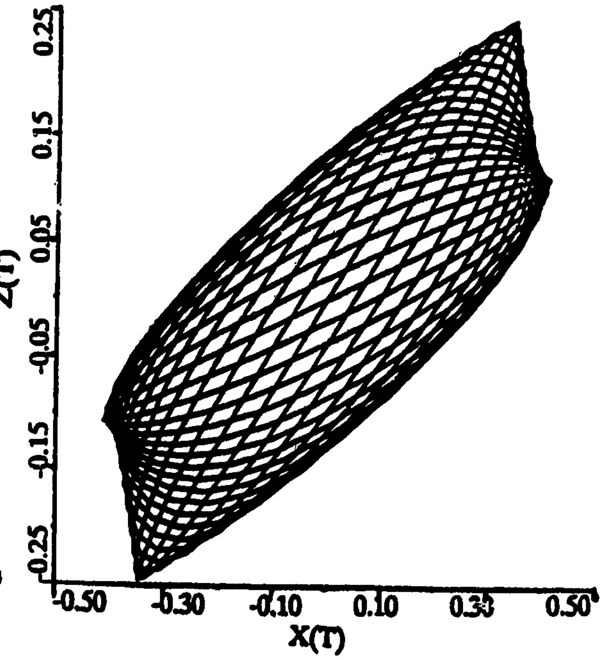

In spite of the apparent continuity of the SCF calculation across the bifurcation, Figure 5.6 shows that Poincaré surfaces-of-section on the (x, z) planes for perturbed SCF trajectories signal precisely the onset of the 1:1 resonant bifurcation. The figure shows sequences of five surfaces-of-section for the plane $x = 0$ after the first bifurcation near $f_x \approx 0.568$ at $R = 4.30$ a.u. and $E = 24.0$ c.e.u. The "pinching-in" of the sides is preliminary, in the case of the true motion, to the splitting of single curves into two closed loops characterizing the $x = 0$ sections for the 1:1 resonant family. The SCF perturbation sequence accurately reproduces the pinching-in of the true sections up to the bifurcation point (as seen in Figure 5.1). However, at the bifurcation, a topological change occurs and the pinches suddenly snap into small inner circles. In contrast to its suppression of the weak 3:5 periodic resonance described earlier, canonically perturbed CSCF theory is able to detect the onset of this strong reorganization of the motion rather accurately.

Figure 5.6: Poincaré surfaces-of-section for SCF perturbation trajectories for $f_z >$ 0.568 (inside the 1:1 resonant region) for $R = 4.30$ a.u. and $E = 24.0$ c.e.u..

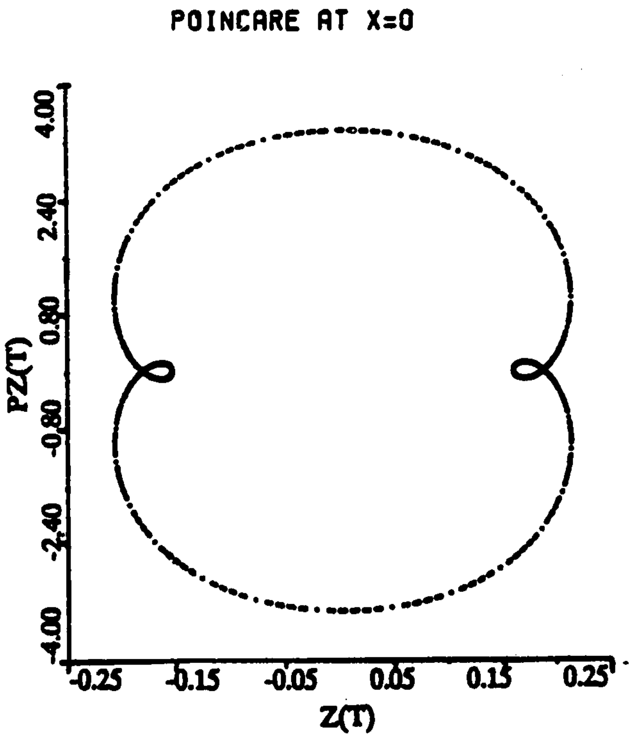

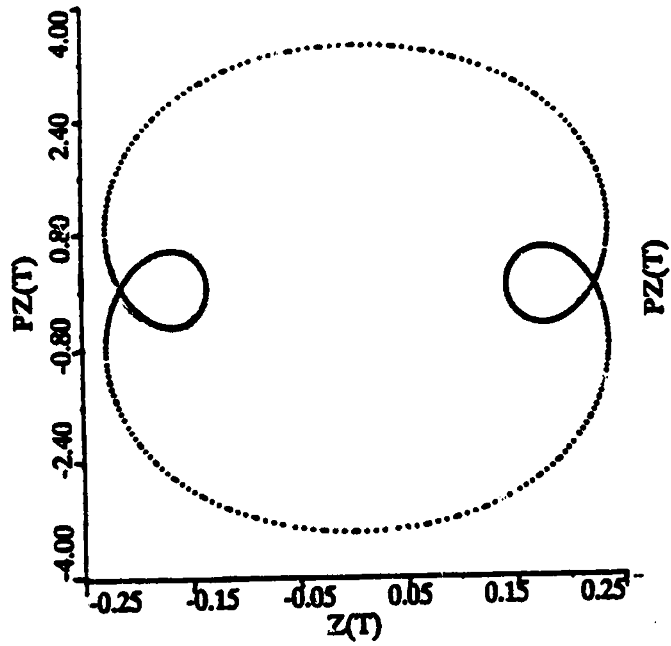

POINCARE AT X=0

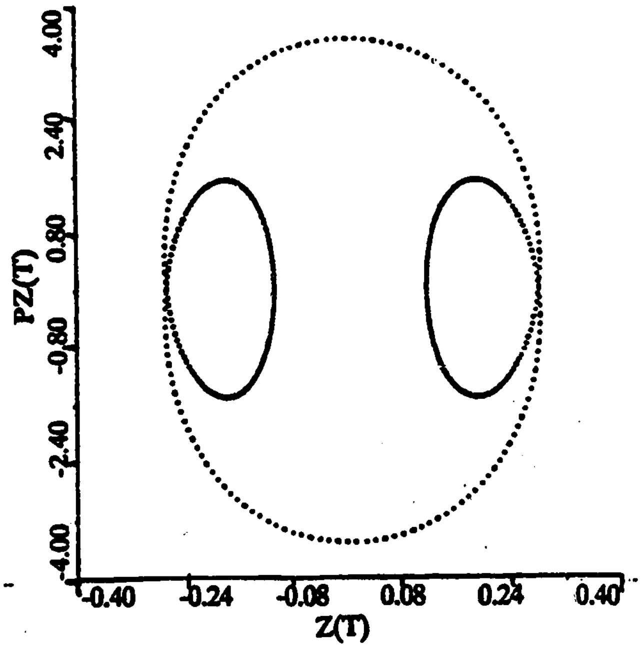

POINCARE AT X=0

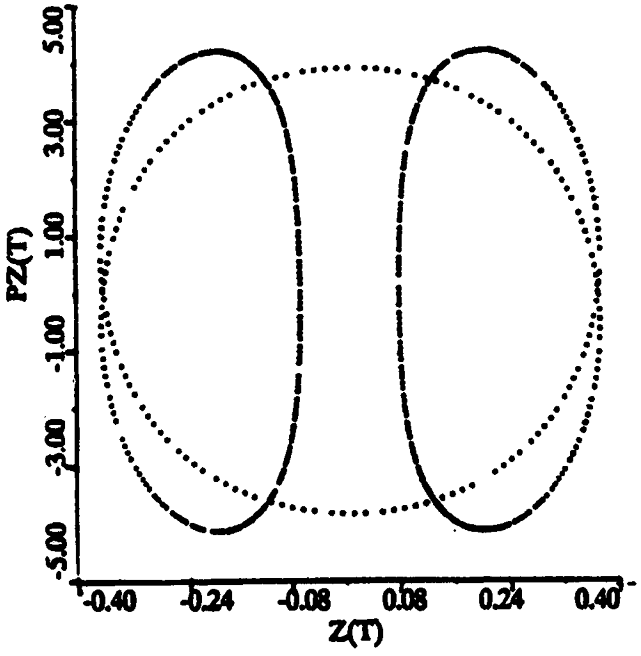

POINCARE AT X=0

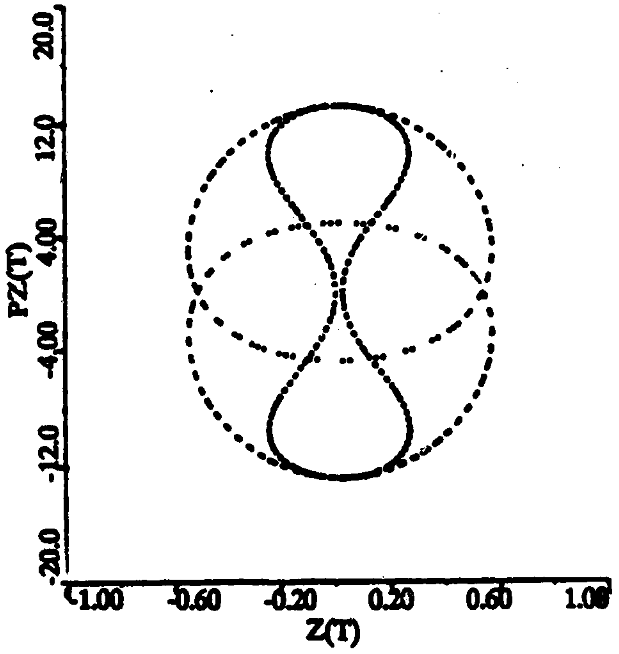

POINCARE AT X=0

POINCARE AT X=0

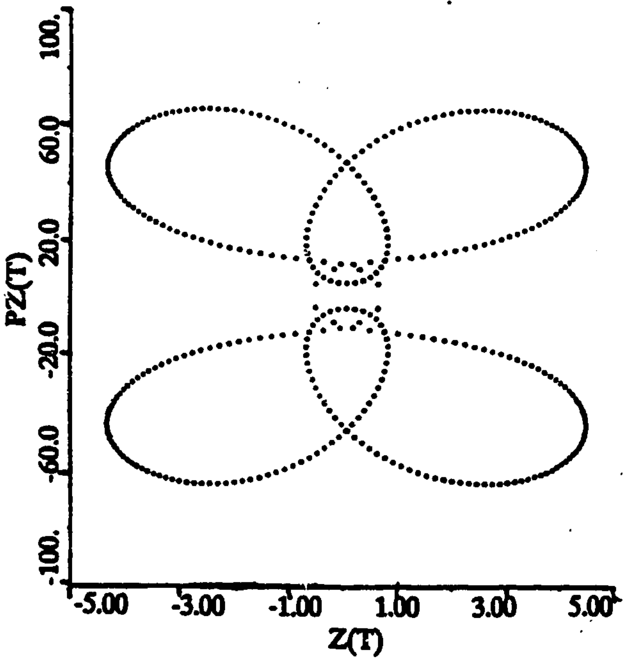

POINCARE AT X=0

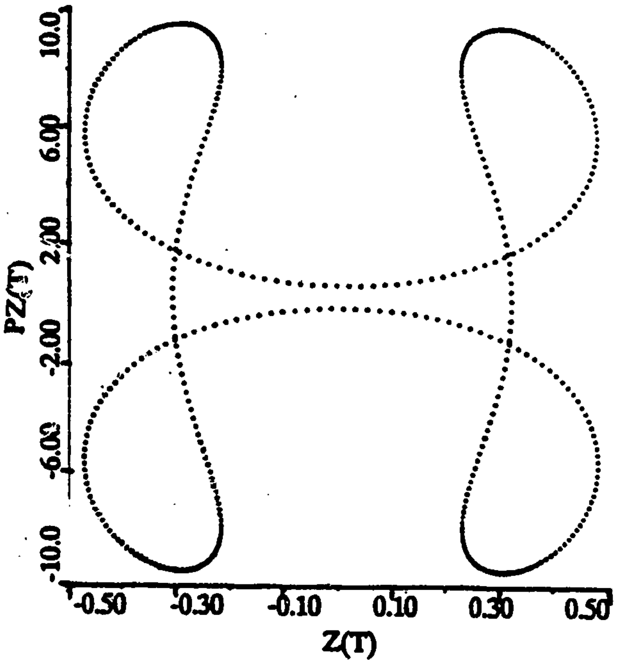

POINCARE AT X=0

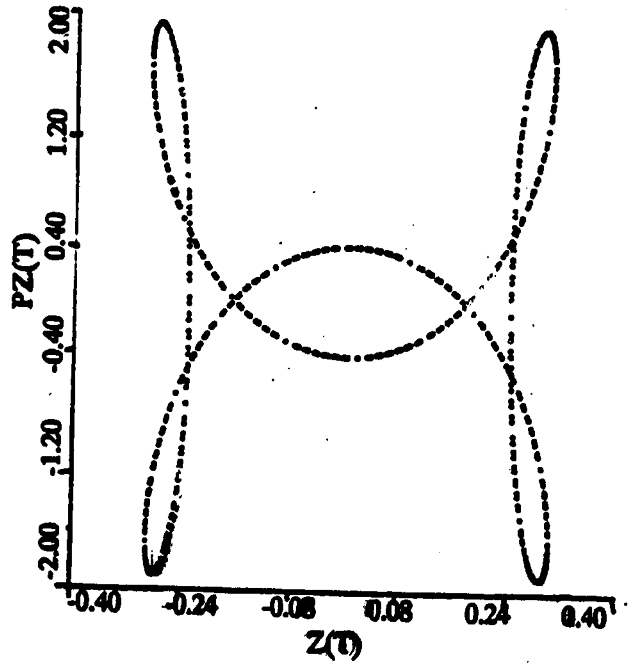

POINCARE AT X=0

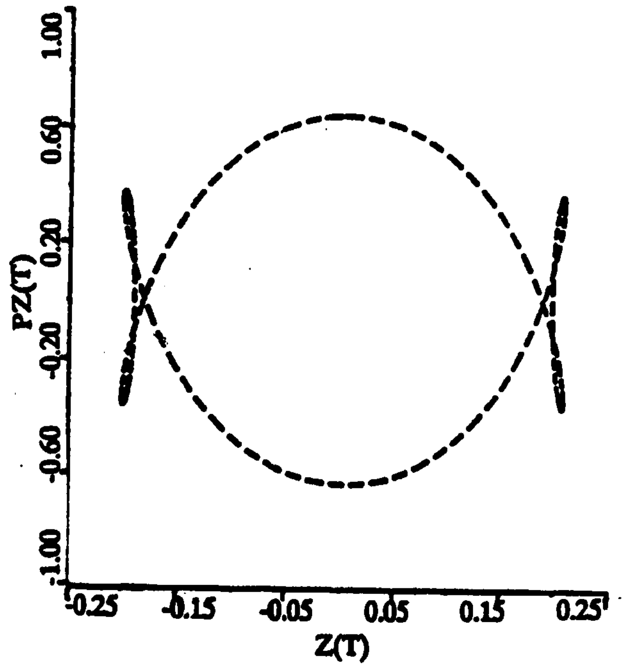

While the pronounced elliptical motion seen in the true dynamics near the bifurcation appears to have a counterpart in the perturbed SCF trajectories shown in Figure 5.5, this appearance is deceiving. The perturbed SCF trajectory does not actually spend a lot of time in an elliptical orbit, as it does in the true dynamics. Instead the SCF trajectory has a rocking motion whose successive passes etch out an elliptical contour similar to the dimensions of the ellipse seen in the true dynamics. This difference between the perturbed SCF and the true motions is most evident in a real-time display of the motion on the (x, z) plane. It is possible, of course, to create an elliptical SCF trajectory. Using the CSCF amplitudes for motion at the CSCF 1:1 periodic resonance and introducing an arbitrary phase shift of $\pi/2$ between the x and z motions, we were able to synthesize a zero-order SCF elliptical periodic trajectory. This orbit resembles the true elliptical motion at the bifurcation in a qualitative fashion but it is not clear that this relates anything important about such motions; in any case, the frequency is seriously in error since this CSCF ellipse was concocted at precisely the 1:1 resonance and not at the bifurcation.

Finally one may ask whether additional insight might be provided by a study of zero-order and perturbed SCF dynamics using a rotated system of coordinates (q_1, q_2) oriented parallel with and transverse to the pronounced potential valley which is responsible for the strong reorganization of motion. Unfortunately, such a calculation is computationally intractable using this model potential, which consists of a finite string of terms each of which is a separable product in the original coordinates; there is no simple corresponding representation in the rotated coordinate frame. Professor Thorson has done some calculations using a five-term polynomial model potential which simulates the true potential at $R = 4.30$ a.u. reasonably well for energies up to about 100 c.e.u. above the minimum. All the qualitative behaviour observed here in both CSCF and true dynamics is also reproduced by the polynomial model, and in addition it is possible to perform CSCF calculations in these rotated coordinates. While the perturbation energies are substantially larger and the first-order trajectories which result are correspondingly less accurate, the asymmetrical shape of the 1:1 family of true trajectories is qualitatively reproduced in these rotated CSCF perturbation calculations. This suggests that the actions J_1, J_2 which form the defining constants of the motion for the 1:1 family are assignable in some crude way to the degrees of freedom q_1, q_2, but further investigation of such an idea is beyond the scope of this study.

In the concluding chapter, we summarize the results of this and previous chapters, focussing in particular on the comparison of quantum reorganizations of states at avoided crossings (Fermi resonances) with the analogous effects seen at much lower energies in the classical dynamics.

Chapter 6

Conclusions

This study has compared classical and quantum descriptions of vibrational dynamics for a strongly nonharmonic, nonseparable potential. It was stimulated by quantum mechanical calculations of Epa and Thorson [1,2,3] for the strongly hydrogen-bonded bifluoride ion $[FHF]^-$ using an extended *ab initio* potential surface. Some preliminary work on classical proton dynamics for $[FHF]^-$ was done, but was replaced by a two-dimensional adaptation chosen to remove unnecessary complications of the bifluoride problem while retaining the physical features of essential interest here. The resulting model surface $V(x, z; R)$ has C_{2v} symmetry and Cartesian coordinates. In the bifluoride system the parameter R is the F–F separation and has similar effects in this model: as it is varied the potential surface changes from a single-minimum well at small R-values to a symmetrical double-minimum structure with intervening potential barrier at $z = 0$ for $R \geq 4.45$ a.u. The most important feature of the surface is the emergence of prominent "corners" or valleys lying at direction ±26° to the x-axis. On the original bifluoride surface, these correspond to the potential valleys for librational oscillation of a dipolar HF molecule about its equilibrium orientation to the opposite F^- ion, which forms as the $[FHF]^-$ system begins to dissociate.

The quantum mechanical calculations of Chapter 2 recover essentially the same features as results obtained by Epa and Thorson for $[\mathrm{FHF}]^-$. Since comparison with classical dynamical calculations in the high-barrier, double-well region for $R \geq 4.60$ a.u. was not expected to be either feasible or instructive, our computations were restricted to regions of smaller R-value. However, the number of eigenstates computed accurately is larger because of the expanded SCF basis used, and detailed attention has been given to nodal structure of eigenfunctions. The SCF approximation is a surprisingly accurate zero-order description of vibrational eigenstates with energies up to about 10,000 cm^{-1}above the ground level *except at R-values near crossings of SCF levels of the same symmetry.* These become avoided crossings of true eigenstates which strongly mix the SCF states and reorganize the nodal structure.

This study concentrated especially on a prominent series of avoided crossings of SCF levels differing by the exchange of two quanta between the x and z degrees of freedom (for example, for A_1 symmetry, the sequence of pairs [(2,0)x(0,2)] , [(4,0)x(2,2)], [(6,0)x(4,2)], etc.) Except at such crossings, these eigenfunctions are essentially of simple SCF type with nodal planes perpendicular to the x and z axes. The mixed eigenfunctions at avoided crossings have a different nodal structure: for the *stabilized* member of each pair, the structure corresponds to a classical radial oscillation along the prominent potential valleys, and to an elliptical classical orbit for the *destabilized* member. At still higher energies (15,000 $\mathrm{cm}^{-1}$to 20,000 cm^{-1}depending on symmetry), the numbers and types of crossings increase rapidly, making the SCF description far less appropriate for all but a few eigenstates in this disordered region.

The Classical SCF method was applied to the same system to calculate semiclassical SCF eigenvalues. These parallel the quantum SCF results. However, even when the full potential $V(x, z; R)$ has a single minimum, the effective

SCF potentials for x and z exhibit a strong double-well structure produced by the prominent surface valleys. If the semiclassical quantization formulas are modified to include effects of tunnelling through the potential barrier, resulting semiclassical eigenvalues differ from their quantum counterparts by errors due mainly to the one-dimensional JWKB approximation for anharmonic oscillators. Such errors may be as large as 80–100 cm^{-1} in exceptional cases but are usually about 5–20 cm^{-1}. The semiclassical SCF calculation provides a stable, qualitatively accurate description of the quantum results correctly locating level crossings and the general behaviour of SCF energy levels for the system. Both quantum and classical SCF descriptions are limited by their common assumption of an x, z mode separation.

Since the quantum SCF approximation gives such an accurate account of the low-lying levels of this system, and the classical SCF results are essentially parallel to these, we had hoped that classical bound state methods involving quantization of classical actions would yield semiclassical eigenvalues, derived from full two-dimensional dynamics, which would closely agree with CSCF results. Such eigenvalues can indeed be calculated for the *ground state* for $3.80 \leq R \leq 4.35$ a.u. and they are as close to the classical SCF values as the quantum CI energies are to the quantum SCF values (1–5 cm^{-1}). However, the method fails entirely for all higher energy levels, and beyond $R = 4.35$ a.u. for even the ground state. Classical motions of the simple "boxlike" type for which the actions J_x, J_z have the required values do not exist; instead, the system is strongly reorganized into a family of quasiperiodic motions centered on a 1:1 resonant periodic trajectory correlated with one of the potential valleys. As the energy is increased, this and other disruptive resonances become more prominent at all R-values; at still higher energies, irregular trajectories fill increasing domains in phase space.

The nearly-harmonic, nearly-separable systems mostly studied in the literature are typical illustrations of the famous KAM theorem, which states that for a system whose Hamiltonian consists of an exactly separable part plus a sufficiently small nonseparable perturbation, most phase space trajectories will remain regular. This explains the success of classical bound state methods for eigenvalue calculation in such systems. Given the results for our model system, the nonseparable terms are clearly not "small" in the sense of the KAM theorem. Obviously then the sort of separability implied in the success of the SCF approximation has no simple relation to the KAM concept of separability.

In the remainder of this study, attention therefore focussed on the properties of classical dynamics in this system with no reference to quantum eigenvalues. Comparison with classical SCF theory remained of interest and was made for a *continuous* range of dynamical conditions. It was necessary to develop a repertory of the methods and numerical techniques used in the literature for the investigation of regular motions and also some further tools for describing detailed motion. Systematic investigations were made at energies near the three lowest CSCF semiclassical energy levels: $E = 24.0, 46.0, 56.0$ c.e.u., and mostly at the equilibrium R-value 4.30 a.u. Some studies were done at other R-values and energies to map out the overall classical dynamics. Actions, frequencies, and Fourier series expansions for dynamical variables were computed for both boxlike and 1:1 resonant families of quasiperiodic motion. The segregation of phase space into these two competing types of motion and the quantum mechanical curve crossings involving exchange of quanta between modes are both related to the prominent valleys or "corners" on the potential surface. It is interesting that at the lowest energy studied irregular motion is practically absent from the bifurcation region separating the two families. This allowed a detailed study of the transition between them, unobscured by classical chaos. An unstable elliptical orbit appears in trajectories just in this neighbourhood. Fast Fourier Transforms of the dynamical variables (x, z) revealed that additional frequencies (distinct from the fundamentals characterizing stable quasiperiodic motion) appear and fundamental peaks broaden when this elliptical motion is evident.

A much closer and revealing comparison between classical SCF and true classical dynamics is obtained by the application of canonical perturbation theory to the zero-order CSCF Hamiltonian, to obtain first-order corrections to the motion and second-order perturbation energies. When the true classical motion is boxlike, with constants of the motion J_x, J_z, the perturbed SCF approximation is extremely accurate. It quantitatively reproduces Poincaré surfaces-of-section, trajectory projections including caustics and closely approximates the Fourier series expansions of dynamical variables. The "torus-preserving" character of the CSCF and perturbed SCF descriptions suppresses or ignores higher-order periodic resonances which cause frequent disruption of the motion, as was illustrated for a 3:5 resonance at $R = 4.30$ a.u. and $E = 46.0$ c.e.u. We even found it possible to extend perturbed SCF descriptions based on boxlike motion into regions where the actual motion belongs to the 1:1 quasiperiodic family. This was done by plotting J_z against J_x for regions where the true motion is boxlike and interpolating a polynomial fit across the "gap" between them. The interpolated "actions" were used to construct zero-order and perturbed CSCF solutions hypothetically valid when the true motion is of the 1:1 resonant type. The second-order perturbation energies are continuous across the bifurcation and increase gradually until the expected divergence is encountered in a narrow region about the 1:1 resonance of the SCF frequencies. The first-order perturbed SCF trajectories were compared qualitatively with a sequence of true motions by doubling each with its mirror-image trajectory for motion in the alternate potential valley. The perturbation analysis made a remarkable effort to localize trajectories in the diagonal valleys. Surprisingly, it was also able to pinpoint the location of the bifurcation through topological changes in Poincaré surface-of-section curves. The enhancement of the CSCF description by low-order perturbation theory results in deeper understanding of the nature of the classical dynamics.

We conclude first of all that the utility of classical bound state methods to determine eigenvalues by quantizing quasiperiodic trajectories is severely limited for a molecular oscillator system of this type. In contrast to the nearly harmonic systems studied in most previous molecular applications, this system does not exhibit the necessary "separability" in the stringent, KAM sense. If the surface studied here is at all representative of strongly nonharmonic vibrational systems, classical bound state eigenvalue methods may not be widely useful in such systems. Recent literature shows a decline of interest in calculating classical eigenvalues themselves, but there is continuing interest in more general relations between periodic trajectories, chaotic motion and quantum behaviour. In anharmonic nonseparable systems of the type we have studied, classical mechanics is hypersensitive at even the lowest energies to details of the potential surface which reorganize the motion [40]. By contrast, quantum mechanics is unable to view these details at such low energies because of coherence and symmetry of eigenfunctions and limited resolution associated with de Broglie wavelengths. The mode separation enforced by the classical SCF scheme suppresses the host of interactions that complicate the true classical dynamics, and therefore more closely simulates the quantum behaviour for cases where an SCF separation is physically appropriate.

It is interesting to note, however, that the features picked up in detail by the classical mechanics at low energies do have analogies in quantum behaviour at higher energies [41]. The unstable elliptical orbit seen in the true motion at the bifurcation and the 1:1 periodic orbit lying at the centre of the 1:1 resonant family of regular motions each correspond to quantum mechanical analogues. These are respectively the "angular" (destabilized) and "radial" (stabilized) eigenfunctions which are formed at avoided crossings between SCF levels differing by the exchange of x and z quanta. This shows clearly that *unstable* as well as stable periodic orbits in the classical dynamics have counterparts in quantum eigenstates.

It may be asked in conclusion whether an exhaustive study of the true classical dynamics in a nonseparable, nonharmonic system of this type has any ultimate utility for an understanding of its quantum behaviour. While this study permits little or nothing to be said about the meaning of the term "quantum chaos" [42,43], it is clear that the appearance of classical chaos in such a system has no connection to what happens in the quantum system at similar energies [44]; whether any relation exists between phase space distributions of irregular trajectories and quantum behaviour at higher energies [45] has not been shown in this work.

Bibliography

[1] V. C. Epa, J. H. Choi and W. R. Thorson, *J. Chem. Phys.*, **92**, 466 (1990).

[2] V. C. Epa and W. R. Thorson, *J. Chem. Phys.*, **92**, 473 (1990).

[3] V. C. Epa and W. R. Thorson, *J. Chem. Phys.*, **93**, 3773 (1990).

[4] (a) R. A. Leacock and P. W. O'Connor, *J. Comp. Phys.*, **62**, 164 (1986); (b) C. Jaffe and W. P. Reinhardt, *J. Chem. Phys.*, **77**, 5191 (1982); (c) R. S. Judson, S. Shi and H. Rabitz, *J. Chem. Phys.*, **90**, 2274 (1989).

[5] (a) M. V. Berry, *J. Phys. A*, **10** 2083 (1977); (b) C. W. Eaker, G. C. Schatz, N. De Leon, E. J. Heller, *J. Chem. Phys.*, **81**, 5913 (1984); (c) R. T. Swimm and J. B. Delos, *J. Chem. Phys.*, **71**, 1706 (1979); (d) Eric J. Heller, *J. Chem. Phys.*, **92**, 1718 (1990); (e) G. Radons, T. Geisel and J. Rubner, *Adv. Chem. Phys.*, **73**, 891 (1989).

[6] (a)Stu Borman, *Chem. & Eng. News*, **69**, 18 (1991); (b)R. V. Jensen, *Amer. Scientist*, **75**, 168 (1987); (c)A. A. Chernikov, R. Z. Sagdeev and G. M. Zaslavsky, *Physics Today*, **41**, 27 (1988); (d)Gary Taubes, *Discover*, 63 (May 1989).

[7] E. N. Lorenz, *J. Atmos. Sci.*, **20**, 130 (1963) (for a precise of this work see: James Gleick, *Chaos: Making a New Science*, (Viking, 1987)).

[8] Michael Tabor, *Adv. Chem. Phys.*, **46**, 73 (1981).

[9] Linus Pauling and E. Bright Wilson, Jr., *Introduction to Quantum Mechanics*, (Dover, 1935). [See in particular: D. R. Hartree, *Proc. Camb. Phil. Soc.*, **24**, 89, 111, 426 (1928).]

[10] (a) Leonard I. Schiff, *Quantum Mechanics*, (McGraw-Hill, 1955). [See in particular: V. Fock, *Z. f. Phys.*, **61**, 126 (1930) and J. C. Slater, Phys. Rev., **35**, 210 (1930).]; (b) P. O. Lowden, *J. Chem. Phys.*, **18**, 365 (1950).

[11] J. M. Bowman, *Acc. Chem. Res.*, **19**, 202 (1986) and references contained within.

[12] H. J. Korsh and H. Laurant, *J. Phys. B*, **14**, 4213 (1981), *J. Phys. B*, **15**, 1 (1982).

[13] S. Y. Lee and J. C. Light, *Chem. Phys. Lett.*, **25**, 435 (1974).

[14] W. E. Milne, *Phys. Rev.*, **35**, 863 (1930).

[15] R. B. Gerber and Mark Ratner, *Adv. Chem. Phys.*, **70**, 97 (1988).

[16] (a)R. B. Gerber and Mark Ratner, *Chem. Phys. Lett.*, **68**, 195 (1979); (b) Mark Ratner, V. Buch, and R. B. Gerber, *Chem. Phys.* **53**, 345 (1980).

[17] J. Mathews and R. L. Walker, ***Mathematical Methods of Physics***, (W. A. Benjamin, 1964).

[18] J. N. L. Connor, *Mol. Phys.*, **15**, 621 (1968).

[19] M. S. Child, *Mol. Phys.*, **12**, 401 (1967).

[20] H. Poincaré, ***New Methods of Celestial Mechanics***, Transl. 1967 NASA Doc# N67-27279.

[21] Herbert Goldstein, ***Classical Mechanics***, Second Edition, (Addison Wesley, 1980).

[22] D. W. Noid, M. L. Koszykowski and R. A. Marcus, *Ann. Rev. Phys. Chem.*, **32**, 267 (1981).

[23] D. W. Noid and R. A. Marcus, *J. Chem. Phys.*, **85**, 3305 (1986).

[24] Ian C. Percival, *Adv. Chem. Phys.*, **36**, 1 (1977).

[25] A. N. Kolmogorov, *Doc. Akad. Nauk.*, **98**, 527 (1954); A. N. Kolmogorov, *Proc. Int. Cong. Math.* (North-Holland, 1957) [English translation: R. Abraham, ***Foundations of Mechanics***, (W. A. Benjamin, 1967)].

[26] V. I. Arnold, ***Russian Math. Surv.***, **18**, 9 (1963); **18**, 85 (1963).

[27] A. Moser, ***Nachr. Akad. Wiss. Göttingen***, 1 (1962); A. Moser, "Stable and Random Motions in Dynamic Systems", ***Annals of Mathematical Studies***, No. 77, (Princeton Press, 1973).

[28] (a) Eric Aubanel and David Wardlaw, *J. Chem. Phys.*, **88**, 495 (1988); (b) M. Founargiotakis, S. C. Farantos and J. Tennyson, *J. Chem. Phys.*, **88**, 1598 (1988); (c) M. A. Mehta and N. DeLeon, *J. Chem. Phys.*, **89**, 882 (1988); (d) J. H. Frederick and G. M. McClelland, *J. Chem. Phys.*, **84**, 4347 (1986).

[29] D. W. Noid, M. L. Koszykowski and R. A. Marcus, *J. Chem. Phys.*, **67**, 404 (1977); D. W. Noid and R. A. Marcus, *J. Chem. Phys.*, **67**, 559 (1977). D. W. Noid, M. L. Koszykowski and R. A. Marcus, *J. Chem. Phys.*, **71**, 2864 (1979); D. W. Noid, M. L. Koszykowski and R. A. Marcus, *J. Chem.Phys.*, **78**, 4018 (1982).

[30] R. A. Marcus, *Farad. Dis. Chem. Soc.*, **55**, 34 (1973).

[31] Walter Eastes and R. A. Marcus, *J. Chem. Phys.*, **61**, 4301 (1974)

[32] D. W. Noid and R. A. Marcus, *J. Chem. Phys.*, **62**, 2119 (1974).

[33] A. Einstein, *Verhand. Deut. Phys. Ges.*, **19**, 82 (1917) [nicely discussed in Percival's review].

[34] (a)C. C. Martens and G. S. Ezra, *J. Chem. Phys.*, **83**, 2990 (1985); (b)C. C. Martens and G. S. Ezra, *J. Chem. Phys.*, **86**, 279 (1987); (c)G. S. Ezra, C. C. Martens and L. E. Fried, *J. Phys.Chem.*, **91**, 3721 (1987); (d)A. Garcia-Ayllon, C. C. Martens, J. Santamaria and G. S. Ezra, *J. Chem. Phys.*, **87**, 6609 (1987).

[35] E. Oran Brigham, *The Fast Fourier Transform and its Applications*, (Prentice Hall, 1988).

[36] Roland Bulirsch and Josef Stoer, *Numer. Math.*, **8**, 1 (1966).

[37] (a)K. S. Sorbie and N. C. Handy, *Mol. Phys.*, **32**, 1327 (1976); (b)K. S. Sorbie, *Mol. Phys.*, **32**, 1577 (1976); (c) Grayson H. Walker and Joseph Ford, *Phys. Rev.*, **188**, 416 (1969).

[38] Robert L. Devaney. *An Introduction to Chaotic Dynamical Systems*, (Addison-Wesley, 1989).

[39] M. Founargiotakis, S. C. Farantos, G. Contopoulos, and C. Polymilis, *J. Chem. Phys.*, **91**, 1389 (1989).

[40] R. S. Judson, S. Shi, and H. Rabitz, *J. Chem. Phys.*, **90**, 2263 (1989).

[41] Craig C. Martens, Robert L. Waterland and William P. Reinhardt, *J. Chem. Phys.*, **90**, 2328 (1989).

[42] Eric J. Heller, "Quantum Chaos", *Lecture Notes in Physics*, 263, (1986).

[43] Eric J. Heller, *J. Chem. Phys.*, **92** 1718 (1990).

[44] Stuart A. Rice and Ronnie Kosloff, *J. Phys. Chem.*, **86**, 2153 (1982).

[45] James L. Anchell, *J. Chem. Phys.*, **92**, 4342 (1990).